DIFFUSION-CONTROLLED OXIDATION OF BINARY ALLOYS WITH SPECIAL REFERENCE TO NICKEL-IRON ALLOYS

DIFFUSION-CONTROLLED OXIDATION OF BINARY ALLOYS WITH SPECIAL REFERENCE TO NICKEL-IRON ALLOYS

by

ASHOK DATTATRAYA DALVI, B.Tech.

A Thesis
Submitted to the School of Graduate Studies
in Partial Fulfilment of the Requirements
for the Degree
Doctor of Philosophy

McMaster University
January 1971

DOCTOR OF PHILOSOPHY (1971)
(Metallurgy and Materials Science)

McMASTER UNIVERSITY
Hamilton , Ontario

TITLE: Diffusion-Controlled Oxidation of Binary Alloys with Special Reference to Nickel-Iron Alloys

AUTHOR: Ashok Dattatraya Dalvi, B. Tech. (Indian Institute of Technology, Bombay)

SUPERVISOR: Professor W. W. Smeltzer

NUMBER OF PAGES: xvii, 310

SCOPE AND CONTENTS

This investigation is concerned with the development of a general ternary diffusion analysis for the diffusion-controlled oxidation of binary alloys based on the concept of local equilibrium and phenomenological diffusion theory and its application to appropriate experimental systems.

The theoretical analysis is in two parts. In the first part diffusion equations for the alloy and oxide phases are obtained and tested against experiments for Ni-10.9% Co alloy at 1000°C. In the second part phenomena observed in binary alloy oxidation such as supersaturation, internal oxidation and morphological instability are qualitatively discussed and the concept of the stationary diffusion path on the isotherm is applied to binary alloy oxidation. In general the ternary diffusion analysis satisfactorily accounts for the diffusion-controlled oxidation properties of several binary alloys.

An experimental investigation of the oxidation of nickel-iron alloys at 1000°C is described. In the first part of the experimental investigation, thermodynamics of the ternary iron-nickel-oxygen system at 1000°C has been investigated in support of the oxidation studies. The second part is comprised of a detailed kinetic and metallographic study of nickel-iron alloys containing upto 25% iron exposed to oxygen atmospheres at 1000°C and determination of the metal concentration profiles in the oxide and alloy phases. The experimental results for these alloys are in good agreement with the theoretical calculations.

ACKNOWLEDGMENTS

I wish to thank my supervisor, Dr. W. W. Smeltzer, for his continuing guidance, encouragement, help and friendship throughout the course of this study. Drs. J. S. Kirkaldy and G. R. Purdy have been especially kind in their interest and encouragement. I feel privileged for the attention and encouragement I received from Dr. Carl Wagner of Max-Planck-Institut für Physikalische Chemie, Göttingen, Germany. I thank Dr. Denton Coates for his warm friendship and his collaboration in formulation of the theory of alloy oxidation. I am indebted to many of the faculty, post-doctoral fellows, graduate students and technical staff in the Department of Metallurgy and Materials Science for their helpful discussions and aid. The manuscript was typed with skill and remarkable patience by Mrs. H. Kennelly, to whom I give special thanks.

I appreciate the help offered by Mr. A. Batt of International Nickel Company of Canada, J. Roy Gordon Research Laboratory, Clarkson, Ontario in obtaining the chemical analyses of the alloys used in this investigation.

Finally, I gratefully acknowledge the following groups for their financial support: the International Nickel Company of Canada, the Department of Metallurgy and Materials

Science (each in the form of graduate fellowships), the Defence Research Board of Canada and the National Research Council of Canada (each in the form of research grants to Dr. Smeltzer).

TABLE OF CONTENTS

LIST OF ILLUSTRATIONS

LIST OF TABLES

CHAPTER 1

INTRODUCTION

1.1 OXIDATION OF METALS-MECHANISMS AND RATE LAWS

Metals and alloys are important structural materials. Unfortunately, metals with a few exceptions react with the environment which may contain oxygen, nitrogen, sulfur or other oxidizing gases and vapours. From a practical point of view it is necessary to prevent or slow down such processes, normally designated by the term "oxidation". Equilibrium data govern the oxidation of metals to the extent that they determine which compounds, if any, are formed, but the rate at which formation occurs is a kinetic problem. The study of oxidation of metals and alloys is thus a study of their response to various environments under various conditions of temperature and pressure. The mechanisms of reaction are concomitantly variable.

When a clean surface of a metal or an alloy is exposed to the attack of a gas such as oxygen, the reaction begins at the metal-gas interface, and unless the reaction products are volatile, they form an intermediate layer between the metal and the gas. At high temperatures where many alloys find application, diffusion of the reacting species through this layer frequently becomes the rate controlling process. It is the purpose of this work to study the diffusion-controlled oxidation of binary alloys in the simplest environments, namely, pure oxygen. A reaction temperature of 1000°C was chosen for several reasons. Firstly, this temperature is sufficiently high that diffusion control is favoured. Secondly, it is the highest temperature at which experimental work can be carried out with facility and without serious materials handling problems. Thirdly, much related work has been carried out at this temperature and hence values of many of the thermodynamic and kinetic parameters required for theoretical analysis are available.

In reviewing the literature on oxidation of these materials, we begin with the simplest case, viz., pure metals since the mechanisms and rate laws for pure metals are often applicable with modification and generalization to the oxidation of alloys. We also discuss the diffusion-controlled mechanism of metal oxidation in the total context of gas-solid reactions and the various mechanisms related to these reactions.

The overall reaction in the oxidation of a metal may be simply characterized as the combination of oxygen with the metal to form an oxide of the metal. Yet in reality the process is very complex since the reaction mechanism and oxidation behaviour of the metal depend upon a large number of variables. The initial step in the metal-oxygen reaction involves the adsorption of the gas on the metal surface. As reaction progresses, oxygen may dissolve in the metal and then form oxide on the surface either as a film or as discrete oxide nuclei. Both adsorption and initial oxide formation are functions of surface orientation, surface preparation, crystal defects at the surface, and impurities in the metal and the gas.

The various phenomena in metal-gas reactions may be related to the zones of chemical activity, viz., the gas phase, the oxide-gas interface, the oxide phase, the metal-oxide interface and the metal phase. Two further factors must be recognized as related to the formation, composition and structure of the oxide film or scale, viz., the thermodynamic stability of the oxide formed and the crystal structure of the oxide layer and of the metal which determine the adhesion between the oxide layer and underlying metal.

1.2 WAGNER'S MODEL FOR PARABOLIC OXIDATION KINETICS

The surface oxide frequently appears as a compact phase separating the metal and oxygen gas. Continuous reaction is then possible only via solid state diffusion of the reactants through the film. As a limiting case when diffusion in an electroneutral zone of the oxide layer is the rate determining process, the course of the reaction can be described by the parabolic law of Tammann(1) and Pilling and Bedworth(2). The layers that are formed in such a case are relatively thick ($>1\mu$). Deviation from the parabolic law of scale formation, for example, growth relations like linear, asymptotic and logarithmic, are attributed to phase boundary control, breakdown and spalling of the oxide layer, short circuit diffusion and transport in an electrical field.

Wagner(3,4,5,6) formulated a quantitative theory for parabolic growth of thick oxide filmes, which has since been tested and verified by several investigators. He postulated that the diffusing species in the oxide scale are ions and electrons which migrate independently. The prerequisite for an ionic species to be mobile is that its sublattices contain point defects such as interstitial ions and vacancies. Reactions at the oxide-gas and oxide-metal interfaces are considered to be sufficiently rapid for local equilibrium to be established at these interfaces. Diffusion is assumed to be the rate determining process and conditions of ambipolar diffusion are assumed to exist. Wagner defined a rational reaction rate constant, k_r, by the equation,

$$\frac{dx}{dt} = V_{eq.} \frac{k_r}{x} \qquad (1\text{-}1)$$

where $\frac{dx}{dt}$ is the rate of thickening of the oxide scale, t is time and V_{eq} is the equivalent volume of the oxide. On the basis of the above assumptions, expressions involving either electrical conductivities or diffusion coefficients were derived for the parabolic rate constant. The expression for the rate constant k_r involving diffusion coefficients is

$$k_r = C_i \int_{a_X^{(m)}}^{a_X^{(s)}} (D_M \frac{z_C}{z_X} + D_X) d\ln a_X \qquad (1\text{-}2)$$

where $C_i = z_M C_M = z_X C_X$ is the concentration of metal or nonmetal ions in the oxide in equivalents per cubic centimeter, a_X is the thermodynamic activity of the nonmetal, and D_M and D_X are the self-diffusion coefficients of the metal and nonmetal, respectively. The superscripts (m) and (s) refer to the oxide-metal and oxide-gas interfaces, respectively.

In Wagner's parabolic oxidation theory, it is assumed that the oxide is homogeneous and does not contain structural irregularities such as pores, grain boundaries or dislocations. Investigations on oxide films by electron microscopy, x-ray diffraction techniques and studies of nucleation of oxide on metal surfaces show that these assumptions may be an oversimplification. Furthermore, diffusion studies in polycrystalline materials have shown that such structural defects act as low resistance paths and may be an important mode of transport, especially at intermediate temperatures.

The minimum temperature at which the mobility of the ions ensures the attainment of true local thermodynamic equilibrium can be estimated by Tammann's rule which relates the temperature T_d, at which lattice diffusion first becomes appreciable, to the absolute melting point (m.p.) T_m° K(7)

$$\left.\begin{array}{ll} \text{for metals} & T_d \simeq 0.33\ T_m \\ \text{for salts, oxides, etc.} & T_d \simeq 0.57\ T_m \\ \text{for covalent compounds} & T_d \simeq 0.90\ T_m \end{array}\right\} \qquad (1\text{-}3)$$

For most metals this temperature is sufficiently low. However for oxides, which usually have very high melting points, this temperature may be fairly high. For NiO with m.p. at 1960°C, T_d is approximately 1000°C; for FeO with m.p. at 1454°C, T_d is approximately 700°C. For most oxides it lies within this range. It is in the temperature range immediately below T_d that short circuit diffusion becomes important.

Smeltzer et. al.(8) have proposed a theory to describe the non-parabolic oxidation kinetics of titanium, hafnium and zirconium. In this theory, lattice diffusion and diffusion along low resistance paths, which decrease in density with time, were assumed to occur simultaneously. Irving(9) proposed a model for non-parabolic oxidation based upon a combination of diffusion along grain boundaries and lattice diffusion. More recently, Perrow, Smeltzer and Embury(10) have employed the above concepts based upon short-circuit diffusion of reactants to explain the non-parabolic oxidation kinetics of nickel. In these analyses, the contribution of the grain boundary diffusion to the effective diffusion coefficient, D_{eff}, is weighted according to the grain size.

$$D_{eff} = D_L(1-f) + D_B f \qquad (1\text{-}4)$$

where D_L and D_B are the lattice and boundary diffusion coefficients, respectively. f is the fraction of available sites lying within the low resistance paths and is inversely proportional to the grain size.

At temperatures sufficiently above T_d, $D_L \sim D_B$ and hence $D_{eff} \sim D_L$. At temperatures much below T_d, D_L is considerably smaller than D_B and hence D_{eff} is a function of grain size. Although at these temperatures the grain size increases rapidly initially, it remains essentially constant at long times, that is, f is a constant at long times. D_{eff} in Eq. (1-4) is therefore constant and a parabolic behaviour is to be expected except during initial stages. Use of Wagner's parabolic oxidation theory at these temperatures is therefore justified even though short circuit diffusion occurs. However, the diffusion coefficient used in the analysis should be the one computed from Eq. (1-4).

1.3 STRESS GENERATION AND RELIEF IN OXIDE FILMS

An important aspect of metal oxidation is the stress generation and relief in growing oxide films. Two types of stresses are generated in the process of oxidation. Most oxides have a specific volume which is different than the metals from which they form. This effect and the requirement of coherency at the metal-oxide interface result in stress development during growth. The other type of stresses result from thermal cycling of the specimen. These are produced due to differential thermal expansion or contraction of the oxide and metal. Here we are mainly concerned with the stresses developed during growth of oxide.

If the stresses in a film are sufficiently high, relief will occur by fracture of the oxide or by plastic deformation of either the film itself or the metal substrate. Parabolic oxidation of metals is controlled by ion diffusion through the film. Fracture of the film permits direct access of the oxidant to the metal, and the oxidation kinetics may undergo a transition from parabolic kinetics to linear kinetics until the film is repaired or a new film has grown. Plastic deformation of the oxide which relieves stresses sustains a lower rate of oxidation than would be expected if fracture occurred.

The effect of lateral compressive stresses in oxide films can lead to blistering if film adhesion is weak or to shear cracking if film adhesion is strong.

Oxide plasticity has an important effect on the defect structures of the scale. The outward migration of cations through a p-type metal deficit oxide results in inward migration of vacancies and their subsequent condensation at the metal-oxide interface. If the oxide plasticity is low, then the annihilation of vacancies by plastic flow in the oxide is difficult resulting in high porosity of the scale. This occurs in NiO.

Excellent summaries of the role of oxide plasticity in the oxidation behaviour of metals are presented by Douglass (11) and Stringer (12).

1.4 OXIDATION OF ALLOYS-CLASSIFICATION OF MODES OF OXIDATION (13)

As in the case of pure metals, the course of oxidation of alloys can be described by the parabolic rate law when diffusion is the rate controlling process. However, even in this case the oxidation mechanism for most alloys is considerably more complicated than for pure metals.

The binary oxides of the alloy components, formed during oxidation may be completely miscible producing an oxide solid solution, may be completely or partially miscible producing multiphase scales or they may form complex mixed oxides such as spinels. For an alloy AB, in which A is the more noble metal and B is the less noble metal, there will exist a relatively narrow composition range near pure A where AO is produced almost exclusively, a relatively wide composition range near pure B where BO is produced exclusively and an intermediate composition range where both AO and BO are produced.

Moreau and Benard (14) presented a general classification of these different modes based on experimental observations. their classification is as follows :

Class I

In this class only one of the alloying elements, B, oxidizes under the prevailing conditions giving BO.

(a) The solute element B oxidizes under the given conditions:

(i) internally, giving BO particles in a matrix of A, e.g. dilute Cu-Si alloys which oxidize internally to produce SiO_2 particles in a copper matrix [Fig. 1-1 (I_A^1)]. The oxygen pressure in the atmosphere is less than the equilibrium dissociation pressure of AO.

(ii) exclusively externally, giving a single layer of BO above an alloy matrix depleted in B, e.g., Cu-Si alloys richer in silicon producing an external SiO_2 layer [Fig. 1-1 (I_A^2)]. The oxygen pressure in the atmosphere is again generally less than the dissociation pressure of AO.

(b) The element B is now the major element and oxidizes exclusively:

(i) leaving the non-oxidizable metal A dispersed in BO, e.g., Cu-Au alloys rich in copper [Fig. 1-1 (I_B^1)].

(ii) leaving the non-oxidizable metal A in an A-enriched zone beneath the BO scale, e.g., Ni-Pt alloys [Fig. 1-1 (I_B^2)].

Class II

Both alloying elements oxidize simultaneously to give AO and BO, the oxygen pressure in the atmosphere being greater than the equilibrium dissociation pressures of both oxides.

(a) AO and BO are virtually insoluble in each other:

(i) The less noble metal B is the minor component. An

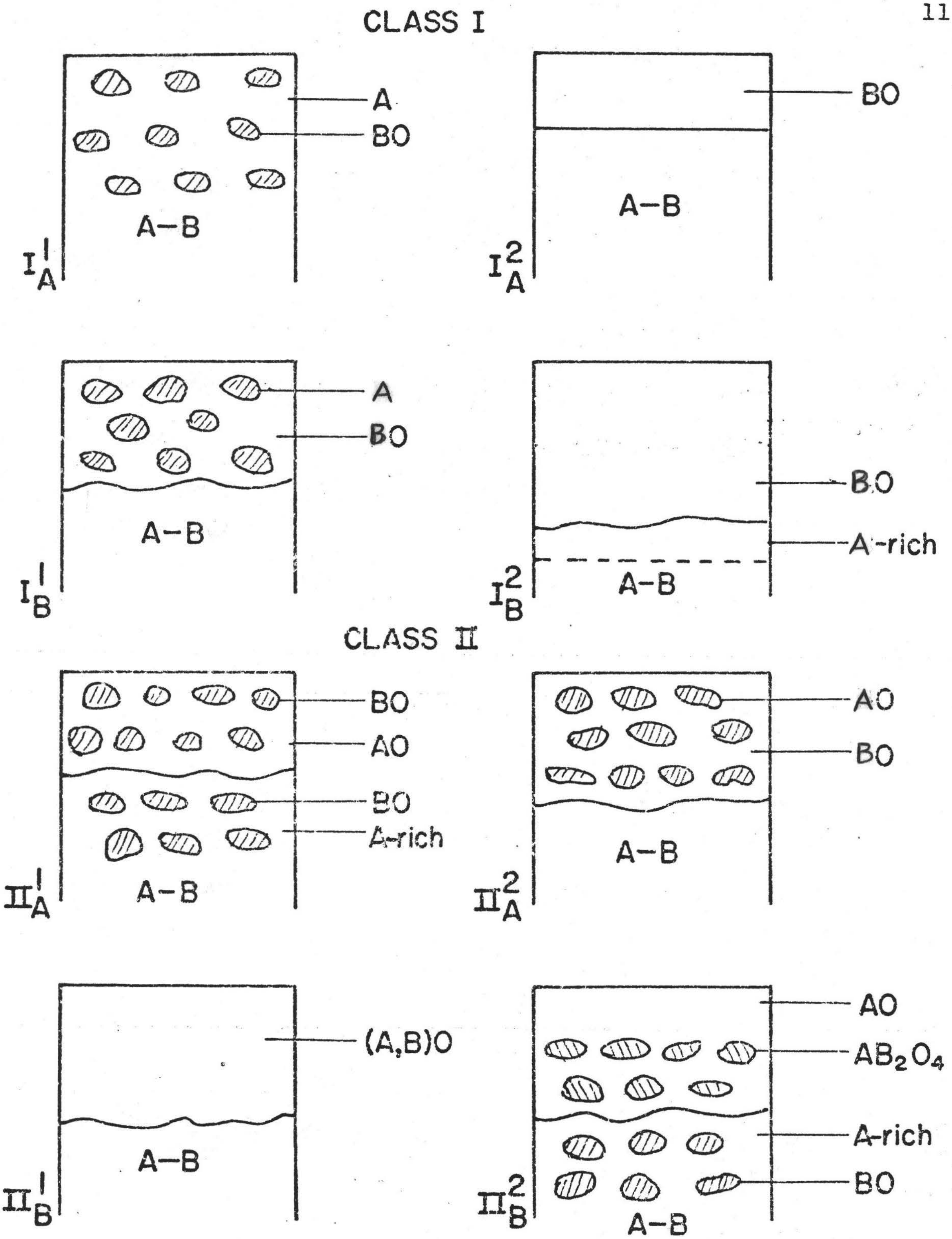

Fig. 1-1: Oxidation modes of binary alloys

internal oxide of BO lies beneath a two-phase layer AO-BO, eg., certain Cu-Ni alloys [Fig. 1-1 (II_A^1)].

(ii) The less noble metal is the major component so that no internal oxidation is now observed [Fig. 1-1 (II_A^2)], e.g., Cu-Ni alloys rich in Ni.

(b) AO and BO react to form a mixed oxide:

(i) AO and BO form a single solid solution (A,B)O, e.g., Ni-Co alloys [Fig. 1-1 (II_B^1)].

(ii) A double oxide is formed, often as a spinel, which may give a complete surface layer of variable composition or give particles incorporated into a matrix of AO with BO formed internally, e.g., dilute Ni-Cr alloys [Fig. 1-1 (II_B^2)].

In many alloy systems several types of behaviour are possible, depending on the composition, oxidation atmosphere, temperature, pressure, time, etc.

1.5 THE STRUCTURE OF OXIDES

1.5.1 Defect Structure and Nonstoichiometry of Oxides

An important class of ionic compounds to which most oxides belong are nonstoichiometric. That is, their chemical formulae cannot be written in terms of small integers. Any systematic treatment of nonstoichiometry must consider the following theoretical aspects:

(a) the mode of incorporation of stoichiometric imbalance in the crystal.

(b) the thermodynamic stability of the nonstoichiometric phase.

(c) the factors influencing the range of composition over which such phases can vary.

The stoichiometric excess or deficit may be incorporated in either the cation or anion sublattice. The corresponding excess charges must be incorporated either as electrons or as positive holes. Accordingly the oxide may be an n-type or a p-type semiconductor, respectively. The defects may be either of the Schottky type or the Frenkel type. The commonly found nonstoichiometric semiconductor oxides are normally divided into two classes:

1. Oxides with cation defects:
    (a) Metal deficient, with cation vacancies on the cation sublattice (p-type semiconductors) e.g., NiO, CoO, FeO.
    (b) Metal-excess, with interstitial cations (n-type semiconductors), e.g., ZnO.
2. Oxides with anion defects:
    (a) Oxygen deficient with oxygen ion vacancies on the anion sub-lattice (n-type semiconductors), e.g., Nb_2O_5, Ta_2O_5.

(b) Oxygen excess with interstitial oxygen ions (p-type semiconductors), e.g. UO_2.

When the concentration of defects is high, ordering of defects to yield superlattice structures or the formation of complex shear structures to accommodate the deficiency in one of the components (Magneli phases) is possible. These are complex phenomena which are not yet completely understood(7).

1.5.2 Mixed Oxide Systems

Since the oxides formed during the oxidation of alloys are necessarily mixed oxides, a brief discussion relating to such systems is in order. The simplest system is one in which a metallic component B dissolves in a binary oxide AO to only a limited extent and replaces A in the cation sublattice. The effect of foreign ion addition to nonstoichiometric oxides may be summarized in terms of the valence model of Schottky and Wagner(15) and Hauffe(16).

1. For n-type oxides ($A_{n+x}O$ or AO_{m-x}) additions of cations of valence higher than that of the cations in the parent oxide will decrease the concentration of oxygen vacancies (in AO_{m-x}) or the concentration of interstitial metal ions (in $A_{n+x}O$). Conversely, addition of cations of lower valence increase the corresponding point defect concentration.
2. For p-type oxides ($A_{n-y}O$ or AO_{m+y}), additions of cations of higher valence increase the concentration of metal ion

vacancies in ($A_{n-y}O$) or the concentration of interstitial oxygen ions (in AO_{m+y}) while cations of lower valence decrease the corresponding point defect concentrations. Additions of foreign ions with the same valence as that of the parent compound will not, according to the valence approach ,cause any change in the defect concentrations.

It is important to emphasize the underlying assumptions in arriving at these rules. The foreign cations are assumed to enter the normal cation positions in the parent oxide, and the effects are thus limited to the extent of solubility of the foreign cations. If the foreign ions enter interstitial positions or as misplaced ions, the rules do not apply and other equilibria must be considered. Effects other than that of valence, for example, size and strain are neglected. The point defects are assumed to be unassociated.

In a general discussion of mixed oxides it is found expedient to refer to structural types, e.g., rock salt (NiO), spinel ($NiFe_2O_4$) and ilmenite (Fe_2O_3). When the two binary oxides constituting a ternary oxide have the same structure, the mixed oxide phase may be regarded as a solid solution of the oxides, the range of which may be more or less restricted by the relative ionic radii of the cations. On the other hand, there are many mixed oxide phases for which this concept is confusing. It will be expedient in these cases to avoid the use of the concept of solid solutions and to think of such phases as being derived from binary oxides by cationic substitutions. This will be indicated by formulae like $Zn_xNi_{1-x}O$, the substituent being placed first in the formula.

One of the important types of oxide structures is the spinel type. Three common binary oxides having the type formula M_3O_4 have the spinel structure, viz., Fe_3O_4, Co_3O_4 and Mn_3O_4, which like the sodium chloride structure, may be described in terms of oxide ions in a close packed cubic arrangement. One half of the octahedral cavities (B-sites) and one eighth of the tetrahedral cavities (A-sites) are occupied by cations having the requisite valence to neutralize the charge of the oxide ions. The unit cell formula is $A_8B_{16}O_{32}$ where A and B represent the different cation sites. If the B-sites are occupied by one kind of ion only, the structure is referred to as a normal spinel. Co_3O_4 is thought to be of this type and may be written $[Co_8^{2+}]_A[Co_{16}^{3+}]_BO_{32}$ whereas in Fe_3O_4 the ferric ion is distributed over A and B sites $[Fe_8^{3+}]_A[Fe_8^{3+}Fe_8^{2+}]_BO_{32}$ and is called an inverse spinel. The deviation from stoichiometry of many phases with the spinel structure occurs in systems in which oxidation may occur or in which an ion of higher valence can be substituted for one of lower valence. Deviation from stoichiometry in spinel-like structure through the introduction of anion deficiencies or interstitial cations is not common. In addition to the defect types mentioned earlier, there are defect types which are specific to the spinel structure. These include lattice disorder, valence disorder and incomplete lattice. Since ternary spinels contain cations of two different types of valence, the influence of varying their proportion on the concentration of lattice defects is not very marked. Additionally, due to the complex structure of spinels, the cationic mobilities in this structure type are low.

A detailed discussion relating to the topics of crystal structure, defects, nonstoichiometry, thermodynamics and transport in binary and mixed oxide systems is to be found in references (16), (17), (18), (19) and (20). Schmalzried$^{(21)}$ has given a summary of a general treatment of defects and transport processes related to the ternary mixed oxides, especially with the spinel structure.

1.6 AIMS OF THE PRESENT INVESTIGATION

Although published analyses of diffusion-controlled alloy oxidation for certain limiting cases based on the pseudo-binary treatment are extensive, work based on a strict ternary approach is very recent. The major work in this field is that of Wagner$^{(22)}$ who gave a theoretical treatment for a ternary diffusion model wherein the concentration gradients of solute cations in the oxide scale are no longer linear. Coates and the author$^{(23)}$ have extended Wagner's model to include oxygen dissolution in the alloy. In the field of internal oxidation Kirkaldy$^{(24)}$ has presented an analysis based on the ternary approach. Although these analyses involve only single phase oxide layers on the alloy, it is possible to extend the treatment to more complex oxide scales. Our purpose in the present work is to utilize this generalized diffusion model together with the concept of diffusion path originally employed by Clark and Rhines(25) and further developed by Kirkaldy and coworkers(26,27), to give a methodology for presenting both the kinetic and thermodynamic aspects of alloy oxidation. Specifically, these concepts are utilized to describe the experimental investigation reported in this dissertation on the oxidation of binary nickel-iron alloys at 1000°C.

1.7 AN OUTLINE OF THE PRESENTATION TO FOLLOW

Oxidation properties of iron, nickel and iron-nickel alloys are summarized in Chapter 2 followed by a summary of the theoretical analysis of the diffusion-controlled oxidation of binary alloys in Chapter 3. The analysis in Chapter 3 is based on the pseudo-binary approach. In Chapter 4, a parallel analysis based on a more general ternary approach is developed. Though a considerable part of this analysis was developed by the author in collaboration with D. E. Coates, it was thought expedient to arrange it with the analysis of other coworkers, notably those of Wagner(22) and Kirkaldy(24), to preserve continuity and to give a comprehensive exposition of the ternary approach. The ideas developed in the theoretical analyses are used in the application of the diffusion path concept to the high temperature oxidation of binary alloys (Chapter 5).

Before proceeding to investigate the kinetics of oxidation of Ni-Fe alloys it was found necessary to investigate the thermodynamics of the ternary Fe-Ni-O system and its phase diagram at 1000°C. Results and discussion pertaining to this work are presented in Chapter 7. The knowledge of the thermodynamics and the phase diagram of the Fe-Ni-O system at 1000°C is utilized in conjunction with the theoretical analysis and the results of the investigation of the kinetics, the oxide-scale morphology and concentration profiles developed in the alloy and the oxide during the oxidation of Ni-Fe alloys at 1000°C (Chapter 8) as the basis of a semi-quantitative model for the oxidation of these alloys (Chapter 9).

Chapters 1 to 5 contain a general discussion on the oxidation of binary alloys. The various theoretical considerations discussed and developed in these chapters are applied subsequently to the study of oxidation of Ni-Fe alloys in pure oxygen at 1000°C.

CHAPTER 2

OXIDATION PROPERTIES OF IRON, NICKEL AND IRON-NICKEL ALLOYS

2.1 OXIDATION OF IRON

Darken and Gurry(28,29) determined the phase diagram of the binary Fe-O system in 1945. Their experimental results have since been verified by several other workers and found to be essentially correct. Three oxides of iron are stable at temperatures greater than 570°C, namely wustite (FeO) magnetite (Fe_3O_4) and hematite (Fe_2O_3) and these lead to formation of multilayered scales on iron at elevated temperatures. Excellent photomicrographs of the oxide layers are given by Paidassi(30).

2.1.1 Crystal Structure, Defects and Transport Mechanisms in the Oxides of Iron

Wustite can be regarded as having the NaCl-type structure, although due to its gross defect structure it is difficult to characterize its crystal structure precisely(7). Magnetite possesses the inverse spinel structure and hematite has the ilmenite structure (Section 1.5.2). In wustite the intrinsic disorder δ is greater than the maximum permitted number of defects and hence the composition range of wustite does not include the ideal stoichiometric compound FeO. In the case of $Fe_{1-x}O$ the minimum value of $x (0.051 \pm 0.002)$ is virtually independent of temperature between 600 and 1000°C and corresponds to the composition $Fe_{0.949}O$. The maximum value of x increases from 0.065 at 600°C to 0.120 at 1000°C thus illustrating the increasing permissible deviation from stoichiometry as the temperature rises (7). A large amount of work on the defect structure and thermodynamics of wustite phase has appeared in recent literature. Vallet and Raccah (31) suggested from their experimental observations that the wustite phase field is not a single phase field. Rather it is comprised of three different types of wustite. Carel (32,33) later reported confirmation of these findings. Rizo and Smith (34), however, do not confirm these findings. They obtained a non-linear variation of the slope of the composition-oxygen potential plot for wustite with temperature and deduced that the change in slope corresponds to a gradual degree of association of defects. Fender and Riley (35) who confirm the finding of three different types of wustite have disputed the observation of Rizzo and Smith. They conclude that the transition within the wustite phase fields are second order transitions. Several investigators (36,37,38,39) have found an apparent p to n transition in wustite in the temperature range 950° to 1300°C. However in recent investigations Kofstad and Hed (40) and Seltzer and Hed (41) discount such a possibility. They have proposed an interstitial-vacancy complex (V_{Fe} Fe_i V_{Fe}), either neutral or singly charged as constituting the defect configuration of wustite. Although the controversy is not yet resolved, a defect model for wustite with lattice defects consisting of vacant cation sites and positive holes will be adopted for the present. However, in using this model we realize that the Wagner-Schottky model of random unassociated defects is only approximately valid and deviations from theoretical results should be expected.

Fe^{+3} ions in magnetite show a slight preference for the tetrahedral sites due to a covalency effect whereas Fe^{+2} strongly favours the octahedral sites. This is the reason why magnetite is an inverse spinel. The crystal defects in magnetite are mainly confined to the cation sublattice. According to experimental data(42), the diffusion coefficient of iron in magnetite equilibrated with hematite at 1115°C is about 150 times greater than the self-diffusion coefficient of iron in magnetite equilibrated with wustite, although the change in the iron-to-oxygen ratio of magnetite at this temperature is only about 1 per cent. Hematite exhibits both cationic and anionic transport(43).

2.1.2 Oxidation Kinetics

For iron, oxidation kinetics are observed to be logarithmic below 200°C(44,45,46). Above this temperature the parabolic law is obeyed in oxygen and air(30,47,48,49). The mechanism of oxidation below 200°C appears to be associated with a thin film model. Simnad, Davies and Birchenall(48) determined the oxidation rates of iron to wustite, wustite to magnetite and magnetite to hematite at high temperatures and found that the parabolic law was obeyed. Himmel, Mehl and Birchenall(50) determined the self diffusion coefficients of iron in the three oxides at various temperatures above 700°C. The experimental oxidation rates were compared with the rates calculated by substitution into Wagner's theoretical rate equation [Eq.(1-2)]. Good agreement was obtained indicating validity of the diffusion-controlled oxidation for iron. Using metallographic techniques Paidassi(30) demonstrated that the rate of thickening of the oxide layers is parabolic and that the relative thicknesses of the layer are approximately 100:5:1 for $x_{FeO}:x_{Fe_3O_4}:x_{Fe_2O_3}$ and independent of time.

2.2 OXIDATION OF NICKEL

Nickel is attacked by oxygen at all temperatures. At low temperatures a tarnishing film of nickel oxide is formed, which grows according to a logarithmic law. At temperatures in the vicinity of 400°C, the empirical oxidation rate law has been reported both as cubic and logarithmic. Engell, Hauffe and Ilschner(51) explained the cubic rates by a model whereby the ion flux through the film is a function of the electric field strength and the concentration gradient. Uhlig, Pickett and MacNairn(52) reported logarithmic rates and found that the rate changed at the Curie temperature. The proposed mechanism was based on electron transfer from the metal to the oxide, and the observed rate change at the Curie temperature was associated with a change in the electron work function. At the temperatures in the vicinity of 400°C initial oxidation does not follow the parabolic rate law. However as the film thickness increases the space charge effects are reduced and a parabolic rate law is observed. Gulbransen and Andrew(53) observed parabolic behaviour for pure Ni at 500° and 600°C for long times. Perrow, Smeltzer and Embury(10) have employed the short circuit diffusion model involving diffusion along grain boundaries and dislocations to explain the non-parabolic oxidation kinetics of nickel at 500° and 600°C.

At higher temperatures nickel oxidizes according to the parabolic law. Various workers have determined the parabolic rate constant for Ni at temperatures between 650° and 1400°K(53,54,55,56,57,58).Reference (58) summarizes the values of k_p for nickel at different temperatures. It has been found that the values of k_p are sensitive to the purity of nickel used in the investigations. Gulbransen and Andrew(59) carried out a detailed theoretical analysis of the processes involved in high temperature oxidation of Ni and using transition state theory computed the values of k_p. They found a close agreement between calculated and observed values. Shim and Moore(60) used the Wagner theory to calculate the value of k_p and also found an excellent agreement with experimental values.

Controversy exists regarding the structure of the nickel oxide layer formed on pure nickel at high temperatures. Sartell and Li(56) found the oxide scale to consist of two distinct layers. They also found that platinum markers used in the experiment were located at the boundary between the two layers after oxidations. From these observations it was concluded that the growth of the outer layer was due to cation movement while the inner layer grows by anion movement. Similarly in the oxidation experiment carried out by Ilschner and Pfeiffer(61) on Ni-0.1 w/o (weight percent) Mn alloy at 1000°C the platinum wires lay in the middle of the scaling layer after experiment. The inner layer was found to be porous. Similar observations were also reported by Birks and Rickert(62). In the experiments carried out by Moore(63), Fueki and Wagner(64) and Mrowec(65) the markers were found to be located at the metal-oxide interface and not within the oxide scale. A critical discussion on the utility of marker experiments was given by Mrowec(66). Meussner and Birchenall(67) explained the anomalous position of the markers in the oxide layer by an "undercutting" mechanism.

In considering the structure of the oxide layer it should be remembered that in metal defecit p-type semiconducting oxide scales the reaction proceeds through outward migration of cations. This results in the formation of a "metal consumption" zone according to Dravnieks and McDonald(68). The resultant scale structure ultimately consists of an inner equiaxed, highly porous, fine grained layer and an outer, dense columnar layer(11). Unless the oxide scale is sufficiently plastic, vacancy condensation at the metal-oxide interface must lead to high porosity or complete detachment of the oxide from the metal. Rhines and Wolf(69) have recently proposed a model for NiO scale formed on pure nickel to explain the stresses created during oxidation. According to their model, secondary oxide is formed along the grain boundaries at a later stage by inward migration of oxygen along the grain boundaries.

Although there is much conflict in the literature, it appears that, if the temperature is high enough, a single-layer dense scale forms, while at lower temperatures a duplex scale is formed(11). Mrowec(70) has proposed that the single-layer scale results when sufficient oxide plasticity occurs to enable the voids to be closed by plastic flow. Alternatively, a high purity nickel oxidized at a given temperature at which the oxide is plastic should form a single-layer scale, but a less pure nickel oxidized at the same temperature might form a duplex scale. Menzies and Stafford(71) performed creep tests on two grades of nickel which had been oxidized to completion. These were approximately 99.0% and 99.99% Ni. The impure nickel obviously formed a solid solution when oxidized to NiO and exhibited much greater creep strength than the high purity NiO. Vasyutinsky and Kartmazov(72) found that a single-layer scale formed on 99.98% Ni but a duplex scale formed on 99.5% Ni when oxidized at 1180°C.

Inert markers placed on the surface of a metal may upon oxidation end up (1) at the metal-oxide interface, if outward cation diffusion is rate controlling; (2) at the oxide-gas interface, if inward anion diffusion is rate controlling; or (3) imbedded in the oxide, if both species diffuse. Outward cation diffusion is associated with inward vacancy diffusion, which as mentioned previously, is usually manifested as the formation of pores in the oxide near the oxide-metal interface. An alternative explanation for the imbedding of the marker within the scale was given by Tylecote(73) in terms of three factors: relatively plastic oxide scale, inward diffusion of oxygen, and decreasing rate of vacancy diffusion compared to the rate of vacancy formation.

Nickel oxide is a p-type metal deficit semiconductor, the defects in this oxide being nickel vacancies and positive holes. Bliznakov et. al(74), Mitoff(75) and Tretyakov and Rapp(76) have found that the vacancy concentration in NiO at 1000°C is of the order of 10^{-4}. However, the degree of ionization of the vacancies in nickel oxide has been a matter of discussion. On the basis of studies on the dependence of electrical conductivity of single crystals of NiO on oxygen pressure, Mitoff(75) concluded that nickel vacancies were doubly ionized at high temperatures. On the basis of e.m.f. measurements Tretyakov and Rapp(76) came to the same conclusion. Pizzini and Morlotti(77) interpreted their results obtained from polycrystalline material in a similar way. On the other hand, results of several other investigations(78,79,80,81,82) indicate that the defects in NiO are singly ionized. Fueki and Wagner(64) derived the self-diffusion coefficient of nickel in NiO as a function of the partial pressure of oxygen for various temperatures in the range 1000-1400°C from the measurement of parabolic rate constant for pure nickel. Their data indicate that D_{Ni} is independent of the oxygen pressure at pressures lower than about 10^{-6} atm, whereas at higher oxygen pressures the self-diffusion coefficients of nickel is a function of p_{O_2} according to the equation

$$D_{Ni} = \text{const.}\ p_{O_2}^{1/n} \qquad (2\text{-}1)$$

the value of n decreasing with increasing temperature. Fueki and Wagner explained their data by assuming the existence of singly charged vacancies at high temperatures and doubly charged vacancies at lower temperatures. They explained the constant value of D_{Ni} at lower pressures by assuming a Schottky or Frenkel defect model for NiO at these pressures. Mrowec(65) has proposed an explanation of these results by consideration of intrinsic electronic defects. However, in the light of more recent investigations, this explanation seems improbable. Jarzebski and Mrowec(83) have recently proposed a complex defect structure model for NiO. According to their model the defects in NiO at very low partial pressures of oxygen consist of nickel ion interstitials and vacancies (Frenkel defect), doubly charged nickel vacancies and positive holes at intermediate pressures and vacancy-interstitial complexes similar to those proposed by Kofstad and Hed(40) for wustite in high oxygen pressure range. This model according to Jarzebski and Mrowec reconciles all available results on the defect structure of nickel oxide.

Volpe and Reddy(84) have recently completed an extensive investigation on cation diffusities and on defect structure of high purity NiO above 1182°C. They find the conductivity of NiO varies with $p_{O_2}^{1/n}$ where n is between 4 - 6. n increases with decreasing temperature. In view of their findings Volpe and Reddy explained the defect structure model for NiO in terms of singly and doubly charged vacancies and electron holes.

In summary, it may be stated that the duplex scale model of NiO formed on pure nickel involving anion transport in the oxide does not appear to be well substantiated. The overwhelming evidence favours cation transport in NiO. The formation of duplex scale is associated with the mechanical properties of the oxide, which are in turn governed by the temperature and the impurity content. Various defect configurations for NiO involving doubly charged vacancies, singly charged vacancies, vacancy-interstitial complexes or combinations of these have been proposed. Of these, the defect model consisting of doubly charged vacancies is, theoretically the simplest to consider. On the foregoing basis and on the basis of recent work by Tretyakov and Rapp(76) we will accept this model, although deviations are expected. At 1000°C, which is above the Tammann temperature for NiO, grain boundary diffusion will not be important. The oxidation of pure Ni at 1000°C is thus assumed to be mainly controlled by volume diffusion through NiO layer. The mean value of k_p for Ni at this temperature is 1.5×10^{-10} $g^2cm^{-4}sec^{-1}$ (53,55,56,57,58,59).

2.3 OXIDATION OF IRON-NICKEL ALLOYS

Wulf et al.(85) studied oxidation of iron-nickel alloys over the entire range of composition. According to Wulf et al.(85) and Foley(86) iron-nickel alloys can be divided into four major types: (1) alloys containing up to 2% Ni which exhibit scales similar to those found on pure iron; (2) alloys containing approximately 2-30% Ni which show a great deal of Ni enrichment at the alloy-oxide surface so that wustite is no longer one of the stable oxides; (3) alloys containing 30-75% Ni. The kinetics of reaction of alloys in this range is governed primarily by the formation and growth of the Ni-containing spinel; (4) nickel rich alloys containing 75-100% Ni. The scales formed on these alloys consist of NiO and spinel. All alloys show an extensive enrichment of nickel at the alloy-oxide interface. Subscale formation is observed in all types. Foley(86) has published a survey of the oxidation properties of iron-nickel alloys.

Menzies and Tomlinson(87) studied oxidation of Fe-2.3% Ni alloy in CO_2 at 600-1000°C. The oxide scale on this alloy consisted of a thick outer layer of spinel and a thinner inner layer of wustite. During the parabolic oxidation stage a continuous nickel-rich rim was built up in the alloy at the alloy oxide interface. Some wustite was precipitated in the alloy inside the nickel-rich region. Morris and Smeltzer(88) oxidized Fe-Ni alloys containing 10, 20, 30, 40% Ni in CO/CO_2 mixtures at 1000°C. The kinetics were linear, the rate of oxidation being controlled by a surface reaction involving incorporation of oxygen in the oxide lattice. Wustite was the only oxide observed in the external scale. Extensive subscale formation was observed. The subscale consisted of wustite finely precipitated in a nickel rich-alloy matrix.

Several investigators have observed oxidation of Fe-Ni alloys containing 25-80% Ni, in air and pure oxygen. Foley(89 90,91,92,93) has observed parabolic scale growth for alloys containing 30-80% Ni. It was also observed that high nickel additions reduce the rate compared to pure iron by a factor of 10^2-10^3. It was concluded that this was due to the disappearance of the wustite layer as a result of the nickel-enrichment at the alloy-oxide interface. Diffusion processes in the remaining spinel and hematite layers were relatively slow.

Bénard and Moreau(94) who investigated the behaviour of alloys containing 5, 10, 20, 30% Ni observed that the films developed on these alloys after oxidation and cooling to room temperature consisted of Fe_2O_3, Fe_3O_4 and a mixed layer of FeO and Fe_3O_4, Little nickel and nickel oxide were detected in any of these layers by chemical analysis. Iron was selectively oxidized and nickel was enriched at the alloy-oxide interface.

In the 30% Ni alloy the surface concentration of Ni after 1 hr. of oxidation was 50% at 850°C, 60% at 950°C and 82% at 1050°C. A deviation from parabolic oxidation during the initial stages was observed for all the alloys investigated except for Fe-20% Ni alloy at 675°C. This deviation from parabolic behaviour was attributed to the highly selective oxidation of iron, the subsequent enrichment of nickel at the surface, and diffusion of iron through this enriched layer in the initial stages. In the later stages, deviations occurred as a result of a decreased oxygen flux across the oxide to the interior of the alloy. Internal oxidation was more severe at the grain boundaries than within the grains. The authors suggested that oxygen diffused down these boundaries and precipitated oxide particles which subsequently coalesced and enveloped the metal grains. Oxygen was transported through the oxide and diffused into the metal lattice and precipitated oxide within the grains similar to the process occuring at the metal oxide interface.

Koh and Caugherty(95) used an x-ray fluorescence technique to study the oxide layer formed on an alloy of 50 Ni-50 Fe composition. A spinel was identified along with weak lines for Fe_2O_3. Hickman and Gulbransen(96) followed the oxidation of an alloy containing 49% Fe, 49% Ni and 2% Mn in purified oxygen at 1 mm pressure from 300-700°C by an electron diffraction method, the observation being made at temperature. A spinel was observed. Kennedy, Calvert and Cohen(97) using a high temperature diffraction apparatus observed the scale structure on three iron-nickel alloys containing 25, 75 and 84% Ni at 800°C in oxygen. The individual oxide layers thickened according to the parabolic law. There was considerable subscale formation, especially in the 25% Ni alloy. This was attributed to scale fracture, allowing the reactant gas to penetrate along the interface and grain boundaries. Yearian, Boren and Warr(98) reported a nickel bearing spinel and hematite layers on a 25% Ni alloy. Menzies and Tomlinson(99), who oxidized an Fe-48% Ni alloy in CO_2 atmosphere at 700-1000°C, also observed a spinel in the external scale.

Kennedy et al(97) reported a compact scale on alloys containing 75 and 87% Ni consisting of a thin outer layer of Fe_2O_3. Beneath this a compact layer of spinel was observed and below this a porous layer of nickel oxide was present. The nickel oxide shaded gradually into the spinel layer. Extensive internal oxidation was observed. The oxidation curves for these alloys were not smooth but contained steps and breaks according to these authors. Wulf et al(85) have also reported similar scale structure for alloys in this composition range.

The alloys investigated in this work are high nickel alloys containing 0-25% Fe. It was the objective of this work to first see whether continuous kinetics could be observed for these alloys and if so to rationalize the oxidation of the alloys in terms of the Fe-Ni-O phase diagram and a ternary diffusion model.

2.4 THERMODYNAMICS OF THE Fe-Ni-O SYSTEM

Kubaschewski and von Goldbeck(100) and Oriani(101) determined thermodynamic activities of Fe-Ni alloys using gas equilibration techniques and concluded that the solid solution behaviour of these alloys was essentially ideal. Brabers, Heideger and Birchenall(102) studied the interaction of iron-nickel alloys with oxygen in order to establish the conditions of equilibrium in the iron-rich section of the ternary Fe-Ni-O system. In a more detailed investigation Brabers and Birchenall(103) studied several samples of iron-nickel alloys oxidized in pure oxygen at 1050°C and subsequently equilibrated in an inert atmosphere at this temperature for periods exceeding one month. From their investigation Brabers and Birchenall concluded that the solubility of nickel in wustite is negligible. They observed that magnetite forms a continuous series of solid solution with nickel ferrite. A three phase region in the iron-rich section of the Fe-Ni-O system was observed. This region, comprised of wustite rich in oxygen and containing only traces of nickel, a spinel containing approximately 10 wt % Ni and an alloy phase containing approximately 55 wt % Ni.

Bryant and Smeltzer(104) who also studied the Fe-Ni-O phase diagram at 1000°C found a different phase composition in the three phase wustite-spinel-alloy region,as compared to the values reported by Brabers and Birchenall. Their observations showed that the maximum solubility of Ni in wustite was 1.8 w/o , the terminal composition of spinel corresponds to a 8.4 w/o Ni content and the alloy phase coexisting with wustite and spinel contained 79.6 w/o Ni.

Viktorovich, Gutin and Lisovskii(105,106) carried out extensive investigations in the wustite-alloy phase field of the Fe-Ni-O system in the temperature range 700°- 1100°C. They observed that the nickel solubility in wustite coexisting with alloys increased with increasing Ni content of the alloy. The maximum Ni content in wustite increased with increasing temperature. The Ni content of the alloy coexisting with wustite and spinel increased from 65 w/o at 700°C to 84.5 w/o at 1100°C. At 1000°C Ni content of this alloy was 81 w/o.

Phase equilibria in the spinel region of the Fe-Ni-O system were investigated by Paladino(107) in the temperature range 1000°-1300°C. It was found that magnetite (Fe_3O_4) and nickel ferrite ($NiFe_2O_4$) form a continuous series of spinel solid solutions which do not exist with a measurable oxygen deficiency. Stoichiometric nickel ferrite represented the limit of nickel solubility in spinels. Hematite containing very little nickel and spinels ranging in composition from magnetite to the stoichiometric nickel ferrite formed the boundaries of a two phase field.

Roeder and Smeltzer(108) determined the dissociation pressure of wustite in equilibrium with iron-nickel alloys using the electromotive force technique of Kiukkola and Wagner(109) with a solid electrolyte. Dissociation pressures of ternary oxides equilibrated with alloys having initial nickel content of 10-55 w/o were obtained. These pressures increased with increasing nickel content of the alloys. These authors observed that wustite dissolved Ni up to 3 w/o at 1000°C. The maximum nickel solubility in wustite reported thus ranges from negligible to 3 w/o. No observations are available on the nickel-rich region of the Fe-Ni-O phase diagram.

In the present investigation a more complete knowledge of the Fe-Ni-O ternary system at 1000°C will be obtained by investigating the nickel-rich region of the phase diagram.

CHAPTER 3

THEORETICAL ANALYSIS OF THE DIFFUSION-CONTROLLED OXIDATION OF BINARY ALLOYS - A SUMMARY OF THE PSEUDO-BINARY APPROACH

3.1 INTRODUCTION

As presented in Chapter 1, the course of oxidation of alloys can be described by the parabolic law where diffusion is the rate controlling process. However, even in such a case a great variety of possibilities for the formation of the oxide scale and a variety of underlying mechanisms exist. It is the purpose of this chapter to enumerate these possibilities and summarize the theoretical treatment for certain limiting cases. Two excellent summaries exist in this field: one by Wagner(110) and the other by Rapp(111).

Before proceeding to discuss these cases it is necessary to explain the term "pseudo-binary" used in this dissertation. It refers to the analyses carried out for certain limiting cases with restrictive assumptions, as described in the following. In their theoretical analyses Rhines et al(112), Thomas(113) and Wagner(114) treated oxidation of alloys with components having widely differing reactivities. One of the components was either a noble metal such as in the case of Cu-Pd, Cu-Pt and Ni-Pt alloys, or much less reactive than the other as in the case of Cu-Si alloys. Due to the strongly differing values of the free energies of formation of the oxides of the two components, usually one of the components enters into the oxidation reaction. The solubility of the more noble component in the oxide of the reactive component was assumed in the limiting case to be zero. The more noble component was enriched at the metal surface and diffused back into the bulk alloy. Ternary interactions (as described in Chapter 4) were neglected. Under these assumptions each phase can be treated effectively as a binary system and transport equations can be formulated accordingly. The binary Gibbs-Duhem equation can be used within single phase regions within the analysis. Thus, even though the system A-B-O is truly a ternary system, it can be effectively treated as a binary system and hence the term "pseudo-binary". In the past, the restrictive assumptions in these analyses have often not been recognized and in certain applications erroneous results have been obtained. In cases where the two alloy components are nearly equally reactive and each component is soluble in the oxide of the other, or when they form complex mixed oxides, the ternary approach is the only valid approach which can be used. However the limiting cases discussed below are valuable for a quantitative understanding of the mechanisms of oxidation of binary alloys.

In the case where the free energies of formation of the alloying components are widely different, the least noble constituent is selectively oxidized to form an outer, often protective layer,and thus the scale consists of but one oxide phase.

However, the occurrence of selective oxidation is dependent not only on the type of alloying addition but also on the concentration of the active alloying component, on the temperature, and on the partial pressure of oxygen.

Under any set of conditions selective oxidation will take place only above a critical concentration of the active alloy component. Wagner(114) has analyzed the conditions necessary for selective oxidation in a binary alloy and has derived a mathematical expression for this critical concentration.

Wagner(114) considered an alloy AB in which B is the less noble metal and A and B do not react to form a double oxide or spinel. Assuming that compact scales are formed three main cases for the oxidation of the alloy AB may be considered(115).

1. At low concentrations of B, only the A oxide will be formed and B will diffuse into the alloy from the alloy-oxide interface (Fig. 3-1(a)). As oxidation proceeds, the concentration of B in the alloy will increase, and formation of the B-oxide will take place when the concentration of B at the interface reaches the equilibrium concentration N_B^*, in the mixture (alloy+A-oxide+B-oxide). The concentration in the bulk alloy, N_B', is smaller than N_B^*.
2. For sufficiently high concentration of B in the alloy, N_B'', only the B-oxide will be formed and A will diffuse into the alloy from the alloy-oxide interface [Fig. 3.1(b)]. Formation of the A-oxide will begin to take place only when the concen-

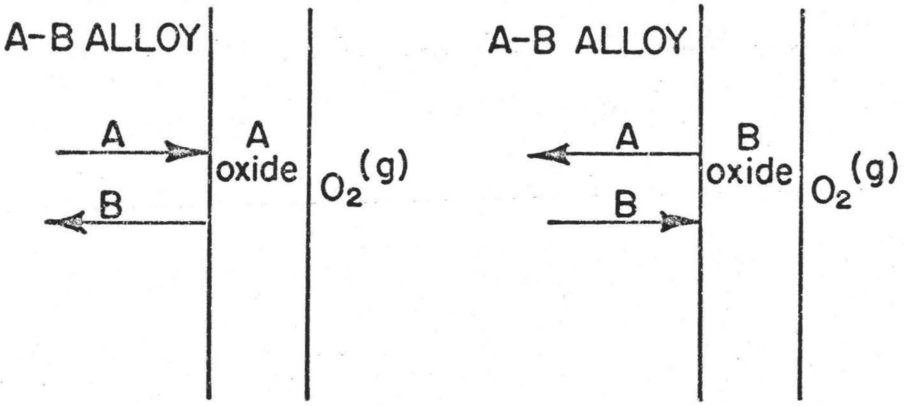

(a) Exclusive formation of A-oxide ($N_B < N'_B$)

(b) Exclusive formation of B-oxide ($N_B > N''_B$)

Fig. 3-1

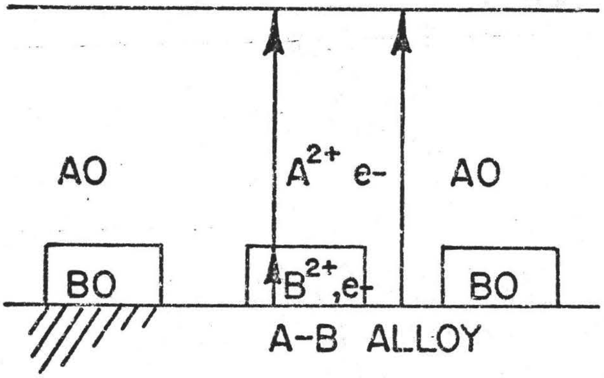

Fig. 3-2: Simultaneous formation of A-oxide and B-oxide in oxidation of A-B alloy assuming cation migration through both oxides. B-oxide grows according to the displacement reaction $AO + B^{2+} = A^{2+} + BO$.

tration of A at the interface reaches the critical composition $N_A^* = 1 - N_B^*$ corresponding to the three phase equilibrium (alloy+A-oxide+B-oxide). Thus $N_B'' > N_B^*$.

3. At concentrations ranging from N_B' to N_B'' the A-oxide and the B-oxide will simultaneously be formed (composite scale). A possible reaction scheme for this case, assuming that cations are the mobile species and AO grows more rapidly than BO, is shown in Fig. 3-2.

Assuming the formation of a compact scale, Wagner(114) showed that the critical concentration N_B'' above which only the B-oxide is formed is given by

$$N_B'' = \frac{V_m}{Z_B M_O} \left[\frac{\pi\, k_p (N_B > N_B'')}{D}\right]^{\frac{1}{2}} \qquad (3\text{-}1)$$

where V_m is the molar volume of the alloy, Z_B is the valence of the B atom, M_O is the atomic weight of oxygen, D is the diffusion coefficient of B in the alloy and k_p is the parabolic rate constant for exclusive formation of the B oxide, i.e., for $N_B > N_B''$ ($k_p = (\Delta m/A)^2/t$).

When oxygen dissolves in the alloy phase during oxidation the less noble alloy component may form oxide within the alloy. This phenomenon is called internal oxidation. Internal oxidation takes place in the scaling of numerous alloy systems. Detailed analyses of internal oxidation have been made for alloys of copper, silver, palladium, nickel etc. with small amounts of less noble alloying elements such as Al, Si, Be, In, Cr, etc. Various features of internal oxidation have been described by

Wagner(110) Rhines et al.(112,116), Darken(117), Meijering and Druyvesteyn(118), Rapp et al.(119,120) and Böhm and Kahlweit(121). In some cases internal oxidation occurs exclusively. However in many cases a surface scale is simultaneously formed.

Wagner(122) has considered the morphological stability of planar alloy-oxide interface. When the interface is unstable a two-phase subscale consisting of the oxide of the less noble metal and alloy rich in the more noble metal may be formed. This case has been theoretically treated by Wagner.

In summary, the following important possibilities exist in alloy oxidation:

1. Single phase external scale formation (selective oxidation).
2. Formation of a two-phase (composite) external scale.
3. Exclusive internal oxidation.
4. Internal oxidation in combination with external scale formation.
5. External scale formation in combination with subscale formation due to morphological breakdown.

3.2 SINGLE PHASE EXTERNAL SCALE FORMATION

Wagner(114) considered the limiting case of oxidation of Ni-Pt alloys wherein only nickel is oxidized. A coherent NiO layer growing parabolically is formed.

In oxidation of pure nickel, the parabolic rate constant can be expressed by

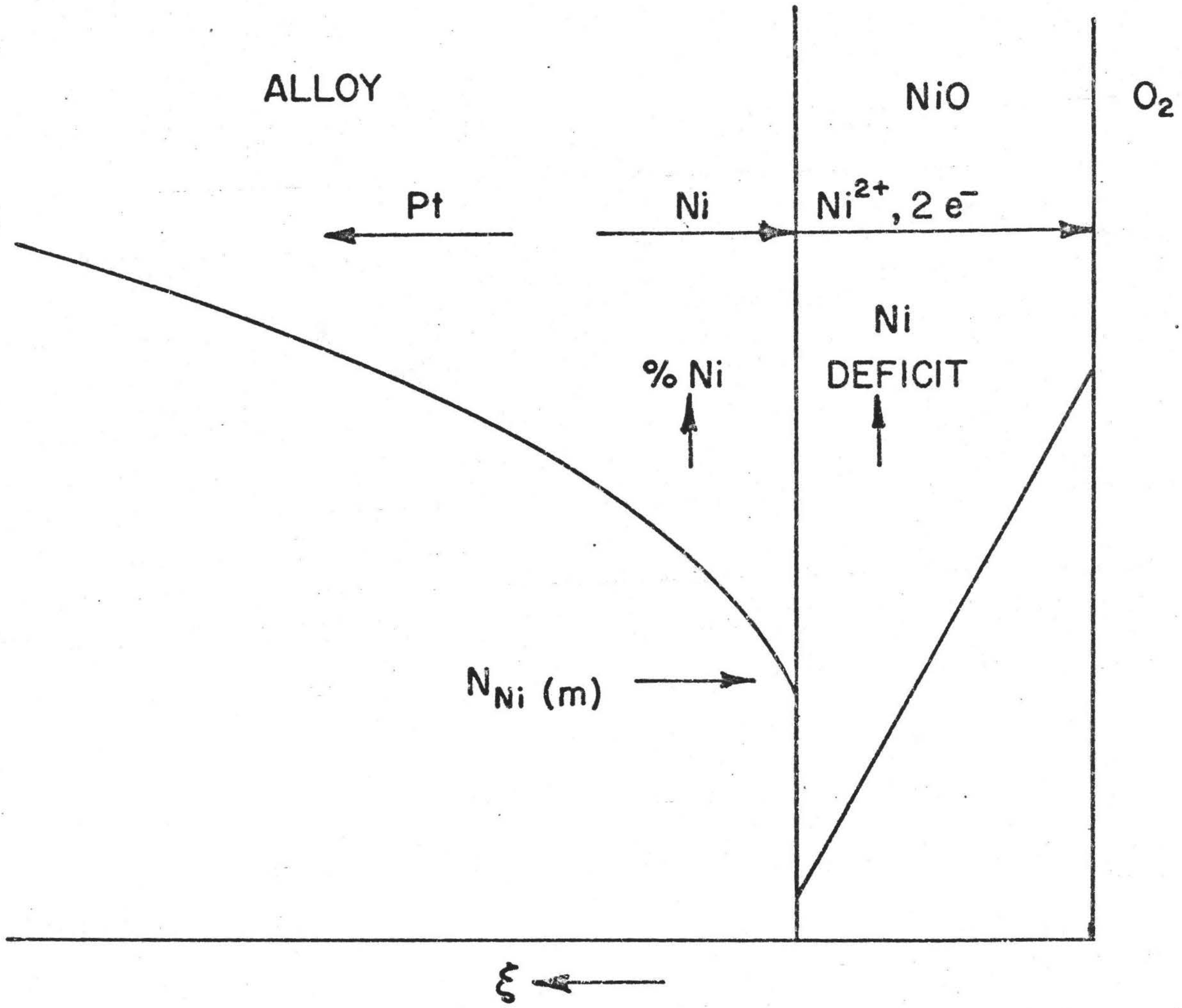

Fig. 3-3: Schematic representation of diffusion processes during the oxidation of nickel-platinum alloys.

$$k_o = \text{const.}\{(p^o_{O_2})^{1/n} - (p^*_{O_2})^{1/n}\} \qquad (3\text{-}2)$$

where $p^o_{O_2}$ is the ambient oxygen pressure, $p^*_{O_2}$ is the dissociation pressure of NiO in equilibrium with pure metal and n is a number which depends on the defect structure of the oxide.

In the oxidation of Ni-Pt alloys, the consumption of nickel results in a concentration gradient of nickel and of Pt in the alloy, leading to diffusion of nickel from the interior of the alloy to the alloy-oxide interface and diffusion of Pt into the alloy (Fig.3-3). As in the oxidation of pure nickel, the growth of the NiO scale proceeds through an outward migration of nickel by the vacancy mechanism. The corrosion constant for Ni-Pt alloys k, may be expressed by replacing $p^*_{O_2}$ in Eq. (3-2) by $p^i_{O_2}$ which is the oxygen equilibrium pressure at the alloy-oxide interface.

Assuming ideal solution behaviour for the Ni-Pt alloy, the ratio of the oxidation of an alloy to that of pure nickel, $\alpha = k/k_o$, therefore, can be expressed by

$$\alpha = \frac{(p^o_{O_2})^{1/n} - (p^i_{O_2})^{1/n}}{(p^o_{O_2})^{1/n} - (p^*_{O_2})^{1/n}} = \frac{1-(N^o_{Ni}/N^i_{Ni})^{2/n}}{1-(N^o_{Ni})^{2/n}} \qquad (3\text{-}3)$$

where N^o_{Ni} represents the mole fraction of nickel in an alloy coexisting with NiO and the ambient oxygen pressure and N^i_{Ni} is the mole fraction of nickel in the alloy at the alloy-oxide interface.

From a knowledge of the value of $p^*_{O_2}$ and the interdiffusion coefficient, D, in the alloy Wagner obtained α as a function of the bulk alloy composition. The agreement between the calculated values and the experimental values obtained by Kubaschewski and Von Golbeck(123) is good at 850°C. At 1100°C some discrepancy is observed which may be attributed to such factors as porosity in the NiO scale, impurities, concentration dependence of D, deviation from ideality in the alloy and variation in the value of n.

3.3 INTERNAL OXIDATION

For the case of exclusive internal oxidation, if diffusion control is assumed, then following Wagner(110) we can express the depth ξ of the internal oxidation zone by

$$\xi = 2\gamma(D_O t)^{\frac{1}{2}} \qquad (3\text{-}4)$$

where D_O is the diffusion coefficient of oxygen in the alloy, γ is a dimensionless parameter and t is time.

Wagner solved the diffusion equations for oxygen and for the less noble component B which exclusively forms the internal oxide, subject to appropriate boundary conditions. He applied the mass balance condition at the precipitation front of the internal oxidation zone to find an expression for γ.

Two limiting cases exist. For $\frac{D_B}{D_O} << \frac{N_O^S}{N_B^O} << 1$ Eq. (3-4) becomes

$$\xi = \left[\frac{2N_O^S D_O t}{\nu N_B^O}\right]^{\frac{1}{2}} \qquad (3\text{-}5)$$

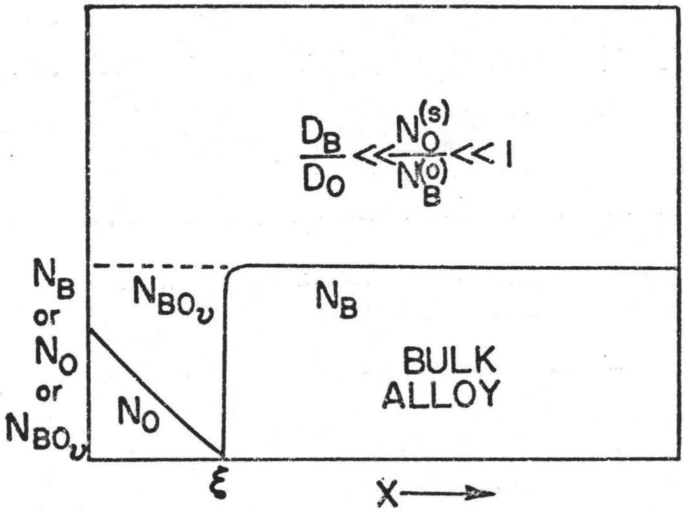

(a) Concentration profiles for the exclusive internal oxidation of alloys

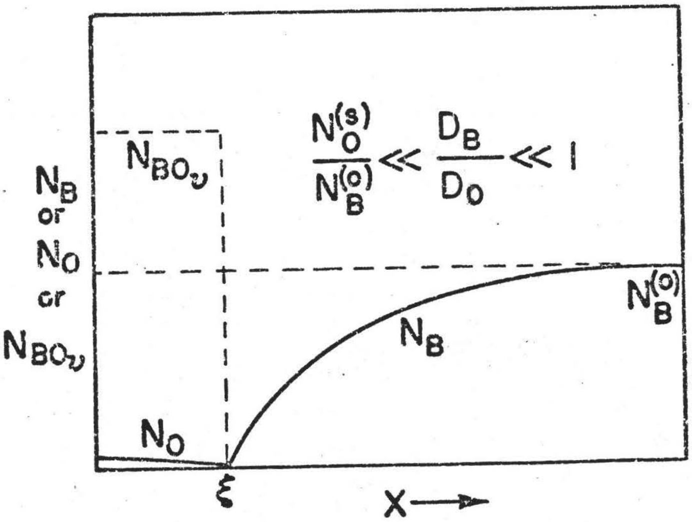

(b) Concentration profiles for the exclusive internal oxidation of alloys

Fig. 3-4

where D_B is the diffusion coefficient of B in the alloy, N_O^S is the mole fraction of oxygen at the outer surface, N_B^O is the mole fraction of B in the bulk alloy, and ν is a number expressing stoichiometry of the precipitated oxide BO_ν. Eq. (3-5) is expected to hold under conditions where the movement of the precipitation front is completely determined by the diffusion of oxygen in the base metal. A schematic drawing of the concentration profiles under these conditions is given in Fig. [3-4(a)]. In a second limiting case

$$\frac{N_O^S}{N_B^O} << \frac{D_B}{D_O} << 1,$$

$$\xi = \frac{N_O^S}{\nu N_B^O} (\pi \phi D_O t)^{\frac{1}{2}} \tag{3-6}$$

where $\phi = D_O/D_B$. In this case, the rate of outward diffusion of the alloying element as well as the rate of inward diffusion of oxygen are important in determining the kinetics of oxidation. A schematic representation of the concentration profiles under these conditions is given in Fig. [3-4(b)].

In most practical applications of alloys at high temperatures the internal oxidation zone is formed below an external oxide scale. Analytic solutions for the kinetics of internal oxidation in combination with a parabolically thickening external scale have been given by Rhines et al(112) and Maak(124). Maak solved the diffusion equations for oxygen and B in the alloy with appropriate boundary conditions and obtained a complicated

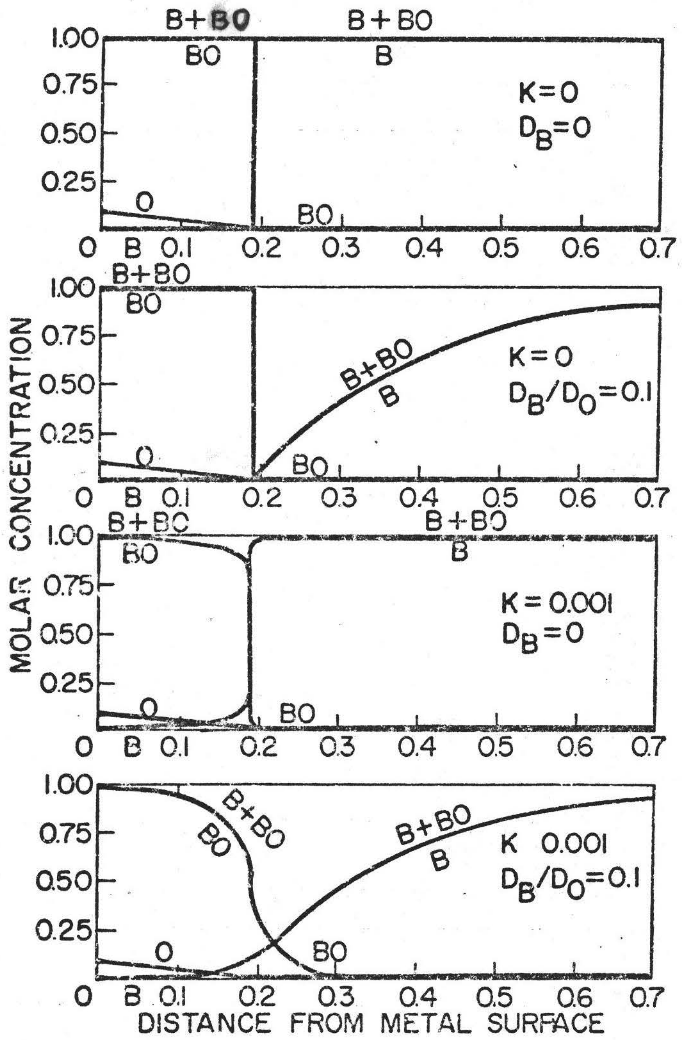

Fig. 3-5: Distribution of elements B and O of compound BO, as influenced by value of solubility product K and of ratio D_B/D_O after Darken.

expression for γ.

Since what is commonly observed under the microscope is the distribution of the precipitated compound, BO, the curve referring to BO is of most immediate interest. Darken$^{(117)}$ considered the various cases which are summarized in Fig. 3-5.

When the solubility product $K = [N_B][N_O]^{\nu}$ is zero [Figs. 3-5(a) and 3-5(b)] there is a discontinuity in the concentration of BO corresponding to a sharp boundary between subscale and unoxidized alloy. Moreover, the concentration of BO in the internal oxidation zone is equivalent to the initial concentration of B. These cases correspond to the two limiting cases considered by Wagner [Figs. 3-4(a) and 3-4(b), respectively]. When K is greater than zero [Figs. 3-5(c) and 3-5(d)] the discontinuity becomes an inflection, which is less steep, the greater the value of K or the ratio D_O/D_B; that is, the boundary between subscale and unoxidized alloy becomes more diffuse as K or the ratio D_O/D_B increases. Since the value of solubility product and of the ratio D_O/D_B changes fairly rapidly with temperature this means that the sharpness of the boundary of the subscale may vary considerably with the temperature at which the diffusion occurs. Obviously, if K is greater than the product of the initial concentration of oxygen and the solubility of B, no precipitation occurs and no internal oxidation zone is formed.

In other words, for internal oxidation to occur oxygen-supersaturation in the alloy ahead of the alloy-scale interface must occur. Wagner(125) utilized the solution of diffusion equations for oxygen and the alloying element B to obtain an expression for the product $N_B N_O^{\nu}$ at any point. The gradient of this product can be related to the diffusion parameters in the alloy, the bulk alloy composition, composition of the alloy at the scale alloy interface and the rate of thickening of the external scale. Wagner evaluated the following parameter in the alloy

$$g_s \equiv \left(\frac{\partial \ell n \ N_B N_O^{\nu}}{\partial x}\right)_{x=x_o} \qquad (3\text{-}7)$$

where x_o is the coordinate of the scale-alloy interface. At the scale-alloy interface, the alloy is saturated with respect to oxide BO_{ν} , i.e. the product $N_B N_O^{\nu}$ equals the solubility product K at $x = x_o$. Thus one has the following cases:

(a) If the value of g_s defined by Eq. (3-7) is negative, the alloy next to the scale is undersaturated with respect to oxide BO_{ν} and no internal oxidation can occur.

(b) If conversely the value of g_s in Eq. (3-7) is positive, the alloy next to the scale is supersaturated with respect to oxide BO_{ν} and internal oxidation may occur. Accordingly the limiting condition for possible internal oxidation is $g_s > 0$.

Qualitatively it is readily understood that internal oxidation is favoured by a flat oxygen concentration profile due to a high value of D_O and further by a steep positive gradient of N_B corresponding to a high value of the corrosion constand and a low value of D_B.

Wagner(125) applied the criterion $g_s > 0$ to Thomas' data on the oxidation of Cu-Pd alloys(4) and obtained a value of about 2600 for g_s thus indicating that the condition for internal oxidation is satisfied.

For a given volume fraction of precipitated internal oxide, the size or number of the precipitates and therefore the precipitate morphology will be determined principally at the reaction front through the competition for solute atoms between the processes of growth of the existing particles and nucleation of new precipitates. Following the method of Wagner(110,126), Böhm and Kahlweit(121) have treated quantitatively the nucleation of BO precipitate in internal oxidation. Böhm and Kahlweit first calculated the concentration profiles and the gross displacement ξ of the reaction front under the assumption of a finite solubility product, K , of the precipitated BO oxide in the matrix. The expressions derived for γ, N_O and N_B are therefore more general. Böhm and Kahlweit's diffusion-controlled model for precipitate nucleation is shown schematically in Fig. (3-6) in which $N_O^* N_B^*$ represents the concentration product critical to the formation of a nucleus of critical size and K is the equilibrium solubility product, with

$$(N_B')(N_O')^{\nu} = K \qquad (3\text{-}20)$$

Fig. [3-6(a)] represents the concentration profile immediately

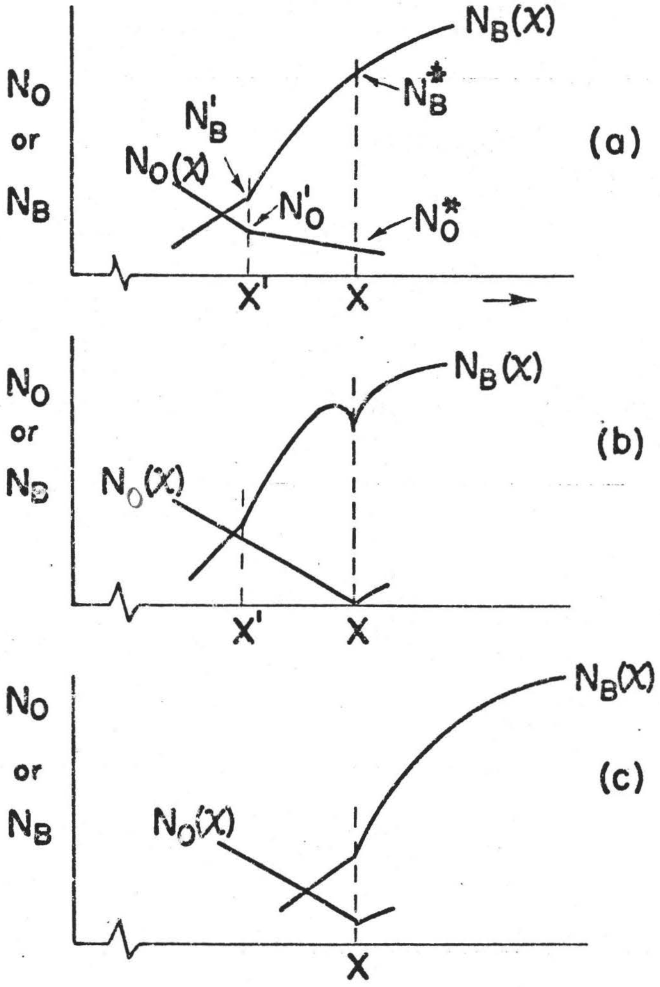

Fig. 3-6: Concentration profiles in the immediate vicinity of the precipitation front after Böhm and Kahlweit$^{(121)}$.

before the start of a precipitation at position x. The intermediate profiles of Fig. [3-6(b)] show that after the start of precipitation the oxygen concentration at x would be reduced to a low value because of the relatively high B concentration. Through the subsequent growth of the precipitate, as shown by the profiles of Fig. [3-6(c)], excess B is substantially removed and the gradient in B about the particle is lowered. Subsequently, fewer of the inward diffusing oxygen atoms are consumed in particle growth, so that the oxygen concentration can again increase to a profile equivalent to that of Fig. [3-6(a)], whereupon the precipitation cycle repeats. However, since the nucleation phenomenon is not coordinated, the precipitation is not periodic.

For the case of diffusion-controlled precipitate growth, the average precipitate spacing is approximated by the distance between two successive points of nuclei formation (127), i.e. $\Delta x = x - x'$. Then the number of precipitates Z(x) per unit volume may be given by the expression

$$Z(x) \simeq (\Delta x)^{-3} = \left(\frac{x}{\Delta x}\right)^{3} \frac{1}{x^{3}} . \qquad (3-21)$$

To evaluate Z(x) in terms of the unknown parameters N_O', N_B', N_O^* and N_B^*, Böhm and Kahlweit solved simultaneously four equations involving these four unknowns and $x/\Delta x$. The number of precipitates per unit volume for a given N_O^s depends inversely on the cube of the distance of the precipitation site from the external surface and the number of precipitates per unit volume at a given x varies directly as the cube of the oxygen mole fraction at the external surface. Further, for systems with known K, $N_O^* N_B^*$, D_O, D_B and N_O^s, the particle density could be quantitatively predicted.

For the condition of negligible solute enrichment in the internally oxidized zone, the radius r(x) of spherical precipitates may be expressed by

$$r(x) = \left(\frac{3V_{BO}N_B^o}{4\pi\beta}\right)^{1/3} \frac{x}{N_O^s} \qquad (3\text{-}22)$$

where

$$\beta = \frac{1}{N_O^s} \frac{x}{\Delta x} \qquad (3\text{-}23)$$

and V_{BO} is the molar volume of the oxide.

Böhm and Kahlweit(121) have experimentally tested Eq. (3-21) in the internal oxidation of Ag-0.98 a/o Cd alloy at 850°C. Bolsaitis and Kahlweit(128) have carried out a similar investigation for internal oxidation of Cu-Si alloys at 928, 998 and 1073°K. The planar particle density was determined as a function of the distance x from the external interface, and this planar density was converted into volume density Z(x) of precipitates. As predicted in Eq. (3-21), Z(x) was found to vary inversely as the cube of x and also directly as cube of N_O^s.

3.4 MORPHOLOGICAL INSTABILITY AND COMPOUND SCALE FORMATION

Wagner(122) has used the most rigorous approach to test the stability of the planar oxide-alloy interface. This approach involved the application of mathematical perturbation methods. A small sinusoidal shape perturbation was introduced

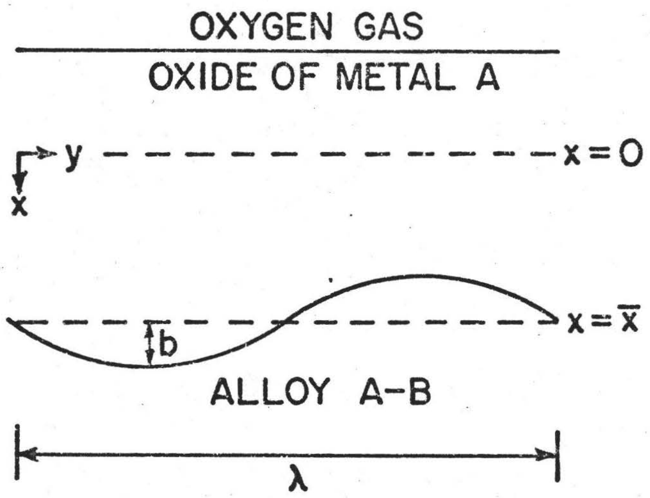

Fig. 3-7: Sinusoidal perturbation in the study of morphological instability of the alloy-oxide interface after Wagner(122).

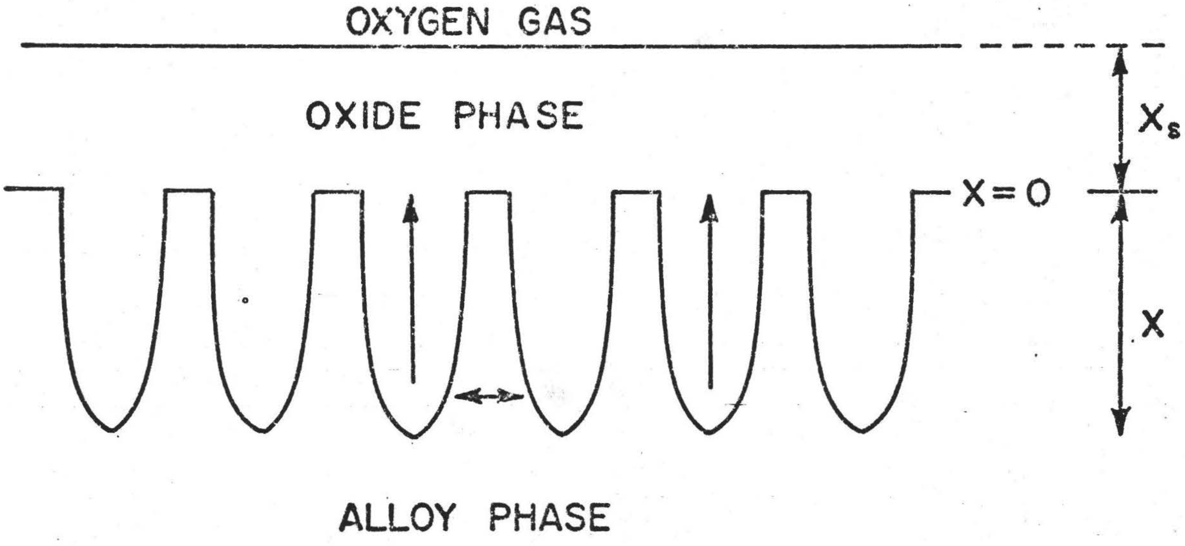

Fig. 3-8: Non-planar interface morphology after Wagner(122).

into an initially planar interface and the pertinent differential equations were solved to decide the fate of this perturbation. If it grows with time, the interface is unstable. On the other hand, if the perturbation decays with time, the interface will maintain a stable planar shape.

Let the perturbation be described by the following equation:

$$x = \bar{x} + b\sin(2\pi y/\lambda) \qquad (3\text{-}24)$$

where $\bar{x}$ is the position of the mean surface, b is the amplitude of the wave, λ its wavelength, and y is the transverse distance coordinate $b \ll \lambda \ll \bar{x}$ (Fig. 3-7). Let u_x be the drift velocity of the oxide toward the bulk alloy due to the recession of the alloy-oxide interface, V_{BO} the volume of oxide BO per mole of B and V_m the molar volume of alloy. Solving the diffusion equations for both planar and perturbed interfaces Wagner showed that the difference between the local value of u_x and the average value $\bar{u}_x$ is

$$u_x - \bar{u}_x = -\bar{u}_x(2\pi b\gamma/\lambda)\sin(2\pi y/\lambda) \qquad (3\text{-}25)$$

where

$$\gamma = \frac{q-1}{q+1} \qquad (3\text{-}26(a))$$

and

$$q = \frac{\bar{N}_B}{1-\bar{N}_B}\,\frac{D_B/V_m}{D_B^{ox}/V_{BO}}\ . \qquad (3\text{-}26(b))$$

$\bar{N}_B$ is the average mole fraction of B in the alloy at the average interface plane and D_B^{ox} is the self-diffusion coefficient of B in the oxide.

If q defined by Eq. (3-26(b)) is greater than unity, γ calculated from Eq. (3-26(a)) is positive. Then it follows that at points where the local thickness of the oxide film exceeds the average value, the local rate of change in the position of the interface is smaller than the average value. Thus, if q>1, there is a tendency that deviation from a planar interface will disappear in the course of time. In other words, a planar interface is stable if q>1, or if

$$\frac{\bar{N}_B}{1-\bar{N}_B}\,\frac{D_B/V_m}{D_B^{ox}/V_{BO}} > 1. \qquad (3\text{-}27)$$

Conversely, if q < 1 a planar interface is not stable since any irregularity tends to increase in the course of time.

Instability of the planar alloy-oxide interface results in its breakdown and leads to an eventual formation of a two phase scale consisting of the oxide of the less noble metal and the alloy rich in the more noble metal. In attempting to solve the problem of formation of this subscale Wagner(122) assumed the morphology as shown in Fig. (3-8) where protruding sections of the oxide BO are supposed to alternate with slender trunks of the alloy depleted with respect to the less noble metal B.

In the two-phase region of the scale, the rate of transport is determined not only by the gradient of the activity of metal B but also by the available cross section of the oxide, i.e. by the volume fraction ψ of the oxide, which is a function of distance x from the original alloy surface. This distance is not a priori known but has to be calculated. Upon solving the appropriate diffusion equations Wagner obtained the volume fraction ψ of the oxide BO as a function of the distance x for various alloy compositions. The value of ψ rapidly rises from zero at the subscale-alloy interface and levels off to a constant value towards the subscale-scale interface. The maximum value of ψ increases with increasing content of B in the bulk alloy.

CHAPTER 4

THEORETICAL ANALYSIS OF THE DIFFUSION-CONTROLLED OXIDATION OF BINARY ALLOYS - A TERNARY APPROACH*

4.1 INTRODUCTION

A study of high temperature oxidation of alloys of necessity involves consideration of thermodynamic and kinetic interactions in multicomponent systems. The simplest of multicomponent systems is encountered in the oxidation of binary alloys, which involves three species, viz., alloying elements A and B and oxygen O. At high temperatures the reaction rates are usually so fast that the overall reaction rate is controlled by transport phenomena$^{(130)}$. In considering such transport controlled processes, it is convenient to recognize the concept of "local equilibrium". In the case of oxidation, the reacting gas and the alloy are separated by an oxide layer soon after the beginning of the reaction. The total free energy change of the reaction then takes place over a large distance and hence one can consider any microscopic volume element as being

---

*For the most part, this chapteris based on two papers by the author and D. E. Coates$^{(23,129)}$.

substantially in equilibrium within itself even during the course of a rapid reaction and characterized by a chemical potential of each element of species. In cases where the condition of local equilibrium prevails, the requirement that the various diffusing species can be conserved at the interfaces leads to a coupling or interdependence of the diffusion fields in the oxide and alloy phases. This interplay between diffusion in the two phases involves both kinetic and thermodynamic considerations.

4.2 PHENOMENOLOGICAL BASIS OF MULTICOMPONENT DIFFUSION THEORY

The phenomenological basis of multicomponent diffusion was outlined completely by Onsager(131) in 1945-46. According to this formulation, for a system near equilibrium the flux-force relations for an n-component isotropic system are linear, i.e.

$$J_i = \sum_{k=1}^{n} L_{ik} X_k \qquad (4\text{-}1)$$

where J_i is the flux of component i, X_k are forces and L_{ik} are empirical proportionality factors. If the system is at constant temperature and pressure then the forces X_k are the negative of the gradients of chemical potentials and Eq. (4-1) becomes

$$J_i = - \sum_{k=1}^{n} L_{ik} \frac{\partial \mu_k}{\partial x} \qquad (4\text{-}2)$$

and μ_k are the chemical potentials.

Equation (4-2) can be transformed to the following expression(132) which involves molar concentrations C_k:

$$J_i = - \sum_{k=1}^{n-1} D_{ik} \frac{\partial C_k}{\partial x} \tag{4-3}$$

with

$$D_{ik} = \sum_{j=1}^{n} L_{ij} \frac{\partial \mu_j}{\partial C_k} \tag{4-4}$$

Equation (4-3) is a generalization of Fick's first law. It is usually assumed that the molar volume of the system is independent of composition. As a result, the concentration of one of the components, usually taken as the n^{th}, is dependent.

The factors L_{ik} in Eq. (4-2) represent coupling between the flux of the i^{th} component and the fluxes of the remaining components. This effect arises because diffusion is a cooperative process and may require such conditions as conservation of lattice sites or electrical charge neutrality. Although L_{ik} do not, in general, vanish for $i \neq k$, we assume, following Darken(132) that these effects are negligibly small. Thus

$$L_{ik} << L_{ii} \ (i \neq k). \tag{4-5}$$

Lane and Kirkaldy(133) have shown that in multicomponent metallic systems, even when these are thermodynamically ideal, L_{ik} $(i \neq k)$ may have appreciable values for solutions which are concentrated. However since the coupling effects in ionic solids are not known and have not been experimentally demonstrated, they are neglected in the following. Eq. (4-5) simplifies the mathematics considerably. Nevertheless it should be treated as an approximation. Eqs. (4-2) and (4-4) then reduce, respectively, to

$$J_i = -L_{ii} \frac{\partial \mu_i}{\partial x} \tag{4-6}$$

and

$$D_{ik} = L_{ii} \frac{\partial \mu_i}{\partial C_k} \tag{4-7}$$

We note however that condition (4-5) does not correspondingly reduce the number of terms in Eq. (4-3).

In Eq. (4-6) μ_i is given by

$$\mu_i = \mu_i^o + RT \ell n a_i \tag{4-8}$$

where μ_i^o is the standard chemical potential of component i, a_i is the activity of the component i based on the standard state, R is the universal gas constant and T is the absolute temperature. Substitution of the expression for μ_i from Eq. (4-8) into Eq. (4-6) leads to

$$J_i = - L_{ii} RT \frac{\partial \ell n a_i}{\partial x} \tag{4-9}$$

Since the mobility B_i of species i is defined as the velocity V_i at any point per unit force, we obtain

$$V_i = - B_i \frac{\partial \mu_i}{\partial x} \tag{4-10}$$

The flux J_i can be then defined as

$$J_i = V_i C_i \tag{4-11}$$

and hence

$$J_i = -B_i C_i \frac{\partial \mu_i}{\partial x} \tag{4-12}$$

Comparing Eqs. (4-6) and (4-12) we obtain

$$L_{ii} = B_i C_i \tag{4-13}$$

Thus, Eq. (4-9) becomes,

$$J_i = -B_i RT \, C_i \frac{\partial \ell n a_i}{\partial x} \tag{4-14}$$

If correlation effects are neglected, then the self diffusion coefficient, D_i, of species i is given by the Nernst-Einstein relation$^{(134)}$

$$D_i = B_i RT \tag{4-15}$$

The flux of species i is obtained by combining Eqs. (4-14) and (4-15)

$$J_i = -D_i C_i \frac{\partial \ell n a_i}{\partial x} \tag{4-16}$$

Since in growing oxide scales strong thermodynamic interactions exist, it is convenient to use equation (4-16) where activity gradients are utilized. An alternative formalism is given by Eq. (4-3) which is more convenient for those cases wherein the thermodynamic interactions are not strong and hence Wagner formalism$^{(135)}$ for activity coefficients may be used. Thus for a ternary system

$$J_i = - D_{ii} \frac{\partial C_i}{\partial x} - D_{ij} \frac{\partial C_j}{\partial x} \, , \; i,j = 1,2 \tag{4-17}$$

From Eq. (4-7) it can be shown that

$$D_{ii} = D_i(1 + C_i \frac{\partial \ell n\gamma_i}{\partial C_i}), \; i = 1,2 \qquad (4\text{-}18)$$

and

$$D_{ij} = D_i C_i \frac{\partial \ell n\gamma_i}{\partial C_j}, \; i, j = 1,2 \qquad (4\text{-}19)$$

where D_i is given by Eq. (4-16) and γ_i is the activity coefficient of component i.

The term D_{ij} defined by Eq. (4-19) is called the diffusion interaction term. In binary alloy oxidation diffusion interactions in the alloy phase can become significant for oxygen which is the faster moving species in the alloy. This may have significant effect on the phenomena of internal oxidation and interface stability during the scaling of the alloy.

4.3 THERMODYNAMIC CONSIDERATIONS

In general, one of the alloy components has considerably more affinity for oxygen and the cations of one of the components have considerably more mobility in the oxide layer that is formed. Accordingly, in many cases, a distinct enrichment of one of the alloy components in certain zones of the oxide layer and in the adjacent alloy occurs.

The Gibbs' phase rule for an n-component system in an isothermal and isobaric system is

$$\phi = n - \pi \qquad (4\text{-}20)$$

where ϕ represents the thermodynamic degrees of freedom and π represents number of equilibrium coexistent phases. Since fluxes J_i are proportional to the gradient of chemical potentials,at least one thermodynamic degree of freedom is required within a phase region for a finite spatial extension of that region.

Contrary to the case of the oxidation of a pure metal, the oxide scale on an alloy AB is often made up of multiphase layers. In the oxidation of pure metals where more than one oxide phase occurs, they are arranged in a unique sequence of single phase layers, e.g., FeO, Fe_3O_4 and Fe_2O_3 in the case of pure iron, with the corresponding chemical potential gradients within each phase acting as the driving force for the diffusion process. Formation of two-phase layers in the oxidation of pure metals is excluded since from the Gibbs' phase rule under isothermal and isobaric conditions two-phase regions in a binary system have no degree of freedom. Because no variation in chemical potential in a two phase field is possible, the possibility of chemical potential gradients and the corresponding diffusion process is excluded in this case. However, in a ternary A-B-O system, a two-phase region under isothermal and isobaric conditions has one degree of freedom and accordingly the possibility of the chemical potential gradient and hence that of diffusion exists. The two-phase regions in this case may appear as non-planar interfaces or as zones of internal oxidation.

4.4 KINETIC CONSIDERATIONS - THE CONCEPT OF DIFFUSION PATH

In the case of oxidation of binary alloys the components of the system under consideration are alloying elements A and B and oxygen O. It has been noted earlier that the concentration of one of the components is dependent under the isothermal and isobaric conditions assumed. In Fig. 4-1, the concentration distribution of the arbitrarily chosen independent components B and O are shown schematically for time t.

In the most general case, the independent concentrations C_B and C_O are functions of the time and distance coordinates. However, if it can be shown that C_B and C_O are parametric solutions to the diffusion equations, i.e., for all values of time, t, and distance, x,

$$C_B = C_B(\lambda) \qquad (4\text{-}21)$$

and

$$C_O = C_O(\lambda) \qquad (4\text{-}22)$$

where

$$\lambda = f(x,t) \qquad (4\text{-}23)$$

then elimination of λ between these expressions yields a time - and-distance - independent relation

$$C_B = C_B(C_O) \qquad (4\text{-}24)$$

The plot of this relation, line O-Q in Fig. 4-2 will there-

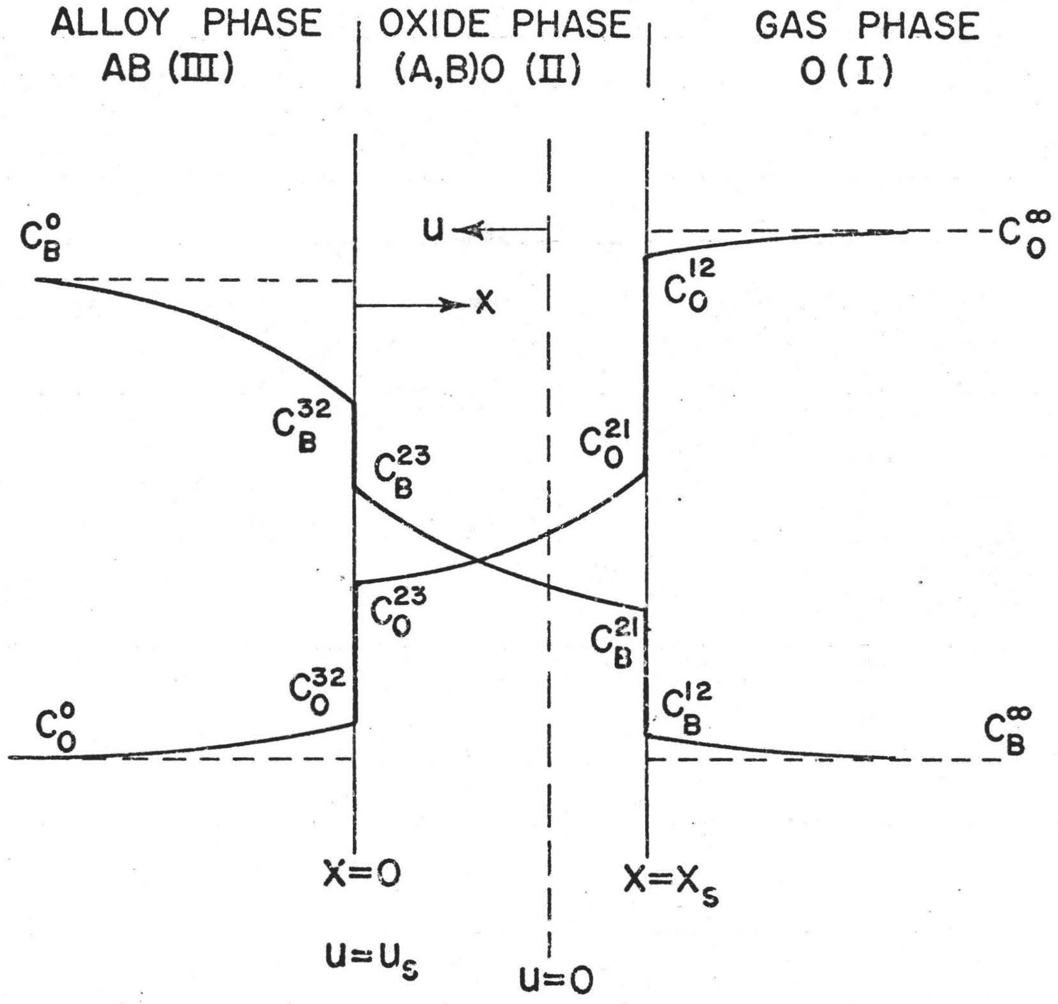

Fig. 4-1: Diffusion model showing the concentration profiles and location of the coordinate frames

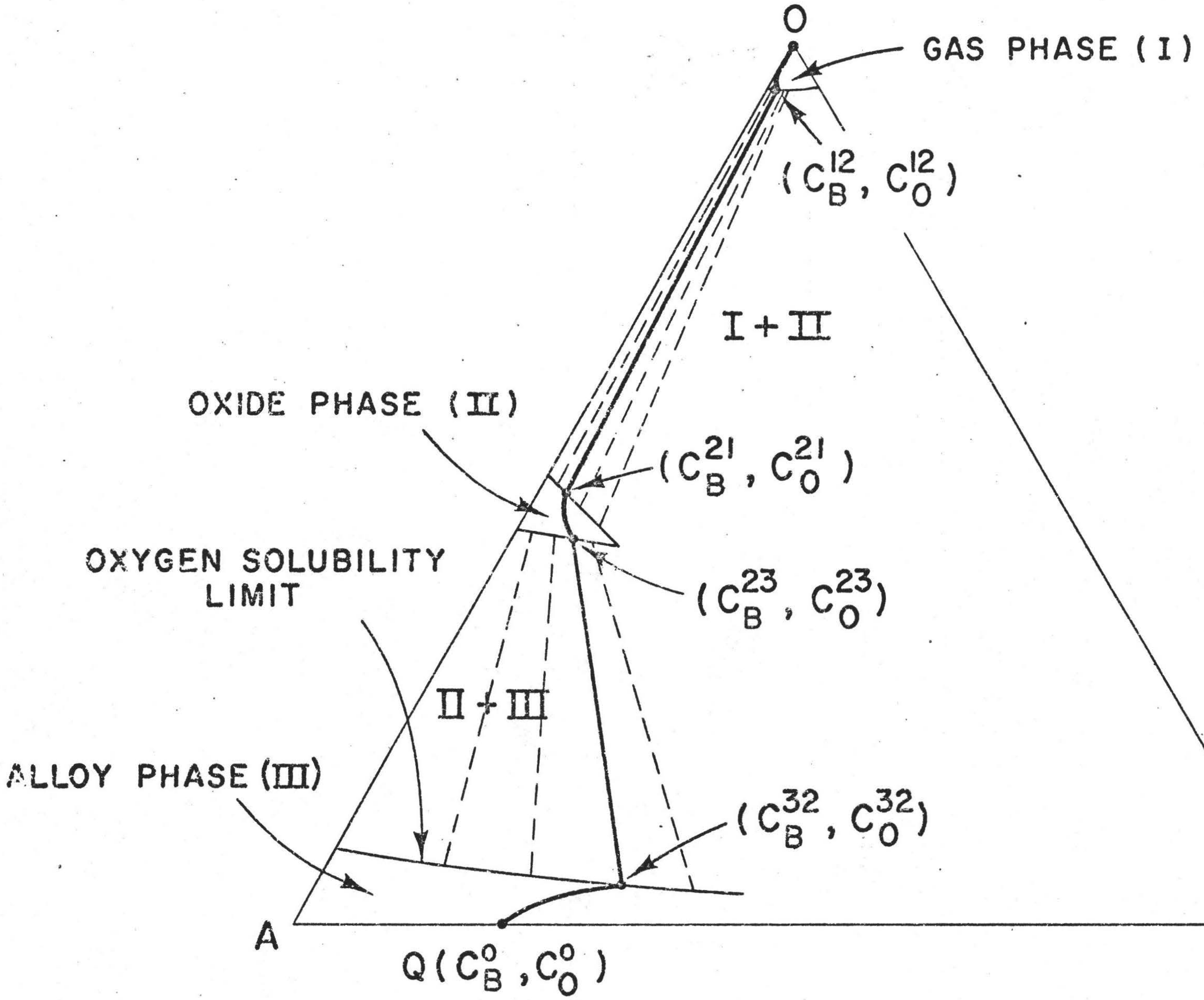

Fig. 4-2: Diffusion path

fore be stationary in time. The relation

$$f(x_s,t) = \text{const} \qquad (4\text{-}25)$$

describes the rate law for the phase transformation, where x_s is the coordinate of the interface. For transformations which are diffusion-controlled with infinite or semi-infinite boundary conditions the parametric substitution of the type

$$\lambda = xt^{-1/2} \qquad (4\text{-}25)$$

is used and this leads to the familiar parabolic oxidation kinetics

$$x_s t^{-1/2} = k_1 \qquad (4\text{-}26)$$

where k_1 is the scaling constant.

This type of oxidation may be termed the "stationary-state oxidation" because relation (4-24) is stationary in time. Stationary-state oxidation is characterized by a well defined microstructure of the oxidizing specimen. Non-existence of parametric solutions to the diffusion equations results in transient oxidation of alloys. Kirkaldy and Brown$^{(27)}$ have pointed out that exact parametric solutions do not exist where precipitation or non-planar development appears. Accordingly, stationary-state oxidation, if and when it appears to occur in such situations, is at best an approximation. It is also clear from the above discussion that parabolic behaviour is only one of the possible stationary-state behaviours since the function f(x,t) in Eq. (4-23) may have any form in general.

In the present work, we are interested primarily in the stationary-state parabolic kinetics. Thus the transient oxidation which occurs during the early stages of alloy oxidation prior to the establishment of the stationary state will be disregarded.

The invariant line O-Q defined by relation (4-24) (Fig. 4-2) is called the "diffusion path" and it is unique for the given terminal compositions and a given set of experimental conditions, e.g., temperature, pressure, etc. The diffusion path concept is a very compact means of representing ternary diffusion behaviour, especially in multi-phase systems. A detailed discussion of the diffusion-path concept follows in Chapter 5.

In view of the preceding discussion it is clear that if the oxidation process is diffusion-controlled and the concentration distributions are parametric in distance and time, then the interfacial compositions (C_B^{12},C_O^{12}), (C_B^{21},C_O^{21}), (C_B^{23},C_O^{23}) and (C_B^{32},C_O^{32}) are independent of time. However, it must be emphasized that these concentrations are not known <u>ab initio</u> and their determination is part of the problem to be solved. This is quite unlike isothermal oxidation of a pure metal in which case the binary phase diagram uniquely specifies the interface concentrations, if local equilibrium is assumed to prevail at the interfaces.

4.5 DIFFUSION MODEL

In this section we will develop a general diffusion model for the oxidation of a binary alloy AB by utilizing the flux equations derived in Section 4-2 together with appropriate boundary conditions. The following analysis is equally applicable to oxidation and sulfidation. Symbol X thus denotes either oxygen or sulfur.

4.5.1 General Assumptions

Temperature T and pressure P are assumed constant during oxidation. The following specific assumptions are made.

1. The alloy AB is assumed to be single phase.
2. Exclusive diffusion control is assumed, i.e., at the alloy-scale and scale-gas interfaces local thermodynamic equilibrium is supposed to prevail.
3. The alloy is assumed to be given as a flat sample of virtually infinite thickness.
4. The alloy-scale interface is assumed to be plane at any given time t > 0. This is assumed in all cases except in the case where there is morphological instability of the alloy-oxide interface. It is assumed that the oxide is compact and free of voids.

5. In general, the oxide and alloy have different molar volumes. The volume change associated with the oxidation reaction is assumed to cause one dimensional plastic flow of the oxide in the direction normal to the original alloy surface, defined as the x-direction. In other words, all the volume change is assumed to be accommodated in the x-direction.
6. In view of the last three assumptions equations are formulated for diffusion in one direction only.
7. In the scale, electronic charge conductance is assumed to prevail, and diffusion of cations of metals A and B rather than diffusion of anions of X is supposed to account for transport of matter across the scale.
8. For the present, only small deviations from the ideal metal-to-nonmetal ratio in the scale are assumed to occur.
9. It is assumed that a negligible amount of A or B escapes into the vapor phase.
10. The molar volume and the interdiffusion coefficient in the alloy are assumed to be concentration independent.
11. In the scale, only a single phase AX is supposed to be present. The symbol AX is used as a shorthand notation for an oxide or sulfide of A with B dissolved in it, i.e. for $B_yA_{n-y}X$. Thus there is no restriction as to the solubility of B in AX.

12. The compounds in the scale are denoted by A(X) and B(X) without specification of the molar ratio of the constituent elements. The equivalent volume, $V_{eq.}$ of the solid solution A(X)-B(X) is presumed to be independent of composition in accord with the fact that in most systems, the volume is predominantly determined by the volume of the larger anions.

4.5.2 Notation and Co-ordinate Frames

The notation which is used in subsequent sections is given below and in Fig. 4-3:

t	time
$k=x_s(dx_s/dt)$	rate constant for thickening of the scale
N_A, N_B	mole fractions of A and B, respectively, in the alloy
N_A^o, N_B^o	mole fractions of A and B respectively, in the bulk alloy
C_X, C_X^o	concentrations, in moles per unit volume, of X in the alloy and bulk alloy, respectively
C_X'	concentration, in moles per unit volume of X in the alloy at the scale-alloy interface
V_m	volume of alloy per mole of Aplus B (V_m is assumed constant)
V_{eq}	volume per equivalent of A(X) and B(X) in the scale (also assumed constant)

a_i	activity of species i
z_i	absolute valence of ions of type i
ξ	local equivalent fraction of B(X) in the scale
ξ_{av}	average equivalent fraction of B(X) in the scale
$J_{i(eq)}$	flux of i(A or B) cations in the scale towards the surface, in equivalents per unit area per unit time, relative to the x-reference frame
D_{alloy}	interdiffusion coefficient for species A and B in the alloy
D_X	interstitial diffusion coefficient of X in the alloy
D_A, D_B	self-diffusion coefficients of A and B cations, respectively, in the scale
C_i^{jk}	concentrations in mole per unit volume of element i in phase j adjacent to phase k.

Superscripts ' and " are used to denote quantities at the alloy-scale and scale-gas interfaces, respectively.

The dependent variables used in the following formulation are different than those shown in Fig. 4-1. It is more convenient to use oxygen or sulfur activity a_X and the equivalent fraction ξ, of B(X) as the variables in the oxide scale. In the alloy phase mole fraction N_B of the alloying element B and the molar concentration C_X, of oxygen or sulfur are used as the variables. The profiles of these variables as well as the various distance coordinate frames at time t are summarized in Fig. 4-3. In describing the diffusion processes in the alloy and oxide, it is convenient to use two different frames of reference. Firstly, the origin of the u-frame is located at the original alloy surface. Because the alloy lattice is stationary with respect to this coordinate system, it is used to describe diffusion in the alloy. The x-frame is attached to the scale-alloy interface and is utilized for the description of diffusion in the oxide.

The bulk alloy composition, N_B^o, C_X^o, correspond to the boundary value at $u = \infty$. $N_B^o = C_B^o/V_m$. In most cases $C_X^o \simeq 0$. Since the diffusion in the gas phase is fast the activities of B and X at the oxide-gas interface are virtually equal to their activities in the bulk gas phase. The values of ξ and a_O at the oxide-surface are therefore used as the remaining boundary conditions.

Since it is assumed that local equilibrium prevails at all phase interfaces and the oxide scale is of sufficient

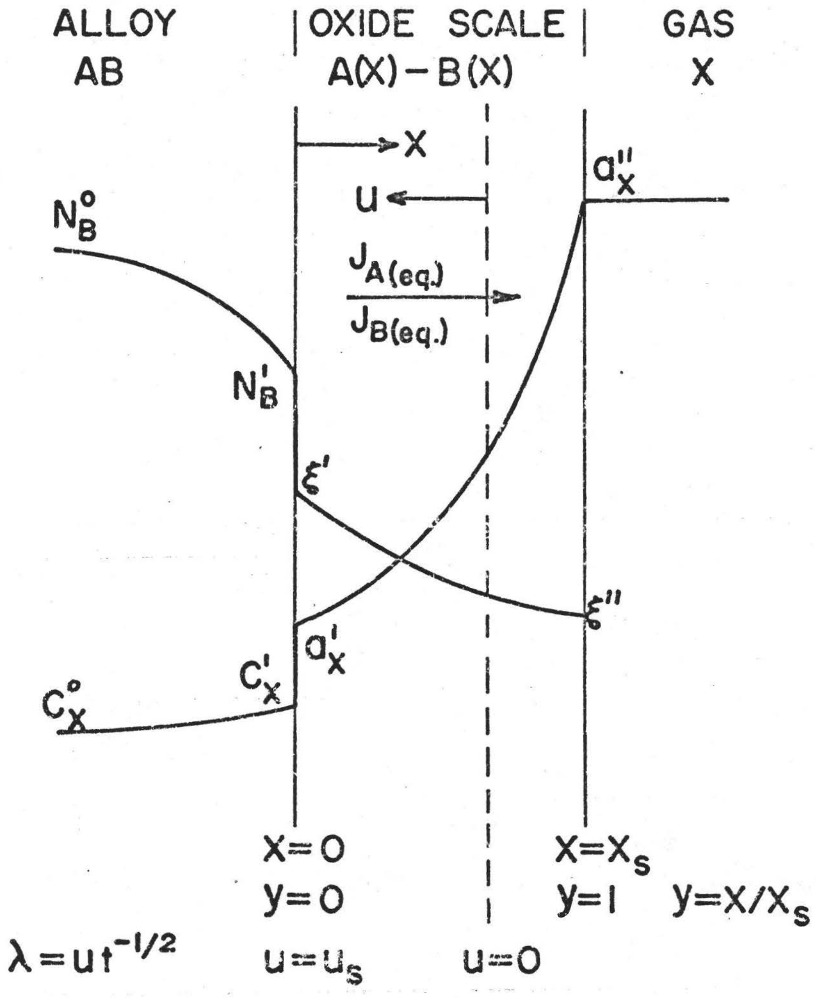

Fig. 4-3: Diffusion model with notations used in the text

thickness that electrical space charge effects can be neglected, the following thermodynamic conditions apply at the oxide-alloy interface:

$$\mu_i^{23} = \mu_i^{32} \qquad i = A, B, X \tag{4-27}$$

where μ_i^{jk} is the chemical potential of component i in phase j adjacent to phase k. The same notation is used for interface concentration in Figs. 4-1 and 4-2. Equilibrium data for a ternary system are generally summarized in terms of an isothermal phase diagram since it is comparatively easy to establish equilibrium concentrations between adjacent phases. Accordingly, relations (4-27) may be replaced by an equivalent set of boundary conditions which relate directly to the ternary phase diagram. In the ensuing analysis a variation of conditions (4-27) will be used.

4.5.3 Mathematical Formulation of the Ternary Diffusion Model

The following formulation of the ternary model is due mainly to Wagner(22). A similar formulation was developed by the author and D. E. Coates(136). However, Wagner's treatment is given below due to its elegance and completeness. Wagner's formulation was later modified and further extended to take into account the oxygen dissolution in the alloy by Coates and the author(23).

For the present, assume that negligible X dissolves in the alloy. Disregarding the correlation effects, Eq.

(4-16) may be utilized to express the fluxes of cations of metals A and B relative to the anion sub-lattice. These fluxes in equivalents per unit area per unit time are

$$J_{A(eq.)} = - \frac{D_A(1-\xi)}{V_{eq.}} \frac{\partial \ell n a_A}{\partial x} \qquad (4\text{-}28)$$

$$J_{B(eq.)} = - \frac{D_B \xi}{V_{eq.}} \frac{\partial \ell n a_B}{\partial x} \qquad (4\text{-}29)$$

where $(1-\xi)/V_{eq}$ and ξ/V_{eq} are the local concentrations of cations of A and B, respectively, in equivalents per unit volume.

A solid solution A(X)-B(X) involving deviations from the ideal metal-to-nonmetal ratio must be treated as a ternary system. In addition to pressure P, temperature T, and equivalent fraction ξ, one therefore has a fourth independent variable which may be chosen to be the activity a_X of the nonmetal X. Thus one may rewrite equations (4-28) and (4-29) upon expressing the activities a_A and a_B of metals A and B in the scale interms of a_X and ξ. The activities of the elements A, B and X and the compounds A(X) and B(X) are interrelated by

$$\mu_A^o + RT\ell n a_A + \left(\frac{z_A}{z_X}\right)(\mu_X^o + RT\ell n a_X) = \mu_{A(X)}^o + RT\ell n a_{A(X)} \qquad (4\text{-}30)$$

$$\mu_B^o + RT\ell n a_B + \left(\frac{z_B}{z_X}\right)(\mu_X^o + RT\ell n a_X) = \mu_{B(X)}^o + RT\ell n a_{B(X)} \qquad (4\text{-}31)$$

In the case of negligible deviation from the ideal stoichiometric metal-to-nonmetal ratio, the activities $a_{A(x)}$ and $a_{B(x)}$ are practically determined by P, T and ξ. Thus one obtains from Eqs. (4-28) to (4-31)

$$J_{A(eq)} = - \frac{D_A(1-\xi)}{V_{eq}} \left(\frac{\partial \ell n a_{A(x)}}{\partial \xi} \frac{\partial \xi}{\partial x} - \frac{z_A}{z_X} \frac{\partial \ell n a_X}{\partial x}\right) \qquad (4-32)$$

$$J_{B(eq.)} = - \frac{D_B \xi}{V_{eq.}} \left(\frac{\partial \ell n a_{B(x)}}{\partial \xi} \frac{\partial \xi}{\partial x} - \frac{z_B}{z_X} \frac{\partial \ell n a_X}{\partial x}\right) \qquad (4-33)$$

where values of $\partial \ell n a_{A(x)}/\partial \xi$ and $\partial \ell n a_{B(x)}/\partial \xi$ are supposed to be known quantities characteristic of the thermodynamics of the mixing of the quasibinary system A(X)-B(X). Because it is assumed that a negligible amount of X dissolves in the alloy, the fluxes relative to the anion sub-lattice are given by the fluxes in the x-frame. The sum of the fluxes of A and B at any distance x is related to the thickening rate of the scale by the equation

$$(J_{A(eq)} + J_{B(eq)})V_{eq} = \frac{dx_s}{dt} \qquad (4-34)$$

In view of the assumption of diffusion control, it is convenient to set

$$\frac{dx_s}{dt} = \frac{k}{x_s} \qquad (4-35)$$

which on integration yields

$$x_s = (2kt)^{1/2} \qquad (4-36)$$

A dimensionless parameter, y, is defined such that

$$y = \frac{x}{x_s} \qquad (4-37)$$

From Eqs, (4-36) and (4-37), we note that $y \alpha x/t^{1/2}$ and therefore because diffusion control is assumed, ξ and a_X should be expressible in terms of y only. Substitution of Eqs. (4-32), (4-33), (4-35) and (4-37) into Eq. (4-34) yields the following first order differential equation:

$$D_A(1-\xi)\left(-\frac{\partial \ell n a_{A(x)}}{\partial \xi}\frac{d\xi}{dy}+\frac{z_A}{z_X}\frac{d\ell n a_X}{dy}\right) + D_B\xi\left(-\frac{\partial \ell n a_{B(x)}}{\partial \xi}\frac{d\xi}{dy}+\frac{z_B}{z_X}\frac{d\ell n a_X}{dy}\right) = k,\ 1 \geq y \geq 0 \quad (4\text{-}38)$$

Applying the continuity equation to Eq. (4- 33) and again assuming ξ and a_X are functions of y only, Wagner obtains the second order differential equation

$$yk\frac{d\xi}{dy} = -\frac{d}{dy}\left[D_B\xi\left(\frac{\partial \ell n a_{B(x)}}{\partial \xi}\frac{d\xi}{dy}-\frac{z_B}{z_X}\frac{d\ell n a_X}{dy}\right)\right],\ 1 \geq y \geq 0 \quad (4\text{-}39)$$

In view of Eq. (4-34), it is clear that one would not obtain another independent differential equaiton by applying the continuity equation to Eq. (4-32). The distribution of the single independent component (arbitrarily chosen as B) in the alloy is a solution of the second order equation

$$\frac{d}{d\lambda}\left[D_{alloy}\frac{dN_B}{d\lambda}\right]+\frac{1}{2}\lambda\frac{dN_B}{d\lambda} = 0,\ \frac{u_s}{t^{1/2}} \leq \lambda \leq \infty \quad (4\text{-}40)$$

where

$$\lambda = \frac{u}{t^{1/2}} \quad (4\text{-}41)$$

One must now specify the appropriate boundary conditions for the set of differential equations (4-38), (4-39) and (4-40). It should be recalled that for a ternary system in which two phases are coexisting in equilibrium under isothermal and isobaric conditions, the Gibbs' phase rule indicates only one thermodynamic degree of freedom. Thus when Wagner assumes the activity of nonmetal X is given at the gas-scale interface, i.e.,

$$a_X \ (y = 1) = a_X''$$

then it follows that the equivalent fraction of B(X) at this interface is fixed by a presumably known relationship of the form

$$\xi'' = g(a_X'') \qquad (4\text{-}43)$$

The material balance of B at the gas-scale interface

$$J_{B(eq)} \ (x=x_s) = \frac{\xi''}{V_{eq}} \frac{dx_s}{dt} \qquad (4\text{-}44)$$

gives, on substituting Eqs. (4-33), (4-35) and (4-37), the following boundary condition

$$- [D_B \xi \ (\frac{\partial \ell n a_{B(X)}}{\partial \xi} \frac{d\xi}{dy} - \frac{z_B}{z_X} \frac{d \ell n a_X}{dy})]_{y=1} = \xi'' k \qquad (4\text{-}45)$$

which serves to establish the position of this interface.

Turning now to the scale-alloy interface and remembering that there is one thermodynamic degree of freedom here, it follows that there exist known functions of the form

$$N_B' = f_1(\xi') \quad \text{at } \lambda = u_s/t^{1/2} \qquad (4\text{-}46)$$

$$a_X' = f_2(\xi') \quad \text{at } y = 0 \tag{4-47}$$

and

$$c_X' = f_3(\xi') \text{ at } \lambda = u_s/t^{1/2} \tag{4-48}$$

These are alternatives to equation (4-27).

ξ' and the position of the interface must be determined with the help of two material balances. The position of the scale-alloy interface is fixed relative to the initial alloy surface by a material balance of sorts, viz., the ratio of the recession u_s of the alloy-scale interface to the thickness of the scale x_s, which is given by

$$\frac{u_s}{x_s} = \frac{V_m}{V_{eq}} \left(\frac{1-\xi_{av}}{z_A} + \frac{\xi_{av}}{z_B}\right) \tag{4-49}$$

where ξ_{av}, the average equivalent fraction of B(X) in the scale is given by

$$\xi_{av} = \int_0^1 \xi(y)\, dy \tag{4-50}$$

A material balance for B at the scale-alloy interface fixes the value of ξ' to be used in Eqs. (4-46), (4-47) and (4-48). Thus one obtains the boundary condition

$$z_B N_B' \left(\frac{1-\xi_{av}}{z_A} + \frac{\xi_{av}}{z_B}\right) + \frac{2^{1/2}\, z_B\, D_{alloy}\, V_{eq}}{k^{1/2}\, V_m} \left(\frac{dN_B}{d\lambda}\right)_{\lambda=u_s/t^{1/2}}$$

$$= -\left[\frac{D_B \xi}{k} \left(\frac{\partial \ell n a_{B(X)}}{\partial \xi} \frac{d\xi}{dy} - \frac{z_B}{z_X} \frac{d \ell n a_X}{dy}\right)\right]_{y=0} \tag{4-51}$$

Notice that because ξ_{av} has the definition given in Eq. (4-50), the above condition is in effect an integral equation which must be solved simultaneously with the other boundary conditions and differential equations. The final boundary condition is the initial alloy composition,

$$\left.\begin{aligned} N_B = N_B^{\,o} \text{ at } [u \geq 0 \quad t = 0] \\ [u = \infty \quad t = 0] \end{aligned}\right\} \text{ i.e. at } \lambda = \infty \qquad (4\text{-}52)$$

An explicit expression for ξ_{av} as an alternative to the formal definition given in Eq. (4-50) can be formulated. By using this expression to eliminate ξ_{av} in Eq. (4-51), one can avoid having to solve an integral equation. The following derivation simply involves application of Eq. (4-34) to the total material balance (i.e., for A + B) at the scale-alloy interface and comparison of this result with Eq. (4-49) to yield the desired expression.

The material balances for A and B at the scale-alloy interface are respectively(22)

$$z_A \left[\frac{N'_A}{V_m}\frac{du_s}{dt} + \frac{D_{alloy}}{V_m}\left(\frac{dN_A}{du}\right)_{u=u_s}\right] = J_{A(eq)}(x = 0) \qquad (4\text{-}53a)$$

$$z_B \left[\frac{N'_B}{V_m}\frac{du_s}{dt} + \frac{D_{alloy}}{V_m}\left(\frac{dN_B}{du}\right)_{u=u_s}\right] = J_{B(eq)}(x = 0) \qquad (4\text{-}53b)$$

Adding these equations together, we obtain

$$\frac{(z_A N'_A + z_B N'_B)}{V_m}\frac{du_s}{dt} + (z_B - z_A)\frac{D_{alloy}}{V_m}\left(\frac{dN_B}{du}\right)_{u=u_s} = (J_{A(eq)} + J_{B(eq)})_{x=0}$$

using the fact that the alloy is assumed to contain only A and B and therefore $dN_A/du = -dN_B/du$. Substitution of Eq. (4-34) into the right side of the above equation leads to

$$\frac{du_s}{dx_s} = \frac{V_m}{V_{eq}}\left(\frac{1}{z_A N_A' + z_B N_B'}\right)\left\{1 - \frac{(z_B - z_A)\, D_{alloy}\, V_{eq}}{V_m}\,\frac{(dN_B/du)_{u=u_s}}{dx_s/dt}\right\}$$

which, on introduction Eqs. (4-36) and (4-41), becomes

$$\frac{du_s}{dx_s} = \frac{V_m}{V_{eq}}\left(\frac{1}{z_A N_A' + z_B N_B'}\right)\left\{1 - \frac{2^{1/2}(z_B - z_A)\, D_{alloy}\, V_{eq}}{k^{1/2}\, V_m}\left(\frac{dN_B}{d\lambda}\right)_{\lambda = u_s/t^{\frac{1}{2}}}\right\} \qquad (4\text{-}54)$$

Noting that the right side of Eq. (4-49) is a constant it follows that

$$\frac{du_s}{dx_s} = \frac{V_m}{V_{eq}}\left(\frac{1-\xi_{av}}{z_A} + \frac{\xi_{av}}{z_B}\right) \qquad (4\text{-}55)$$

From Eqs. (4-54), (4-55) and the fact that $N_A' + N_B' = 1$, we obtain

$$\left(\frac{1-\xi_{av}}{z_A} + \frac{\xi_{av}}{z_B}\right) = \frac{1}{z_B N_B' + z_A(1-N_B')}\left\{1 - \frac{2^{\frac{1}{2}}(z_B - z_A)\, D_{alloy}\, V_{eq}}{k^{\frac{1}{2}}\, V_m} \times \left(\frac{dN_B}{d\lambda}\right)_{\lambda = u_s/t^{\frac{1}{2}}}\right\} \qquad (4\text{-}56)$$

which leads to the following expression for ξ_{av}

$$\xi_{av} = \frac{1}{z_B N_B' + z_A(1-N_B')}\left\{z_B N_B' + \frac{z_A z_B\, 2^{\frac{1}{2}}\, D_{alloy}\, V_{eq}}{k^{\frac{1}{2}}\, V_m}\left(\frac{dN_B}{d\lambda}\right)_{\lambda = u_s/t^{\frac{1}{2}}}\right\} \qquad (4\text{-}57)$$

Equations (4-56) and (4-57) are independent of equation (4-51) and therefore can be used to eliminate ξ_{av} in the latter equation.

Thus on substitution of Eq. (4-56) into the first term of Eq. (4-51), one obtains

$$\frac{z_B N_B'}{z_B N_B' + z_A (1-N_B')} + \frac{2^{\frac{1}{2}} z_A z_B D_{alloy} V_{eq}}{k^{\frac{1}{2}} V_m [z_B N_B' + z_A (1-N_B')]} \left(\frac{dN_B}{d\lambda}\right)_{\lambda = u_s/t^{\frac{1}{2}}}$$

$$= - \left[\frac{D_B \xi}{k} \left(\frac{\partial \ln a_{B(X)}}{\partial \xi} \frac{d\xi}{dy} - \frac{z_B}{z_X} \frac{d \ln a_X}{dy}\right)\right]_{y=0} \qquad (4\text{-}58)$$

which is a much easier boundary condition to deal with. Unlike Eq. (4-51) with Eq. (4-50) as the definition of ξ_{av}, Eq. (4-58) is not an integral equation.

Equation (4-57) simply relates ξ_{av} to the total amount of B depleted from the alloy and thus it is an expression of mass conservation. Its validity can be tested with known limiting cases. If $N_B^o = 0$, then since $N_B' = dN_B/d\lambda = 0$, Eq. (4-57) yields $\xi_{av} = 0$. Alternatively, if $N_B^o = 1$, then since $N_B' = 1$ and $dN_B/d\lambda = 0$ Eq. (4-57) yields $\xi_{av} = 1$. Consider the oxidation of an alloy AB in which B is a noble metal. Because B is noble, $z_B = 0$ and Eq. (4-57) yields $\xi_{av} = 0$. If there is negligible diffusion in the alloy, then $N_B' \cong N_B^o$, $dN_B/d\lambda \cong 0$ and Eq. (4-57) yields

$$\xi_{av} \cong \frac{z_B N_B^o}{z_B N_B^o + z_A (1 - N_B^o)} = \xi_{alloy} \qquad (4\text{-}59)$$

where ξ_{alloy} is the equivalent fraction of B in the bulk alloy.

It is essential to keep in mind that the system in question involves three components. Therefore there are two independent mass balances at the scale-alloy interface. To obtain the boundary condition (4-58), material balances for B and A + B were employed. Clearly, by using other combinations (eg., A and B, or A and A + B) one could derive a number of expressions which are equivalent to Eq. (4-58).

4.6 APPLICATION OF THE TERNARY DIFFUSION MODEL - CONCENTRATION PROFILES IN NiO-CoO MIXED OXIDE FORMED DURING OXIDATION OF Ni-10.9% Co ALLOY AT 1000°C IN PURE OXYGEN

The Ni-Co system at 1000°C is a very suitable system for testing the ternary diffusion model described earlier. Ni and Co are adjacent transition metals in the periodic table and have nearly equal ionic radii in corresponding valence states(7). This fact together with the fact that NiO and CoO have almost equal free energies of formation at 1000°C(109,137) gives rise to their observed mutual solubility across the entire phase diagram. Zintl(138,139) has recently carried out an extensive investigation of the defect structure of the NiO-CoO mixed oxide at 1000°C. Using electron-probe microanalysis Wood and Ferguson(140) have determined the distributions of Ni and Co across the alloy and scale for Ni-10.9% Co alloy oxidized in pure oxygen at 1000°C. Their data for oxidation over several periods of time, is summarized in Fig. 4-4.

4.6.1 Theory

The solid solution CoO-NiO may be considered to be nearly ideal in view of data for the analogous systems CoO-MgO and NiO-MgO(141,142). Accordingly

$$\frac{d\ell n a_{CoO}}{d\ell n \xi} = 1 \qquad (4\text{-}60)$$

where ξ is the equivalent fraction (which is equal to the mole fraction) of CoO in the scale.

It is generally agreed that the transport of Ni and Co in the scale takes place via cation vacancies. In both pure NiO and pure CoO the metal deficit, corresponding to the presence of cation vacancies (singly or doubly ionized) and electron holes, is proportional to a fractional power of the oxygen partial pressure p_{O_2}. Since in the case of diffusion via vacancies, the tracer diffusion coefficient is essentially proportional to the concentration of cation vacancies, D_{Ni} and D_{Co} in the respective oxides are expected to be proportional to $p_{O_2}{}^{1/n}$ where n is between 4 and 6(75,143,144,145,146,147).

Work on the self-diffusion of Ni in NiO and Co in CoO on the defect structures of the respective oxides(18,60,75,143,144,145,146,147,148,149) shows that the activation energies for vacancy migration are nearly equal, 30 kcal/mole and 28.5 kcal/mole for CoO and NiO respectively. On the other hand, the activation energies for vacancy formation differ considerably, 15 kcal/mole and 35 kcal/mole for CoO and NiO, respectively. Accordingly the mobilities of Ni and Co cations in the respective oxides should be nearly equal. However, the vacancy concentrations in these oxides will differ considerably under similar conditions, resulting in significantly different self diffusion coefficients in the oxides. It is to be expected that in a continuous NiO-CoO solid solution, D_{Ni} and D_{Co} will be functions of ξ. Zintl(138,139) has found that in NiO-CoO solid solution the metal deficit and likewise the cation vacancy concentration at constant p_{O_2} decreases nearly exponentially upon addition of NiO to CoO. This quasi-exponential decrease of the cation vacancy concentration in CoO upon addition of NiO is ascribed to loss of quantum mechanical resonance(138). Analogous situations have been found in the systems Cu_2S-Ag_2S, and Cu_2Se-Ag_2Se(150,151,152).

Wagner(153) has suggested that in view of the above considerations, the mole fraction $N_{\square}$ of cation vacancies in NiO-CoO solid solutions, as a function of ξ and oxygen activity, may be expressed as follows:*

$$\log N_{\square} = \log N_{\square}^{NiO} + \xi \log(N_{\square}^{CoO}/N_{\square}^{NiO}) + \log a_O^{1/\nu} \qquad (4\text{-}61)$$

where $a_O \equiv [p_{O_2}(\text{atm.})]^{1/2}$, $N_{\square}^{NiO}$ and $N_{\square}^{CoO}$ are the cation vacancy

---

*In the following analysis correlation effects are neglected.

mole fractions at $p_{O_2} = 1$ atm. in NiO and CoO, respectively, and $\nu = n/2$. The tracer diffusion coefficient of cobalt may be approximated by$^{(153)}$

$$\left.\begin{aligned} D_{Co} &= D^{o}_{Co}\,\frac{N_{\square}}{N^{CoO}_{\square}} \\ \text{where} & \\ D^{o}_{Co} &= D_{Co}(\text{in CoO, } p_{O_2} = 1 \text{ atm.}) \end{aligned}\right\} \qquad (4\text{-}62)$$

Similarly, the tracer diffusion coefficient of nickel may be approximated by

$$\left.\begin{aligned} D_{Ni} &= D^{o}_{Ni}\,\frac{N_{\square}}{N^{NiO}_{\square}} \\ \text{where} & \\ D^{o}_{Ni} &= D_{Ni}(\text{in NiO, } p_{O_2} = 1 \text{ atm.}) \end{aligned}\right\} \qquad (4\text{-}63)$$

$N_{\square}$ in Eqs. (4-62) and (4-63) is given by Eq. (4-61). Since $N^{NiO}_{\square}$ is small, the properties of NiO are very sensitive to impurities. Hence one may replace Eq. (4-63) by

$$D_{Ni} = p\, D_{Co} \qquad (4\text{-}64)$$

where the constant p is essentially the ratio of the jump frequencies of nickel and cobalt ions into an adjacent cation vacancy. Zintl$^{(138)}$ has calculated $p = 0.42$ from the data of Price and Wagner$^{(145)}$ and $p = 0.72$ from the data of Carter and Richardson$^{(144)}$ and Choi and Moore$^{(149)}$.

From Eqs. (4-61), (4-62) and (4-64)

$$\left.\begin{aligned} D_{Co} &= D^{o}_{Co}\ \beta^{\xi-1} a_{O}^{1/\nu} \\ \text{and} \qquad & \\ D_{Ni} &= pD^{o}_{Co}\ \beta^{\xi-1} a_{O}^{1/\nu} \end{aligned}\right\} \qquad (4\text{-}65)$$

where

$$\beta = N_{\square}^{CoO}/N_{\square}^{NiO} \qquad (4\text{-}66)$$

The value of β is estimated to be 62 from the data of Zintl$^{(139)}$.

Let the oxidation constant k for the alloy be defined by Eq. (4-36) and let y be the dimensionless parameter defined by Eq. (4-37). The Gibbs-Duhem equation for the NiO-CoO solid solution may be expressed as

$$d\ell n a_{NiO} = -\frac{\xi}{1-\xi}\, d\ell n a_{CoO} \qquad (4\text{-}67)$$

In the NiO-CoO solid solution the vacancies of the components are $z_{Ni} = z_{Co} = Z_O = 2$.

Substitution of Eqs. (4-60) and (4-67) into Eq. (4-38) yields

$$(D_{Ni} - D_{Co})\frac{d\xi}{dy} + \frac{d\ell n a_O}{dy}\,[(1-\xi)D_{Ni}+\xi D_{Co}] = k \qquad (4\text{-}68)$$

From Eqs. (4-65) and (4-68) we obtain,

$$\frac{d\ell n a_O}{dy} = [\frac{k'}{\beta^{\xi-1} a_O^{1/\nu}} - (p-1)\,\frac{d\xi}{dy}]/[p-(p-1)\xi] \qquad (4\text{-}69)$$

where

$$k' = k/D^{o}_{Co} \qquad (4\text{-}70)$$

Eqs. (4-39), (4-64), (4-65), (4-66) and (4-69) yield after carrying out the intended differentiations,

$$[p-(p-1)\xi]\,\frac{d^2\xi}{dy^2} + [(1-\frac{1}{\nu})(p-1)+[p-(p-1)\xi]\ln\beta]\;(\frac{d\xi}{dy})^2$$

$$-\frac{k'(d\xi/dy)}{\beta^{\xi-1}a_O^{1/\nu}}\,[(1-\frac{1}{\nu}) - \frac{y[p-(p-1)\xi]^2}{p}] = 0 \qquad (4\text{-}71)$$

From Eqs. (4-45), (4-64), (4-65) and (4-66) we have after rearrangement,

$$k' = -\frac{p\,\beta^{\xi''-1}(a_O'')^{1/\nu}(\frac{d\xi}{dy})_{y=1}}{\xi''(1-\xi'')(p-1)} \qquad (4\text{-}72)$$

Substitution of Eq. (4-72) into Eq. (4-71) gives the following differential equation to describe the variation of the mole fraction of CoO, ξ, in the scale as a function of y.

$$[p-(p-1)\xi]\,\frac{d^2\xi}{dy^2} + \{(1-\frac{1}{\nu})(p+1)+[(p-(p-1)\xi]\ln\beta\}\;(\frac{d\xi}{dy})^2$$

$$+\beta^{(\xi''-\xi)}(a_O''/a_O)^{1/\nu}\,\{\frac{p(1-\frac{1}{\nu})\;-y[(p-(p-1)\xi]^2}{\xi''(1-\xi'')(p-1)}\}\;(\frac{d\xi}{dy})_{y=1}(\frac{d\xi}{dy})=0 \qquad (4\text{-}73)$$

where $\xi'' = \xi(y=1)$, $a_O'' = a_O(y=1)$. If $\xi << 1$, then the factor $p-(p-1)\xi$ in Eqs. (4-69) and (4-73) can be approximated by p.

Equations (4-69) and (4-73) are non-linear differential equations in which the dependent variables ξ and a_O are inseparable. Thus equation (4-69) and (4-73) must be solved simultaneously. Two boundary values ($\xi(y=0)$, and $\xi(y=1)$) are required for the solution Eq.(4-73) and one boundary value, a_O'', is required for the solution of Eq.(4-69). The values of the parameters, p, k', β and ν should also be known.

4.6.2 Numerical Solution

From the data of Wood and Ferguson(140), the boundary values are estimated to be $\xi(y=0) = 0.041$ and $\xi(y=1) = 0.315$. Since pure oxygen was used in their oxidation experiment, $a_O'' = 1$. Wood and Ferguson give the average value of the parabolic rate constant for the Ni-10.9% Co alloy investigated as $k_p = 4.9 \times 10^{-10}\ g^2 cm^{-4} sec^{-1}$. This k_p is related to the corrosion constant k defined in Eq. (4-35) by the following expression

$$k = \frac{k_p}{2}(V/16)^2\ cm^2/sec \qquad (4\text{-}74)$$

where V is the molar volume of the oxide. For the NiO-CoO solid solution, an average value of 11 cm^3 for V may be assumed. Thus $k = 1.18 \times 10^{-10}\ cm^2/sec$. The value of D_{Co}^o lies in the range $2.6 - 4.0 \times 10^{-9}\ cm^2/sec$, from references (60, 144, 146, 154). Thus $k' = k/D_{Co}^o = 0.036$ for an average value of D_{Co}^o (i.e., $3.3 \times 10^{-9}\ cm^2/sec$). In the analysis the value of p was taken as 0.5. Recall that β was estimated to be 62. Using these values and various values of ν, Eqs. (4-69) and (4-73) were solved numerically with the help of a computer to obtain ξ and a_O as functions of y. Meaningful results could not be obtained for ν = 2. The best result

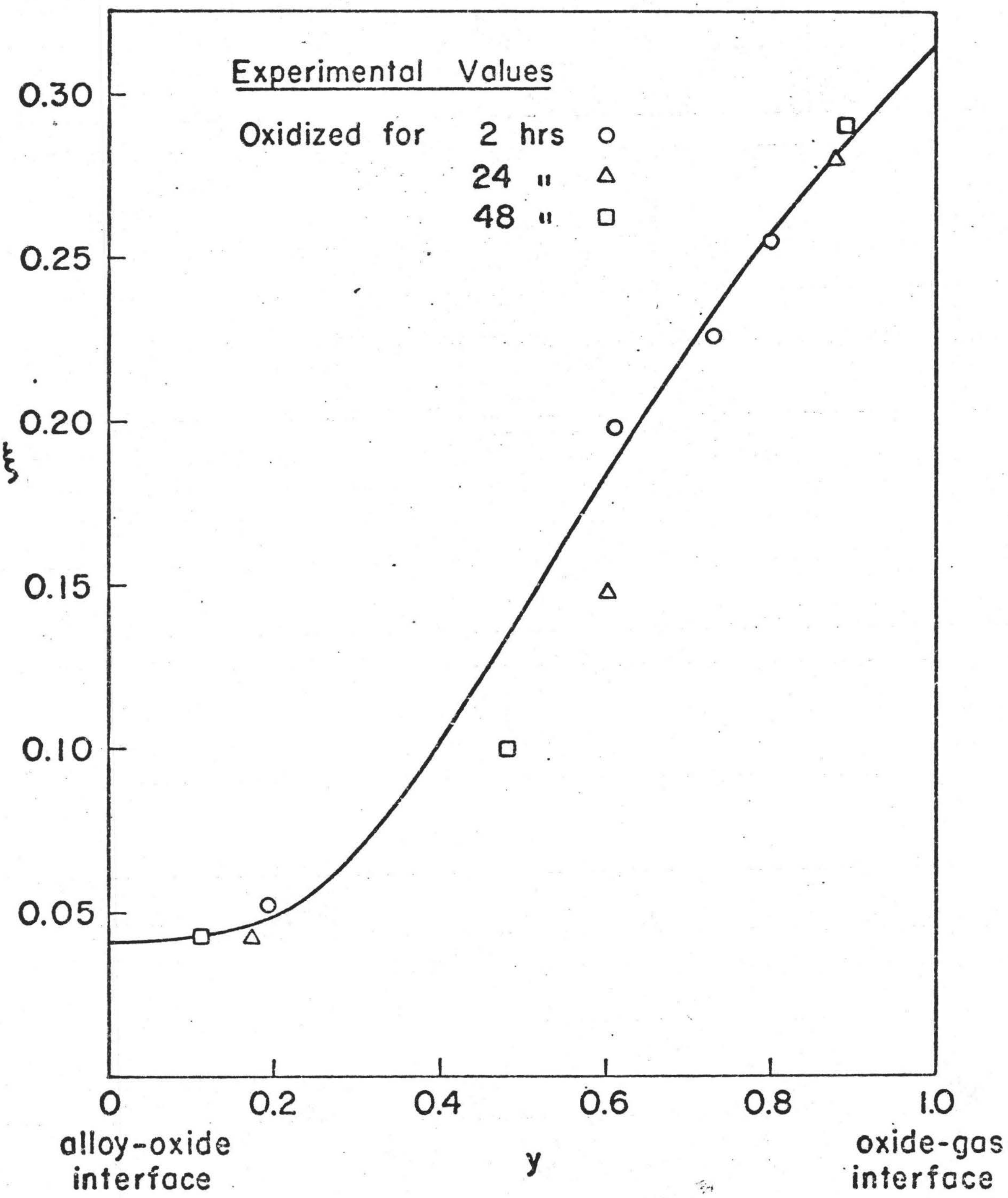

Fig. 4-4: Equivalent fraction of CoO, ξ, as a function of normalized distance coordinate y in the NiO-CoO oxide scale formed on Ni-10.9% Co alloy oxidized at 1000°C in pure oxygen. Solid line represents calculated values from Eqs. (4-69) and (4-73). Experimental points are from reference (140).

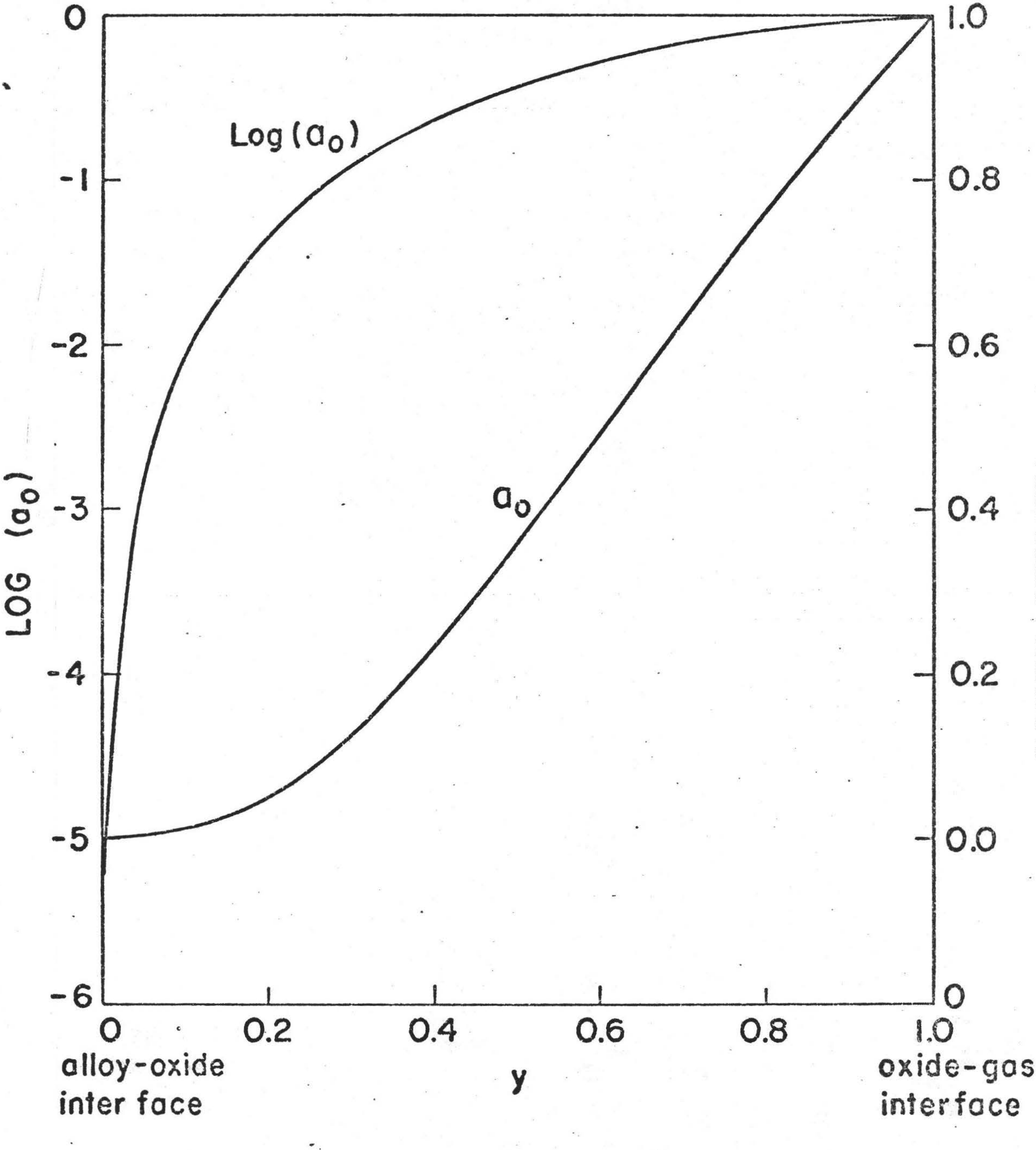

Fig. 4-5: Oxygen activity versus normalized distance in the NiO-CoO oxide scale for $k/D^{o}_{Co} = 0.036$ from Eqs. (4-69) and (4-73).

was obtained for $\nu = 2.5$ which corresponds to a $p_{O_2}{}^{1/5}$ dependence on the vacancy concentration in the oxide.

The values of β and k' were adjusted slightly so as to yield the approximate equilibrium oxygen activity at the alloy-oxide interface. This may be estimated as follows: We have(109,137)

$$\left.\begin{aligned} &NiO + Co = CoO + Ni \;, \Delta G^{o}_{1000} = -4470 \text{ cal} \\ &Ni + 1/2\, O_2 = NiO \;, \quad \Delta G^{o}_{1000} = -30{,}150 \text{ cal} \end{aligned}\right\} \quad (4\text{-}75)$$

Assuming ideality of the Ni-Co and NiO-CoO systems and noting that $N_{NiO} + N_{CoO} = 1$ for the oxide, one obtains

$$a_O = (0.171 + 0.829\, N_{NiO}) \times 6.7 \times 10^{-6} \qquad (4\text{-}76)$$

Corresponding to $\xi = 0.04$ at the alloy-oxide interface, one has $a_O = 6.47 \times 10^{-6}$. The value of a_O at the alloy-oxide interface from the calculations is 6.39×10^{-6}.

The calculated and observed values of ξas a function of the normalized distance parameter y are given in Fig. 4-4. The corresponding values of the oxygen activity a_O in the scale are given in Fig. 4-5. The results yield $(d\xi/dy)_{y=1} = 0.25$ and $(d\xi/dy)_{y=0} = 7.2 \times 10^{-6}$.

4.6.3 Discussion

Comparison of the calculated and observed values of ξ in the scale in Fig. 4-4 shows a fairly close agreement except for the two experimental points in the centre of the scale.

Considering the uncertainties (which are of the order of 50-100%) involved in the values of the various parameters and the probable errors involved in the experimental points, the results appear to be satisfactory and self consistent. It is interesting to note that the oxygen activity profile is very similar to $\xi(y)$. The oxygen activity variation flattens out as the scale-alloy interface is approached since a negligible amount of oxygen is assumed to dissolve in the alloy.

Eqs. (4-69) and (4-73) effectively show the way in which the various kinetic and thermodynamic parameters interact and their effects on one another. Thus the oxygen activity profile is steep for larger values of k' and β and smaller values of ν. Steeper oxygen activity gradients result in steeper gradients of $\xi(y)$.

In considering the agreement between the theory and experiment, it must be pointed out that since experimental values $\xi(y=0)$ and $\xi(y=1)$ have been used in the analysis, the slope of the distribution curve, in the <u>middle</u> region between $y = 0$ and $y = 1$ has been calculated. However, the results from the analysis due to Wagner explains why diffusion of cations against their concentration gradients is possible in these mixed oxides.

Normally, one would expect Co or Ni to diffuse down its own gradient. Since there is no source of either Co or Ni in the oxide. This means that no cation gradients in the oxide would be possible. This is because, since both Co and Ni are on the same sub-lattice, it is not possible to have decreasing concentrations of one without having correspondingly increasing concentrations of the other. In the present treatment this difficulty is eliminated because thermodynamic interactions are taken into account. Consider equation (4-33). Let B be Co and X be O. The first term in this equation is the normal Fick term corresponding to diffusion down the concentration gradient. In the present case, since $\frac{d\xi}{dy}$ is positive, this will yield negative values of diffusion flux. However the term that overcomes this effect is the second term in the equation corresponding to the oxygen activity gradient. This term is positive and for positive values of J_{Co}, has to be numerically greater than the first term. It is clear from Eq. (4-33) that no uphill diffusion of Co is possible without the presence of an oxygen activity gradient. Uphill diffusion in multicomponent systems was discussed by Darken(117,155) as early as 1942 and explained in terms of thermodynamic interactions. It is nevertheless worthwhile to reemphasize that in problems such as the present one, activity gradients rather than concentration gradients should be used in writing the flux equations since strong thermodynamic interactions exist.

It is noteworthy that a relatively minor difference in the jump frequencies of Co and Ni cations corresponding to p = 0.5 results in a very significant enrichment of the more mobile constituent next to the outer surface of the scale.

In the present analysis only three boundary conditions, viz. $a_O(y=1)$, $\xi(y=0)$, $\xi(y=1)$, were initially used for the solution of the differential equations (4-69) and (4-73). The boundary value $a_O(y=0)$ calculated from the the thermodynamic conditions was used only to check the experimental value of k'. Alternatively one can solve Eqs. (4-69) and (4-73) with four boundary conditions and consider k' as a parameter which is unknown but determined by the two differential equations. In this way the value of $a_O(y=0)$ is utilized more significantly to calculate the value of k' and consequently the parabolic rate constant for the alloy. In numerical solutions this has to be done by trial and error procedures. Thus we start with a tentatively assumed value of k' and calculate $a_O(y=0)$ and compare this with the thermodynamically calculated value. The value of k' is then adjusted until these two values match. The procedure adopted in this analysis in effect corresponds to this. Since the starting value is the experimental value, the number of trials are reduced. However, it should be noted that one may start with any arbitrary value of k' to arrive at the correct solution. The parabolic rate constant of the alloy is thus obtained as part of the solution.

Schmalzried and Holt(156) have calculated the concentration profiles for interdiffusion in the system NiO-MgO. Their results show a marked asymmetry in the concentration distribution. The profiles calculated by these authors are at constant oxygen potential and the analysis is correspondingly simpler.

The agreement between theory and experiment (Fig. 4-4) may be regarded as worthwhile support for the validity of Wagner's general treatment. The present analysis also serves to confirm the assumptions(138,139) which are made regarding the nature of the (Ni,Co)O mixed oxide system.

4.7 OXYGEN DIFFUSION IN THE ALLOY AND INTERNAL OXIDATION

It has been assumed in the preceding sections that the oxygen solubility of the alloy is negligible and hence oxygen diffusion in the alloy has been neglected. However oxygen diffusion in the alloy, in general, may be accounted for by permitting a dissociation reaction to take place at the scale-alloy interface. The oxygen thus released into the alloy may be assumed to diffuse interstitially inwards. That the dissociation reaction and the subsequent diffusion will occur is clear when one recognizes the very substantial driving forces. Under conditions in which there is no anion transport in the scale, the dissociation reaction $A(X) + B(X) \rightarrow A+B+nX$ must take place in order to supply sufficient X to the alloy to establish an activity a_X' at the scale-alloy interface and hence to maintain local equilibrium with the scale.

In the absence of internal precipitation it is observed that for most systems the total amount of oxygen or sulfur dissolved in the alloy is small in comparison to the total amount of oxygen in the scale at a given time. (Notable exceptions are metals such as zirconium and niobium). Therefore the scaling rate of an alloy is usually not influenced to a significant extent by solution of oxygen in the alloy(157). Thus, if the solubility of X in the alloy is small, one can determine the distribution of X in the alloy by first solving Wagner's system of equations which ignores the non-metal content of the alloy. This gives C_X' from eq. (4-48) and also $u_s = u_s(t)$ and $x_s = x_s(t)$. One then uses these values together with the boundary conditions,

$$C_X = C_X^o \quad \text{at} \quad \left.\begin{array}{ll} u \geq 0 & t = 0 \\ u = \infty & t > 0 \end{array}\right\} \quad \text{i.e. at } \lambda = \infty \qquad (4\text{-}77)$$

to solve the following diffusion equation for X in a straightforward manner:

$$\frac{d}{d\lambda}\left[D_X \frac{dC_X}{d\lambda}\right] + \frac{1}{2}\lambda \frac{dC_X}{d\lambda} = 0, \quad \frac{u_s}{t^{1/2}} \leq \lambda \leq \infty \qquad (4\text{-}78)$$

For situations in which internal oxidation does take place, the relative amount of oxygen which goes into the alloy can be quite significant. Under the present transport conditions this corresponds to appreciable oxide dissociation occurring at the scale-alloy interface.

Given that the solution of X in an internal precipitate-free alloy normally has little influence on the scaling rate of the alloy, the question arises as to why the distribution of X in the alloy is important. The interest in the presence and transport of X in the alloy is primarily prompted by a desire to be able to predict whether or not internal precipitation will occur during oxidation or sulfidation in a given system A-B-X. Clearly, a first step in such a direction is the determination of what the metal and nonmetal distributions in the alloy would be in the absence of any internal precipitation. Knowing these distributions one can use the appropriate ternary phase diagram to establish if a supersaturated zone would exist in the alloy adjacent to the scale-alloy interface and hence whether or not to expect internal oxidation or sulfidation. Let us suppose that the various concentration distributions have been calculated for the alloy, under the assumption that no internal oxide forms. Thus the relation

$$C_B = C_B\,(C_X) \tag{4-79}$$

is known. Plotting this function on the ternary isotherm corresponding to the system A-B-X one might have a configuration similar to that given in Fig. 4-6.

In Fig. 4-6, three possibilities are shown for the virtual diffusion path calculated with the assumption of existence of only planar interfaces:

(a) the virtual diffusion path does not enter the two-phase field and therefore one would expect no internal oxidation. In this case, the actual concentration distributions will coincide with the calculated ones;

(b) the virtual path passes into the two-phase field. This indicates that the alloy adjacent to the scale-alloy interface is not thermodynamically stable. Thus one expects internal oxidation and/or morphological instability of the scale-alloy interface to occur, thus relieving the supersaturated state;

(c) this virtual path corresponds to an unstable situation in which ternary diffusion interactions between the various components in the alloy has produced a maximum in the distribution of the nonmetal.

Given solutions to the diffusion equations for the internal precipitation zone of the alloy,a rather straightforward modification of the concepts developed in this section would give a unified solution to the problem. A solution which simultaneously gives the thickening rates of the external

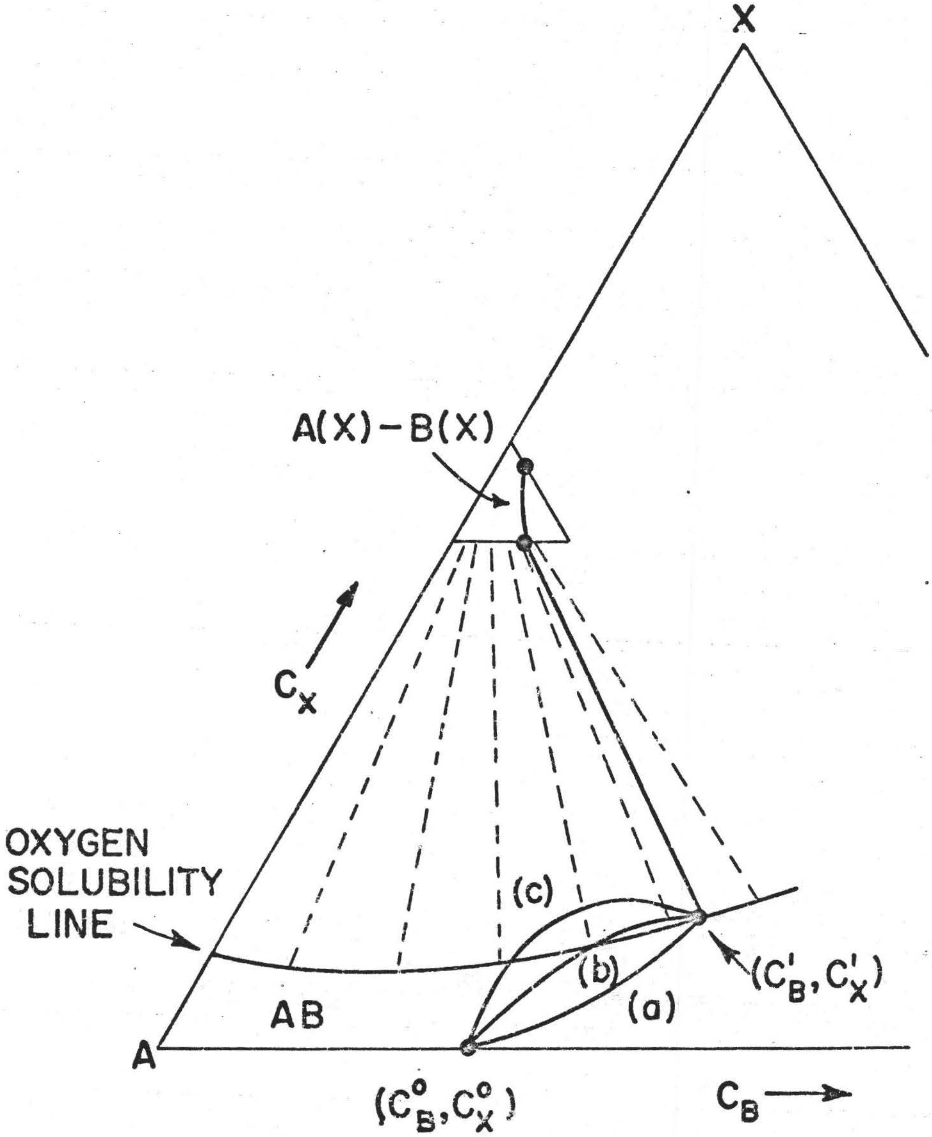

Fig. 4-6: Possible virtual diffusion paths for oxidation or sulfidation of a binary alloy AB

scale and of the internal precipitation zone in this alloy, and the concentration distributions in the external scale and the alloy. In most practical cases the internal oxidation zone contains a significant amount of internal precipitate, which in many cases has variable composition as for example when spinels occur as internal precipitates. Unfortunately, at present there does not exist an adequate treatment of transport in the internal precipitation zone to account for such a case. However, Kirkaldy(24) has given an analysis for a special case, in which the concentration distributions in the alloy are calculated for situations involving a very finely dispersed internal precipitate with low particle density and constant composition. This treatment is summarized in the following. Kirkaldy(158) has also recently considered the blockage effect in the alloy matrix due to the presence of internal precipitate particles and the effect of variation of the internally precipitated oxides.

In his analysis of internal oxidation, Kirkaldy(24) has assumed that the ternary solubility curve is accurately known by the relation

$$C_B = C_B\ (C_X) \qquad (4\text{-}80)$$

With these assumptions Kirkaldy formulated the following diffusion equations for the matter transport in the precipitation zone:

$$-\frac{\partial}{\partial u} D_X \frac{\partial C_X}{\partial u} + \frac{\partial C_X}{\partial t} = -\frac{\partial p_X}{\partial t} \qquad (4\text{-}81)$$

$$-\frac{\partial}{\partial u} D_{alloy} \frac{\partial C_B}{\partial u} + \frac{\partial C_B}{\partial t} = -n\frac{\partial p_X}{\partial t} \qquad (4\text{-}82)$$

where the sink term or rate of precipitation $\frac{\partial p_X}{\partial t}$ is the number of moles of precipitate formed per second per unit volume expressed in terms of component X, and n is a number expressing the composition of the precipitate phase (e.g. for NiO, n=1). Assuming that parabolic solutions to Eqs. (4-81) and (4-82) exist and using the condition of continuity of flux and concentration of component X between the precipitate and non precipitate zone, i.e.,

$$\left.\frac{\partial C_X}{\partial u}\right|_{\text{precip.}} = \left.\frac{\partial C_X}{\partial u}\right|_{\text{non precip.}} \qquad (4\text{-}83)$$

and

$$\left.C_X^p\right|_{\text{precip.}} = \left.C_X^p\right|_{\text{non precip.}}$$

at the boundary between these zones defined by $u = u_p$. Kirkaldy has solved Eqs. (4-81) and (4-82) for p as a function of x and u_p, the penetration of the zone of internal oxidation. The depth of the internal precipitation zone, ξ, can be estimated approximately by

$$\xi = (2\sqrt{D_{alloy}})t^{1/2} \qquad (4\text{-}85)$$

for the conditions $D_{alloy} << D_X$ and $|dC_B/dC_X| >> 1$.

CHAPTER 5

APPLICATION OF THE DIFFUSION PATH CONCEPT TO THE OXIDATION OF BINARY ALLOYS

5.1 THE CONCEPT OF DIFFUSION PATH

In their explanation of the internal oxidation of copper and silver alloys, Rhines and coworkers(112,116,159) were the first to make use of the ternary A-B-O phase diagram. Thomas(113) later made use of the "locus of composition" in conjunction with the ternary phase diagram to explain the scale structure developed during binary alloy oxidation. However the concept of diffusion path was primarily introduced by Clark and Rhines(25) to rationalize the metallographic structures obtained in diffusion layers in the ternary Al-Mg-Zn system. Clark and Rhines superposed experimental composition paths on the corresponding ternary phase diagram and discussed the rules governing the course of composition path in multi-layered ternary diffusion structures. A composition path is the sequence of compositions and phase structures as obtained from one end of a diffusion couple to the other, as plotted on the ternary phase diagram. A formal definition of diffusion path was introduced in Section 4.4. This was developed by Kirkaldy and coworkers(26,27) from a phenomenological point of view. It is implicit in their analysis that local equilibrium obtains at all times.

Relation 4-24 when plotted on the corresponding ternary phase diagram describes the "virtual" diffusion path(26.27) (Line O-Q in Fig. 4-2). The reason this diffusion path is referred to as "virtual" is that it is calculated on the assumption that all the interfaces are planar and stable and that there is no internal precipitation. Using the virtual diffusion path in conjunction with a knowledge of the thermodynamic and diffusion parameters of the system, one can decide whether or not to expect the occurrence of morphological breakdown or internal oxidation. Then to describe the actual configuration of the system one must take into account such phenomena (if they are predicted by the virtual path) and solve the diffusion equations with a reformulated set of boundary conditions. A relationship of the form of Eq. 4-24 thus obtained will be referred to as the "actual" diffusion path. It is possible to determine the relation $C_B = C_B(C_O)$ experimentally either by using metallographic techniques as was done by Clark and Rhines in the study of Al-Mg-Zn system or by using electron probe analysis. Following Clark and Rhines we term a relationship thus obtained the "actual composition path". If the theoretical analysis is correct, then the "actual diffusion path" and "actual composition path" for a system should be the same.

We note that in constructing diffusion paths, the shift in the alloy composition from the bulk-alloy to the alloy-oxide interface is away from the component which is preferentially oxidized. Kirkaldy and Brown$^{(27)}$ have developed a number of useful theorems pertaining to the construction of diffusion paths on ternary isotherms. Following are some of the important rules in the construction of diffusion paths with reference to alloy oxidation.

1. A diffusion path on the ternary A-B-O isotherm must either coincide or cross at least once the straight line joining the bulk alloy composition to the oxygen corner of the phase diagram. This rule is a simple consequence of the mass balance for the alloying elements A and B. In most cases the loss of A and B through evaporation is negligible. Therefore the mean ratio of A to B in the system as a whole must be the same as in the original alloy. The locus of such a relation wherein the ratio of A to B is fixed and is equal to the original alloy composition is the straight line joining the original alloy composition to the oxygen corner. Now if the diffusion path were to lie all on one side of this line, then the mean composition of the system will have to be off the line, in contradiction to the original mass balance requirement.
2. To the extent that lateral diffusion and non-uniformity of layer interfaces can be ignored or averaged out, the diffusion paths involving two-phase regions may be approximated by a stationary path connecting a continuous series of local equilibria.

3. A diffusion path that passes through a two-phase region coincident with a tie - line contains a planar interface whose local equilibrium specification is given by that tie-line.
4. A diffusion path in a two-phase region may not reverse its order of crossing the tie-lines.
5. Paths that pass through three-phase triangles must do so along a straight line representing at its extreme the local equilibrium existing at a planar interface.
6. Since the sources for the alloying elements A and B are in the alloy only, for mass transport of these components in the oxide phases their activities must decrease monotonically in the external oxide scale towards the oxide gas interface. Similarly, since the oxygen source is in the gas phase only, the activity of oxygen should monotonically decrease from the gas phase to the bulk alloy.

These rules are applicable to both single layer and multilayer scales.

5.2 CONSTITUTIONAL SUPERSATURATION

The concept of constitutional supersaturation is analagous to the concept of constitutional supercooling which was first discussed by Rutter and Chalmers(160) in connection with unidirectional crystallization of dilute tin alloys, and later given quantitative basis by Tiller et al.(161). In the case of constitutional supercooling the third "component" is heat and its potential corresponds to temperature. In the case of constitutional supersaturation the third component is oxygen with its corresponding chemical potential. Every point in the alloy ahead of the alloy-oxide interface corresponds to definite concentrations of the alloying elements, and thus a definite oxygen solubility as given by the ternary A-B-O phase diagram. There is also a definite oxygen concentration gradient in the alloy imposed by the growth conditions. If the oxygen concentration at a certain point as maintained by the diffusion gradient is higher than the oxygen solubility at that point as predicted by the ternary equilibrium diagram, then the alloy at that point will be "constitutionally supersaturated" with respect to oxygen. Constitutional supersaturation is created during alloy oxidation due to low diffusion coefficients of the alloying elements in the alloy phase resulting in a steep concentration gradient of these elements and a shallow gradient of oxygen due to its high diffusivity in the alloy. The conditions for internal oxidation and constitutional supersaturation are thus the same. This is because constitutional supersaturation is a necessary - although not sufficient - condition for internal oxidation.

Using the methods outlined in Chapter 4, let us assume that the virtual diffusion path has been calculated. Three possibilities are shown in Fig. 4-6. Because the calculated diffusion path for the alloy cuts tie-lines in the two phase field in cases (b) and (c), it is clear that a zone of "constitutional supersaturation" would be developed in the alloy adjacent to the planar alloy-oxide interface. This zone of supersaturation can be sustained in a system only if the surface tension between the matrix phase and the incipient precipitate phase is infinite. This however is not obtained in practice and precipitation or morphological instability occurs. The initial "virtual" diffusion path which corresponds to the presence of the zone of supersaturation only predicts the existence of unstable solutions corresponding to the occurrence of two-phase regions. The valid solutions are those corresponding to the "actual" diffusion path which is obtained after taking such predictions into account and reformulating the problem. The actual diffusion path yields the final configuration of the system corresponding to the local equilibrium at the precipitate-matrix interface . The diffusion analysis thus gives only the final stationary-state configuration of the system and is therefore not applicable to the transient periods of nucleation and growth for which the interface reactions control the transformation and during which changes in microstructure occur.

5.3 FORMATION OF TWO-PHASE LAYERS

Kirkaldy and Brown(27) have pointed out that an exact parametric solution of the form $C_i = C_i(\lambda)$ does not exist in a two-phase region. Accordingly, parabolic behaviour, if and when it occurs in such situations is an approximation. Approximate parabolic solutions to the diffusion equations may be obtained, as recently demonstrated by Kirkaldy(24, 158) for the case of internal oxidation and sulfidation of binary alloys. It is assumed in the subsequent discussion that such approximate parabolic solutions exist for the cases discussed so that a stationary-state configuration may be defined.

It has been mentioned earlier that in order to calculate the actual diffusion path, the diffusion problem must be reformulated. For example, let us assume the presence of a zone of internal oxidation within the alloy adjacent to the alloy-oxide interface. The essential problem is to determine the concentration distribution in the precipitate and matrix zones and the relative amounts of the two phases. Limiting cases based on pseudo-binary approach and a general case based on a ternary approach have been discussed in sections 3.3 and 4.7, respectively. In these manners an actual diffusion path is obtained as shown in Fig. 5-1.

It is worthwhile clarifying the role that ternary diffusion interaction plays in producing internal oxidation. Consider the virtual diffusion paths designated as (1) and (2) in Fig. 5-2. In case (1) a maximum in the oxygen distribution

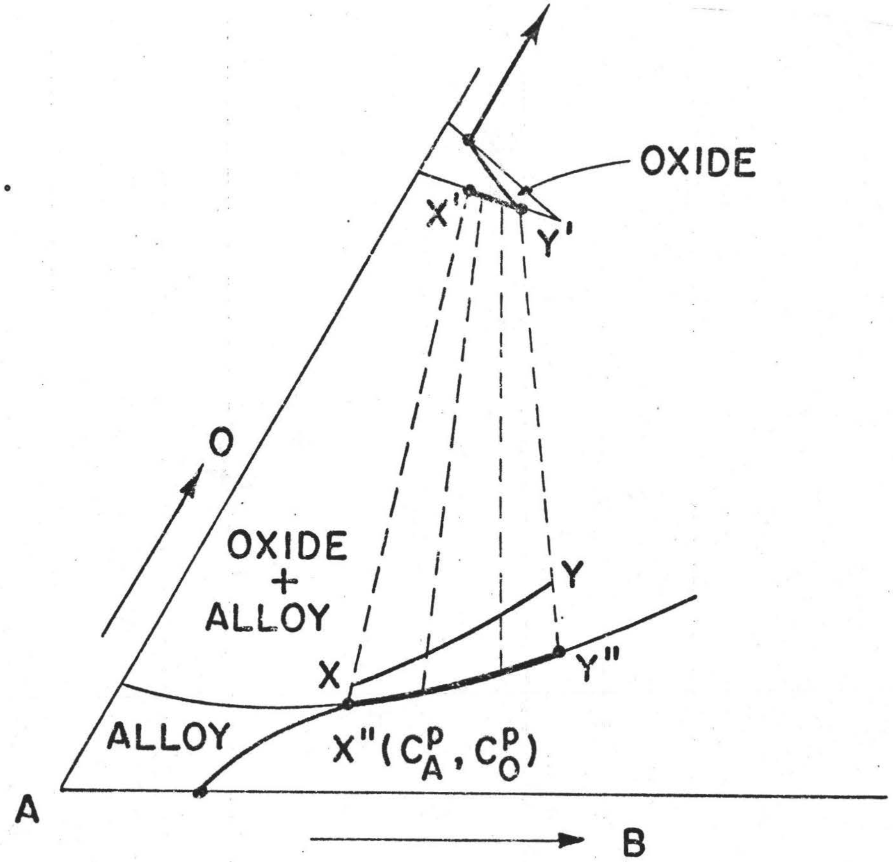

Fig. 5-1: Actual diffusion path involving internal oxidation. The variations in the composition of the internal oxide and alloy matrix are given by X'Y' and X"Y", respectively. The line XY represents the average composition of the subscale region.

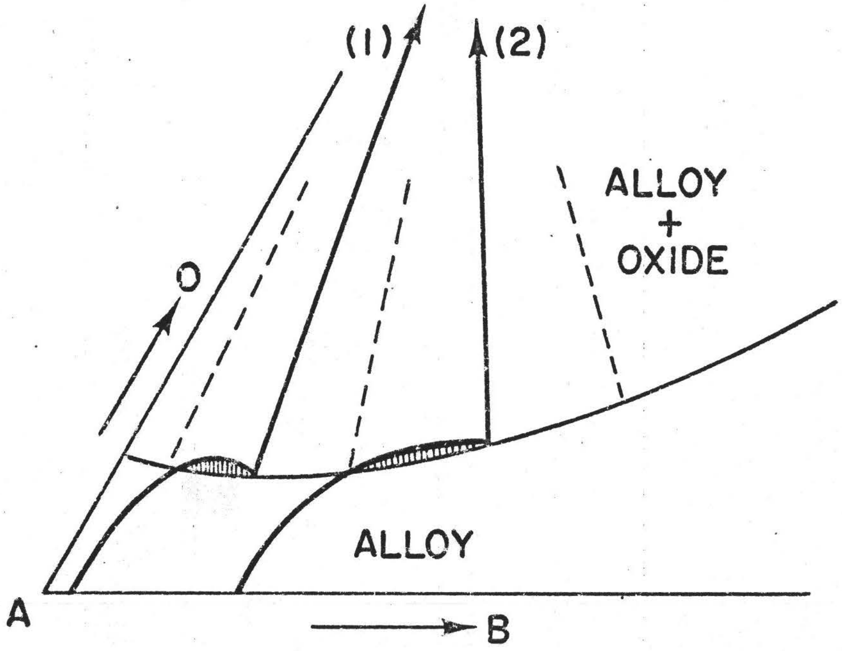

Fig. 5-2: Two "virtual" diffusion path possibilities which illustrate the influence of ternary diffusion interaction.

in the alloy has resulted in a maximum in the virtual diffusion path in the alloy. As a consequence of this, it is possible for the virtual diffusion path to cut into the two phase field even in the cases where oxygen solubility in the alloy increases with increasing distance from the alloy-oxide interface. A maximum in the oxygen distribution requires that there be strong diffusion interaction with the other independent species in the alloy. Note that in case (2) unlike case (1), it is not necessary to have diffusion interaction in order to produce supersaturation.

Two-phase regions in ternary systems may also be produced by morphological instability. A general analysis of morphological instability by Coates and Kirkaldy(162,163) has revealed that there are situations in which it is possible to maintain a planar alloy-oxide interface, in spite of supersaturation in the alloy. In contrast, it also was found that there are situations in which an alloy-oxide interface will become unstable in the absence of any supersaturation. That is to say, an alloy-oxide interface can be unstable for kinetic reasons alone, a special case already treated by Wagner(122).

There remains a need to clarify certain kinetic considerations relating to problems of interface stability although it is emphasized that the ensuing discussion is by no means rigorous.

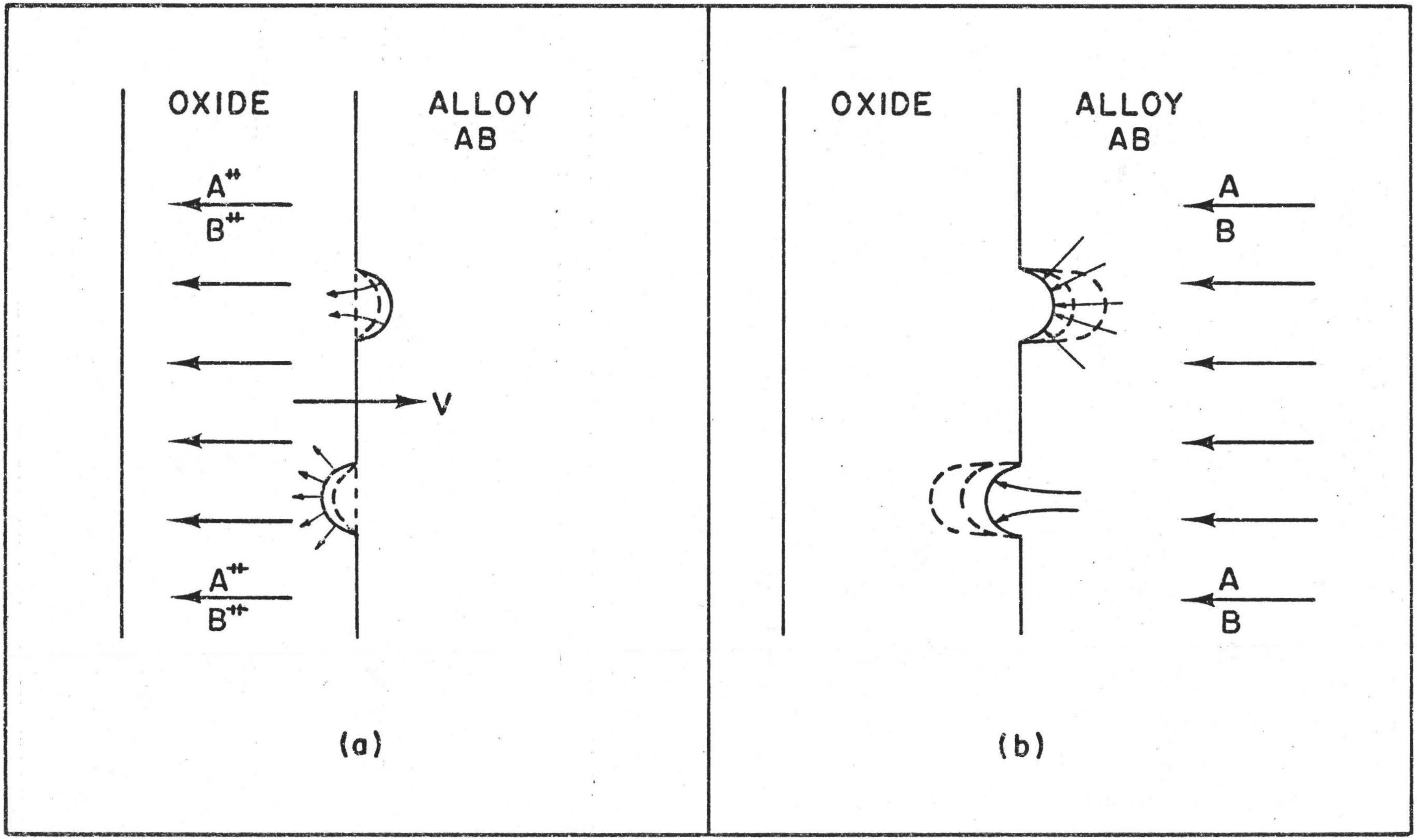

Fig. 5-3: Schematic drawing to indicate the evolution of shape perturbations in an oxide-alloy interface. Cases (a) and (b) relate to situations in which the oxidation rate is determined by transport in the oxide and alloy, respectively. The dotted lines at the perturbations indicate the successive stages of their decay or growth. The horizontal sets of arrows indicate the slower steps in the transport process.

Consider that the motion of cationic, rather than anionic, species is the means of matter transport in the oxide scale. Let one of the alloying elements be preferentially oxidized. There are two possibilities which are of interest: (i) if transport of the metal atoms is rapid in the alloy, then the rate of oxidation (i.e. the velocity of the scale-alloy interface) is determined mainly by transport in the oxide. Let us investigate the fate of very small disturbances in the shape of a bulge on the scale-alloy interface for such circumstances (Fig. 5-3(a)). When the interfacial bulge is toward the alloy, flow in the oxide (in the region of the bulge) is constricted and therefore the process of oxidation at the bulged section of the interface slows down relative to the planar sections until the bulge disappears. Similarly , when the bulge is toward the oxide, flow in the oxide is enhanced because of the interfacial flux divergence and the process of oxidation accelerates at this region until the bulged section of the interface disappears. Thus we conclude that when the rate determining process is transport of cations in the oxide, then the scale-alloy interface will maintain a stable planar shape. (ii) if transport of cations across the scale is rapid, then the oxidation rate is determined mainly by transport in the alloy. Consider Fig.5-3(b). When an interfacial bulge is toward the alloy, the metal atoms can more easily reach the interface and therefore the bulged section of the interface accelerates relative to planar sections. Thus the disturbance grows in amplitude. When the bulge is toward the oxide, the metal atoms have more difficulty reaching the interface and therefore the bulged section slows down relative to planar sections. Again, we see that the disturbance grows. Thus we conclude that when the rate determining process is transport of metal atoms in the alloy, there is a strong kinetic tendency for a planar scale-alloy interface to undergo morphological instability.

It is possible to consider situations in which the oxidation process involves transport of oxygen anions across the scale to the scale-alloy interface. By using the above methodology, it is easily demonstrated that as in the above case, there is a tendency for instability if transport in the alloy is rate determining.

The qualitative stability criteria just outlined arise out of the assumption that transport in one or other of the phases is rate determining. This assumption is reasoable only for extreme limiting cases. For more general cases which are complex the perturbation methods are required.

If a planar scale-alloy interface is morphologically stable, any supersaturation developed in the alloy can be relieved by internal oxidation only. On the other hand, if the interface is not stable in the presence of supersaturation both morphological breakdown and internal oxidation are possible.

5.4 APPLICATIONS

In this section we consider specific systems and use the principle of superposition of the "virtual" or the actual diffusion path onto the appropriate ternary phase diagram. Smeltzer and Perrow(164,165) have used this method in the analysis of oxidation of Fe-Ni and Fe-Cr alloys. We hope to illustrate how this technique provides a means of appraising the role played by both the kinetic (diffusion) and thermodynamic parameters in oxidation of binary allows.

We consider first the oxidation of binary iron alloys, Fe-Me, and inquire into the role played by the alloying element Me Alloying elements in iron may decrease the rate of oxidation by lowering the composition range of wustite or by eliminating it as a stable phase in the presence of the alloy and spinel phases. Additional protection may be obtained if the alloying element lowers the range of defect concentration in the spinel phase or decreases the ion mobilities. Alternatively, protection may be obtained if Me is sufficiently reactive that its oxide is the only constituent of the external scale and is adherent and resistant to diffusion of ionic species, as in the case of Cr_2O_3 formed on Fe-Cr alloys.

The effect of alloying element Me is best understood by considering the ternary phase diagram Fe-Me-O. Substantial information on ternary Fe-Ni-O and Fe-Cr-O phase diagrams at 1000°C is now available (Figs.5-4 and 5-5). One may note certain common features in these diagrams. The alloy side of the diagram is divided into three regions by points A_1 and A_2. Wustite is the oxide that coexists with alloy up to the point A_1. Between points A_1 and A_2 a spinel phase becomes the stable oxide phase and beyond point A_2 the oxide of the alloying element becomes the stable phase coexisting with the alloy. Points A_1 and A_2 are vertices of the wustite-spinel-alloy and spinel- MeO -alloy three phase fields, respectively. The stability ranges with respect to alloy composition of wustite and the oxide MeO of the alloying element will depend on their relative free energies of formation. In the Fe-Ni-O system (Fig. 5-4) wustite has a much larger negative free energy of formation than nickel oxide and therefore the stability range of the former extends up to 80 a/o Ni in the alloy whereas the stability range of the latter is almost negligible (0 - 0.5 a/o Fe). Replacement of Ni by a more reactive component such as Cr reduces the stability range of wustite with respect to the alloy composition to a negligible value and extends the stability range of MeO, i.e., Cr_2O_3 (Fig. 5-5) Thus as increasingly more reactive elements are introduced as component Me in Fe-Me, points A_1 and A_2 shift toward the iron corner of the phase diagram. This demonstrates the profound effect of the alloying element Me on oxide stability.

In the following discussion, we will disregard the phenomena of internal oxidation and morphological breakdown of the alloy-oxide interface. These we will discuss subsequently in a separate section.

5.4.1 Oxidation of Fe-Ni Alloys*

For dilute Fe-Ni alloys (0 - 20% Ni) and despite the presence of wustite in the external scale the oxidation rates drop drastically with respect to the oxidation rate of pure iron. Because the solubility of nickel in wustite is almost negligible nickel enrichment occurs in the immediately underlying alloy. This enrichment can be extremely high. Menzies and Tomlinson$^{(87)}$ observe up to 15% Ni at the wustite-alloy interface of Fe-2.3% Ni alloys and 65% Ni at the interface for Fe-48% Ni alloys after only 30 minutes of oxidation. Wulf et al$^{(85)}$, Morris and Smeltzer$^{(88)}$ and Brabers and Birchenall$^{(103)}$ also observed similar enrichment. This enrichment of nickel at the interface results in the diffusion path in the alloy shifting towards nickel side of the phase diagram$^{(103,164)}$ (e.g. B_1P_1' and B_1P_1'' in Fig. 5-4).

One can see that the composition range of wustite from the inner to outer interface is much lower than for pure Fe. As a result, the driving force for diffusion through

---

*The alloy composition cited in the following sections are understood to be in wt. % unless otherwise stated.

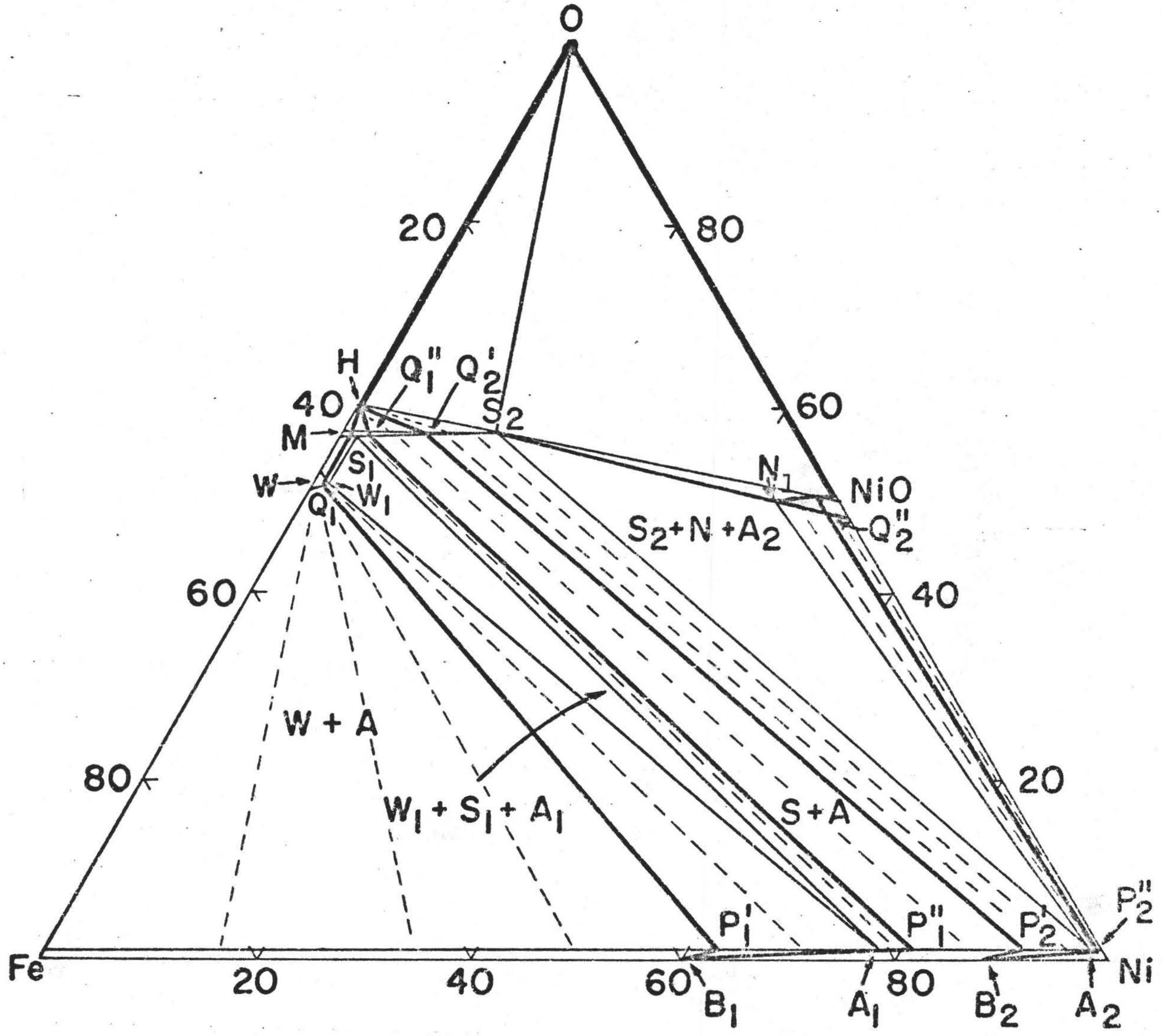

Fig. 5-4: 1000°C isotherm of Fe-Ni-O system in atomic per cent (103,106,166) and possible diffusion paths for alloy compositions B_1 and B_2 in the Fe-Ni-O system at 1000°C. W_1 - $Fe_{0.87}Ni_{0.01}O$; S_1 - $Ni_{0.04}Fe_{2.96}O_4$; S_2 - $NiFe_2O_4$; N_1- $Ni_{0.87}Fe_{0.13}O$; A_1 - 79.6 a/o Ni, 20.4 a/o Fe; A_2 - 99.5 a/o Ni, 0.5 a/o Fe.

wustite is reduced and therefore the oxidation rate is lowered. Formation of wustite is dependent upon a supply of iron at the wustite-alloy interface. Because there is a depletion of iron at this interface, then due to relatively slow diffusion of Fe and Ni in the alloy, the oxidation rate would be further reduced from that of pure Fe.

Let us consider in more detail the possible configurations to be expected from oxidation of Fe-Ni alloys. For an alloy with bulk composition B_1 (Fig. 5-4), the diffusion path for a situation in which wustite is present in the external scale is $B_1P_1'Q_1'$ etc. It is, however, possible that Ni enrichment in the alloy near the interface could push the interface alloy composition beyond A_1 and wustite would no longer be stable. The diffusion path corresponding to this situation is $B_1P_1''Q_1''$ etc. in Fig. 5-4 which involves spinel in the external scale. For an alloy with bulk composition B_2 we may observe either the diffusion path $B_2P_2'Q_2'$, etc, corresponding to formation of spinel in the external scale or alternatively the diffusion path $B_2P_2''Q_2''$ where the interfacial alloy composition has shifted beyond A_2 so that nickel oxide becomes the stable oxide.

The above semi-quantitative description of Fe-Ni alloy oxidation compares very favourably with experimental results. According to Foley(86,89,90,91,92,93) wustite is found in the external scale only for low nickel alloys. For alloys containing up to 30% Ni low nickel spinels are observed in the external scale whereas for alloys containing higher nickel, high nickel spinels with a formula close to $NiFe_2O_4$ is obtained. A layer of Fe_2O_3 above spinel layer is observed in both cases. Similarly, in a recent investigation Wulf et al.$^{(85)}$ have found that for Fe-Ni alloys containing up to 2% Ni, wustite is present in the external scale (ie. corresponding to the diffusion path $B_1P_1'Q_1'$ etc.). For alloys containing 35 to 80% Ni it was observed that spinel is the oxide present in the external scale adjacent to the alloy (ie. corresponding to diffusion path $B_1P_1''Q_1''$ etc.) (See also ref. (164)).

5.4.2 Oxidation of Fe-Cr Alloys

In connection with the oxidation of Fe-Ni alloys we have seen that due to selective oxidation, the diffusion path in the alloy is biased towards the Ni corner. It is emphasized that this bias is towards the more noble element. In the oxidation of Fe-Cr alloys, since Cr preferentially oxidizes, the diffusion path should shift toward Fe. Thus, although it appears from the Fe-Cr-O phase diagram (Fig. 5-5) that wustite is not stable for almost the complete bulk alloy composition range, it may in fact eventually become a stable phase due to the interface alloy composition shift toward the Fe corner of the phase diagram.

Because the oxidation of dilute Fe-Cr alloys is of such

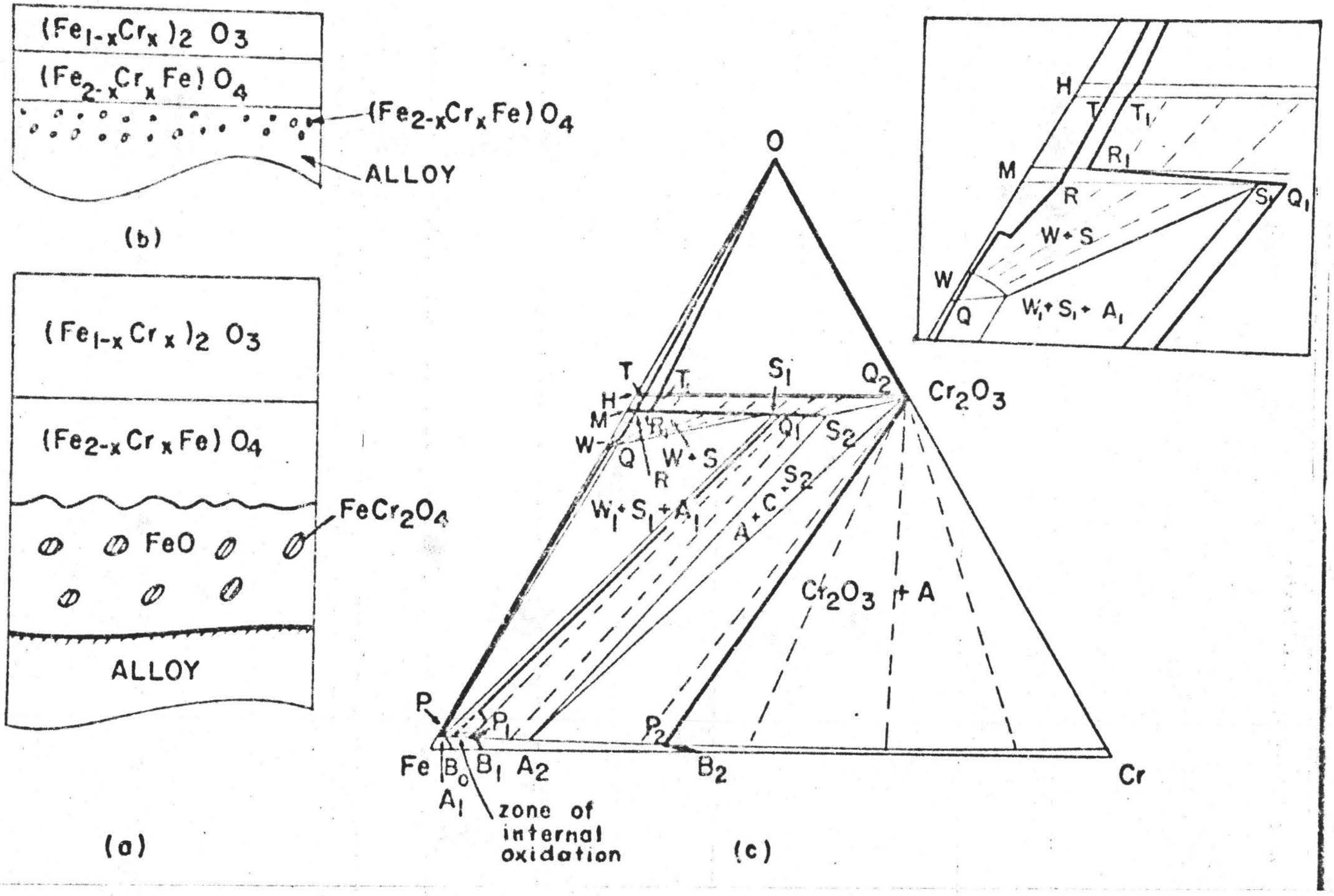

Fig. 5-5: (a) Schematic representation of scale structure corresponding to the oxidation of (i) a very dilute Fe-Cr alloy (after Moreau(167)), (ii) a dilute Fe-Cr alloy(168). (b) 1000°C isotherm of Fe-Cr-O system in atomic per cent(169,170), and possible diffusion paths corresponding to the oxidation of Fe-Cr alloys.
W_1 - $Fe_{0.97}Cr_{0.02}O$; S_1 - $Fe_{1.5}Cr_{1.5}O_4$; S_2 - $FeCr_2O_4$; C - <1 a/o Fe; A_1 - <1 a/o Cr; A_2 - 13.6 a/o Cr, 76.4 a/o Fe.

commercial importance let us examine the problem more carefully. Fig. 5-5 shows the oxide scale structure for a very dilute alloy as observed by Moreau. In Fig. 5-5(b) is shown a possible diffusion path for a very dilute Fe-Cr alloy (B_O) which has wustite in the scale. The segment of this diffusion path OT corresponds to the equilibrium at the scale-gas interface. The diffusion path then passes through the single phase Fe_2O_3-Cr_2O_3 solid solution region which corresponds to the presence of this phase, $(Fe_{1-x}Cr_x)_2O_3$, in the oxide scale as found by Moreau. The segment TR represents the equilibrium between the Fe_2O_3-Cr_2O_3 solid solution $(Fe_{1-x}Cr_x)_2O_3$ and the spinel phase $(Fe_{2-x}Cr_xFe)O_4$. The passage of the diffusion path through the spinel phase field corresponds to the presence of this phase in the scale. If the actual diffusion path were subsequently to follow a tie-line in the two-phase field wustite-spinel then we would obtain a planar interface between spinel and wustite and a wustite layer with no precipitate particles in it. However, a two-phase "$FeCr_2O_4$"-FeO region is indicated in Fig. 5(a) and therefore the actual diffusion path must cut across tie-lines in the two-phase wustite-spinel field. From the phase diagram, it can be seen that the spinel in equilibrium with wustite varies in composition from Fe_3O_4 to $Fe_{1.5}Cr_{1.5}O_4$. It follows that any spinel precipitate which coexists with wustite must have a composition in this range if the assumption of local equilibrium is valid.

As the bulk alloy composition is situated further away from the Fe-corner of the phase diagram, it is expected that wustite would be eventually eliminated as a stable phase. Only a trace of chromium is required at the alloy-oxide interface to stabilize the spinel phase. Experimental evidence on the scale structure of oxidized dilute iron-chromium alloys (e.g. Fe-5% Cr) is conflicting. Some investigators(167,171) have found wustite occurring in the external scale while others(165,168) report no such occurrence. Careful considerations of the experimental results indicate that the wustite phase may be stabilized due to impurities such as Mn. The diffusion path corresponding to the situation is shown in Fig. 5-5(c), $(B_1P_1Q_1R_1T_1O)$.

It is interesting to note the interplay between the thermodynamic and kinetic factors which results in this unusual diffusion path. Due to high reactivity of Cr it tends to preferentially oxidize resulting in Cr depletion in the alloy adjacent to the oxide-alloy interface. However since the diffusion coefficient of Cr in γ-Fe-Cr alloys is small, Cr can not reach the interface fast enough. On the other hand, for thermodynamic equilibrium at the oxide-alloy interface, the partitioning of Cr in the spinel phase has to be relatively high. The thermodynamic and kinetic factors thus militate against each other resulting in a steep Cr gradient in the spinel. The resultant diffusion path shifts sharply tpwards the Fe corner within the spinel phase field. The Cr content of the ferric-chromic oxide in equilibrium with the low Cr spinel is thus very low. The low Cr content of the ferric-chromic oxide balances against high Cr content of spinel resulting in relatively small net excess of Cr in the entire duplex scale and hence a small depletion of Cr in the alloy. Note that because the diffusivity of Cr in the alloy is low and the rate of thickening of the scale is relatively high, the existence of a scale containing a ferric-chromic oxide of high Cr content violates the principle of mass conservation.

For Fe-Cr alloys containing greater than about 13 a/o Cr the diffusion path is uncomplicated, viz. $B_2P_2Q_2O$. Thus Cr_2O_3 is the only oxide formed in the external scale. Formation of Cr_2O_3 depletes the alloy of Cr and therefore shifts the diffusion path toward the Fe corner of the phase diagram. However, since Cr_2O_3 is highly adherent to the alloy and resistant to diffusion, further oxidation is very slow. It is necessary that interfacial alloy composition shift B_2P_2 is small and the diffusion path does not shift towards the Fe corner beyond point A_2. Wulf et al.(172) have calculated the concentration profiles in the alloy for alloys containing 23.5%,32%,41% and 46% Cr and oxidized in pure oxygen at 1250°K. These authors used a concentration dependent diffusion coefficient in the alloy and exclusive oxidation of Cr. A considerable Cr-depletion in the alloy occurred in agreement with experimental results

5.4.3 Oxidation of Ni-Cr Alloys

The Ni-Cr-O phase diagram is similar to the Fe-Cr-O diagram (Fig. 5-6(b)). Since nickel is more noble than iron,

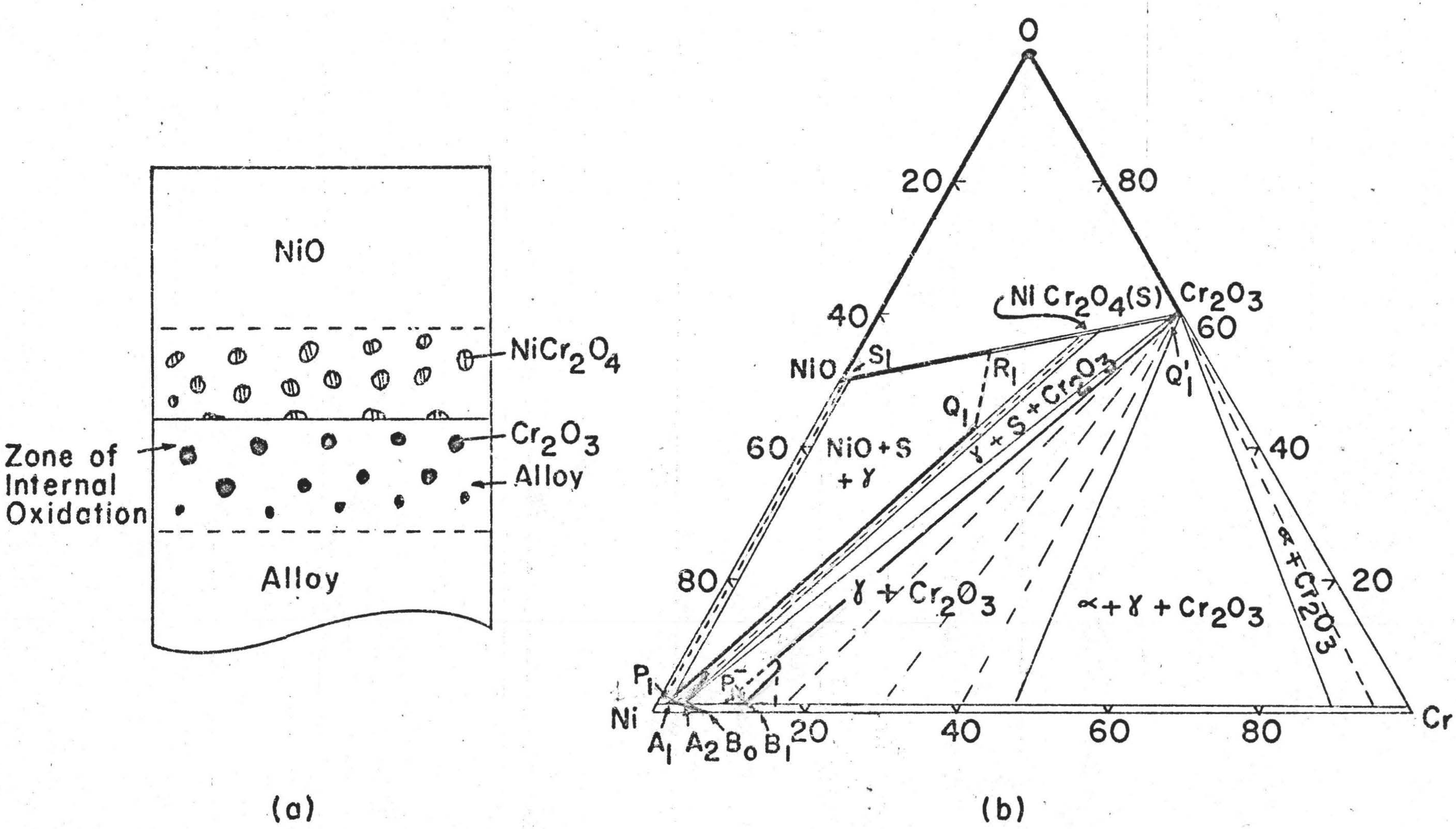

Fig. 5-6: (a) Schematic representation of scale structure corresponding to oxidation of Ni-5% Cr alloy at 1000°C. (b) possible diffusion paths corresponding to the oxidation of Ni-Cr alloys at 1000°C.

it is expected that the points A_1 and A_2 would shift further toward the Ni corner compared to their position in the Fe-Cr-O diagram. Thermodynamic calculations(62,111) suggest that point A_1 corresponds to only a trace of Cr in the alloy and point A_2 corresponds to less than 1a/o Cr. Therefore most of the alloy composition range lies adjacent to the two-phase field alloy-Cr_2O_3. Croll and Wallwork(173) have recently suggested that point A_2 in Fig. 5-6(b) corresponds to 10a/o Cr. This observation appears to be in disagreement with the thermodynamic calculations(62,111) and with the numerous observations of a Cr_2O_3 internal oxide coexisting with virtually pure Ni matrix during the oxidation of dilute Ni-Cr alloys at 1000°C (62,174,175,176). If one accepts the observation of Croll and Wallwork, the identity of internal oxide particles (Cr_2O_3) or the validity of local thermodynamic equilibrium will be in question. For the purposes of the present work, the theoretical values for the compositions corresponding to the points A_1 and A_2 are assumed since these are more in accord with most experimental observations and with the thermodynamic data on the Ni-Cr alloy system.

Oxidation of dilute Ni-Cr alloys has been studied by Moreau and Benard(174), Birks and Richert(62), Pfeiffer(177) and recently by Douglass(58). Small additions of Cr to Ni increases the oxidation rate, reaching a maximum at about 8% Cr. The oxidation rate then decreases abruptly with an increase in Cr content above 8% and is about equal to that of pure Ni at 10% Cr. Chromium additions of about 20% markedly reduce the oxidation rate by the formation of Cr_2O_3 in lieu of a film of NiO(58).

Moreau and Bénard(174) have studied the oxidation of a Ni-5% Cr alloy. The oxide scale structure for such an alloy at 1000°C is shown in Fig. 5-6(a). Instead of four phases coexisting at the oxide-subscale interface, NiO, $NiCr_2O_4$, Cr_2O_3 and alloy, only three phases, NiO, $NiCr_2O_4$ and alloy are shown to coexist for consistency with the assumption of local equilibrium and the consequent requirement of the Gibbs' phase rule for a ternary isothermal, isobaric system. Since the point A_2 corresponds to less than 1a/o Cr, the reason for the existence of complex scale structures such as shown in Fig. 5-6(a) for Ni-Cr alloys containing less than 8% Cr must be the shift of the diffusion path (in the alloy) toward Fe. A possible diffusion path for such an alloy (bulk composition B_0) is $B_0P_1Q_1R_1S_1$, etc. in Fig. 5-6(a). The system is apparently unstable with respect to NiO-$NiCr_2O_4$, i.e., these phases cannot coexist at a planar interface. The breakdown of the interface eventually leads to formation of a two phase zone, NiO-$NiCr_2O_4$. The interface between the zone of internal oxidation and NiO-$NiCr_2O_4$ region corresponds to the dotted line R_1Q_1 in Fig. 5-6(b), viz., the three phase region NiO-Alloy-$NiCr_2O_4$. The zone of supersaturation between P_1 and B_0

results in formation of an internal oxide which from Fig. 5-6(b) is Cr_2O_3.

It appears form the experimental results that for Ni-Cr alloys containing more than 15% Cr, the Cr depletion in the alloy is not sufficient to shift the interfacial alloy composition beyond point A_2. For these alloys, the diffusion path is $B_1P_1'Q_1'$, etc.,in Fig. 5-6(b) corresponding to formation of a single Cr_2O_3 layer. The adherence of Cr_2O_3 to the alloy, its compactness and diffusion resistance result in it being very protective. The diffusion path $B_1P_1'Q_1'$, etc. is an experimental diffusion path corresponding to concentration profiles given by Wood and Hodgkiess(178).

We note here the similarity between Fe-Cr alloys (Fig. 5-5) and Ni-Cr alloys (Fig. 5-6). This similarity provides a clue to the oxidation resistance of Ni-Cr and similar alloys.

5.4.4 Internal Oxidation and Morphological Instability

In the literature, the terms "internal oxide" and "subscale" have been used with different meanings and at times interchangeably. In the present paper, the term internal oxide is used to describe discreet precipitation of oxide of the solute or the solvent metal or a mixed oxide of these within the alloy matrix. The term "subscale" is used in a more general sense to describe the internal oxide as well as the zone below the external scale containing both the alloy and oxide phases usually resulting from morphological instability of the system. It will transpire in view of the subsequent descrip-

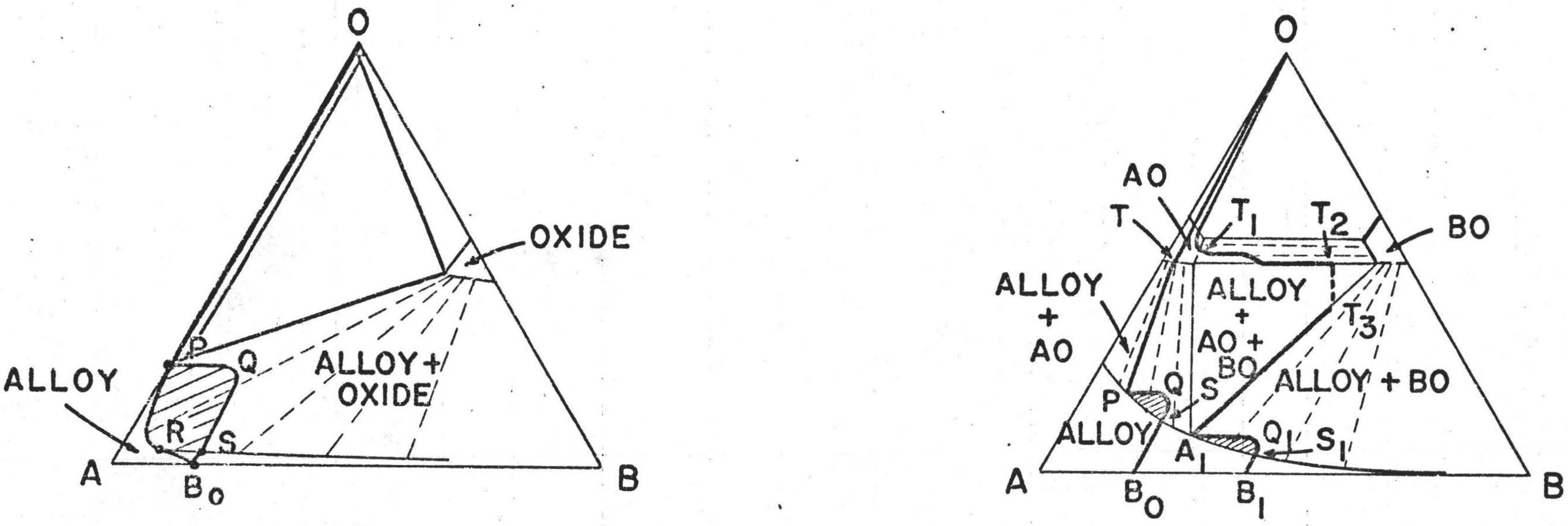

(a)

(b)

Figure 5-7: (a) Diffusion paths corresponding to the case of internal oxidation without an external scale. (b) Possible diffusion paths corresponding to the case of internal oxidation with an external scale.

tion that this is a satisfactory usage.

In discussing the phenomenon of internal oxidation, Wagner(110,125) has considered only limiting cases in which the free energies of oxidation of metals A and B are significantly different and therefore one of them, say A, acts as a noble metal and the other, B, is very reactive. In his review of the phenomenon of internal oxidation, Rapp(111) considered two cases for dilute alloys of B in A : (a) internal oxidation without external scale, and (b) internal oxidation with external scale. Each of these two cases can be easily understood in terms of the "virtual" diffusion path concept.

We first consider case (a), internal oxidation without external scale, a good example being in the Ag-In system(111). In Fig. 10(a), B_O represents the bulk alloy composition which corresponds to dilute solution of metal B in metal A. For the sake of clarity, the oxygen solubitility line PRS, etc. is exaggerated. If metal A does not form an oxide at the temperature of oxidation and the activity of metal B in the alloy phase is small enough that the oxide BO also does not form as an external scale, then the "virtual" diffusion path corresponds to $OPQSB_O$ in Fig. 5-7(a). Line PQ is almost horizontal because oxygen diffusion through the alloy is much faster than for B. The zone of supersaturation PQS will lead to internal precipitation. After internal precipitation, the diffusion path within the alloy matrix shifts to PRB_O; part PR corresponds to the internal oxidation zone in which the concentrations of B and O are reduced to relatively small values and part RB_O corresponds to the steep rise in concentration of B to the bulk concentration value B_O beyond the internal oxidation zone. It should be noted that the tie-lines cut by the "virtual" path yield the approximate local compositions of the alloy matrix and precipitate phase BO.

Let us now consider case (b) in which internal oxidation occurs in conjunction with an external scale. This situation is schematically represented in Fig. 5-7(b). Metal A forms an external oxide AO at the temperature of oxidation. $OTPQSB_O$ is the diffusion path for the simplest case wherein both the external scale and internal oxide precipitate are AO. The Cu-Pd system exhibits thie type of internal oxidation (110,113) behaviour. A more complex but frequently-observed case is that in which the external scale consists of a single phase zone of oxide AO and then a two-phase AO-BO zone followed by an internal oxidation zone consisting of BO precipitate particles in the alloy matrix. This case corresponds to the diffusion path $OT_1T_2T_3A_1Q_1S_1B_1$ in Fig. 5-7(b). Note that in this case, the diffusion path passes through the three phase field $AO + A_1 + BO$ (the segment T_2T_3) and this represents the interface between a two-phase AO-BO region and the alloy. Example of this case occurs for dilute Cu-Be alloys (179). These alloys show a tendency to form a single external layer of oxide BO at higher concentrations of metal B in the bulk alloy.

5.4.5 Subscale Formation During the Oxidation of Fe-Ni Alloys

Earlier we have seen that for Fe-Ni alloys with bulk composition B_0 such that $0 < Ni(B_0) < Ni(A_1)$, two types of diffusion paths exist — one corresponding to the presence of wustite in the external scale and the other corresponding to the presence of spinel in the external scale. One would expect different subscale formations in these cases. Consider first subscale formation when wustite appears in the external scale. The diffusion path corresponding to this situation is shown in Fig. 11(c). As we have noted earlier, formation of wustite leads to a depletion of iron in the alloy at the interface. This results in a steep iron concentration gradient as shown in Figure 5-8(a). The gradient combined with an oxygen solubility which increases with Ni content and a fast rate of oxygen diffusion in the alloy gives rise to a zone of supersaturation as shown in Fig. 5-8(a)(180). The supersaturation provides a driving force for internal oxidation and/or morphological breakdown. Notice that the iron concentration in wustite is much higher than that in the alloy at the wustite-alloy interface. In addition, the diffusion of iron through wustite is several orders of magnitude higher than its diffusion through the alloy(17). Therefore the wustite-alloy interface should be morphologically very unstable according to the criteria we have discussed earlier in the section on morphological instability. In summary, subscale formation is ex-

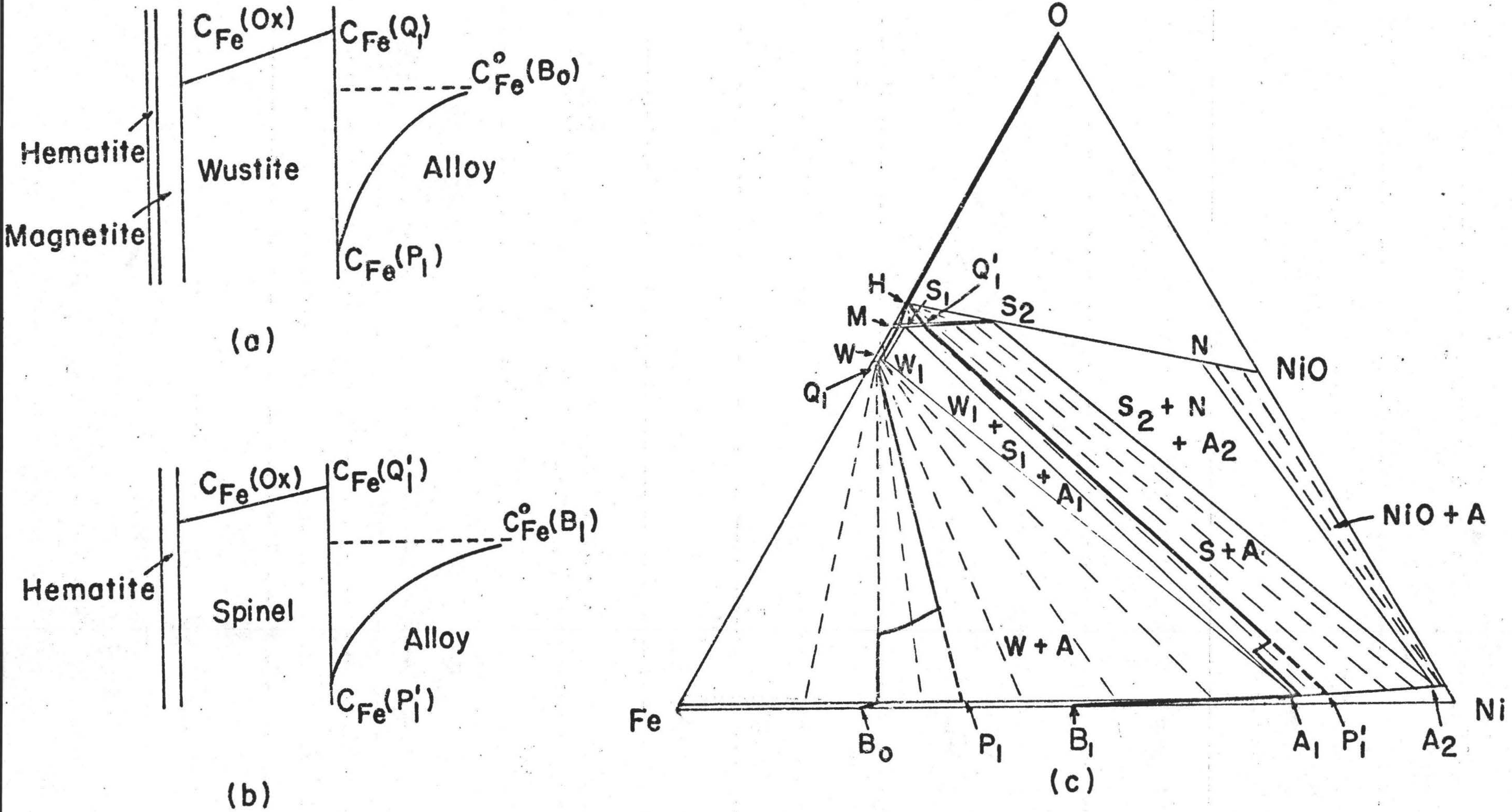

Fig. 5-8: (a) and (b) are respectively, schematic representation of scale structure and Fe concentration profiles for bulk alloy compositions B_0 and B_1 (c). (c) Corresponding actual diffusion paths.

pected to occur by both internal precipitation and morphological instability of the oxide-alloy interface. That such is the case is suggested by the micrographs in references (85) and (88). It is apparent from earlier discussions, that the diffusion path within the alloy matrix would go along the oxygen solubility line after the internal precipitation has occurred.

Oxidation of Fe-Ni alloys containing 35-80% Ni is very interesting(85,86). The diffusion path for these alloys is as shown in Fig. 5-3(c). From the diffusion path it is clear that the external scale for such alloys would consist of hematite and spinel. The interfacial alloy composition has shifted to P_1', beyond A_1. In the zone of supersaturation, the tie-lines which are cut lie in the two-phase field spinel - alloy and thus the internal oxide is expected to be spinel. According to Wulff et al., wustite does not appear as the internal oxide for these alloys. The concentration profile for Fe, corresponding to the diffusion path in Fig. 5-8(c) is shown in Fig. 5-8(c). This distribution appears to be almost identical to the case in which wustite is present in the external scale and hence one might again expect to observe morphological instability. However, after noting the fact that diffusion of iron through spinel is slower than that in the alloy(17), we see that the criteria for occurrence of morphological breakdown (as discussed earlier) are not satisfied.

Hence, one expects to observe only internal oxidation, as is indicated by the observations of Wulff et al. Fe-Ni alloys containing ∿ 30% Ni exhibit borderline behaviour. The spinel formed in the external scale in this case contains very little Ni resulting in high cationic mobilities. This may lead to a morphological instability of the oxide-alloy interface for these alloys despite the elimination of wustite in the external scale.

CHAPTER 6

EXPERIMENTAL TECHNIQUES AND PROCEDURES

6.1 SUMMARY OF TECHNIQUES

The experimental techniques used in this investigation include argon arc melting, vacuum annealing, a volumetric technique of weight gain measurements, metallography, x-ray diffraction and electron probe microanalysis.

Kinetic curves were obtained for Ni-Fe alloys of different composition which were prepared in the laboratory. Fig. 6-1 shows the alloy compositions with respect to the equilibrium Fe-Ni-O phase diagram at 1000°C. Carefully prepared specimens of these alloys were used to obtain kinetic curves. The oxidized alloys were mounted in cold setting resin and subjected to metallographic examination, x-ray analysis and electron probe microanalysis. Some specimens were equilibrated in pure argon over an extended period of time and subjected to electron probe microanalysis in order to study phase equilibria in the Fe-Ni-O system. More detailed descriptions of the materials and methods are given below.

6.2 MATERIALS AND SPECIMEN PREPARATION

The iron and nickel used in this study came from two different sources. In most cases electrolytic iron and nickel were used in preparation of the alloys. However, in some cases ultrahigh purity iron and nickel from Gallard-Schlesinger were

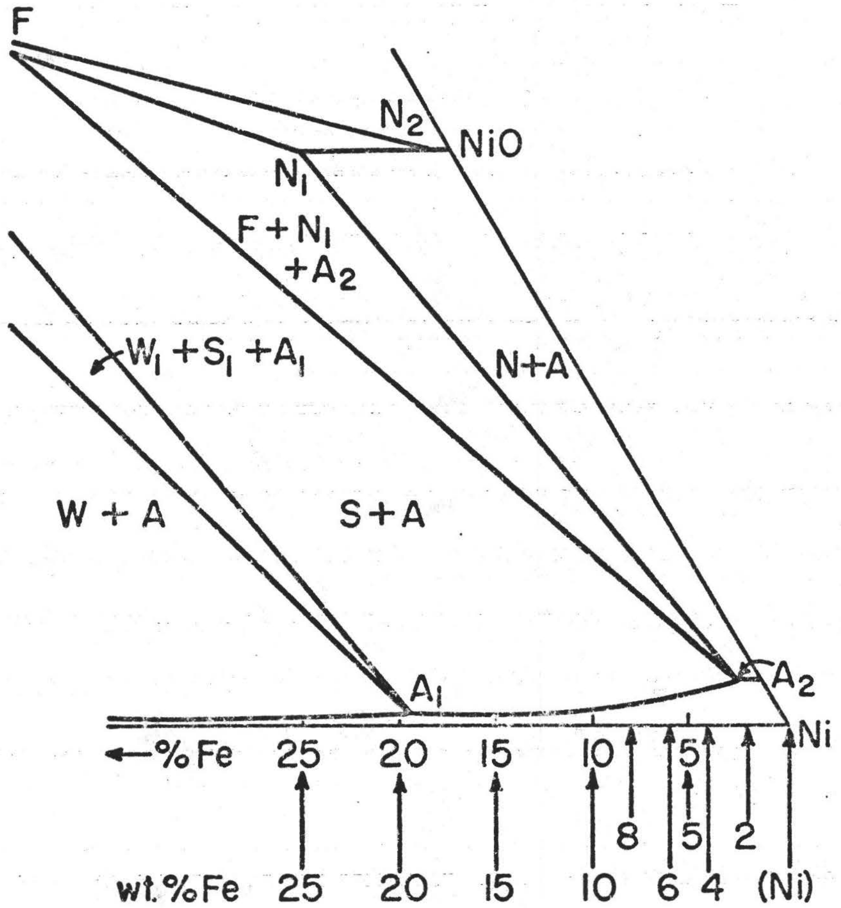

Fig. 6-1: Compositions of the investigated alloys with respect to the Fe-Ni-O phase diagram at 1000°C.

used. The chemical composition of the metals used is given in Table 6-1.

Portions of each material were accurately weighed to yield alloys nominally containing 0, 2, 4, 5, 6, 8, 10, 15, 20, 25, 50 weight percent iron. Approximately 50 grams of material was placed in the melting chamber of a non-consumable arc furnace with tungsten electrode. The melting operation was carried out under 200 mm. pressure of argon. Each charge was melted, inverted and then remelted, until a total of four melting operations had been completed, in order to prevent any long range segregation. The alloy samples were obtained in the form of buttons approximately 30 mm in diameter and 10 mm thick. These buttons were homogenized in vacuum at 1000°C for two days; then alternately cold rolled and vacuum annealed at 950°C until flat sheets 0.7-1 mm thick were obtained. The surfaces of each sheet were cleaned by abrasion using 320 grit silicon carbide polishing paper.

Specimens for oxidation tests were obtained by cutting the sheets into platelets 1 cm × 2 cm. on a precision shear. The plates were batch annealed in vacuum at 1000°C for 5 hrs and then furnace-cooled to room temperature. The annealing operation eliminated any stress and short range segregation in the sample and allowed the specimen to attain an equilibrium grain size.

Prior to oxidation the specimens were metallographically polished by the following procedure (181). The plates were mounted flat in bakelite and polished through 240, 320, 400, 600 grit silicon carbide papers using water as lubricant followed by polishing on a wax lap impregnated with 15 μ alumina to obtain a flat surface. The final polishing was done on 6μ and 1μ diamond wheels with kerosene as lubricant. The samples were cleaned with petroleum ether and stored under acetone until required. Immediately before an experimental test a specimen was dried and weighed to ±2 micrograms, and its surface area was computed by measuring the specimen dimensions with a micrometer. The specimen was then etched in dilute sulphuric acid, rinsed in distilled water and dried in acetone.

The chemical compositions of the alloys used in this investigation are given in Table 6-2.

Specimens for the equilibrium phase studies in the Fe-Ni-O system were prepared by two methods. Mixtures of powders containing iron and nickel in given proportions and one or more of the c.p. reagent grade oxides-nickel oxide, hematite and nickel ferrite- were compressed into tablets, 12.5 mm diameter and 2 mm thick, at a pressure of 6.5 ton/cm^2 by means of a hydraulic press using small amounts of acetone as binder. In the second method, alloy plates of various compositions ranging from 5-60% Fe were oxidized to desirable degree in oxygen at 1000°C. The tablets and oxidized alloy specimens were sealed in quartz tubes containing ultra high purity argon. All escapulated specimens were equilibrated at 1000°C ± 2.5°C and then cooled to room temperature within 5 minutes by means of an air quench. Tablets were equilibrated for 30 days whilst the oxidized alloy plates were equilibrated for a period up to 75 days.

The metal and oxide powders used in the preparation of the tablets were obtained from A. D. McKay and Co. Their purities are given in Table 6-3. The composition of the UHP grade argon obtained from Matheson is given in Table 6-4.

Nickel ferrite used in the preparation f the tablets was made using the following method of Wickham(182). Using Fisher A.R. grade chemicals, a solution of nickel and iron was made by dissolving $NiSO_4 \cdot 6H_2O$ and $FeSO_4 \cdot 7H_2O$ in distilled water in proportion to give a desired ratio Fe/Ni = 2. This solution was added dropwise to a hot solution of ammonium oxalate and oxalic acid, which was continuously stirred. The precipitate formed was stirred for three to four hours to mix the small oxalate crystals. The precipitate was filtered, dried and ignited. By igniting the precipitate in air at 1100°C and slowly cooling, nickel ferrite of extremely small particle size resulted.

6.3 OXIDATION APPARATUS

In the present investigation the volumetric method was used for measuring the oxidation rates. Arrangement consisted of three main parts: equipment for determinations of large volume of oxygen adsorbed together with the furnace assembly and its control, oxygen supply system and air admittance system.

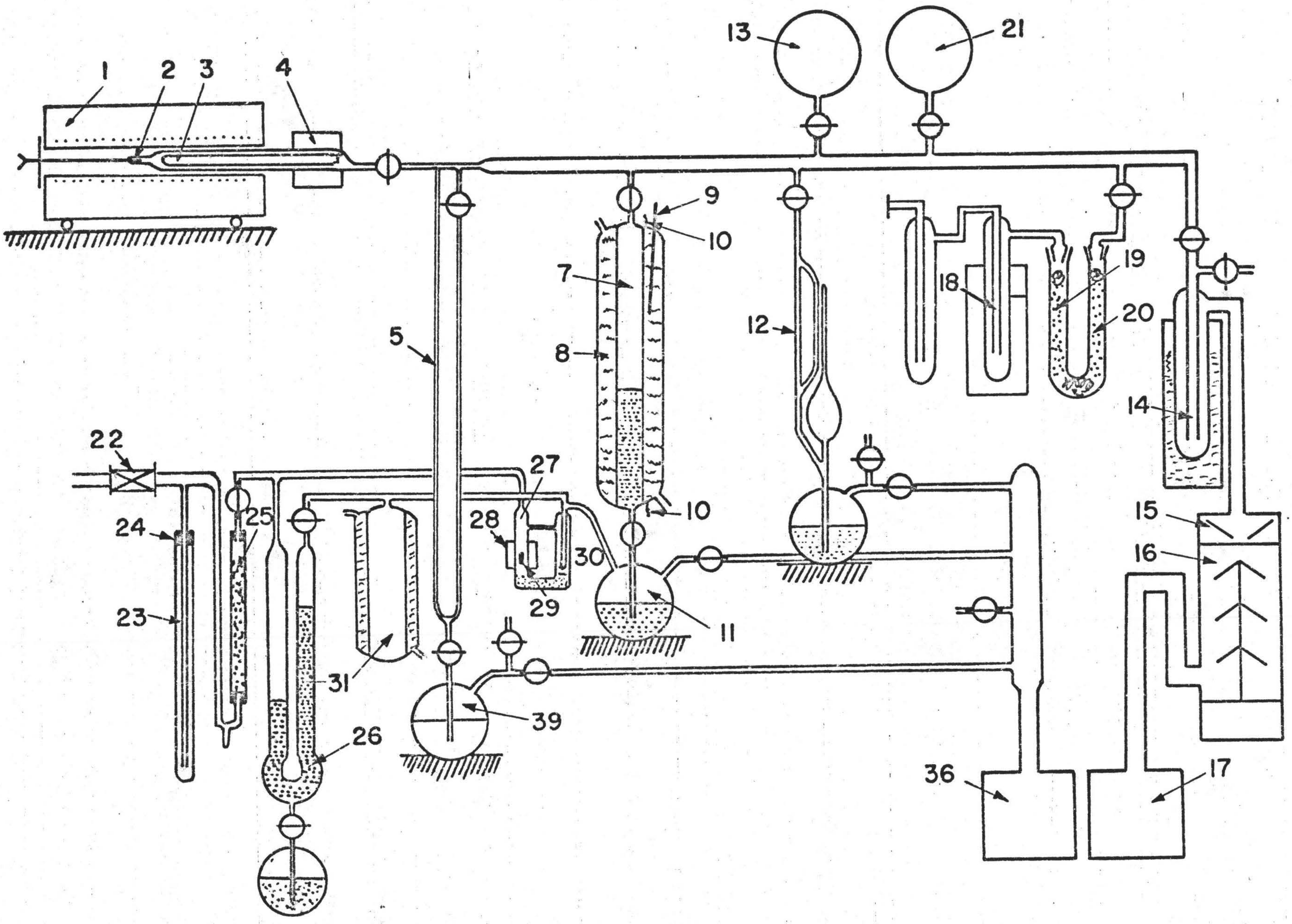

Fig. 6-2: Schematic diagram of main components of the volumetric apparatus.

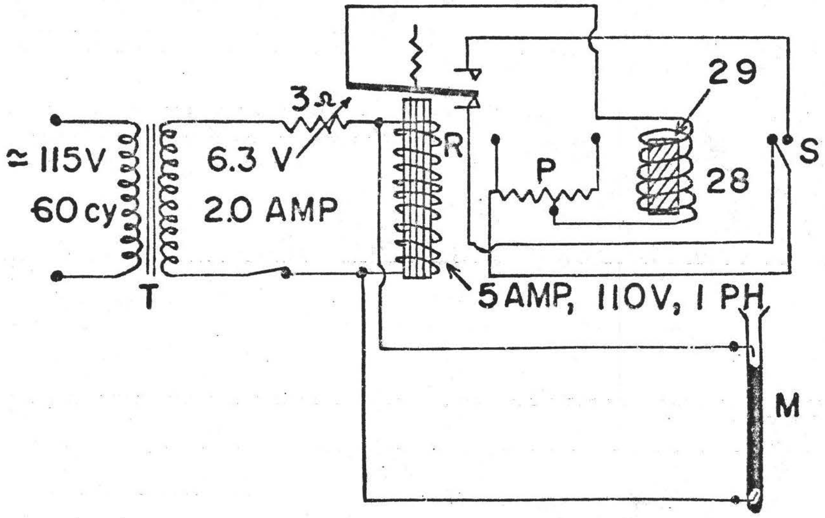

Fig. 6-3 Pressure Control System

Fig. 6-2 is an overall picture of the apparatus and Fig. 6-3 represents a schematic diagram of the pressure control system.

A suitably prepared specimen was placed in a demountable silica chamber (2). To avoid the possibility of silicon contamination and to expose a maximum surface of the sample, it was supported by platinum wire wrapped around it. To decrease the 'dead' space of the reaction chamber an evacuated silica tube(3) was placed concentrically inside the glass tube (2),thus increasing the sensitivity of the apparatus. The 'dead' volume between these two tubes is 58 c.c. A water cooled joint (4) was incorporated in order to maintain a good vacuum seal at the operating temperature of 1000°C.

The furnace (1),which was positioned around the reaction assembly by a vertical slide consisted of a 22 × 2.5" diameter closely wound Nichrome coil.

The uniform temperature zone was 3.5" in length at 1000°C with the temperature variation of ± 2.0°C. The temperature of the furnace was controlled by a Honeywell proportional controller. The temperature of the reaction cell was measured by a standardized chromel-alumel thermocouple which was placed very close to the specimen in a cavity designed for this purpose, as shown in Fig. 6-2.

The glass-chamber (2) was connected by means of a capillary tube to the mercury manometer (5) which in turn was joined with the calibrated 250 c.c. glass burette (7). To permit burette readings in rapid succession at constant pressure the manometer was equipped with sealed-in electrical contacts (6) and these were connected to the relay winding (R) as shown in Fig. 6-3, to keep the pressure constant.

A water jacket (8) placed around the burette prevented excessive changes of gas volumes due to variations in the room temperature. The water temperature was measured by the inserted thermometer (9) and the rate of water flow was regulated accordingly.

The whole assembly was evacuated by a Balzer's oil diffusion pump (16) coupled with a rotary mechanical 'Duo-Seal'pump (17). To obtain a better vacuum by preventing the 'back streaming' of hot vapour molecules of oil and by condensing the water vapour, the water-cooled trap (15) and a liquid air trap (14) have been incorporated into the system. A standard McLeod gauge (12) was utilized for measuring vacuum. Vacuums ranging from 6×10^{-6} to 5×10^{-4} torr could be achieved depending on the degassing time and type of oil used. Container (13) served as a vacuum reservoir.

Matheson ultra high purity oxygen was used as the environment for the oxidation studies. (The analysis of the gas used is given in Table 6-5). Before introducing into the system, the oxygen was passed through the expansion trap and cold trap (18) and through purifiers (19) containing silica gel for removing moisture, ascarite for removing CO_2 gas and magnesium perchlorate for removing any residual water vapour. The admitted oxygen was stored in spherical containers (21) of such volume that it permitted the use of the same gas for 4 to 5 experimental runs.

Laboratory air, passing through the dust remover (22) and moisture adsorber (25) containing magnesium perchlorate, exerted pressure on one side of the U-tube (26) filled with vacuum oil. The pressure difference could be adjusted in two ways: either by the position of the mercury bubbler (23), which was covered with a cotton stopper to prevent the harmful particles of mercury from contaminating the surrounding, or by evacuating the U-tube by the mechanical pump (36). Moisture-free air enters the automatically operated mercury valve (27). In the case of a gap between the mercury level and the upper wire connection (6) as shown in Fig. 6-2 or Fig. 6-3 and for position of the double pole-double throw switch (S) as in Fig. 6-3, the solenoid (28) becomes energized and lifts plunger (29). Mercury in (27) levels up and exposes the porous plug (30) to air which when passing through it breaks the vacuum in container (11) and raises the mercury level in burette (7). Simultaneously the gap between the mercury column and the electrical contact is closed. The cycle repeats itself while the gas is being displaced by the oxidizing alloy sample. To prevent overshooting of mercury in the automatic pressure manometer a damping volume

(31) was incorporated into the glass circuit.

In a typical oxidation experiment the apparatus was first flushed with pure oxygen. After obtaining a vacuum of 10^{-4} torr, the furnace was positioned around the reaction cell. The temperature of the cell is brought to and controlled at 1000° ± 2.5°C. This took about 10 minutes. After obtaining the required temperature the system was isolated from the vacuum pumps, the pressure relay was energized and pure dry oxygen was let into the burette. The burette temperature was maintained at a constant temperature by means of a water jacket and the experiment was started by opening the stopcock to the reaction chamber. Readings of the mercury level in the burette were taken at regular intervals. The volume of oxygen absorbed was converted to weight gain by application of the ideal gas laws. After the experiment the apparatus was connected to the vacuum system and the furnace moved so that the specimen would be quickly cooled to room temperature. The oxide surface was examined under the microscope and part of the specimen was mounted edgewise in epoxy resin for metallographic examination.

6.4 METALLOGRAPHY

Metallographic polishing of composite samples containing oxide and alloy phases presented a special problem. Since the oxide phases are hard and brittle and the alloy phase is comparatively soft and plastic, they tend to polish at different rates and in different manners. Both mounting and polishing processes play important parts in producing a flat and smooth surface. It was found that epoxy cold setting resin gave the best results. The oxidized platelets were cut into two pieces bya jeweller's saw. One-half of the plate was used in x-ray diffraction studies and the other half was mounted in the epoxy resin in a lucite ring for metallographic examination.

It was found that water, if used as a lubricant erodes the oxide surface. Therefore kerosene was used as the lubricant throughout the polishing operation. Specimens were polished on silicon carbide papers 200 through 600 grit then polished on a wax lap impregnated with 15 μ alumina. This procedure resulted in the best retention of oxide grains and in obtaining a flat surface. The final polishing was done on 6 and 1 μ diamond wheels with napless cloths and kerosene as lubricant.

It was necessary to etch the oxidized samples to reveal their grain structure. Since most oxidized specimens contained NiO, an etchant containing one volume of acetic acid, one volume of hydrofluoric acid and four volumes of distilled water was used. The etching was done electrolytically at 10-15 volts, 25°C for a period of about 1 min. with stainless steel as the cathode. The solution was continuously stirred during etching.

Equilibrated specimens were subjected to etching for phase identification by optical microscopy. A 5% concentrated hydrochloric acid solution in ethyl alcohol was used to preferentially etch wustite in structures containing wustite, spinel and alloy. A 50% concentrated hydrochloric acid solution in water which preferentially etched spinel, was used as etchant for structures containing nickel ferrite, nickel oxide and alloy.

Specimens were examined and photographed using standard metallographic technique. In several cases the rates of growth of layers of the external scales and zone of internal oxidation were determined. These results were obtained by measuring the thickness of the scale using a calibrated filar eyepiece with a Zeiss metallograph at a suitable magnification.

6.5 X-RAY DIFFRACTION

A Philips x-ray diffractometer fitted with a copper tube and nickel filter was used for the purpose of phase identification and determination of preferred orientation in the oxide scale. Sintered tablets and oxidized plates could be directly used in the diffractometer. However, the oxide scale was powdered in some cases and the powder deposited on masking tape which was inserted in the diffractometer. Diffraction angle and relative intensities of various peaks were obtained from the diffractometer chart and these were compared with standard ASM data.

6.6 ELECTRON PROBE MICROANALYSIS

A complete description of the theory associated with electron probe microanalysis may be obtained from references (183), (184), (185) and (186). In the present investigation a CAMECA MS-64 model electron probe microanalyser was used for chemical analysis. The x-ray take-off angle of this instrument was 18°. The operating conditions to obtain the best results for the Fe-Ni-O system were found to be an acceleration voltage of 15 keV and a specimen current of approximately 150 nanoamps. Fe and Ni K_α lines were used for the purpose of analysis. Since Ni fluoresces Fe in the sample, the fluorescence correction was a major problem.

In order to use the microprobe for quantitative analyses it is necessary that it be calibrated for the elements of interest. If standards containing known amounts of the elements in a homogeneous distribution can be obtained, the calibration is a relatively simple process. The x-ray intensity from a given element minus the background intensity is proportional to the amount of the element present. The background intensity is determined by counting the spectrometer set at a few degrees off peak or as in the case of iron-nickel system, by setting the spectrometer for nickel and counting on pure iron. Since the observed corrected absolute intensity varies from day to day, only the relative intensity ratio of the corrected intensity for an alloy or oxide to the corrected intensity from the pure element is of interest.

Electrolytic Fe and Ni were used as standards.

The microprobe was calibrated according to the method described by Friskney and Howarth(187,188). The method consisted of successively applying atomic number(189), absorption(190) and fluorescence(191,192) corrections to an assumed set of compositions for a solid phase and calculating the intensity ratio for each metal to that for pure metal. This procedure yielded iron and nickel calibration curves for each solid. In all cases, the fluorescence correction was significant. The atomic number correction was significant for the oxides due to the presence of oxygen. Standards used to check the calibration curves for the alloys were alloys of several known compositions. The calibration procedure for wustite phase could only be verified for pure wustite. For spinels, the calibration procedure was verified for magnetite and nickel ferrite. The calibration curves for iron-nickel alloys, wustite, spinel and nickel oxide phases are given in Figs. 6-4 to 6-7.

The homogeneity of each phase in an equilibrated specimen was determined by subjecting different areas to point counts. X-ray and electron back scatter pictures of a suitably magnified specimen can provide a visual representation of the component distributions in various phases of a system. Scanning an electron beam across a specimen will excite characteristic K_α radiation. Electronic pulses derived from these projected onto a cathode ray screen from the image of the distribution of the specific element responsible for a particular radiation. Alternatively, this image can be directly recorded onto a photographic film. Photographic images thus obtained were used for phase identification and to qualitatively determine composition in various phases.

Line scans for iron and nickel in a specimen yield concentration profiles of these elements in various phases. Concentration profiles in the alloy and oxide phases were obtained qualitatively by this method. For more accurate results point counts were obtained within the oxide and alloy phases at various distances from the alloy-oxide interface. Corrections were applied to these readings and phase compositions were thus obtained as a function of the distance from the interface for samples oxidized for different time periods. It is necessary in this procedure that the polished edge of the sample be perpendicular to its surface and the probe spot be moved perpendicular to the oxide-alloy interface. In addition the concentration must vary only normal to the interface so that planar functions may be used to represent concentration profiles.

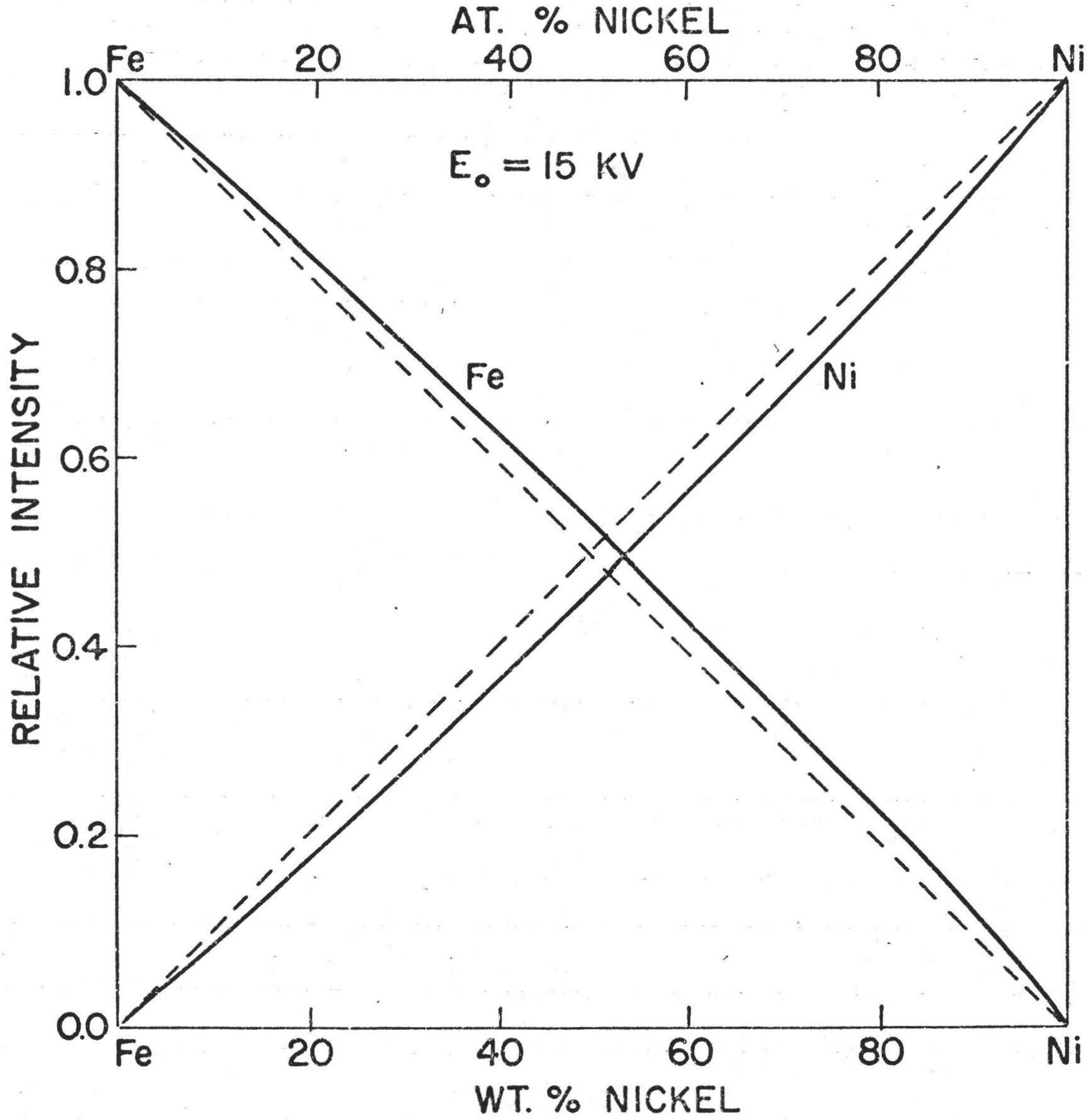

Fig. 6-4: Electron probe calibration for iron-nickel alloys.

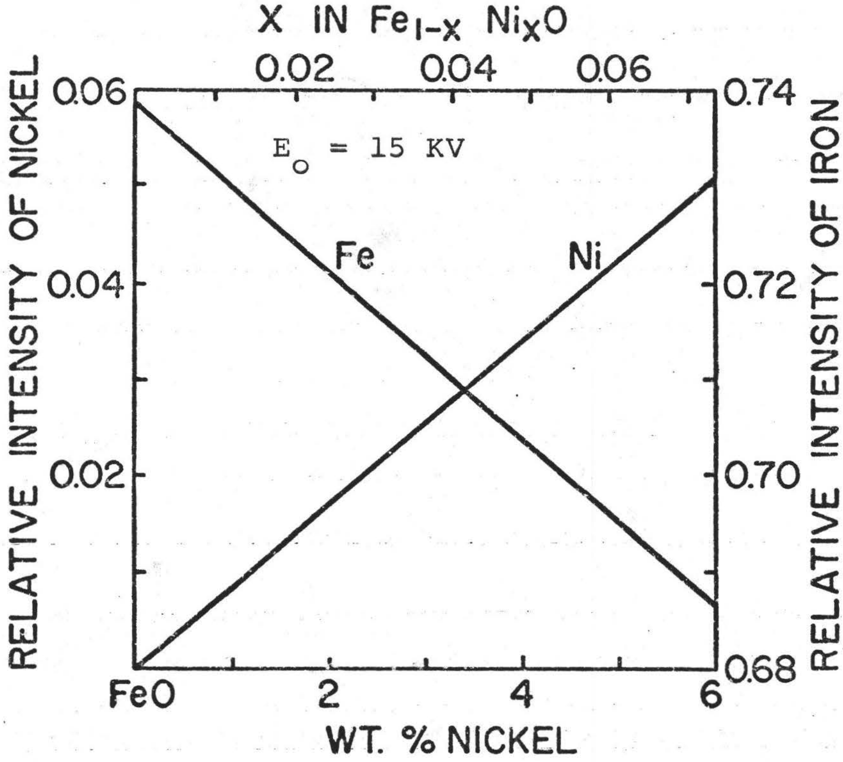

Fig. 6-5: Electron probe calibration for wustite.

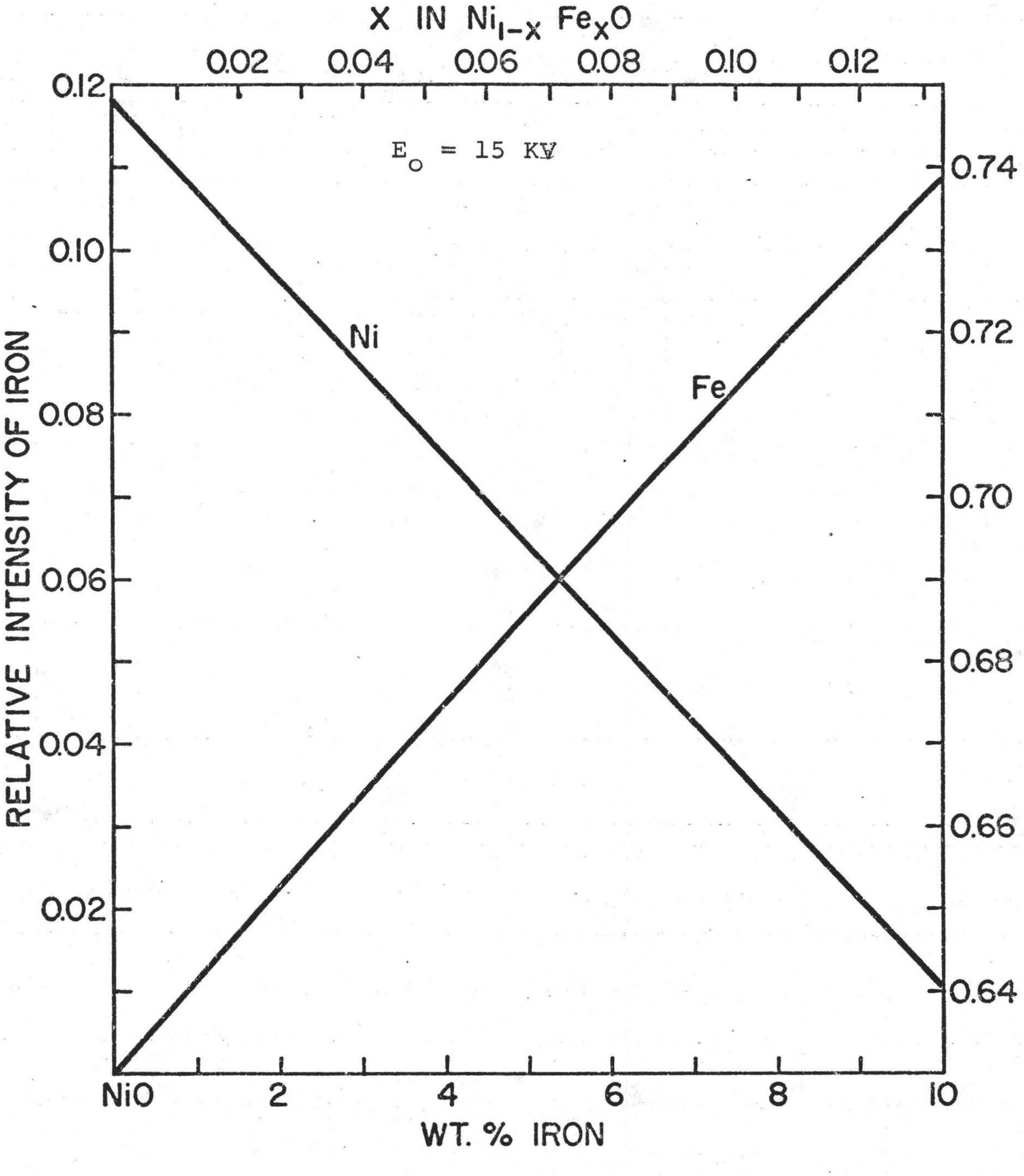

Fig. 6-6: Electron probe calibration for nixkel oxide.

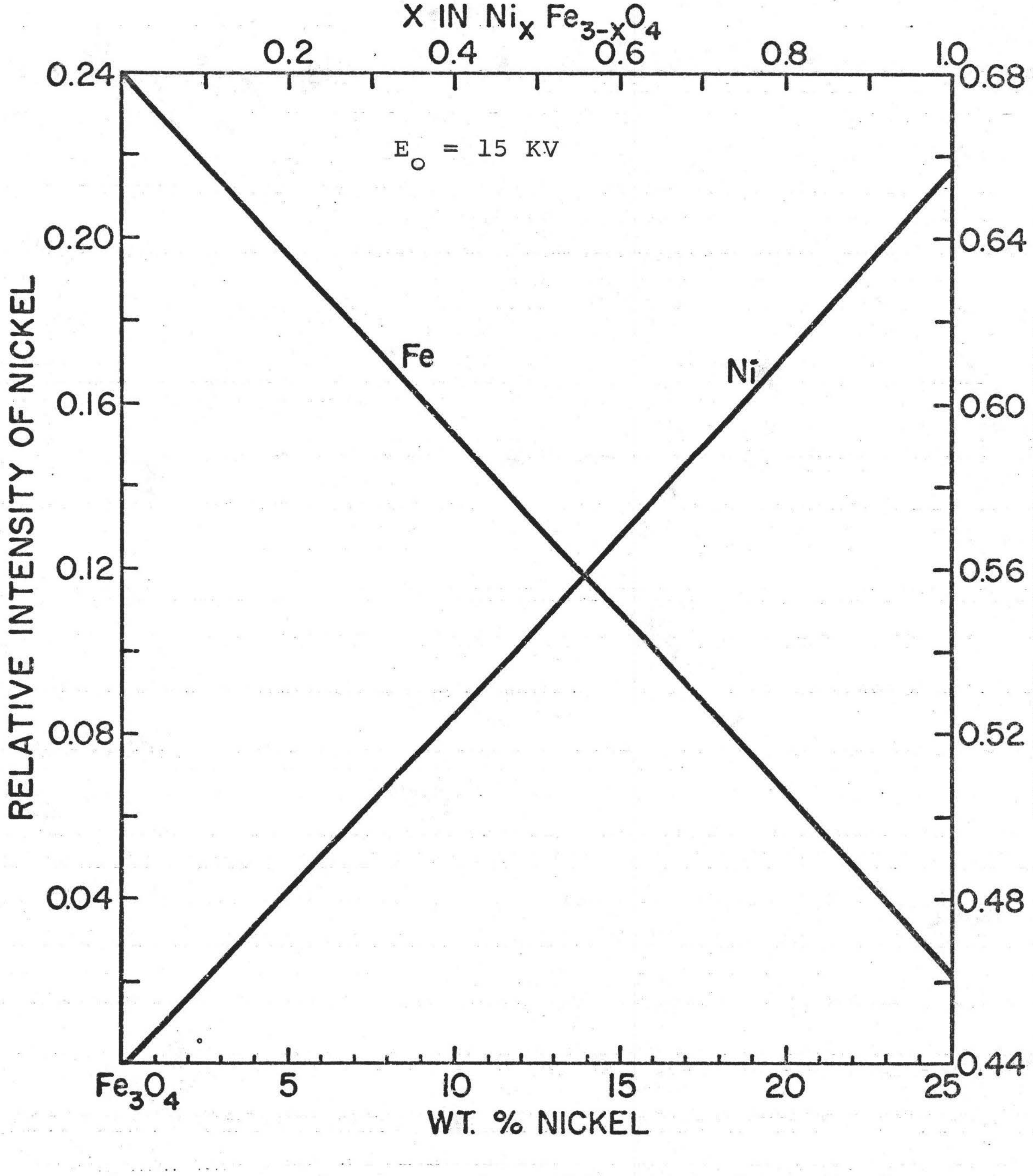

Fig. 6-7: Electron probe calibration for spinels.

Table 6-1

Chemical Analysis of Iron and Nickel
Spectrochemical Analysis
(in p.p.m.)

	Al	Cd	Cr	Co	Cu	Fe	Mg	Mn	Mo	Si	Ti	V
Fe	tr	nd	tr	nd	10	-	30	tr	tr	30	tr	tr
Ni	12	20	54	tr	28	55	4	nd	tr	15	tr	tr

tr-trace ; nd - not detected

Table 6-2

Actual Chemical Compositions of the Investigated Alloys
(Wet Chemical Analyses)

Nominal Composition	Actual Composition	
	wt % Fe	wt % Ni
Ni-2% Fe	1.85	98.15
Ni-4% Fe	4.5	95.5
Ni-5% Fe	5.4	94.6
Ni-6% Fe	6.6	93.4
Ni-8% Fe	8.3	91.7
Ni-10% Fe	10.4	89.6
Ni-15% Fe	15.3	84.7
Ni-20% Fe	20.3	79.7
Ni-25% Fe	25.5	74.5
Ni-50% Fe	47.7	52.3

Table 6-3

Purities of Metal and Oxide Powders, and Salts Used

Material	Purity
Iron (Fe)	99.9+ %
Nickel (Ni)	99.9+ %
Hematite (Fe_2O_3)	99.8%
Magnetite (Fe_3O_4)	99.5%
Nickel Oxide (NiO)	99.8%
Nickel Sulfate ($NiSO_4 \cdot 6H_2O$)	99.7%
Ammonium Oxalate $(NH_4)_2C_2O_4 \cdot H_2O$)	99.5%

TABLE 6-4

Analysis of Matheson Ultra High Purity Argon

Impurity	Contents
CO_2	<0.5 ppm
O_2	<2.0 ppm
H_2	<1.0 ppm
Co	<0.5 ppm
N_2	<5.0 ppm
H_2O	<2.0 ppm
CH_4	<0.4 ppm

TABLE 6-5

Analysis of Matheson Ultra High Purity Oxygen

Impurity	Contents
N_2	6.5 ppm
Kr	13.7 ppm
Xe	0.6 ppm
N_2O	0.01 ppm
H_2O	2.0 ppm
Ar, CO_2, CH_4	not detected

CHAPTER 7

THERMODYNAMICS OF THE IRON-NICKEL-OXYGEN SYSTEM AT 1000°C*

7.1 RESULTS

The photomicrograph in Figs. 7-1 to 7-3 illustrate typical oxide-alloy structures of equilibrated specimens. The structures obtained from both compacts and oxidized alloy plates exhibited an essential feature in that the different phases, which are bonded to one another, are sufficiently large for accurate analysis by the electron microprobe. The diameter of the x-ray production zone in the sample can be estimated by the formula$^{(193)}$

$$d = 0.077\ (V_o^{1.5} - V_c^{1.5})/\rho \text{ in microns} \qquad (7\text{-}1)$$

where V_o is the acceleration voltage, V_c is the excitation voltage for the elements analysed (V_c is 7.1 keV for Fe K_α and 8.3 keV for Ni K_α lines) and ρ is the density of the phase analyzed. At the acceleration voltage of 15 keV used for the analyses the diameter of the x-ray production zone was only about 2μ and hence the minimum size of particles for accurate analysis had to be 5μ. The minimum size of particles analyzed in this investigation was 15μ. Identification of the phases present in a specimen by x-ray diffraction and

---

*This work is based on a publication by the author and W. W. Smeltzer$^{(166)}$.

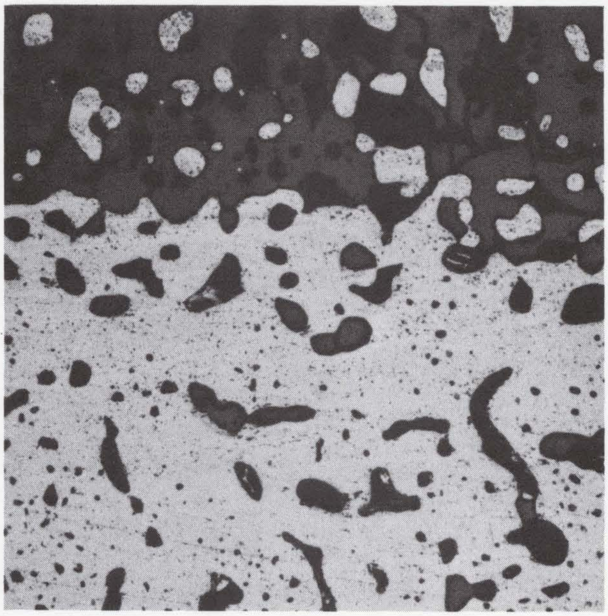

(a) wustite + alloy etched in 5% Hcl in ethyl alcohol, 250×

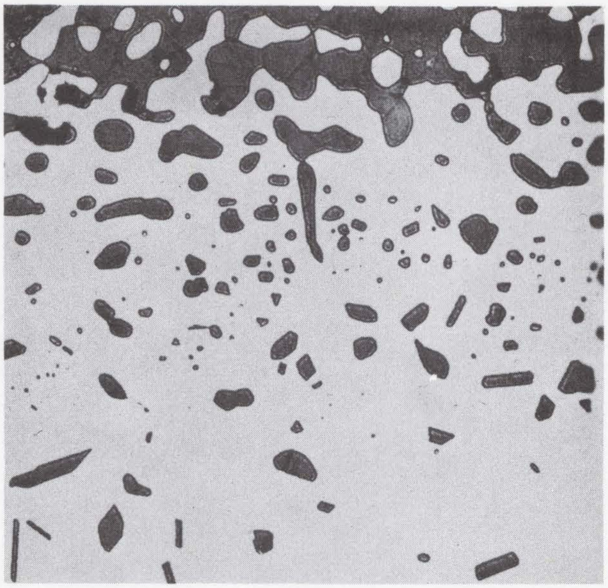

(b) spinel + alloy etched in 50% HCl in water, 320×.

Fig. 7-1: Equilibrium two-phase fields wustite-alloy and the spinel-alloy. In both micrographs, the dark phases are the oxide phases and the bright phase is the alloy phase.

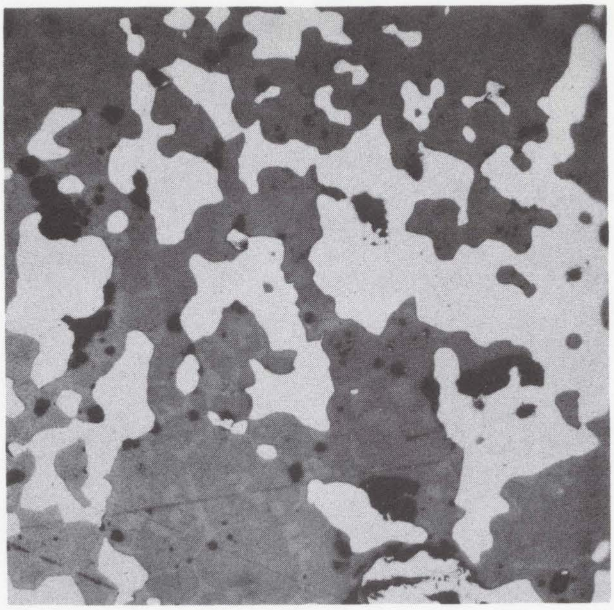

(a) Microstructure before etching, 200×

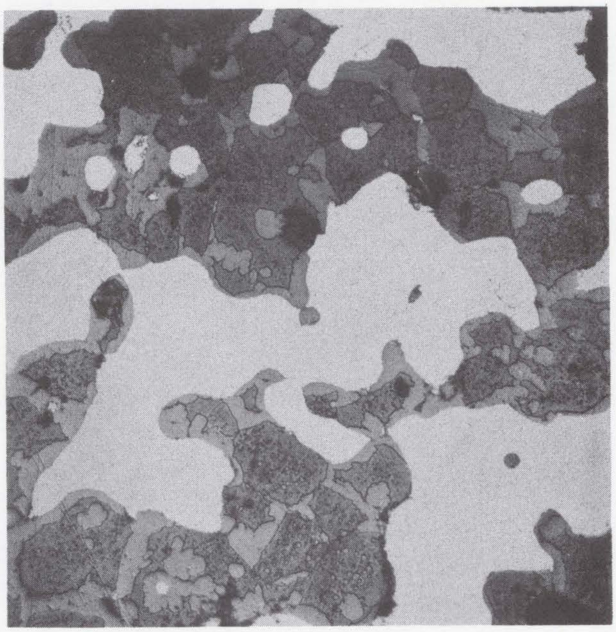

(b) Specimen surface after etching in 5% HCl in ethyl alcohol, 400×; bright phase - alloy, dark matrix phase - wustite, grey precipitates - spinel.

Fig. 7-2: Equilibrium three-phase field wustite-spinel-alloy.

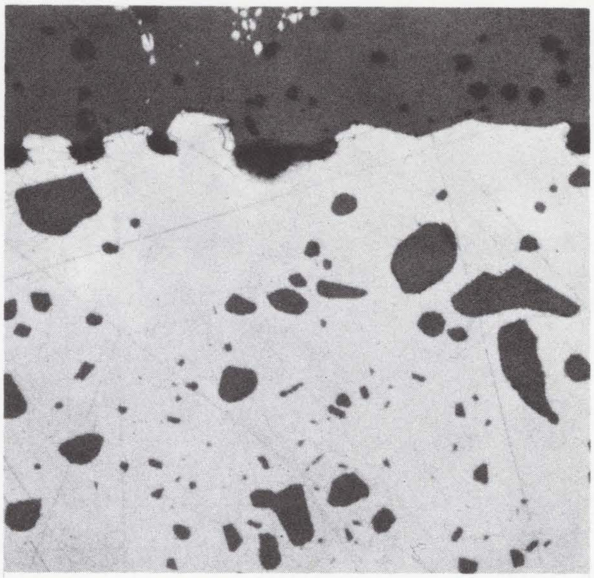

(a) Microstructure before etching, 400×

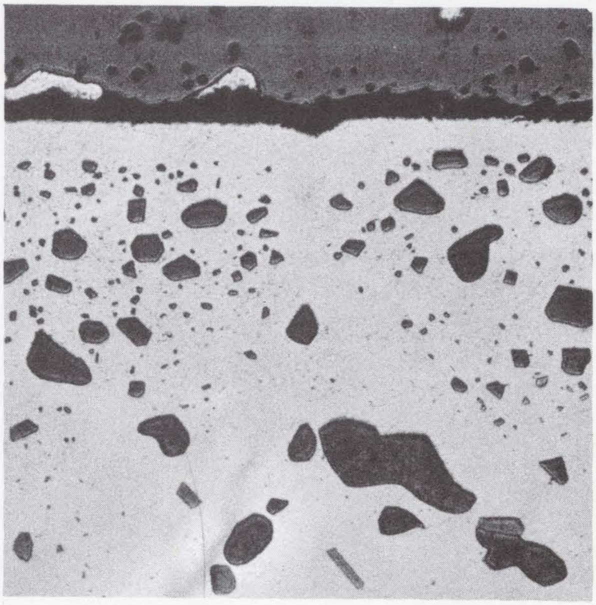

(b) Specimen surface after etching in 50% HCl in water, 320×; bright phase-alloy, surface layer and unetched grey particles - nickel oxide, dark etched oxide - nickel ferrite.

Fig. 7-3: Equilibrium three phase field nickel ferrite-nickel oxide-alloy.

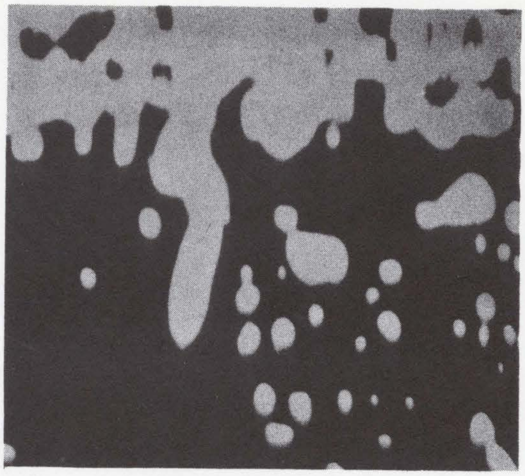

(a) Electron back scatter image. The spinel phase appears as bright and the alloy phase appears as dark.

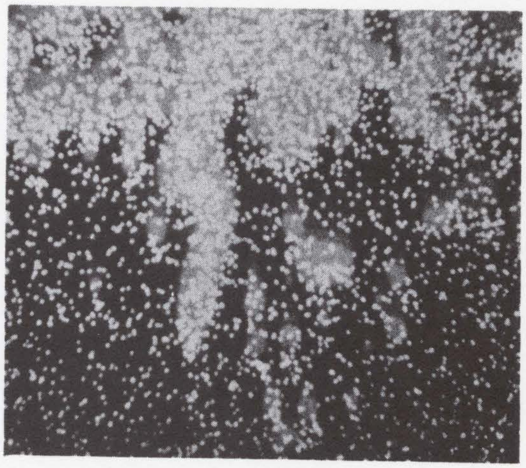

(b) Fe-K_α x-ray image showing distribution of iron in the two phases.

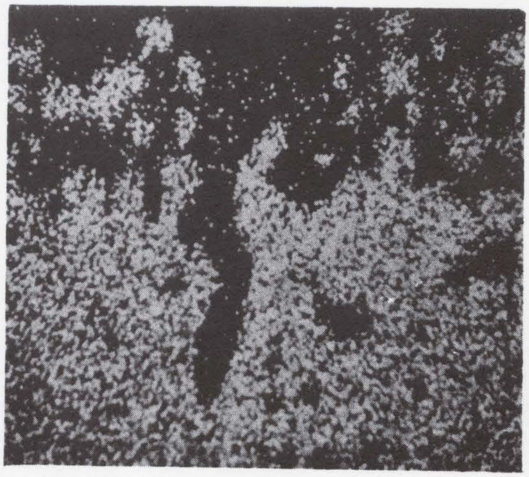

(c) Ni-K_α x-ray image showing nickel distribution

Fig. 7-4: Electron probe images of sample in the two-phase field spinel + alloy, 1000×

Table 7-1

Electron microprobe analysis of coexisting alloy and oxide phases at 1000°C

Sample Number	Composition of alloy						Oxide Phase Identification	Composition of Oxide Phases					
	W/O Ni	Error	W/O Fe	Error	a/O Ni	a/O Fe		W/O Ni	Error	W/O Fe	Error	a/O Ni	a/O Fe
1	60.0	0.5	40.0	0.4	48.8	41.2	I	0.13	0.05	76.0	0.4	0.1	47.7
2	62.9	0.5	37.1	0.4	61.8	38.2	I	0.13	0.05	75.9	0.4	0.1	47.6
3*	81.0	0.5	19.6	0.4	79.7	20.3	I	0.84	0.05	75.4	0.4	0.50	53.3
							II	0.91	0.05	71.5	0.4	0.51	42.2
4*	80.5	0.5	20.1	0.4	79.1	20.9	I	0.85	0.05	75.4	0.4	0.51	53.3
							II	1.08	0.05	71.4	0.4	0.61	42.1
5*	81.1	0.5	19.3	0.4	80.0	20.0	I	0.85	0.05	75.4	0.4	0.51	53.3
							II	1.10	0.05	71.4	0.4	0.62	42.1
6	84.0	0.5	16.0	0.4	83.3	16.7	II	1.4	0.1	71.0	0.4	0.79	42.1
7	86.3	0.5	14.0	0.4	85.3	14.6	II	1.7	0.1	70.5	0.4	0.96	41.7
8	88.0	0.5	12.1	0.4	87.4	12.6	II	2.3	0.2	70.1	0.4	1.29	41.4
9	88.5	0.5	12.2	0.4	87.6	12.4	II	2.7	0.2	69.8	0.4	1.51	41.2
10	93.8	0.6	6.0	0.4	93.6	6.4	II	5.9	0.3	66.5	0.4	3.32	39.3
11	96.0	0.6	4.5	0.4	95.4	4.8	II	9.0	0.3	63.5	0.4	5.07	37.6
12	97.5	0.6	3.7	0.3	96.2	3.8	II	11.7	0.3	60.8	0.4	6.60	36.1
13	98.7	0.6	1.5	0.2	98.4	1.6	II	16.8	0.5	55.6	0.4	9.53	33.1
14	98.9	0.6	1.2	0.2	98.8	1.2	II	20.0	0.5	52.4	0.4	11.37	31.3
15**	99.5	+0.3 -0.7	0.5	0.1	99.5	0.5	II	25.0	0.5	47.4	0.5	14.26	28.4
							III	68.7	0.5	9.8	0.3	43.5	6.5

* Three phase field wustite-spinel-alloy

** Three phase field nickel ferrite-nickel oxide-alloy

Phase numbers correspond to: I wustite; II spinel; III nickel oxide

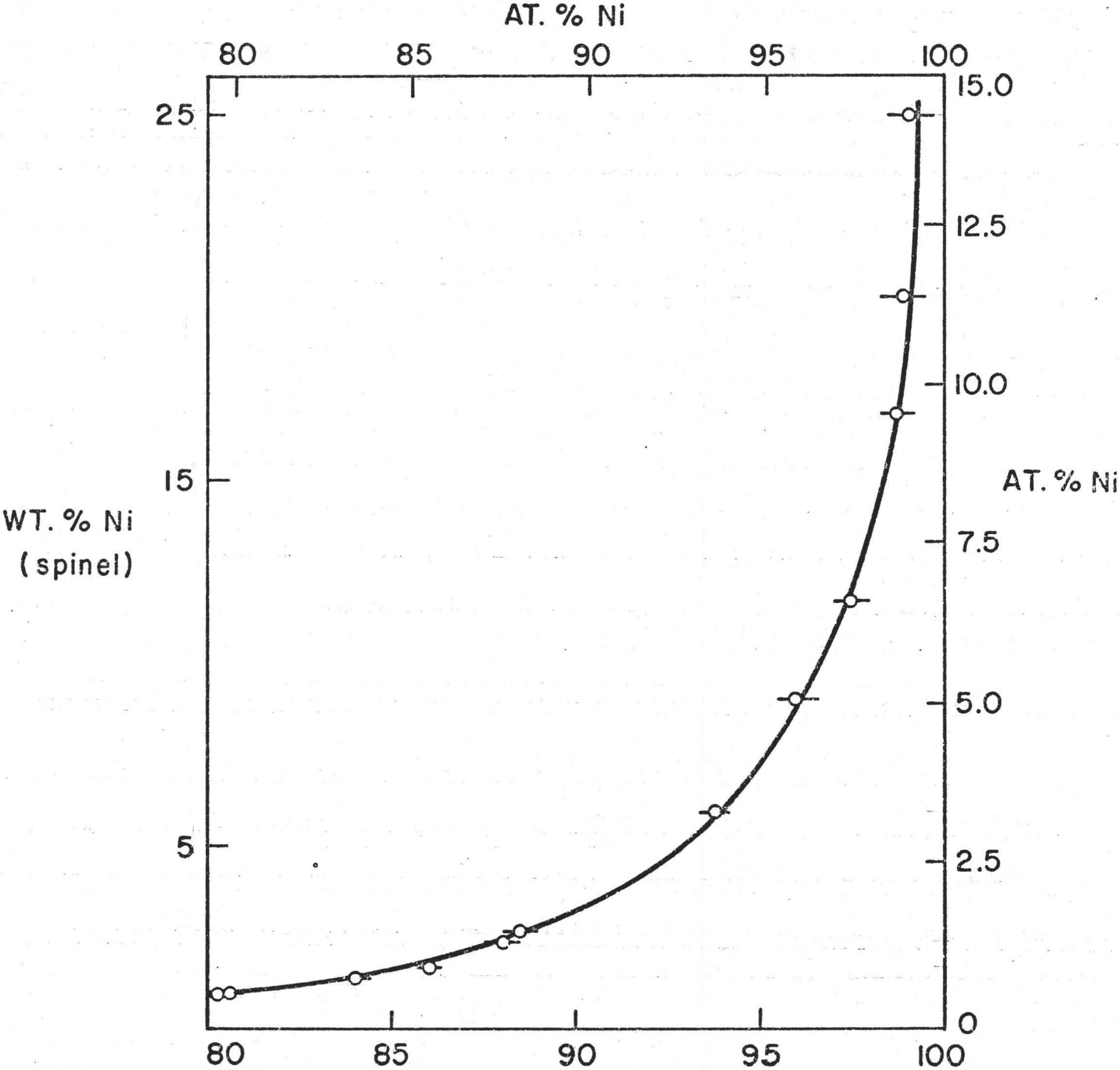

Fig. 7-5: Composition of spinel in equilibrium with alloy as a function of the alloy composition. Data from Table 7-1.

microscopic observation showed complete agreement.

Information given by the electron-probe micrographs was very useful. For example the micrographs shown in Fig. 7-4 were obtained from a specimen consisting of spinel containing 1.4 w/o Ni, and 71 w/o iron and an alloy containing 84% w/o Ni. In the electron back scatter image the alloy was black and the spinel white. Also the x-ray intensities clearly defined the amounts of iron and nickel in the different phases.

Wustite coexisted with alloys containing up to 79.6 a/o Ni, the maximum nickel solubility in wustite being 0.51 a/o. It was found that spinel coexisted with alloys containing from 79.6 to 99.5 a/o Ni. The spinel in equilibrium with wustite and alloy contained 0.6 a/o Ni whilst the compositions of the spinel in equilibrium with nickel oxide and alloy corresponded to stoichiometric nickel ferrite. The maximum iron solubility in nickel oxide was 6.5 a/o.

7.2 DISCUSSION

The isothermal section of the phase diagram at 1000°C constructed from the compositional determinations is illustrated in Fig. 7-6. The oxygen solubilities in the alloys have been magnified for clarity and are in fact negligibly small and unknown. The diagram is symmetric about the spinel-alloy field which is bounded by three-phase fields containing wustite-spinel-alloy and nickel oxide-spinel-alloy. These fields are bounded in turn by two-phase fields containing wustite and alloy on the iron rich side and nickel oxide and alloy on the nickel rich side of the diagram. Wustite, which exhibits only a small nickel solubility, is stable over a wide range of alloy composition; on the other hand, nickel oxide exhibits a relatively large iron solubility but its stability is confined to a very narrow range of alloy composition. The tie-lines in the wustite-alloy and spinel-alloy fields are not proportionately spaced. They fan out from oxide in the iron-rich region and from the alloy in the nickel-rich region of the diagram.

A terminal nickel solubility of 0.51 a/o in wustite agrees with a reported value(105) and it lies between two determinations where the nickel contents were reported virtually absent(103) and 1.3 a/o(108). The iron concentration as well as the total metal concentration in wustite decreased with increasing nickel content of the alloy. At the terminal composition, the total amount of metal was 46.7 a/o. since this value is equal to the iron concentration in wustite upon its equilibrium with magnetite, it would appear that there is an isomorphous substitution of nickel for iron in the wustite lattice. The nickel composition of 0.6 a/o for spinel S_1, shows wide divergence from an earlier determination of 5 a/o(103). Magnetite exhibits an inverse spinel structure with ferrous ions occuping octahedral sites and and ferric ions occupying both octahedral and tetrahedral sites between oxygen ions(17). Apparently nickel replaces iron in the divalent sites in the spinel up to the terminal composition corresponding to nickel ferrite(107,194).

The values reported for the dissociation pressures and nickel contents of wustite are sufficient for thermodynamic evaluation of the solution behaviour of nickel in wustite. Values reported for the dissociation pressures of wustite containing nickel in solid solution are compared to that for pure wustite in Fig. 7-7. The Gibbs-Duhem relationship may be applied to the alloy and oxide phases because these pressures determine oxygen activities:

$$N_0^A \, d\ell n \, a_0^A + N_{Ni}^A \, d\ell n \, a_{Ni}^A + N_{Fe}^A \, d\ell n \, a_{Fe}^A = 0 \tag{7-2}$$

$$N_0^W \, d\ell n \, a_0^W + N_{Ni}^W \, d\ell n \, a_{Ni}^W + N_{Fe}^W \, d\ell n \, a_{Fe}^W = 0 \tag{7-3}$$

where N is a mole fraction and a is an activity in the alloy (A) and wustite (W) phases. At equilibrium, equations (7-2) and (7-3) yield the variation of oxygen activity with respect to nickel activity.

$$\frac{d\ell n \, a_0}{d\ell n \, a_{Ni}} = - \frac{N_{Ni}^A - N_{Ni}^W \, N_{Fe}^A / N_{Fe}^W}{N_0^A - N_0^W \, N_{Fe}^A / N_{Fe}^W} \tag{7-4}$$

Since the oxygen solubility in the metal is extremely small, 0.0003 - 0.015 w/o$^{(180,195)}$, we may neglect the term N_0^A in integrating Eq. (7-4). Therefore

$$\ell n\ P_{0_2}/P_{0_2}^o = 2 \int_o^{N_{Ni}^A} \left\{\frac{N_{Ni}^A - N_{Ni}^W N_{Fe}^A/N_{Fe}^W}{N_0^W N_{Fe}^A/N_{Fe}^W}\right\} d\ell n(\gamma_{Ni}^A N_{Ni}^A) \qquad (7\text{-}5)$$

where $P_{0_2}^o$ is the dissociation pressure of pure wustite. This equation was integrated numerically by means of a computer since values are available for the mole fractions of iron, nickel and oxygen in wustite as well as the activity coefficients of nickel in the alloy$^{(100,101,105,196)}$.

Equation (7-4) may be simply integrated to the following expression if it is additionally assumed that the small concentration of nickel in wustite approximates to zero and that the mole fractions of iron and oxygen are equal as for stoichiometric wustite,

$$\log P_{0_2}/P_{0_2}^o = 2 \log (1/1 - N_{Ni}^A) \qquad (7\text{-}6)$$

This expression is also obtained by comparing the dissociation pressures of pure wustite with that of wustite equilibrated with the alloy,

$$FeO(W) \rightleftarrows Fe(A) + 1/2\ O_2 \qquad (7\text{-}7)$$

under the approximations of unit activity for wustite and of ideal solution behaviour of iron in the alloy.

Comparison of the values for the dissociation pressures calculated by means of equations (7-5) and (7-6) to those determined experimentally are shown in Fig.7-7. Although there are large uncertainties in the evaluations of the alloy compositions in the case where dissociation pressures were determined for wustite-alloy compacts(108), both equations serve as a first approximation to the experimental results. The better fit, however, is obtained by Eq. (7-5) where account has been taken of the degree of nickel solubility in wustite and to the activity coefficients for the alloy components. Eq. (7-5) gives the invariant oxygen partial pressures in the wustite-spinel-alloy phase field as 3.26×10^{-14} atm, a value considerably larger than the dissociation pressure of pure wustite, $P^{o}_{O_2} = 1.32\times10^{-15}$ atm. Since the dissociation pressure of wustite containing the maximum nickel content is less than that for wustite-magnetite equilibrium, 1.62×10^{-13} atm, it can be inferred, as was found, that the limiting nickel content of wustite, 0.51 a/o, should be less than the corresponding value for spinel, 0.60 a/o.

A useful approximation to the wustite solid solution may be made by assuming that nickel dissolves in wustite as nickel oxide. The following displacement reaction may then be considered,

$$\mathrm{Fe(A)} + \mathrm{NiO(W)} \rightleftarrows \mathrm{Ni(A)} + \mathrm{FeO(W)} \qquad (7\text{-}8)$$

where

$$K = \frac{a_{Ni}^{(A)} \cdot a_{FeO}^{(W)}}{a_{Fe}^{(A)} \cdot a_{NiO}^{(W)}} = \frac{(\gamma_{Ni} \cdot N_{Ni})_A \cdot (\gamma_{FeO} \cdot N_{FeO})_W}{(\gamma_{Fe} \cdot N_{Fe})_A \cdot (\gamma_{NiO} \cdot N_{NiO})_W} \quad . \qquad (7\text{-}9)$$

The value of K is determined to be 186 at 1000°C from electromotive force measurements of Kiukkola and Wagner$^{(109)}$. Since the values of the activity coefficients for the alloy components are known, the nickel oxide content of wustite was calculated for the case of oxide ideal solid solution behaviour as a function of nickel content of the alloy phase. This relationship and the experimental relationship are shown in Fig. 7-8. The curve through the experimental points was determined by a least squares analysis using a computer. Division of the corresponding values obtained by these two relationships yields the activity coefficient ratio, $\gamma_{NiO}/\gamma_{FeO}$, as a function of equilibrium alloy composition. The curve representing this activity coefficient ratio is also shown in Fig. 7-8. It can be seen that the ratio of the activity coefficient remains constant at 3.72 for the alloy compositon range of 0 - 40 a/o Ni and then decreases to a value of 2.33 at the limiting alloy composition for stability of wustite. Consequently nickel oxide solubility in wustite displays a Henry law behaviour only to a mole fraction of 0.008. A similar calculation using Eq. (7-9) yields $\gamma_{FeO}/\gamma_{NiO} = 4.88$

at the limiting tie-line of the nickel oxide-alloy region where the alloy composition is 99.5 a/o Ni, the activity coefficients of nickel and iron in the alloys are 1.0 and 0.78 respectively, and the mole fraction of wustite in nickel oxide is 0.13.

The iron contents of the nickel oxide, N_2, and the alloy, A_2, occurring in the spinel-nickel oxide-oxygen and in the spinel-nickel oxide-alloy regions, respectively, may be evaluated from appropriate standard free energies of formation. The following reactions may be considered

$$NiFe_2O_4 = Ni + 2Fe + 2O_2 \qquad (7\text{-}10)$$

$$FeO = Fe + 1/2\ O_2 \qquad (7\text{-}11)$$

$$NiO = Ni + 1/2\ O_2 \qquad (7\text{-}12)$$

Since the standard free energies for these reactions at 1000°C are 152, 43 and 30 kcal respectively(136,197), we obtain for the equilibrium constants in terms of standard oxygen activities for the pure metals and oxides

$$K_{10} = (a_O^o)^4_{10} = a_{Ni}\ a_{Fe}^2\ a_O^4 = 7.65 \times 10^{-27} \qquad (7\text{-}13)$$

$$K_{11} = (a_O^o)_{11} = a_{Fe}\ a_O/a_{FeO} = 4.14 \times 10^{-8} \qquad (7\text{-}14)$$

$$K_{12} = (a_O^o)_{12} = a_{Ni}\ a_O/a_{NiO} = 7.06 \times 10^{-6} \qquad (7\text{-}15)$$

From Eqs. (7-13), (7-14) and (7-15) we obtain

$$a_O \cdot a_{FeO}^2 \cdot a_{NiO} = 8.22 \times 10^{-7} \qquad (7\text{-}16)$$

In the three-phase region spinel-oxygen-nickel oxide,

$a_O \simeq 1$ and $a_{NiO} \simeq 1$. Therefore Eq. (7-16) yields $a_{FeO} \simeq 10^{-3}$. Accordingly the iron content in nickel oxide, N_2, corresponds to approximately 0.05 a/o. In the three phase region spinel-nickel oxide-alloy, $N_{NiO} = 0.87$ and $a_{Ni} = 1$. Therefore from Eq. (7-16) $a_{FeO} = 0.38$ and $a_O = 6.15 \times 10^{-6}$. Accordingly the mole fraction of iron in the alloy, A_2, $N_{Fe} = a_{Fe}/\gamma_{Fe} = 0.0047/0.78 \simeq 0.006$. That is, the nickel-iron alloy existing in equilibrium with spinel and nickel oxide contains approximately 0.6 a/o iron. This calculated value is to be compared to the value of 0.5 a/o obtained in the present investigation.

Using the Gibbs-Duhem equations for alloy and oxide phases in the spinel-alloy region, variation of oxygen activity with respect to the alloy composition in this region can be obtained. This relationship which is similar to that for the wustite-alloy region given by Eq. (7-5) simplifies to the following when it is seen that in this region $\gamma_{Ni} \simeq 1$ and for the spinel $Ni_x Fe_{3-x}O_4$, $N^s_{Ni} = \frac{x}{7}$, $N^s_{Fe} = \frac{3-x}{7}$ and $N^s_O = \frac{4}{7}$,

$$\ln P_{O_2}/P^*_{O_2} = 2 \int_{N^*_{Ni}}^{N^A_{Ni}} \frac{3N^A_{Ni} - 7\, N^s_{Ni}}{4N^A_{Ni}\ (1-N^A_{Ni})}\, dN^A_{Ni} \qquad (7\text{-}17)$$

In Eq. (7-17) $P^*_{O_2}$ is the oxygen potential in the three phase field wustite-spinel-alloy and N^*_{Ni} is the mole fraction of nickel in the alloy in equilibrium with wustite and spinel.

Since from the experimental results N_{Ni}^{S} is known as a function of N_{Ni}^{A} (Fig. 7-5), Eq. (7-17) can be numerically integrated. Davies(198) has computed the variation of oxygen potential across the spinel-alloy phase field by numerical integration of Eq. (7-17). From the results obtained by Davies it appears that for values of N_{Ni}^{A} upto 0.96,the errors in the nickel content of the spinel has little effect upon the computed oxygen potential. In this range, the calculated values are affected only by errors in the measurement of $P_{O_2}^{*}$ and N_{Ni}^{*} The computed values will be reliable for this region of the phase field. The calculation is very sensitive to experimental errors in the value of the upper limiting composition, A_2, and should not be used to predict this particular ratio viz. $P_{O_2}^{**}/P_{O_2}^{*}$ where $P_{O_2}^{**}$ is the oxygen potential in the three phase field spinel-nickel oxide-alloy.

A more reliable value of $P_{O_2}^{**}$ is obtained from the oxygen activity in the three phase field spinel-nickel oxide-alloy calculated from equation (7-16). This yields $P_{O_2}^{**} = 3.7 \times 10^{-11}$ atm. Davies(198) has obtained the value of $P_{O_2}^{**}$ experimentally from solid state emf measurements. The calculated value of $P_{O_2}^{**} = 3.7 \times 10^{-11}$ atm is to be compared with the value obtained by Davies of $P_{O_2}^{**} = 2.5 \times 10^{-11}$ atm. Since the calculations involve the assumption of ideality for nickel oxide in the FeO-NiO solid sitution an interpretation of the discrepancy between the calculated and observed values is that γ_{NiO} is in fact not unity. The two values will then yield $\gamma_{NiO} = 0.81$. The value of γ_{NiO} can also be obtained from values of the ratio $\gamma_{FeO}/\gamma_{NiO} = 4.88$ and $\gamma_{FeO} \simeq 3$ earlier obtained. This yields $\gamma_{NiO} = 0.63$. The difference in two values for γ_{NiO} at the terminal composition of nickel oxide in equilibrium with spinel and alloy may be attributed to the experimental errors involved in the various investigations. It can be seen that in NiO-FeO solid solution FeO exhibits positive deviation from ideality whereas NiO exhibits a negative deviation at the NiO end of the solutions in equilibrium with Ni-Fe alloys. NiO however appears to show positive deviation at the wustite end of the solid solutions in equilibrium with Fe-Ni alloys.

From the calculated values and results obtained by various investigators$^{(105,108,198)}$ oxygen potentials in the Fe-Ni-O system at 1000°C can be plotted as a function of composition of the system. This yields an oxygen potential diagram for the system (Fig. 7-9) which is essentially complementary to the phase diagram given in Fig. 7-6. The two are related through the Gibbs-Duhem relations.

Fig. 7-6: Iron-Nickel-Oxygen phase diagram at 1000°C (a/o)

W_1 - $Ni_{0.01}Fe_{0.87}O$ (wustite); S_1-$Ni_{0.04}Fe_{2.96}O_4$ (spinel)

A_1 - 79.6 a/o Ni, 20.4 a/o Fe (alloy)

F - $NiFe_2O_4$ (ferrite); N_1-$Fe_{0.13}Ni_{0.87}O$ (nickel oxide)

A_2 - 99.5 a/o Ni, 0.5 a/o Fe (alloy)

N_2 - $Fe_xNi_{1-x}O$ where $x \simeq 0.0005$ (nickel oxide)

Phase notations:

W - wustite, $Ni_xFe_{1-(x+y)}O$; M - magnetite, Fe_3O_4;
S - spinel ($Ni_xFe_{3-x}O_4$); H - hematite, Fe_2O_3 ;
N - nickel oxide, $Fe_xNi_{1-x}O$; A - alloy.

The dashed line across the bottom of the diagram represents oxygen solubilities in the alloy magnified for clarity. Dashed lines in the vicinity of the oxygen corner represent undetermined boundaries of phase fields involving oxygen. The insets on either side represent corresponding phase regions on an expanded scale.

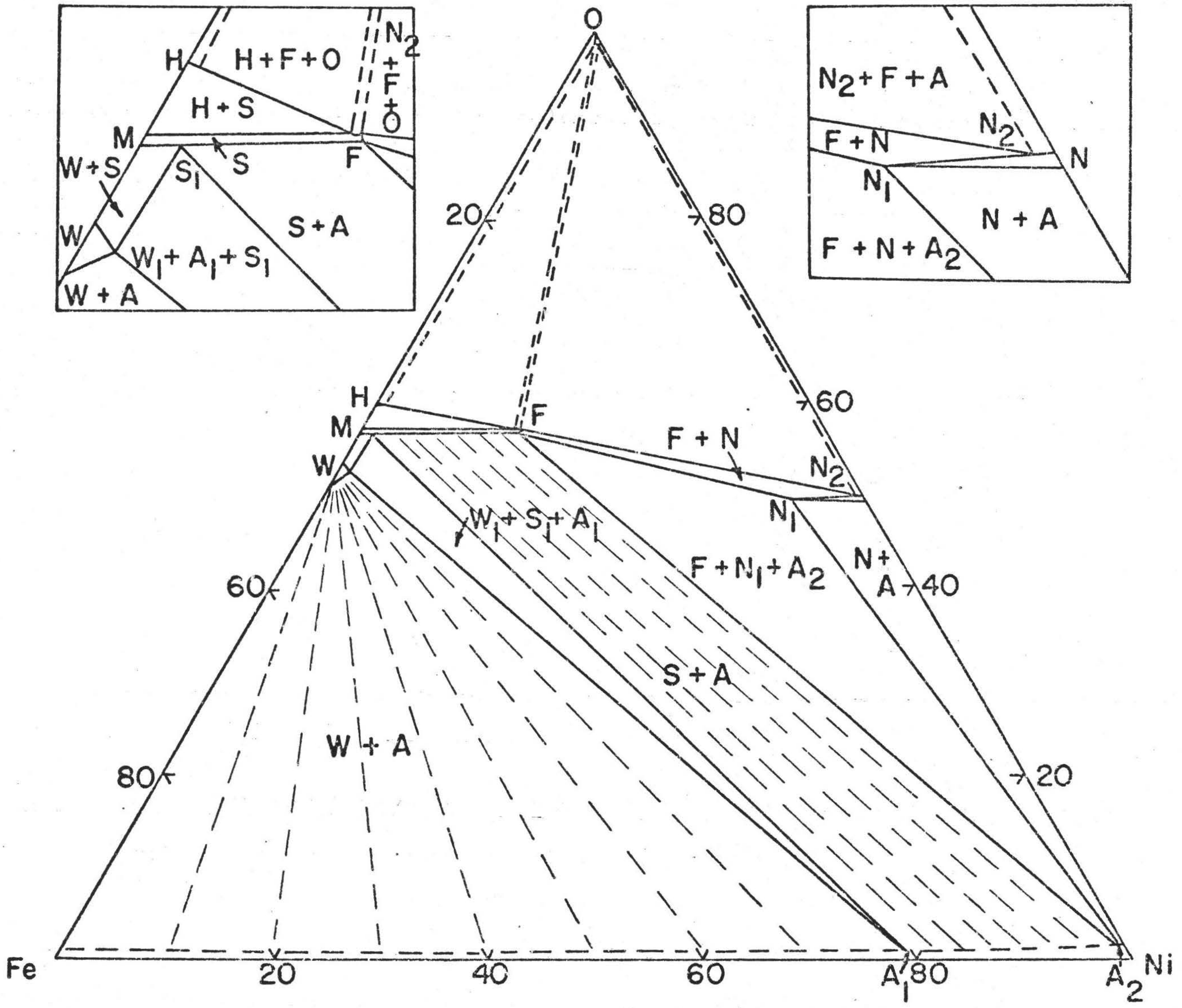
H
H + F + O
N2
+
F
+
O
H + S
M
S
F
W + S
S1
S + A
W
W1 + A1 + S1
W + A
N2 + F + A
N2
F + N
N
N1
N + A
F + N + A2
O
20
80
H
60
M
F
F + N
W
N2
N1
W1 + S1 + A1
F + N1 + A2
N +
A
40
60
S + A
W + A
80
20
Fe
20
40
60
A1
80
A2
Ni

Fig. 7-7: Equilibrium oxygen partial pressure in the two phase field wustite-alloy as a function of alloy composition. The solid and dashed curves were calculated according to Eqs. (7-5) and (7-6), respectively. The data were obtained from ref. (101) (●) and ref. (108) (O).

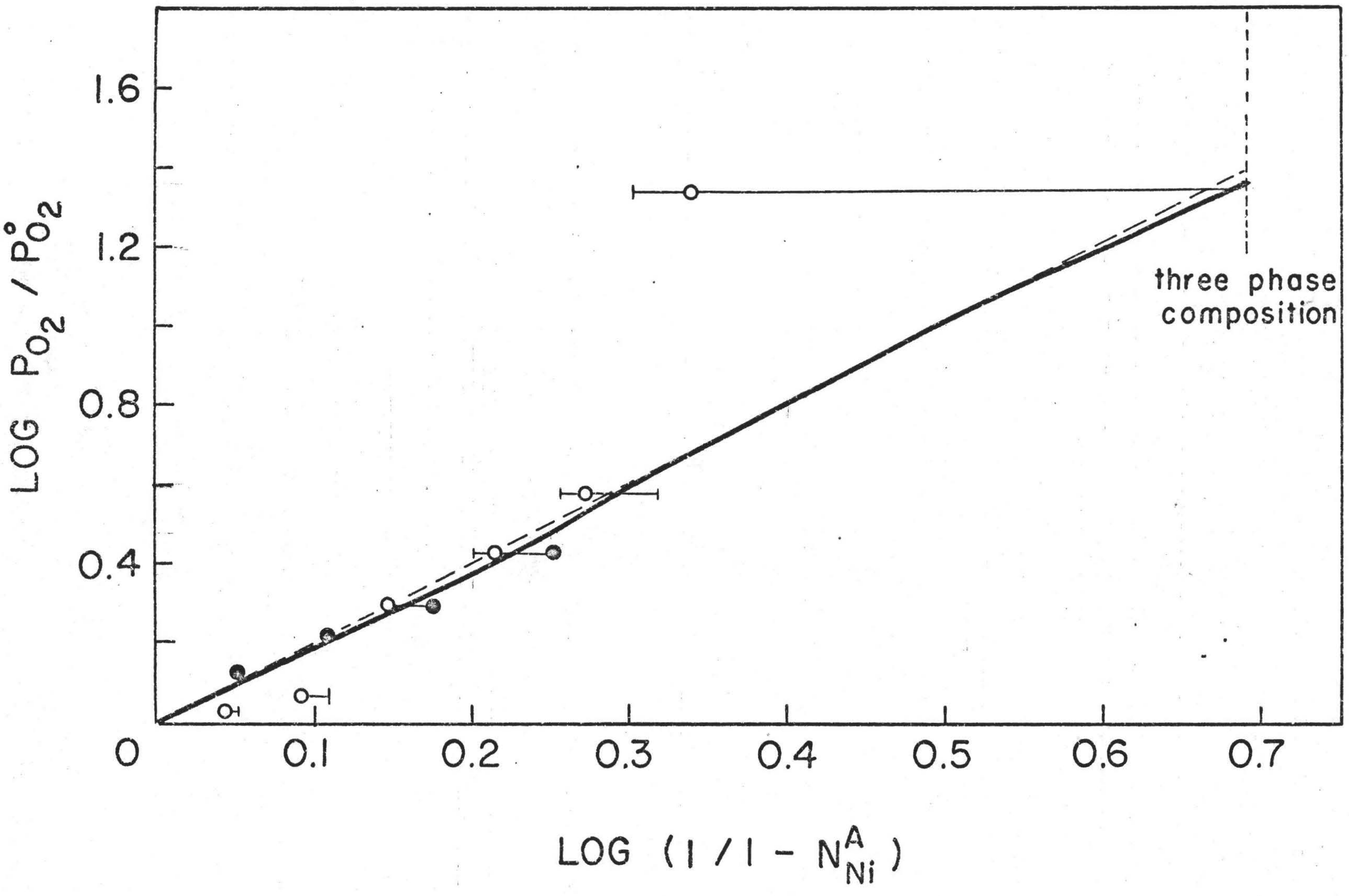
1.6
1.2
0.8
0.4
0
0.1
0.2
0.3
0.4
0.5
0.6
0.7
LOG $P_{O_2} / P^{\circ}_{O_2}$
LOG $(1 / 1 - N^{A}_{Ni})$
three phase
composition

Fig. 7-8: Solubility of nickel oxide in wustite as a function of equilibrium alloy composition. The dashed curve was obtained with the assumption of ideality for the wustite-nickel oxide system. The data for the experimental curve were obtained from this investigation, (●) and from ref. (105) (O). The activity coefficient ratio $\gamma_{NiO}/\gamma_{FeO}$ for the wustite phase as a function of equilibrium alloy composition was obtained from the above two curves on dividing calculated values obtained on the assumption of ideality by the corresponding experimental values, Eq. (7-9).

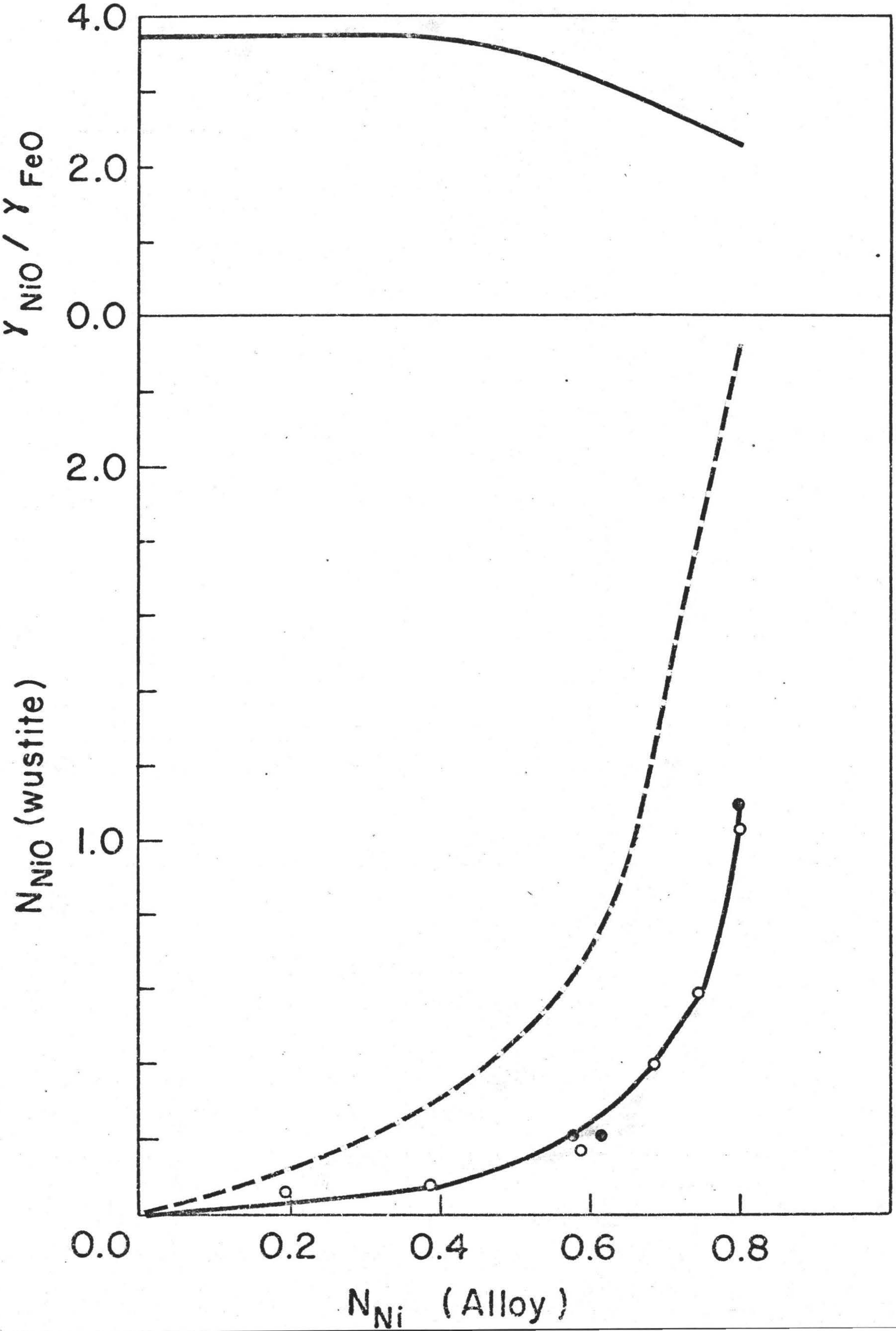
4.0
2.0
0.0
$\gamma_{NiO} / \gamma_{FeO}$
2.0
1.0
N_{NiO} (wustite)
0.0
0.2
0.4
0.6
0.8
N_{Ni} (Alloy)

Fig. 7-9: Oxygen potential diagram for the Iron-Nickel-Oxygen system at 1000°C

Key

o...Calculated values from Gibbs-Duhem equations (Eqs. (7-5) and (7-7)) and data of Table 7-1.

●...Experimental values of Davies (198)

Δ...Experimental values of Roeder and Smeltzer (108)

▼...Experimental values of Oriani (101)

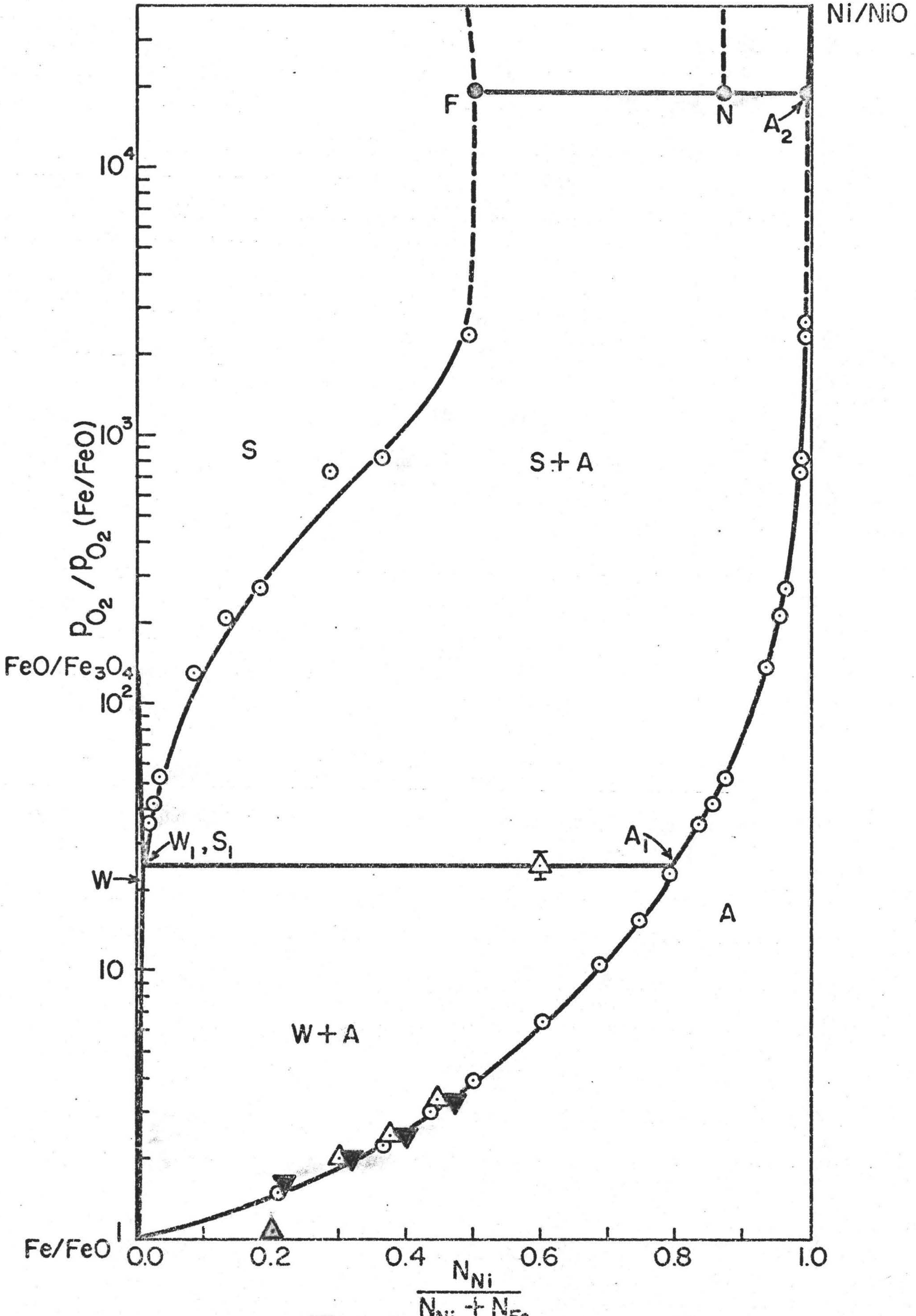
Ni/NiO
F
N
A2
10^4
10^3
S
S + A
pO2 / pO2 (Fe/FeO)
FeO/Fe3O4
10^2
W1, S1
A1
W
A
10
W + A
Fe/FeO
1
0.0
0.2
0.4
0.6
0.8
1.0
NNi / NNi + NFe

CHAPTER 8

OXIDATION OF Ni-Fe ALLOYS AT 1000°C - RESULTS

8.1 OXIDATION KINETICS

The kinetic data were obtained using the volumetric apparatus and recorded as the volume of oxygen consumed at constant temperature and pressure. This was then converted to weight gain of the specimen. The kinetic data (weight gain per unit area as a function of time) for alloys of various compositions containing 0-25% Fe are illustrated graphically in Figs. 8-1 to 8-10. In all cases the weight gains are expressed in mg/cm^2 and the time in hours. All the experiments were carried out at 1000°C in pure oxygen at a pressure of 400 torr. The period of oxidation was generally about 50 hours. However for some samples periods of up to 100 hours were employed. In each case more than one sample were oxidized to check the reproducibility of the kinetics. The graphical representation shows data for more than one sample for each composition. The parabolic plots [(wt. gain per unit area)^2 vs. time] corresponding to the kinetic data are shown in Figs. 8-11 to 8-20.

Pure nickel was used as the basis of comparison for the kinetics. It was observed that continuous long range kinetics could be obtained for nickel-iron alloys carefully prepared metallographically. Parabolic kinetics were observed for pure nickel through the entire oxidation period. Linear or cubic kinetics were not observed at any stage of oxidation. In the case of the alloys, an initial non-parabolic transient period of upto 12 hours was observed. After a stationary state was obtained the alloys oxidized parabolically. No deviation was observed from this mode of kinetics even after long periods of time. The reproducibility of the results was good.

The parabolic rate constants for the alloys investigated were determined from the slopes of the parabolic plots at long times, and are given in Table 8-1. The relative parabolic rate constant with respect to pure Ni [(i.e.k_p(alloy)/k_p(Ni)] is plotted as a function of the bulk alloy composition in Fig. 8-21. The rate of oxidation of nickel-iron alloys <u>increases</u> initially upon addition of iron and subsequently <u>decreases</u> to a nearly constant value. The maximum oxidation rate was observed for the Ni-5% alloy. The shape of this curve should be noted. A quantitative diffusion model will be utilized to explain the scale structure of the alloys containing upto 5% Fe. A schematic model will be utilized to explain the shape of the whole curve.

In addition to obtaining the kinetic data in the

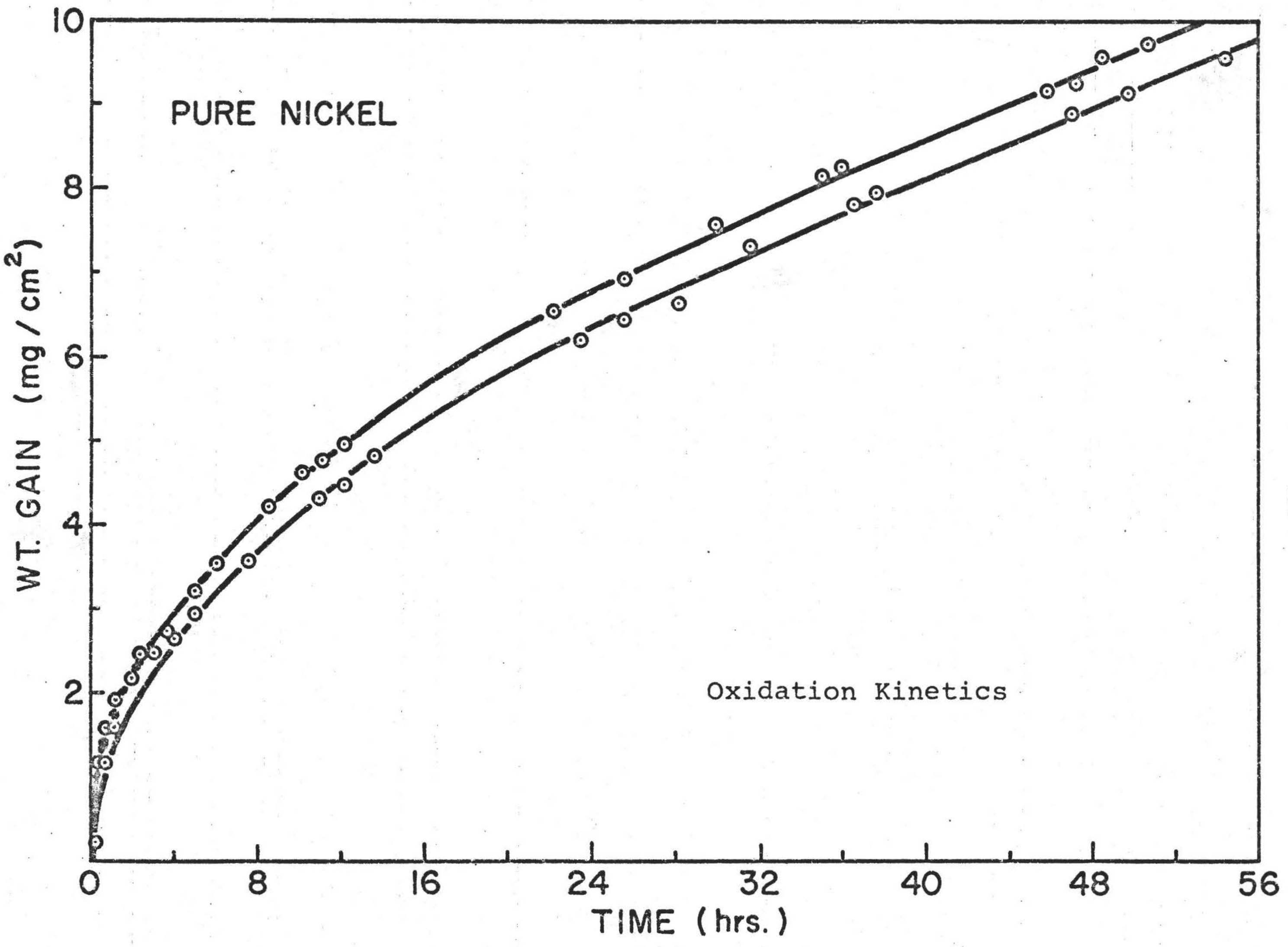
PURE NICKEL
Oxidation Kinetics
WT. GAIN (mg/cm²)
TIME (hrs.)
0
2
4
6
8
10
0
8
16
24
32
40
48
56

Fig. 8-1

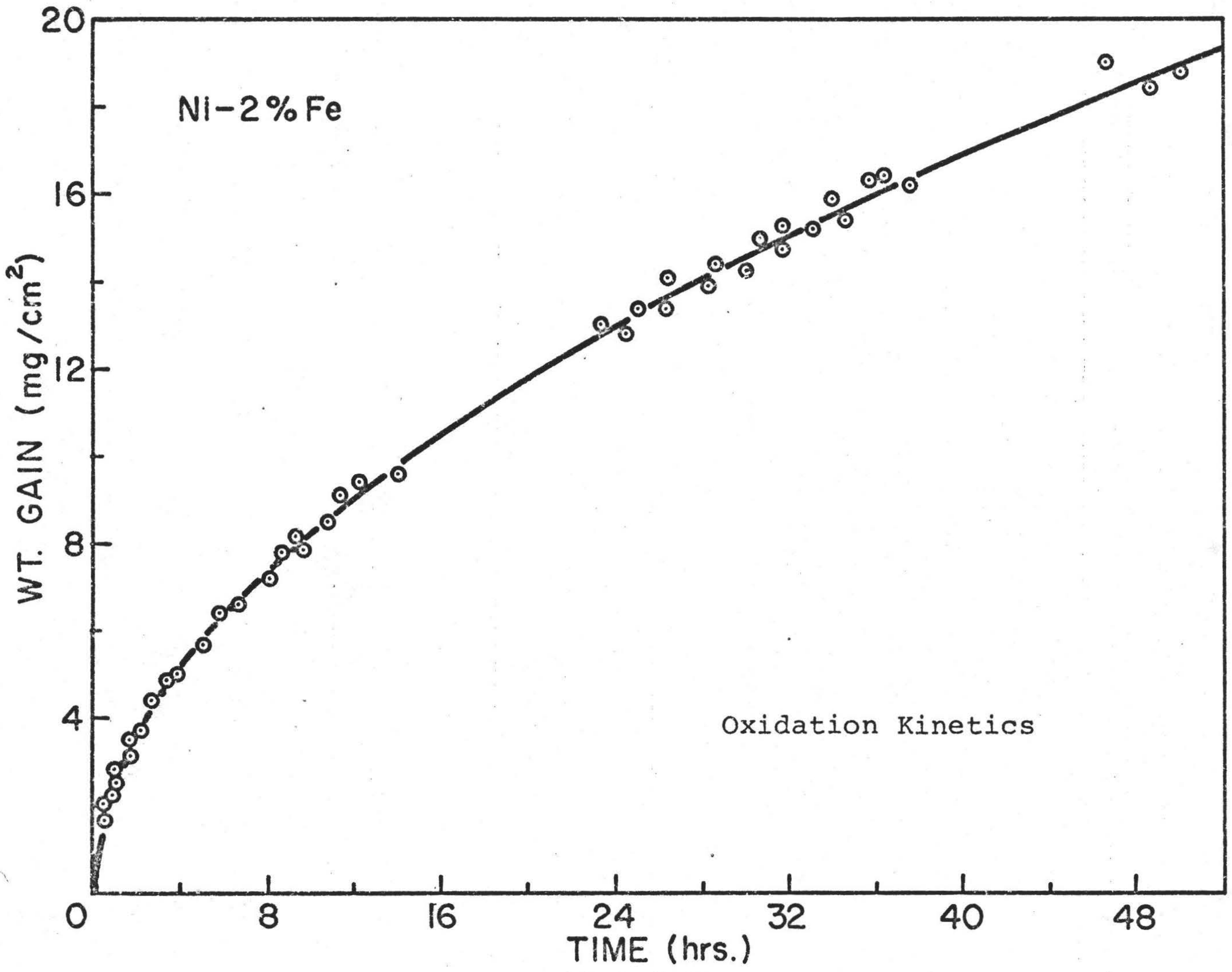
Ni-2% Fe
WT. GAIN (mg/cm^2)
20
16
12
8
4
0
8
16
24
32
40
48
TIME (hrs.)
Oxidation Kinetics

Fig. 8-2

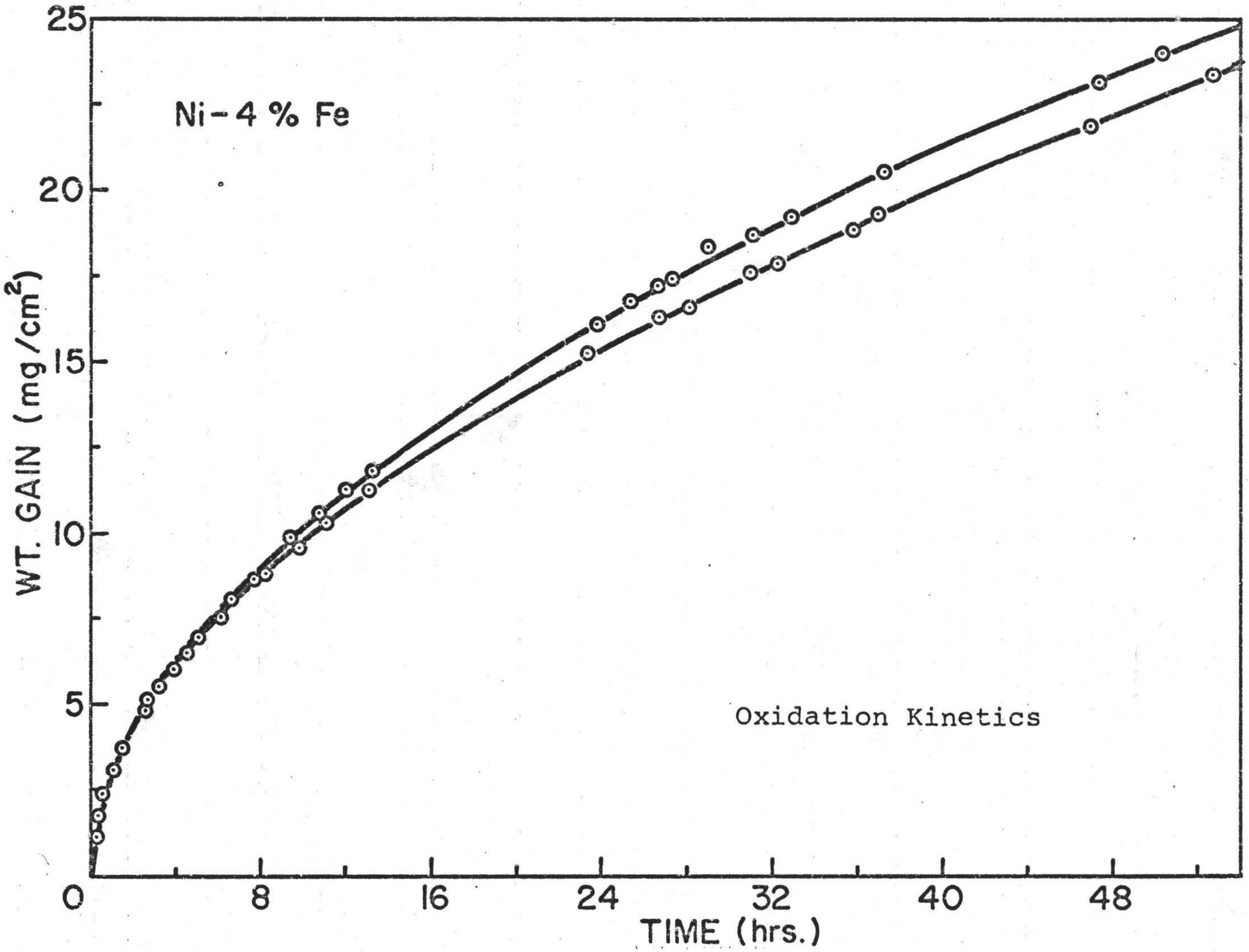
Ni-4 % Fe
Oxidation Kinetics
WT. GAIN (mg/cm²)
25
20
15
10
5
0
8
16
24
32
40
48
TIME (hrs.)

Fig. 8-3

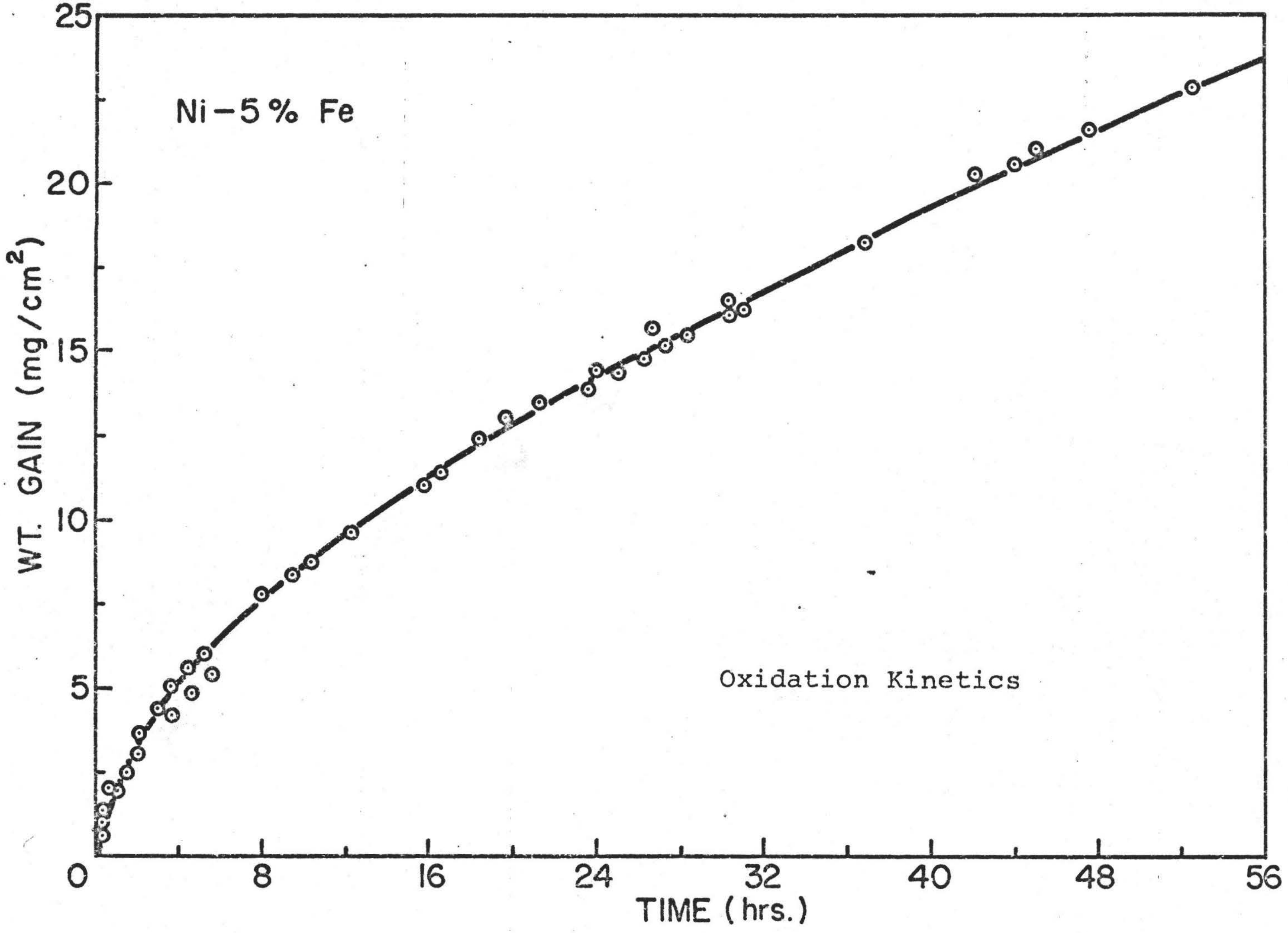
Ni-5% Fe
Oxidation Kinetics
WT. GAIN (mg/cm^2)
0
5
10
15
20
25
0
8
16
24
32
40
48
56
TIME (hrs.)

Fig. 8-4

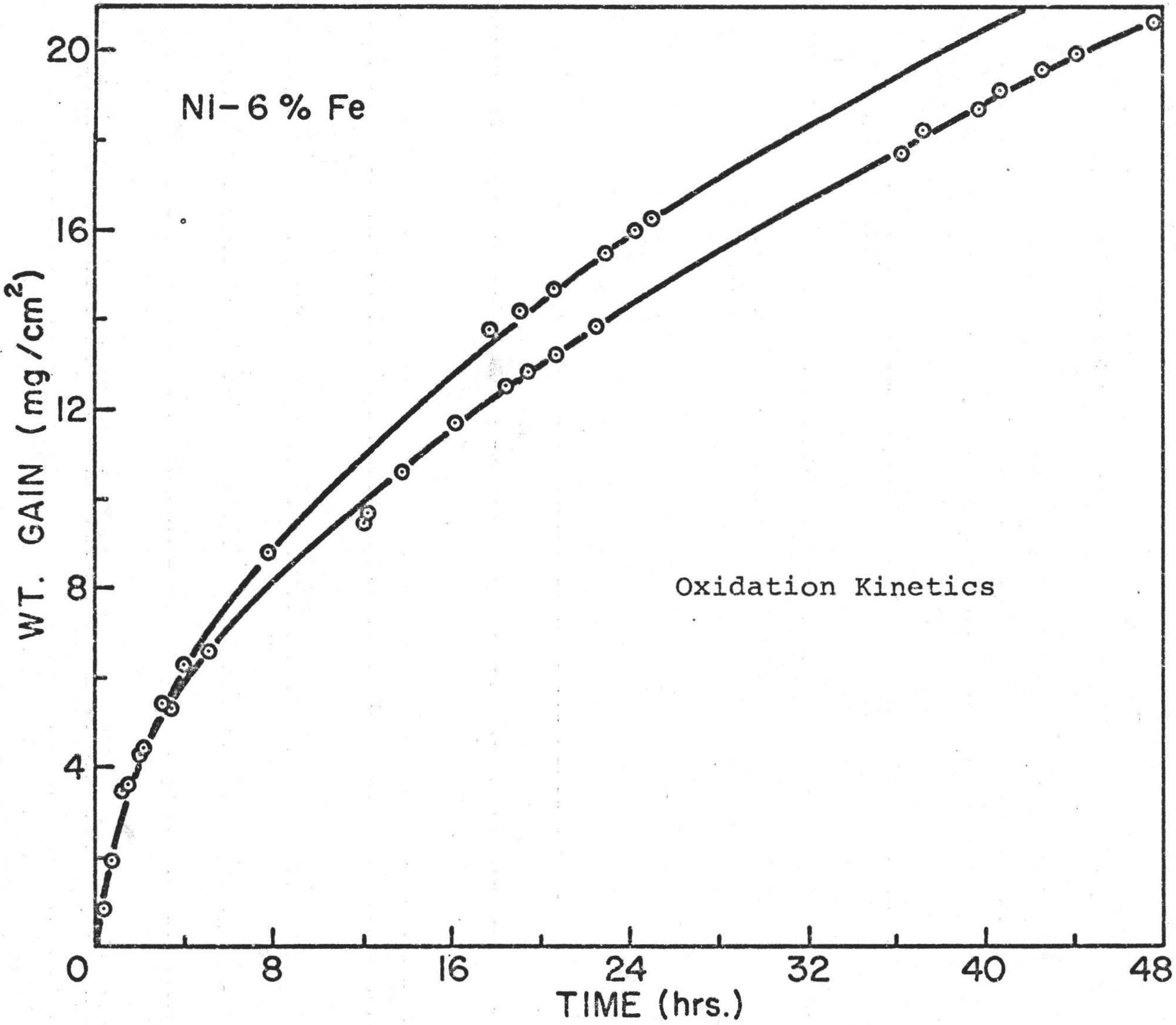
NI-6 % Fe
Oxidation Kinetics
WT. GAIN (mg/cm^2)
20
16
12
8
4
0
8
16
24
32
40
48
TIME (hrs.)

Fig. 8-5

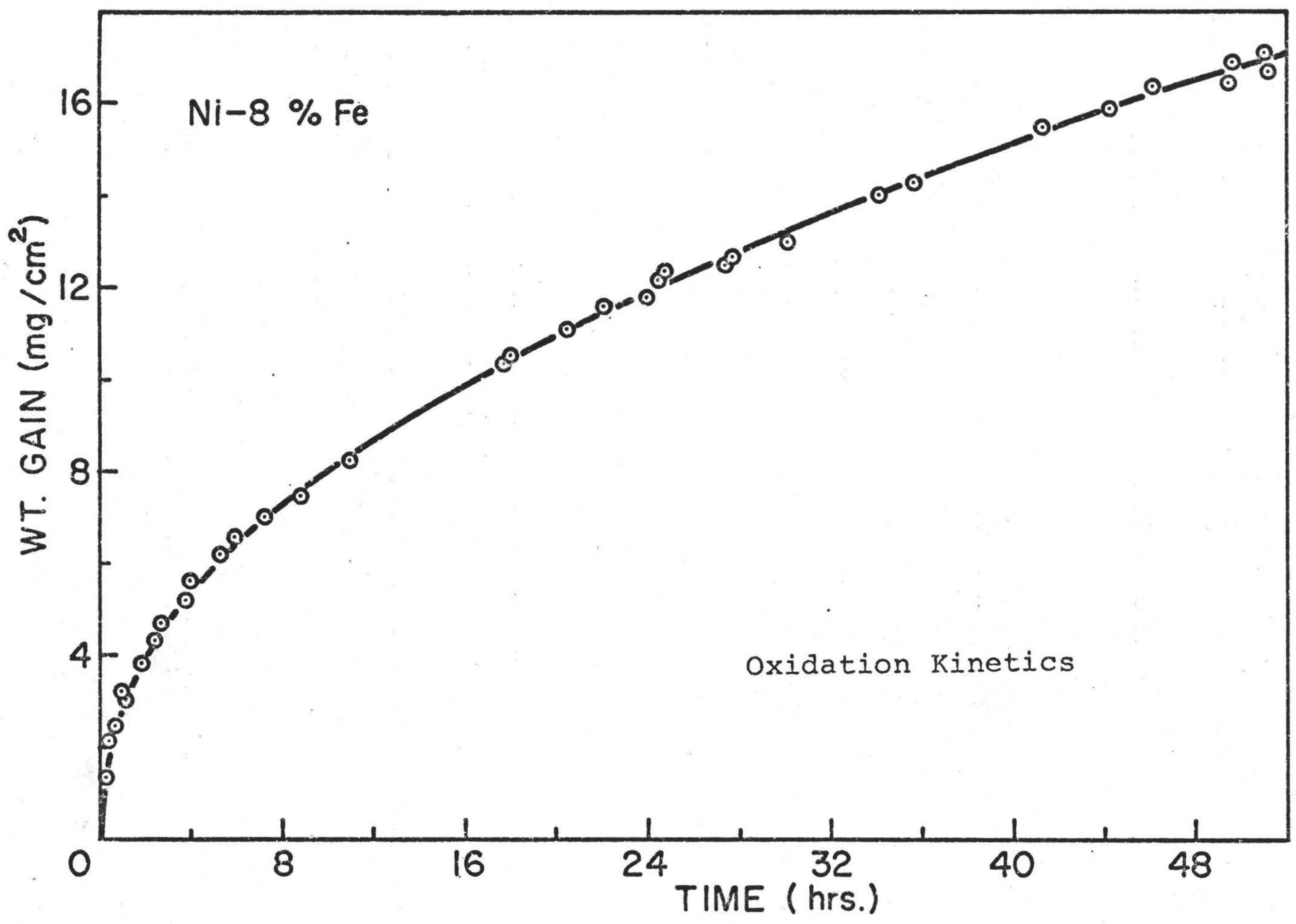
Ni-8 % Fe
Oxidation Kinetics
WT. GAIN (mg/cm²)
16
12
8
4
0
8
16
24
32
40
48
TIME (hrs.)

Fig. 8-6

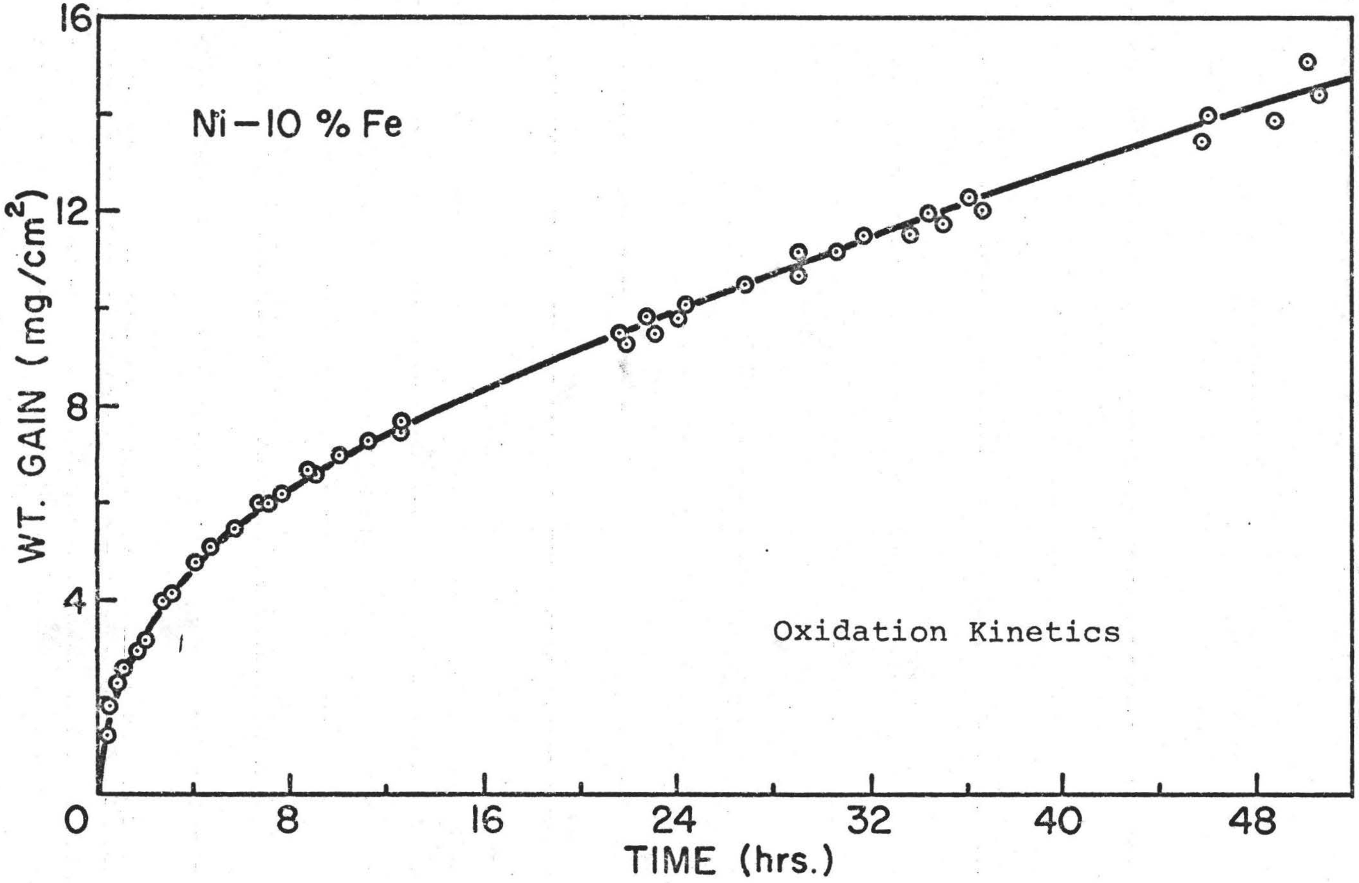
16
12
8
4
0
WT. GAIN (mg/cm^2)
Ni-10 % Fe
Oxidation Kinetics
8
16
24
32
40
48
TIME (hrs.)

Fig. 8-7

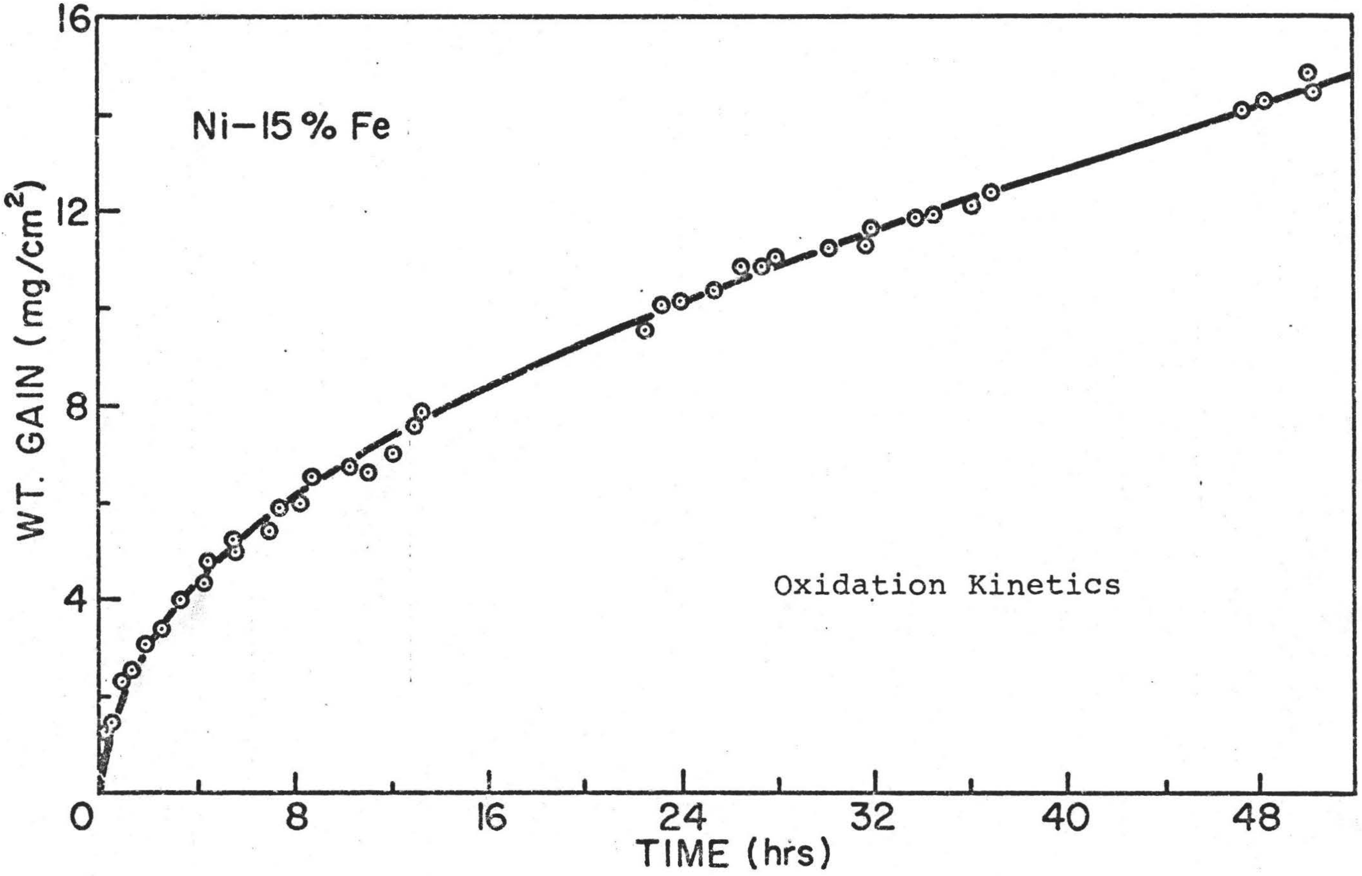
Ni-15 % Fe
Oxidation Kinetics
WT. GAIN (mg/cm²)
16
12
8
4
0
8
16
24
32
40
48
TIME (hrs)

Fig. 8-8

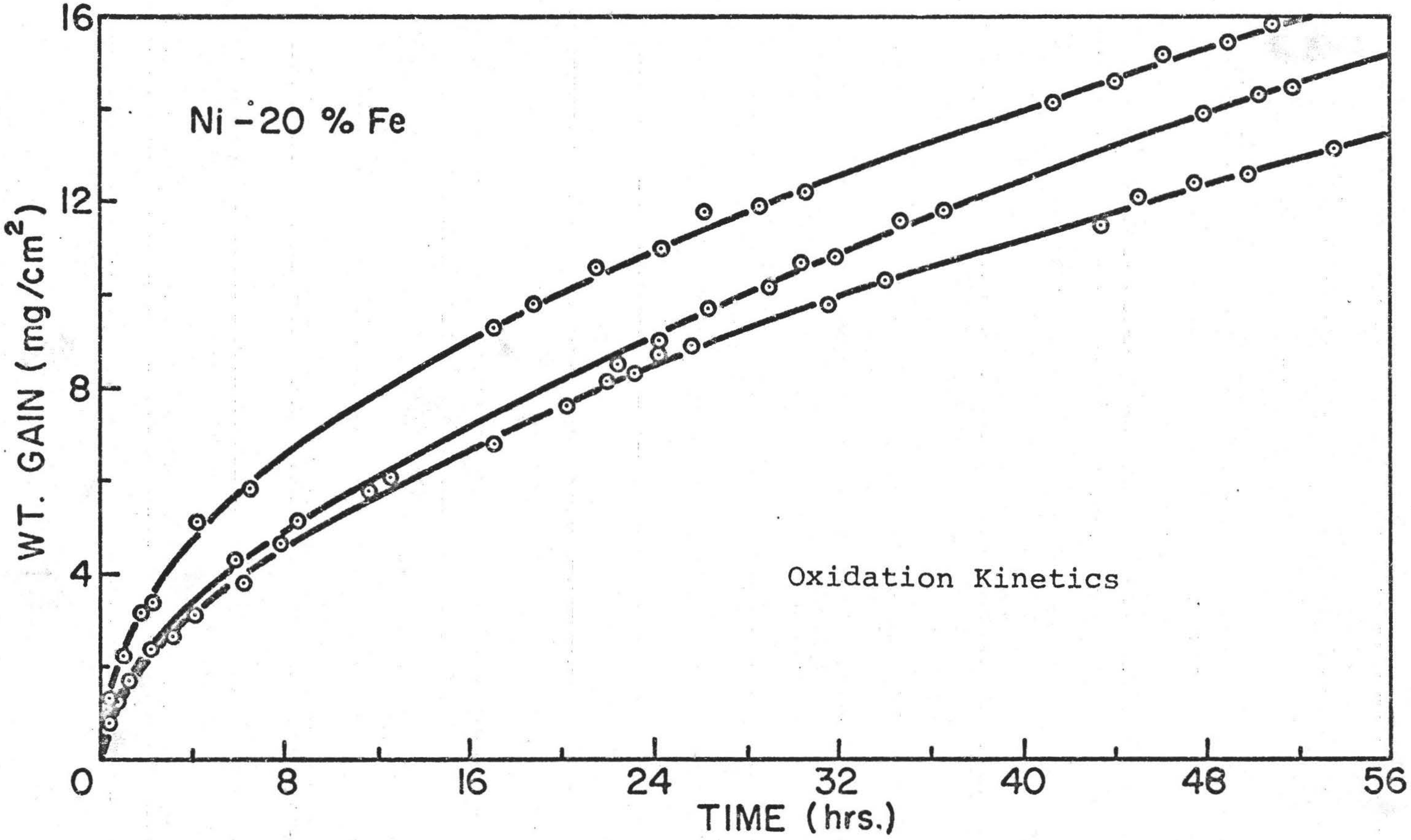
Ni - 20 % Fe
Oxidation Kinetics
WT. GAIN (mg/cm^2)
16
12
8
4
0
8
16
24
32
40
48
56
TIME (hrs.)

Fig. 8-9

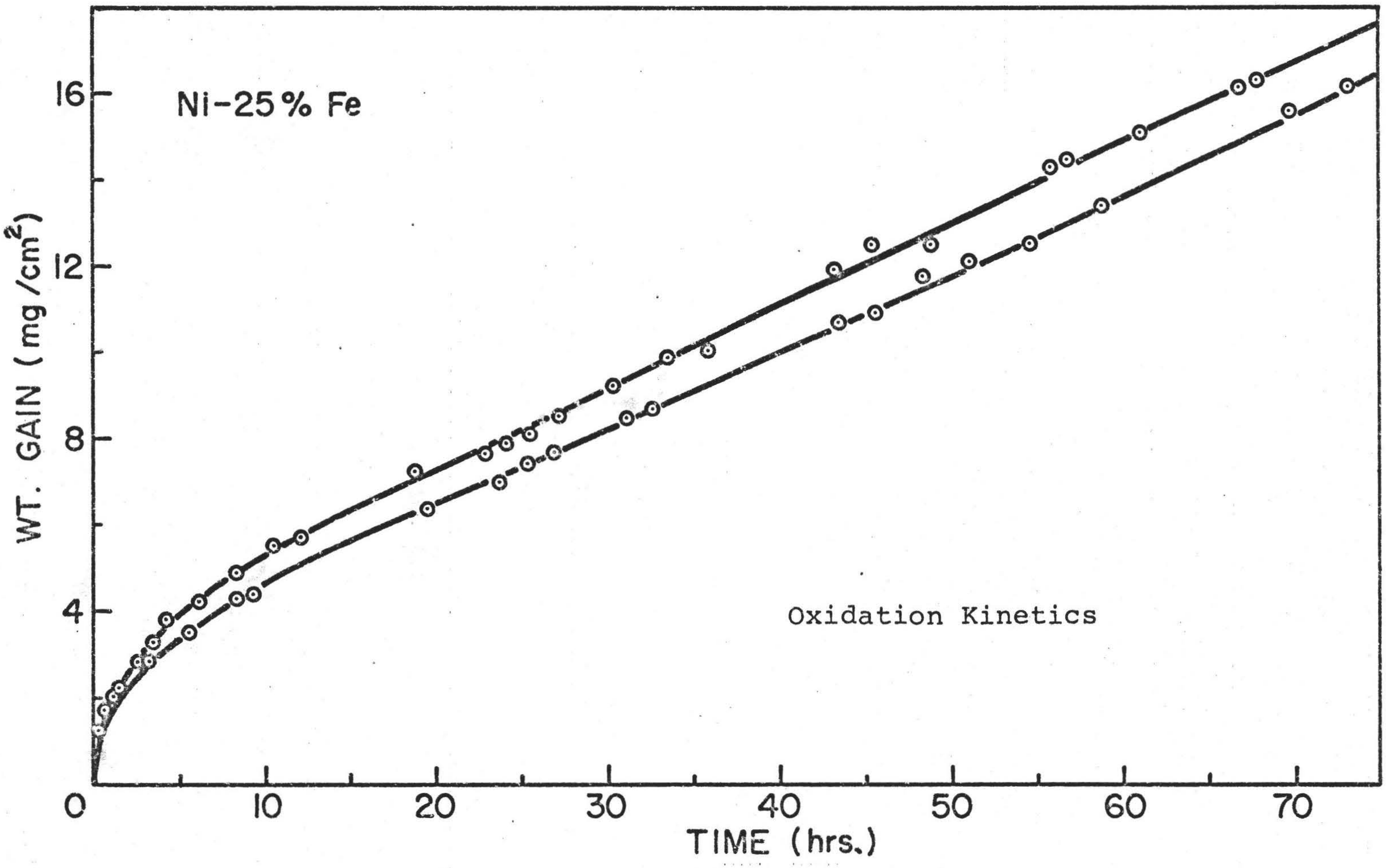
Ni-25% Fe
Oxidation Kinetics
WT. GAIN (mg/cm^2)
16
12
8
4
0
10
20
30
40
50
60
70
TIME (hrs.)

Fig. 8-10

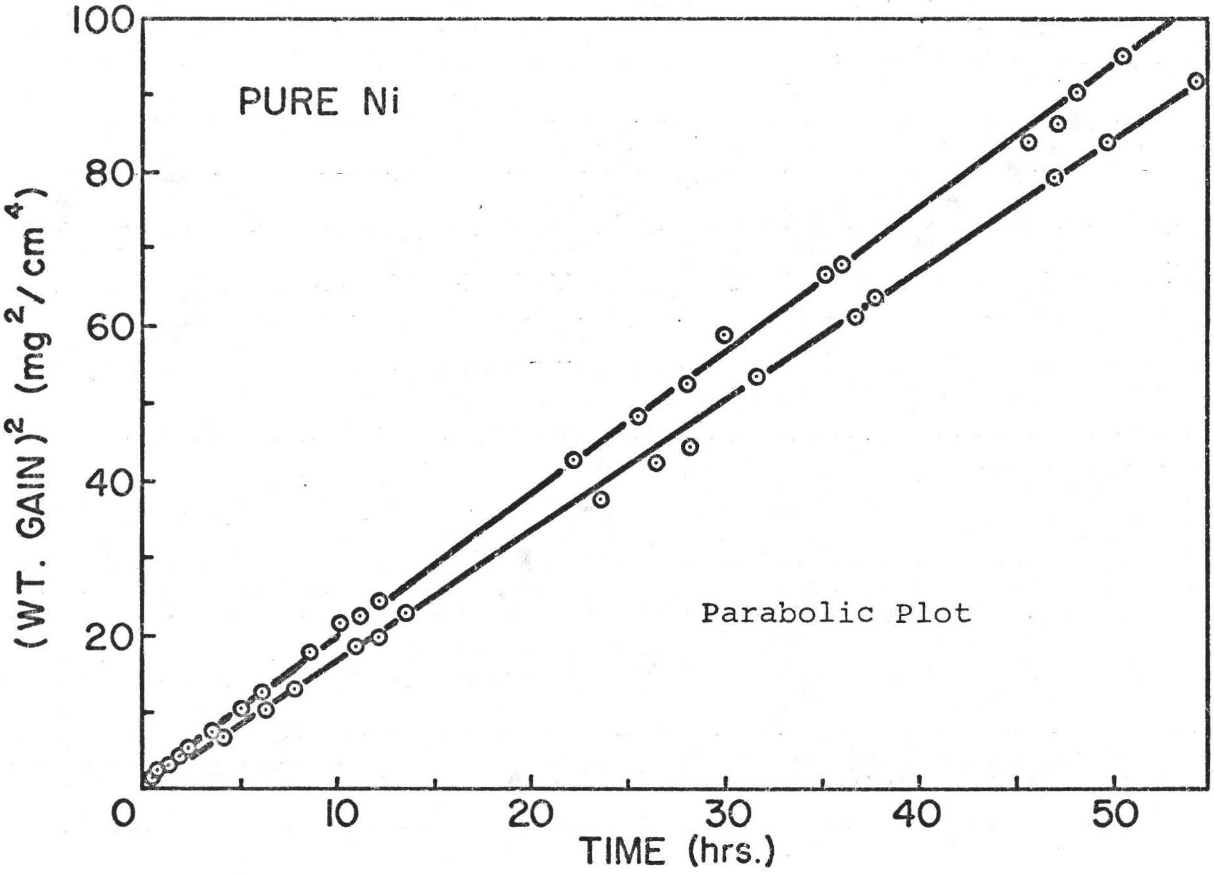

Fig. 8-11

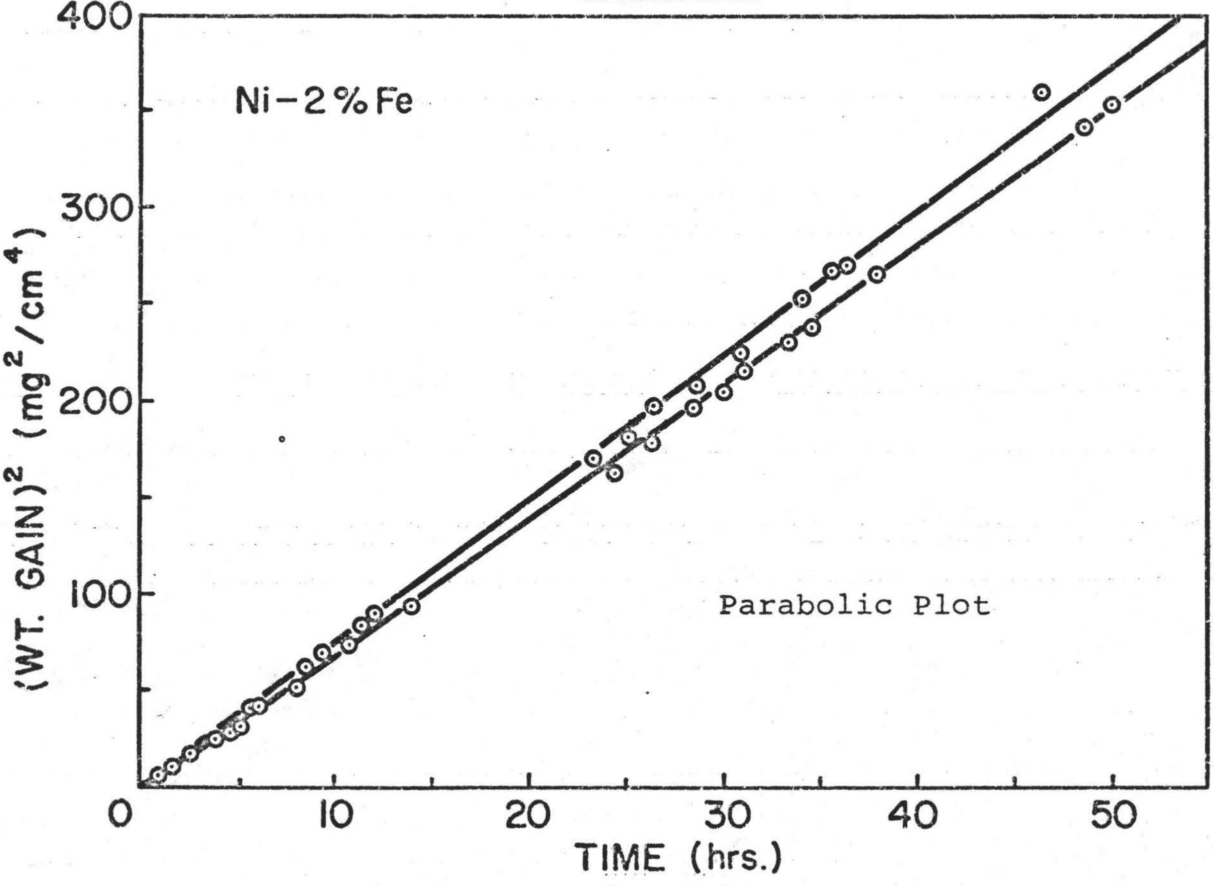

Fig. 8-12

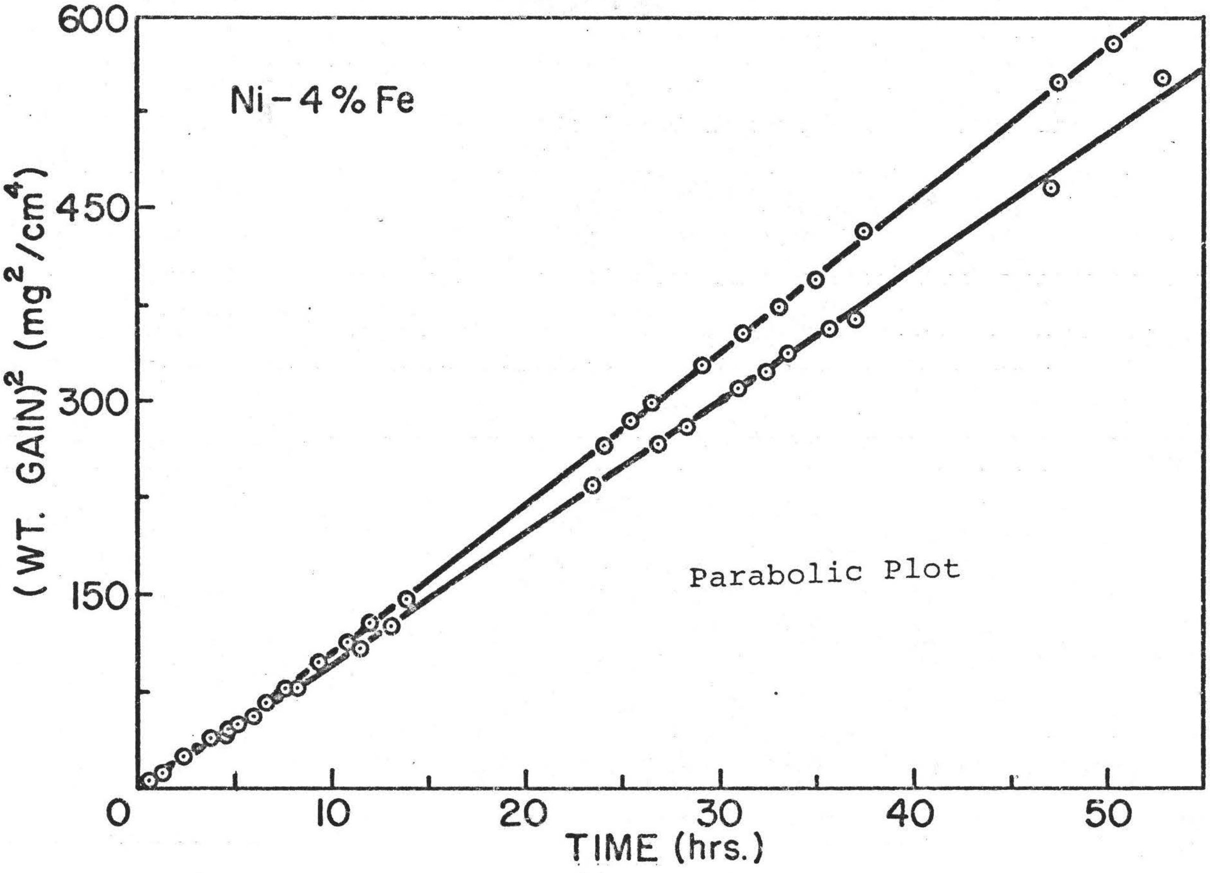

Fig. 8-13

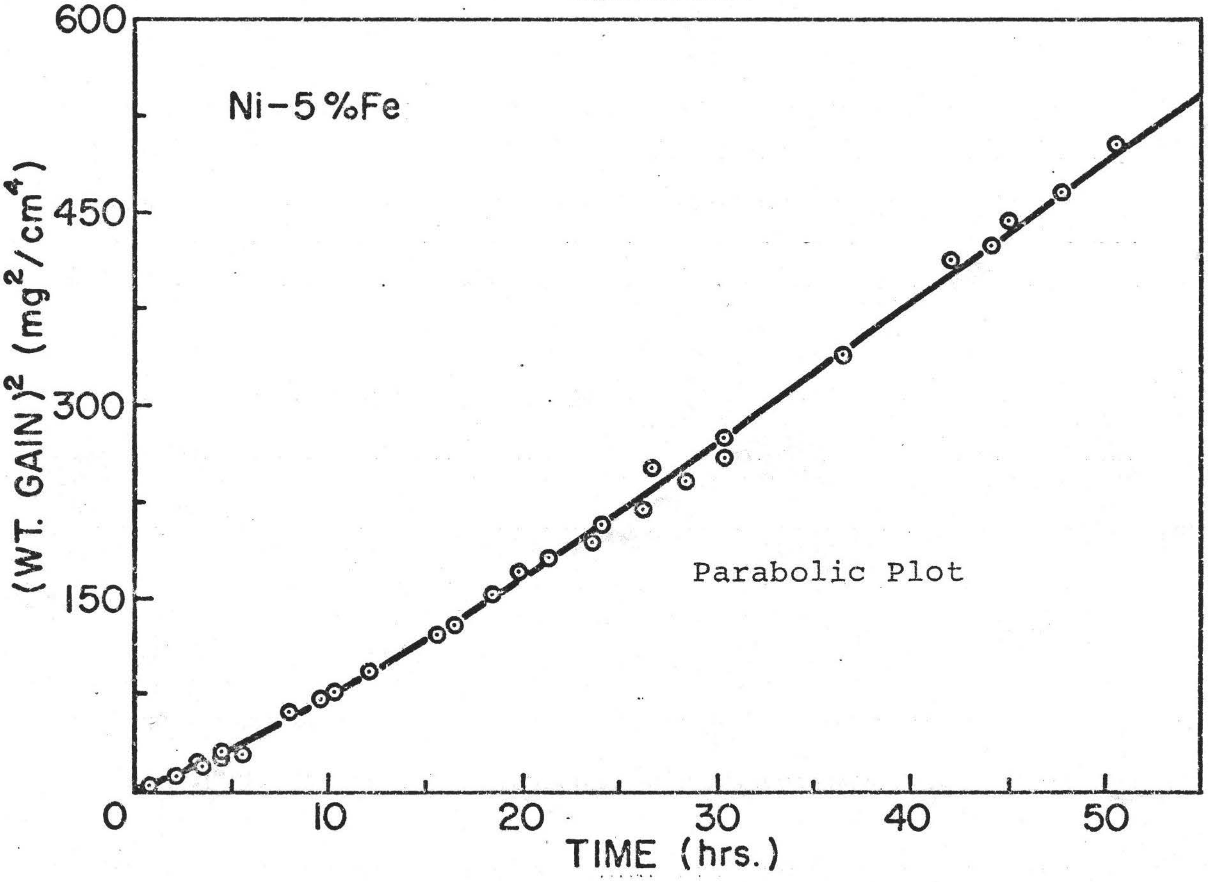

Fig. 8-14

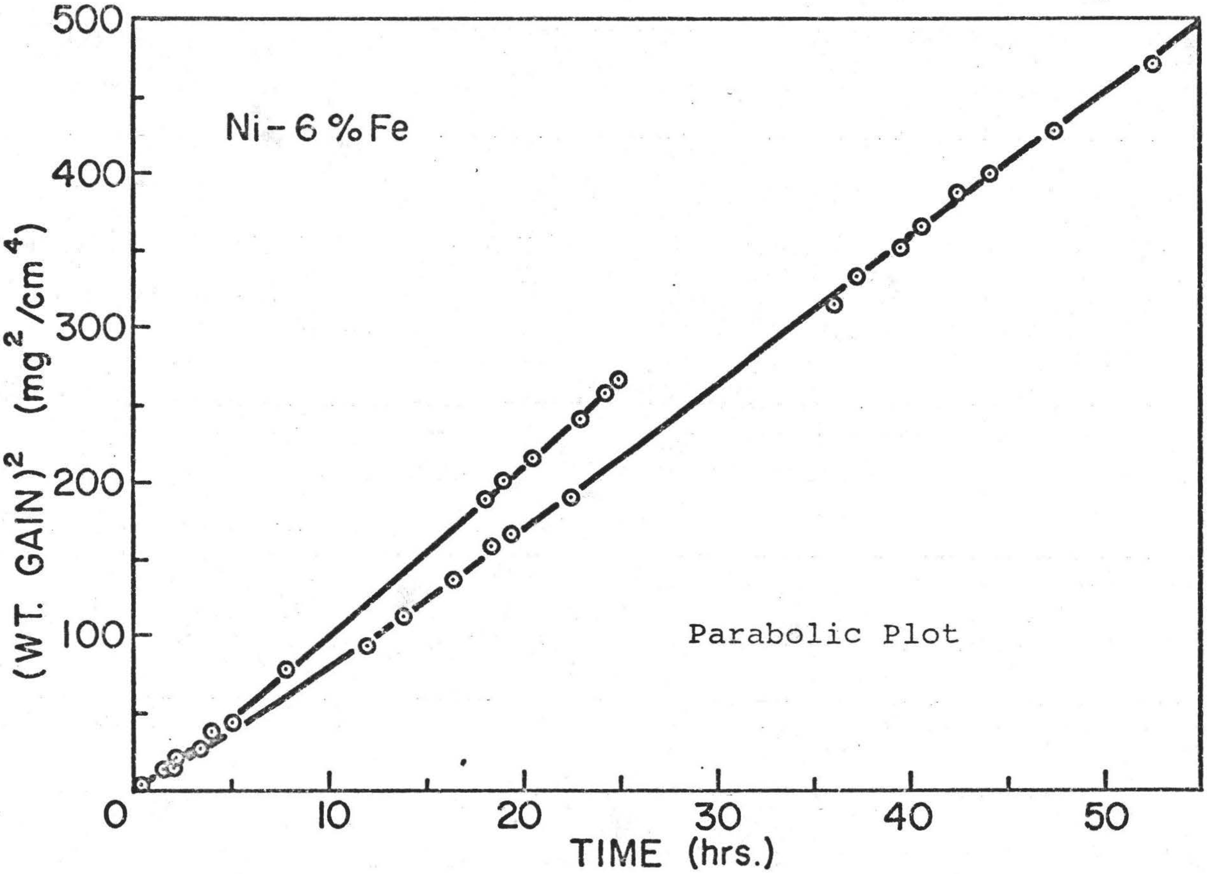

Fig. 8-15

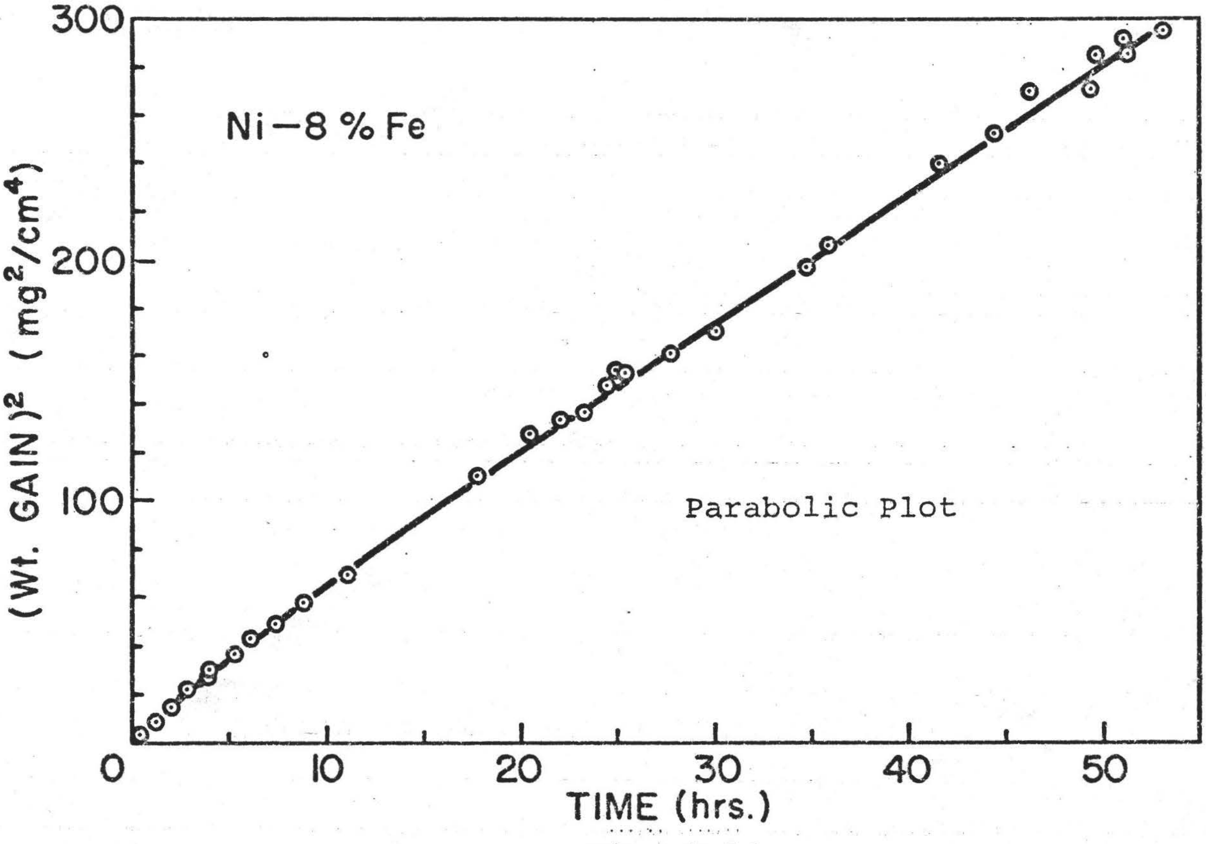

Fig. 8-16

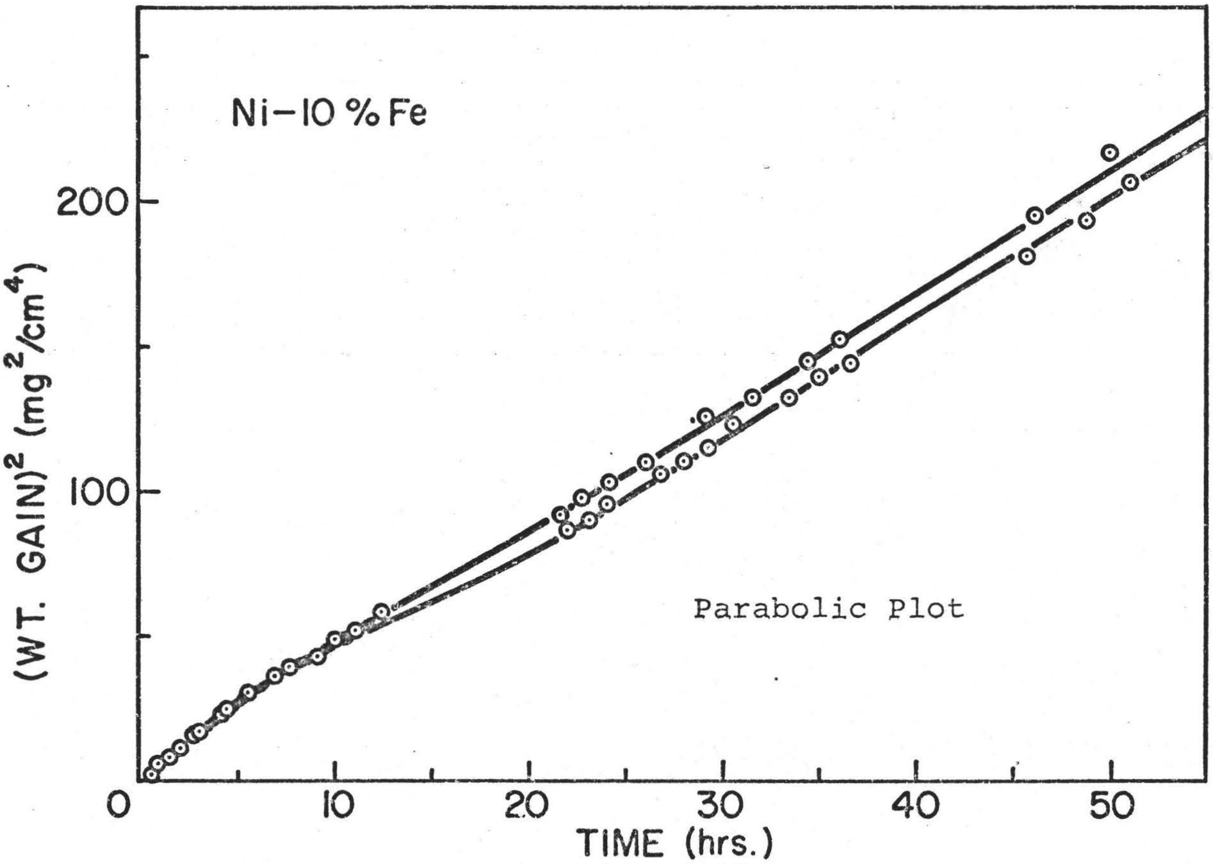

Fig. 8-17

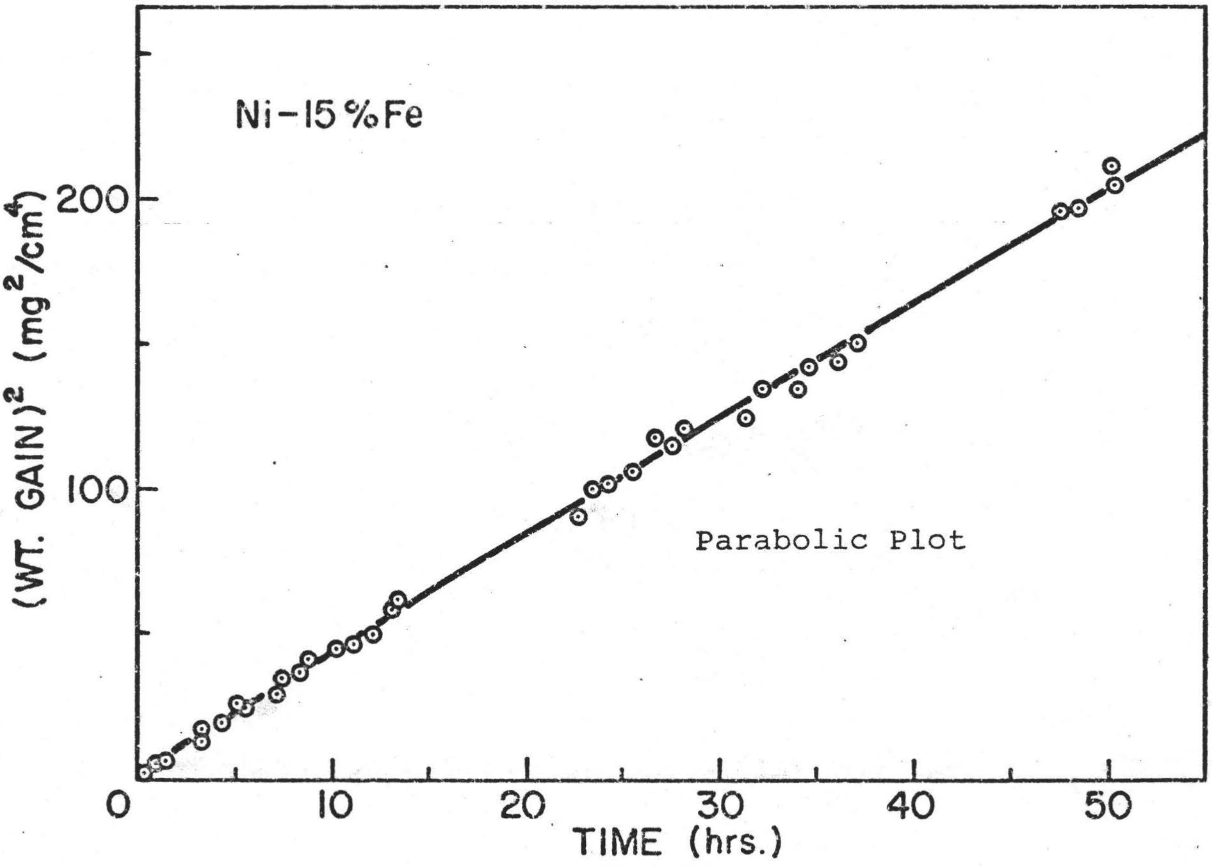

Fig. 8-18

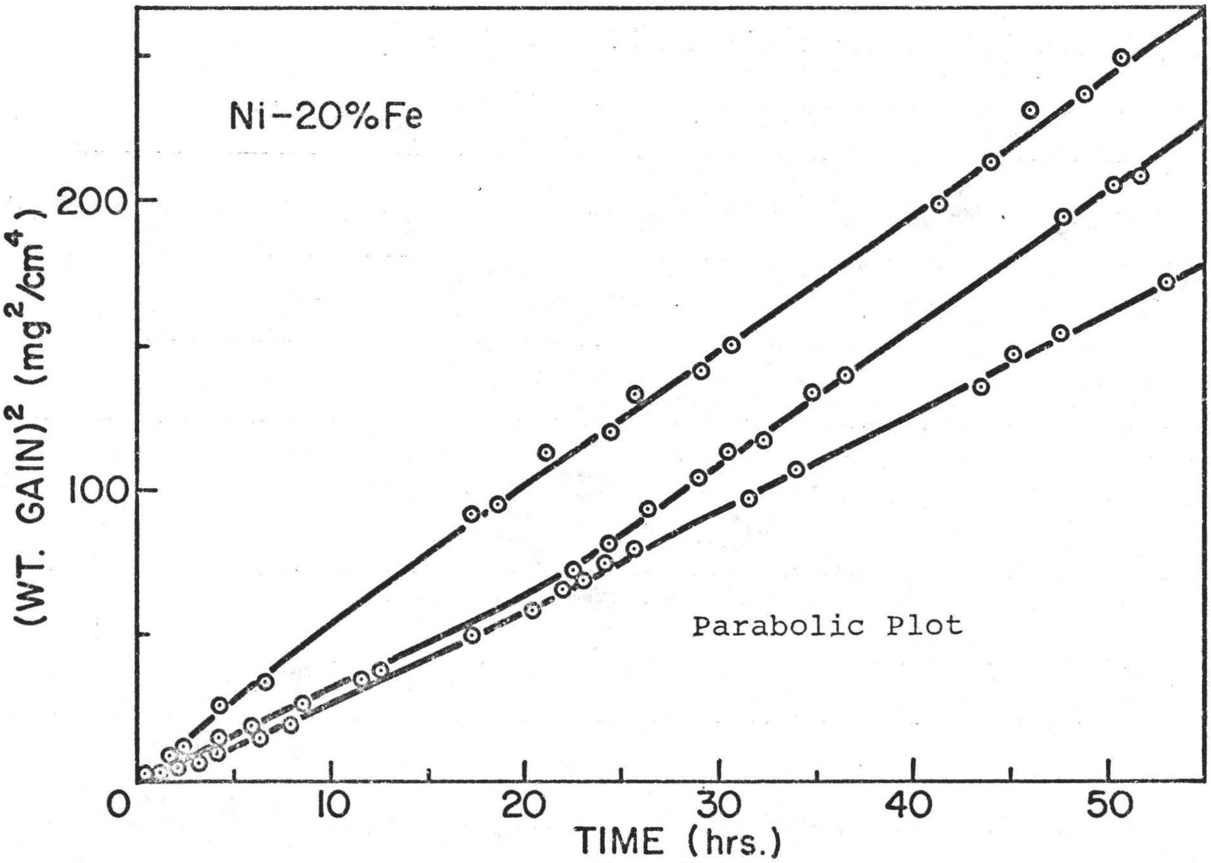

Fig. 8-19

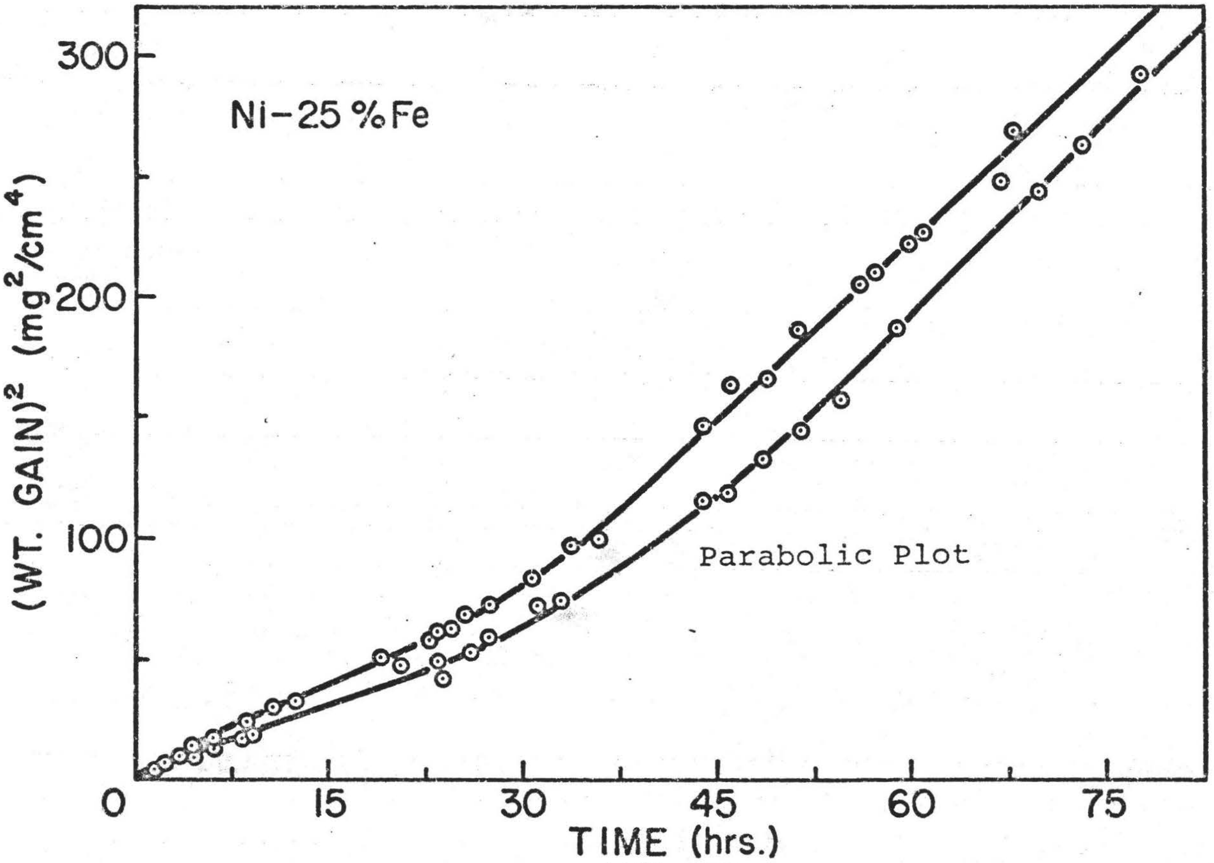

Fig. 8-20

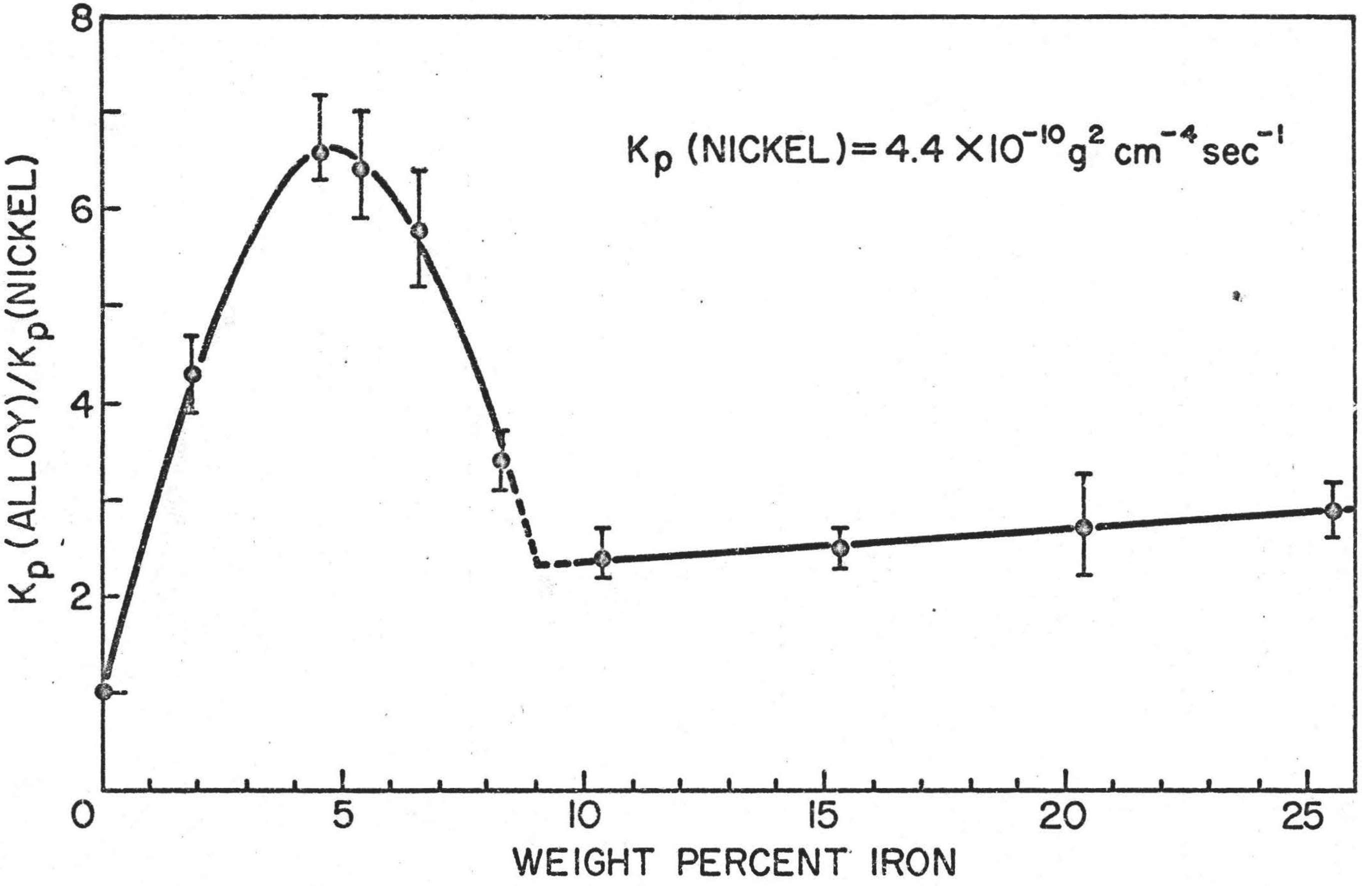

Fig. 8-21 Variation of the relative oxidation rate constant $[k_p(\text{alloy})/k_p(\text{Ni})]$ with the bulk alloy composition.

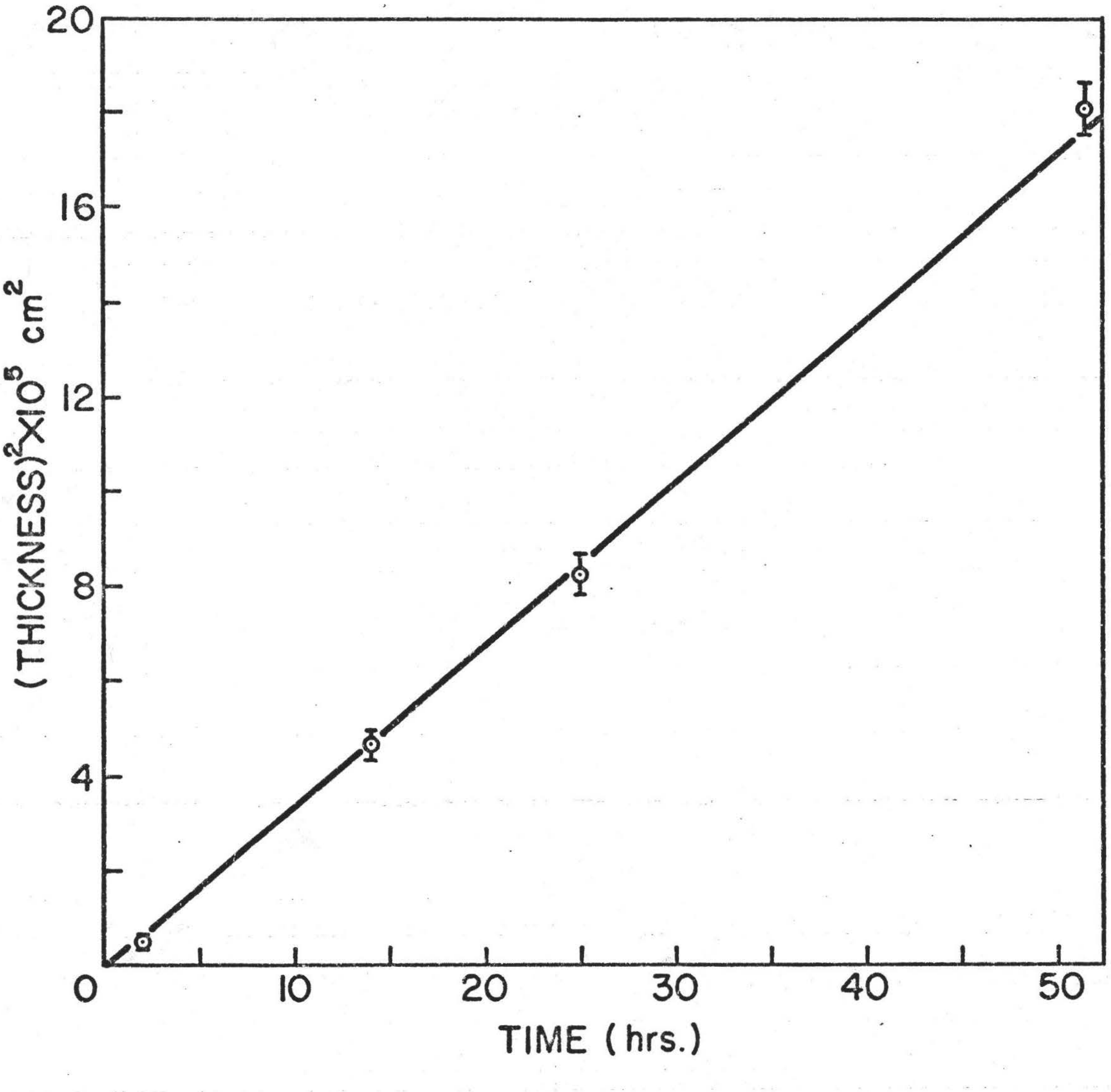

Fig. 8-22: External scale growth for Ni-2% Fe alloy.

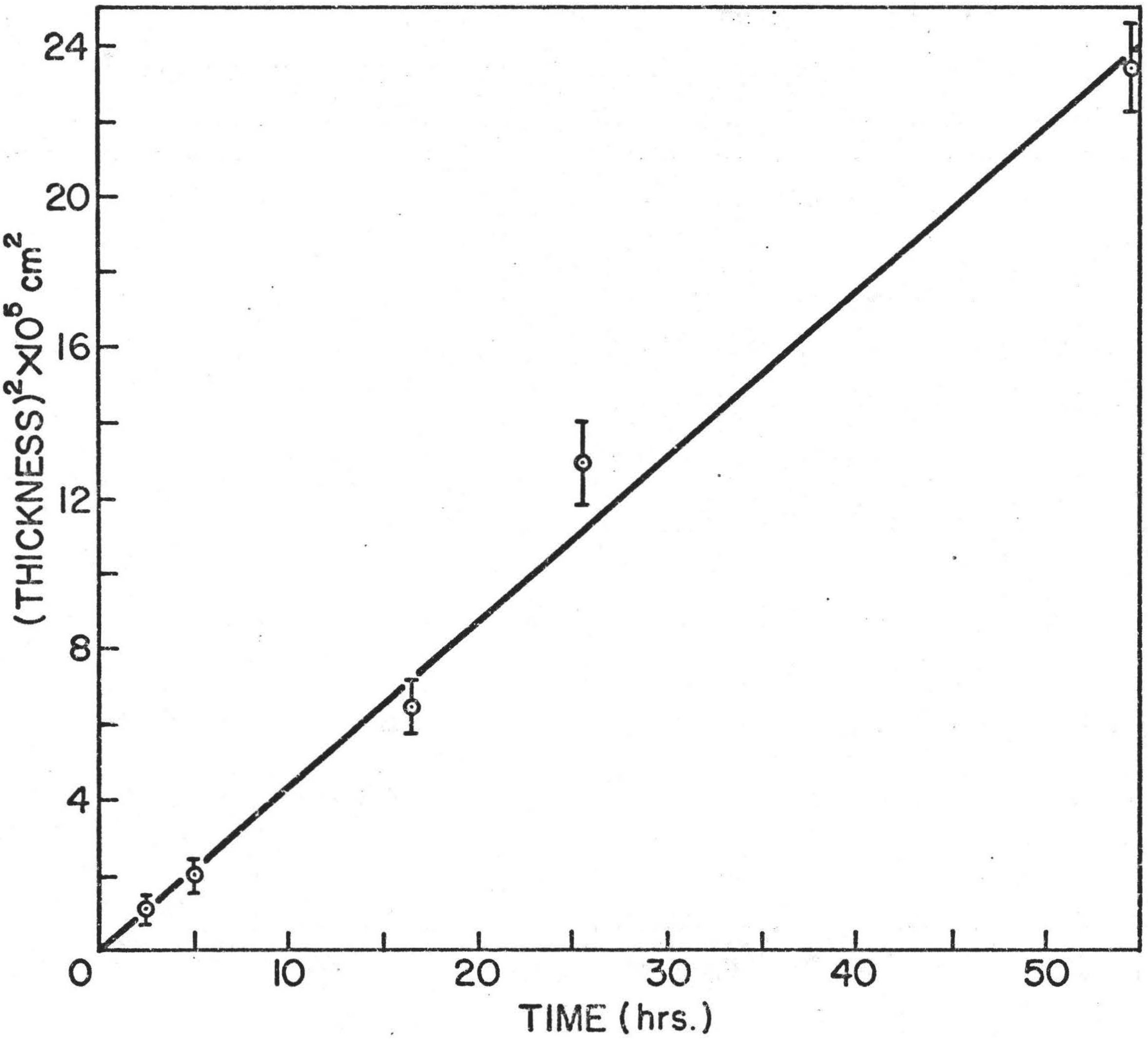

Fig. 8-23: External scale growth for Ni-4% Fe alloy.

form of weight gain of the sample, data was also obtained as rate of thickening of the external scale and the rate of penetration of the internal oxidation zone. This was obtained by metallographic examination of samples oxidized for different periods of time. The rate of scale thickening for Ni-2% Fe and Ni-4% Fe alloys is shown in Figs. 8-22 and 8-23 as parabolic plots. This yields values of scaling constant, k, (rate of thickening of the external scale), defined in Eq. 4-35 for the corresponding alloys which will be used in the diffusion analysis for the oxidation of these alloys.

8.2 INTERNAL OXIDATION

Internal oxidation occurred for all the alloys investigated. In all cases, the internal oxide was identified as nickel-containing spinel ($Ni_xFe_{3-x}O_4$), with variable nickel content. The nickel content of the spinel appears to increase from the bulk alloy towards the alloy-oxide interface. The qualitative analysis was done with the help of an electron probe microanalyser. Quantitative analysis could not be carried out due to very small particle size. The particle size varied from a fraction of a micron to 10 microns depending on such variables as bulk alloy composition, oxidation time and the position of the precipitate.

The average particle size, particle density and correspondingly, the extent of internal oxidation increased with increasing iron in the bulk alloy. A comparison of the structure of the zone of internal oxidation is made in Figs. 8-24 to 8-29, with respect to the iron content of the bulk alloy for samples oxidized for similar periods of time. The alloy grain boundaries appear to provide a preferential site for the nucleation of the spinel (199) (Fig. 8-30); however, preferential penetration along the grain boundaries was not observed (Fig. 8-31).

Fig. 8-32 shows the growth of the internal oxidation zone in a Ni-6% Fe alloy. Both the penetration and particle size increase with time. Since the solubility product for the spinel phase is comparatively high, there is no discontinuity in either the concentration or the concentration gradient at the interface between the zone of internal oxidation and the unoxidized alloy. (Section 3.3). Accordingly there is no sharp boundary defining the zone of internal oxidation. The measured penetration of the zone of internal oxidation are thus only approximate. The penetration as a function of time illustrated in Fig. 8-33, as a parabolic plot for various alloys shows that the rate of penetration of the internal oxidation zone is nearly independent of the bulk alloy composition. However, since the particle density and size vary with composition, the amount of oxygen consumed in the zone of internal oxidation is a function of the bulk alloy composition. Fig. 8-33 also illustrates that the rate of advance of the internal

Fig. 8-24: Internal oxidation in Ni-2% Fe alloy oxidized for 51.5 hours. 200×

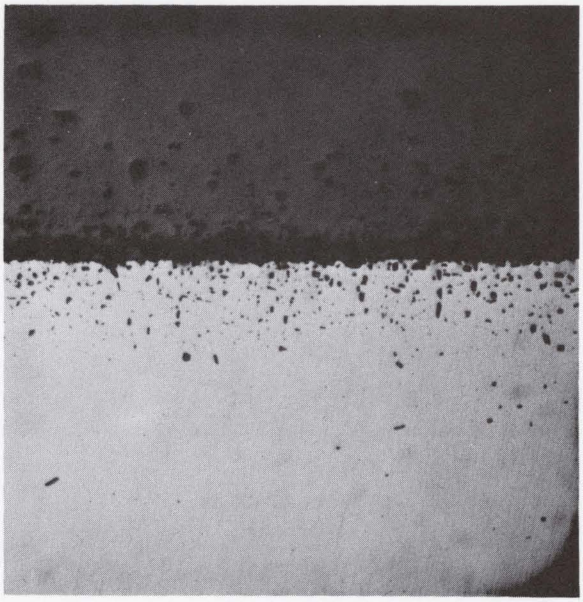

Fig. 8-25: Internal oxidation in Ni-4% Fe alloy oxidized for 50.2 hours. 200×

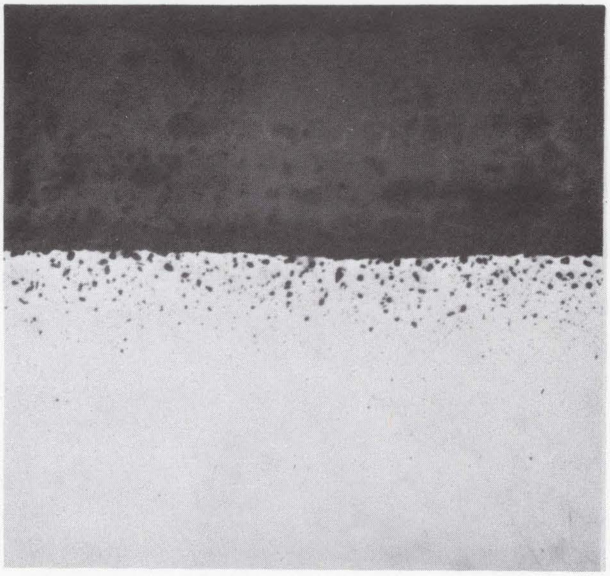

Interchange
photomicrographs
in Figs. 8-38
and 8-39.

Fig. 8-26: Internal oxidation in Ni-6% Fe alloy oxidized for 47.5 hours. 200×

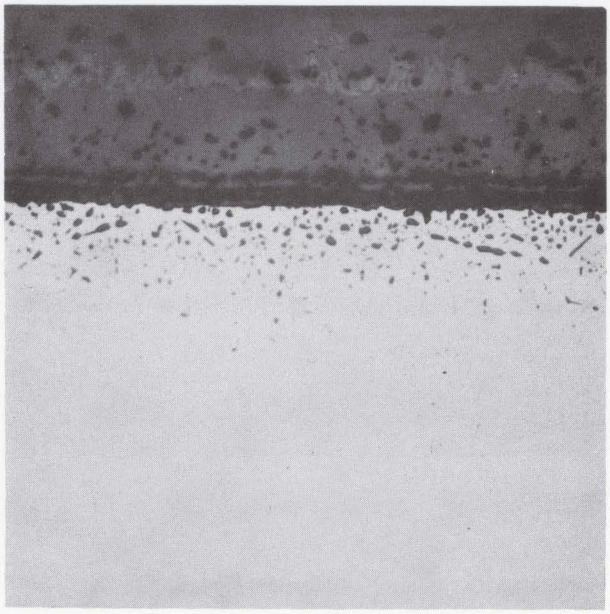

Fig. 8-27: Internal oxidation in Ni-8% Fe alloy oxidized for 48.5 hours. 200×

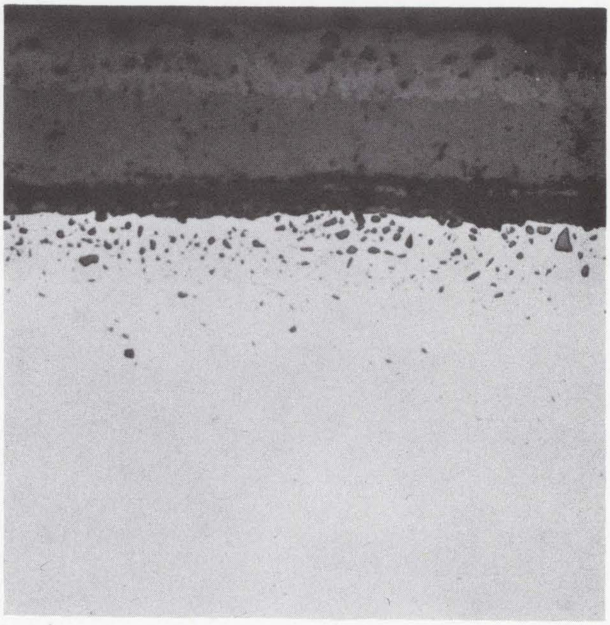

Fig. 8-28: Internal oxidation in Ni-10% Fe alloy oxidized for 50 hours. 200×

Fig.8-29: Internal oxidation in Ni-25% Fe alloy oxidized for 61 hours. 200×

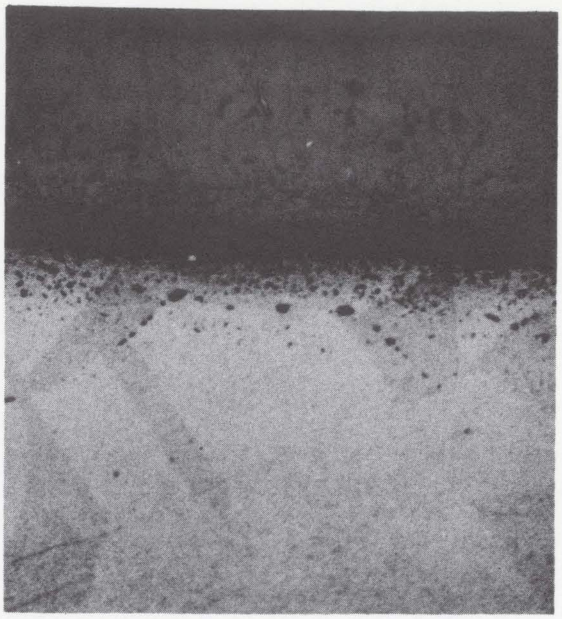

Fig. 8-30: Zone of internal oxidation. Ni-4% Fe alloy oxidized for 25.2 hours. Etched, 250×.

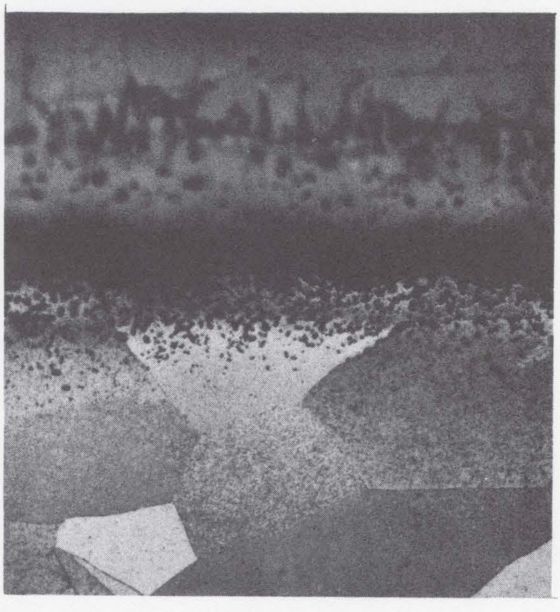

Fig. 8-31: Zone of internal oxidation. Ni-6% Fe alloy oxidized for 47.5 hours. Etched, 200×.

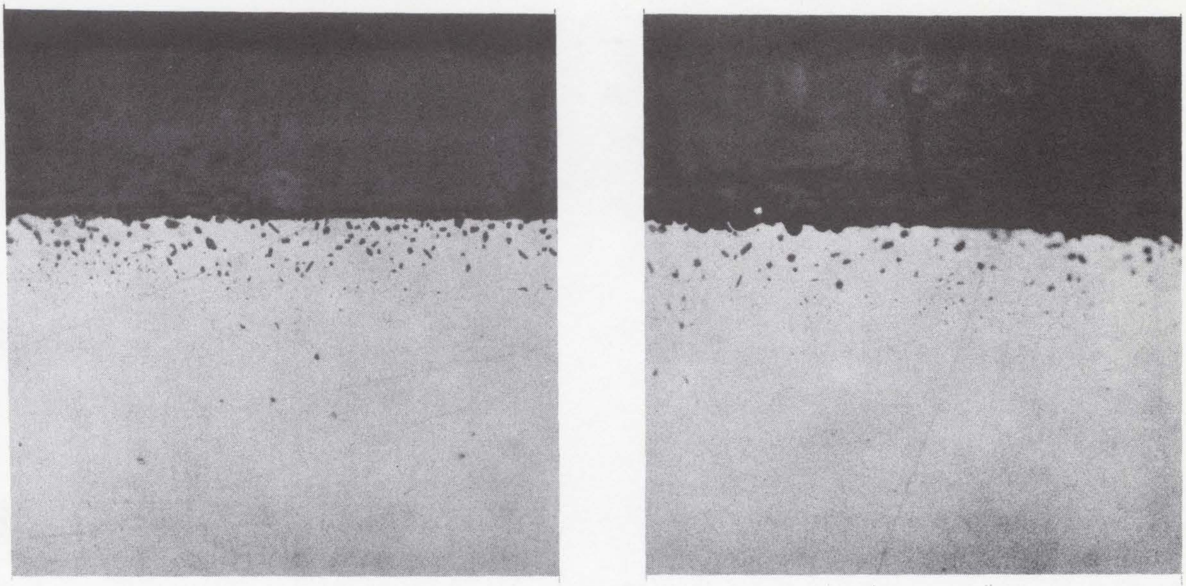

(a) oxidized for 5 hours

(b) oxidized for 12.5 hours

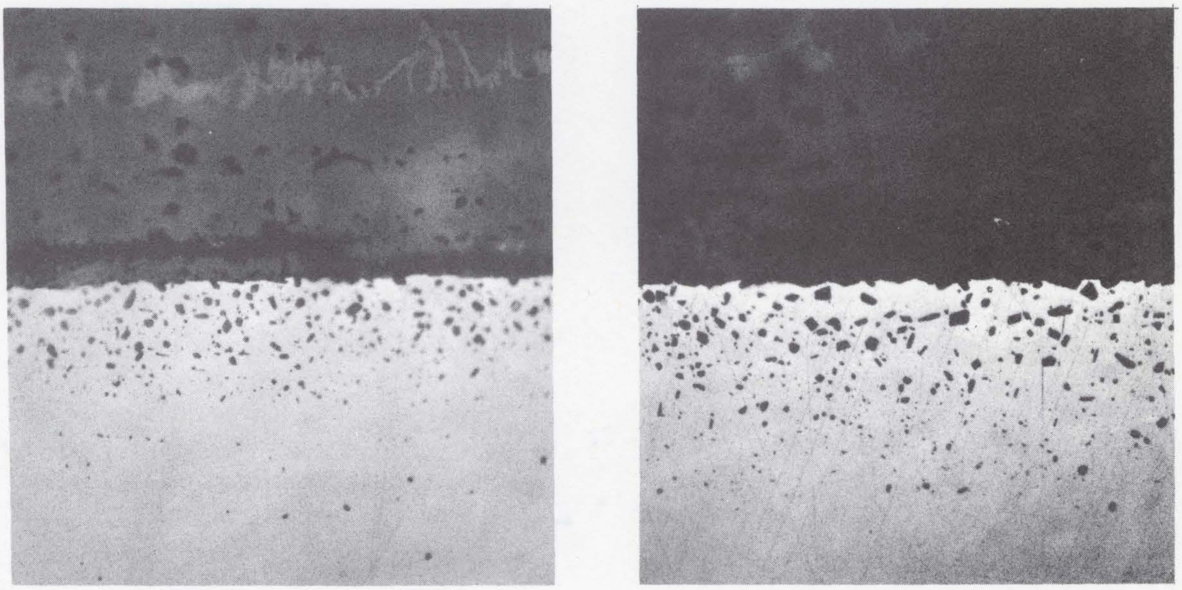

(c) oxidized for 30 hours

(d) oxidized for 47.5 hours

Fig. 8-32: Growth of internal oxidation zone in Ni-6% Fe alloy oxidized in pure oxygen at 1000°C. 400×.

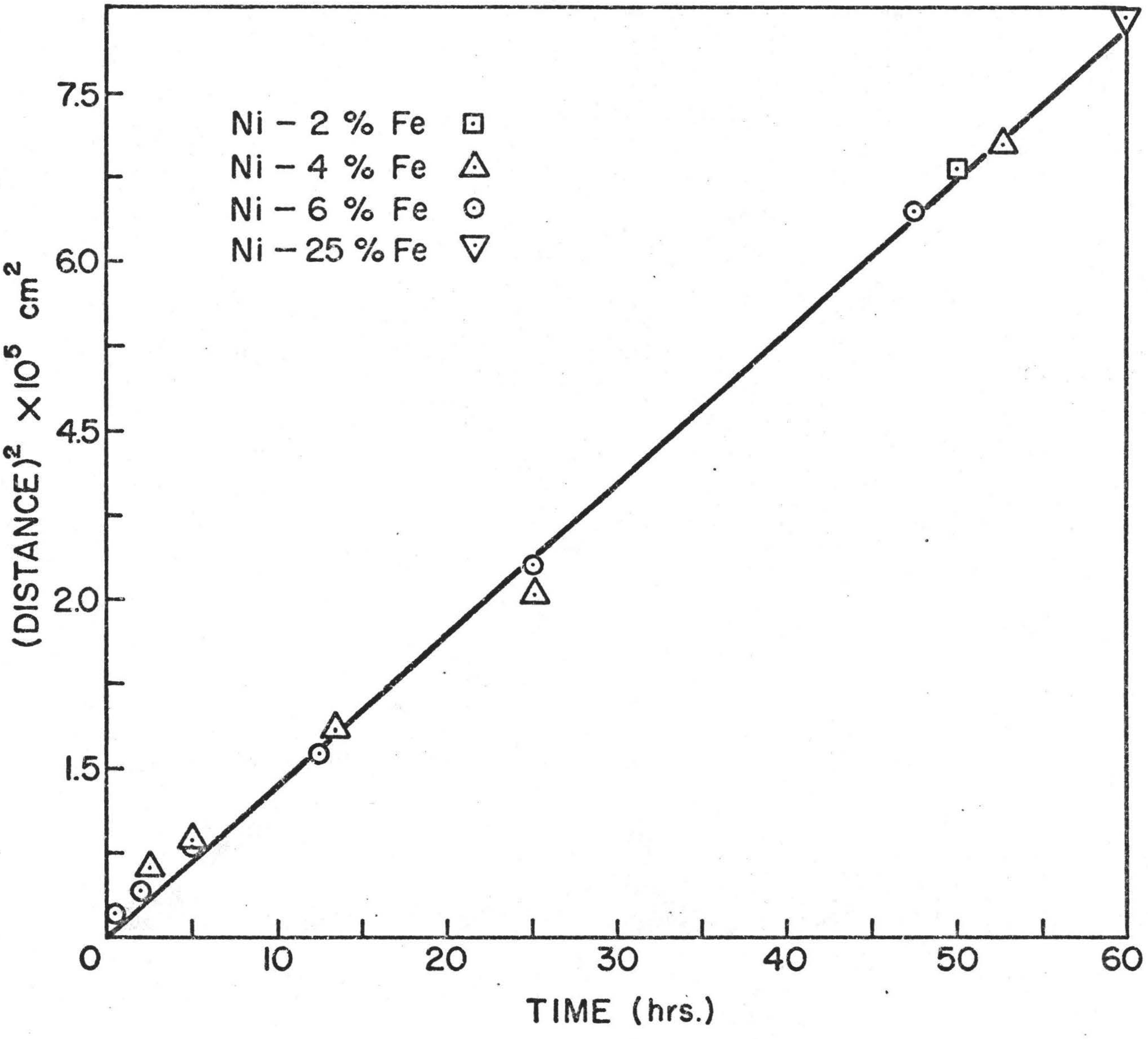

Fig. 8-33: Penetration of the zone of internal oxidation in nickel-iron alloys at 1000°C.

oxidation zone is parabolic. The rate constant for the internal oxidation zone obtained from Fig. 8-33 is $3.73\times10^{-10}\mathrm{cm}^2/\mathrm{sec}$. As noted in Section 5.3 precise parabolic growth is not expected in cases where precipitation or non-planar development occurs. Accordingly, parabolic behaviour in this case must be taken as an approximation.

8.3 PHYSICAL CHARACTERISTICS OF THE OXIDE SCALES

None of the oxidized samples showed any tendency of scale breakaway during oxidation. The scales showed excellent adherence during oxidation and smooth oxidation kinetics. However scales formed on some alloys showed a tendency to blister or spall during quenching. The NiO scale formed on pure nickel showed excellent spalling resistance. The colour of the NiO scale was black at the oxide-gas interface (oxygen rich NiO) and green at the metal-oxide interface (oxygen poor NiO).

The adhesion of the oxide scale to the alloy substrate was excellent during oxidation and after quenching , was also excellent for alloys containing upto 6% Fe. The oxide scale surface on these alloys appeared black, glazy and with an orange peel texture.

The oxide scale formed on alloys containing 8-10% Fe adhered to the alloy substrate fairly well after quenching to room temperature, lifting up only in places. The surface had a mixed texture, i.e., part of the surface appeared dull and part of it shiny. The colour of the oxide was black on the outer surface.

The scales on Ni-10% Fe and Ni-15% Fe alloys showed a tendency to blister and spall upon quenching. The scales on Ni-20% Fe alloy were comparatively adherent after quenching though it showed a tendency to blister. The oxide scale on Ni-25% Fe alloy showed good adherence and spalling resistance. The oxide scale on Ni-10,15, 20 and 25% Fe alloys was black in appearance. The scale on Ni-25% Fe alloy showed a pronounced orange peel effect on the outer surface. The oxide scale showed a greenish colour at the alloy-oxide interface in all cases.

The thermal shock resistance of the oxide scale depended on the time of oxidation for a given alloy. Thus for Ni-2% alloy, oxide scale on sample oxidized for 2 hours spalled completely upon quenching, a sample oxidized for 12 hours showed tendency to blister, whereas a sample oxidized for 50 hours showed excellent adherence even after quenching.

The oxide scales formed on alloys containing up to 6% Fe were relatively compact. Porosity was observed mainly at the scale-alloy interface. Porosity was estimated to be about 2% for Ni-2% Fe alloy, increasing with increasing iron content of the bulk alloy. The oxide scale near the alloy-oxide interface appeared to be porous in the case of alloys containing 8 to 25% Fe.

8.4 SURFACE TOPOGRAPHY AND CRYSTALLOGRAPHIC ORIENTATION OF THE OXIDE SCALES

A series of micrographs of the surface topography of scales formed on Ni-5% Fe alloy at various stages of oxidation are shown in Figs. 8-34 to 8-37. These figures show the process of nucleation and growth of oxide crystallites during the early stages of oxidation. Features illustrated in Fig. 8-34 indicate that the grain boundaries and the defect sites on the alloy substrate act as preferential nucleation sites. The small crystallites initially formed tend to bunch coalesce and grow, forming bigger grains with a terraced structure (Figs. 8-35 to 8-37). The terraced structure appears to have formed during the process of growth. The preferred orientation as indicated by x-ray diffraction measurements is such that <110> directions are parallel to the surface of the oxide. The surface orientations investigated by x-ray diffraction measurements for a Ni-10% Fe alloy oxidized for 50 hrs. is shown in Table 8-2. The terraced and ledged structure on a surface spot on the same alloy is shown in Fig. 8-38. The angle between the ledge directions in this micrograph is 60° indicating that they are <110> directions. Although this structure is atypical of oxide layers formed on this alloy it is shown to illustrate the oxide growth morphology on a microscopic scale. The ledge structure is more typical of fast growing scales such as those found in Ni-5% Fe alloy, as illustrated in Fig. 8-39.

The oxide grain structure at the alloy-oxide interface was observed with the help of electron microscope, as illustrated in Fig. 8-40. using a carbon replica. The oxide grains are thus small and equiaxed at the alloy oxide interface.

It may be concluded from the above observations that the oxide growth occurs at the scale-gas interface by stacking of the respective ions against the ledges to form close-packed {111} planes at the outer surface.

During the initial stages, the oxide orientation and growth rates depended on the orientation of the alloy grains as illustrated in Fig. 8-41. However these differences smoothed out at long times. A striking correlation between the surface topography and the oxidation rate constant was obtained as illustrated in Figs. 8-42 to 8-47. Thus for slow growing nickel oxide on pure nickel the surface structure was smooth without any visible terraces and ledges (Fig. 8-41). As the oxidation rate increased with increasing iron content the terrace and ledge structure becomes more pronounced until it is most pronounced for fastest growing oxide on Ni-5% Fe alloy (Figs. 8-40 and 8-41). As the oxidation rate decreased with further additions of Fe to the bulk alloy the ledge structure becomes less pronounced. (Figs. 8-41 to 8-46). For slow growing nickel oxide on high iron alloys the surface is devoid of ledges as in the case of pure nickel (Figs. 8-42 and 8-47). The oxide seen at the outer surface

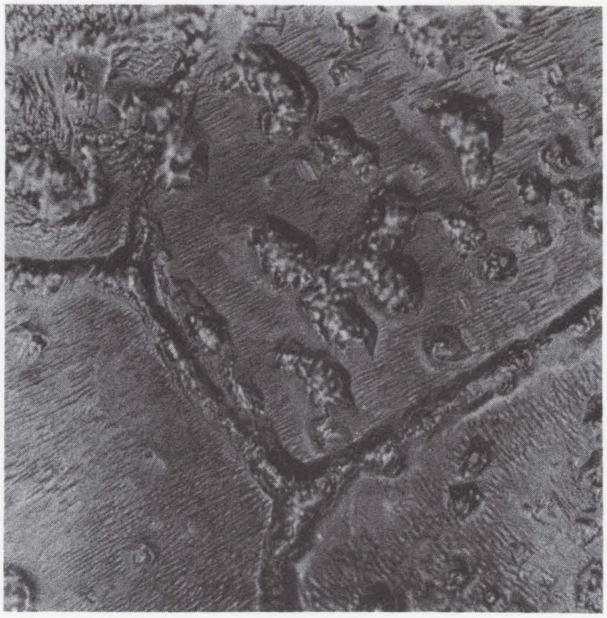

Fig. 8-34: Oxide surface topography: Grain boundary nucleation. Ni-5% Fe alloy oxidized for 25 minutes. 400×.

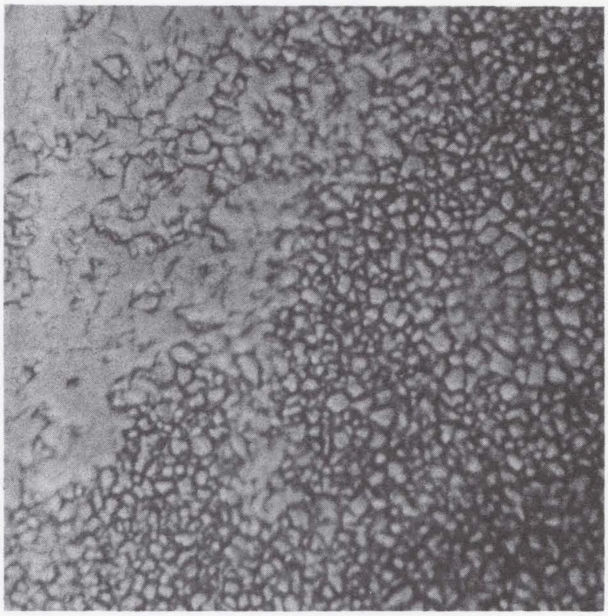

Fig. 8-35: Oxide surface topography: Clustering of crystallites and coalescence by surface diffusion. Ni-5% Fe alloy, oxidized for 60 minutes. 400×.

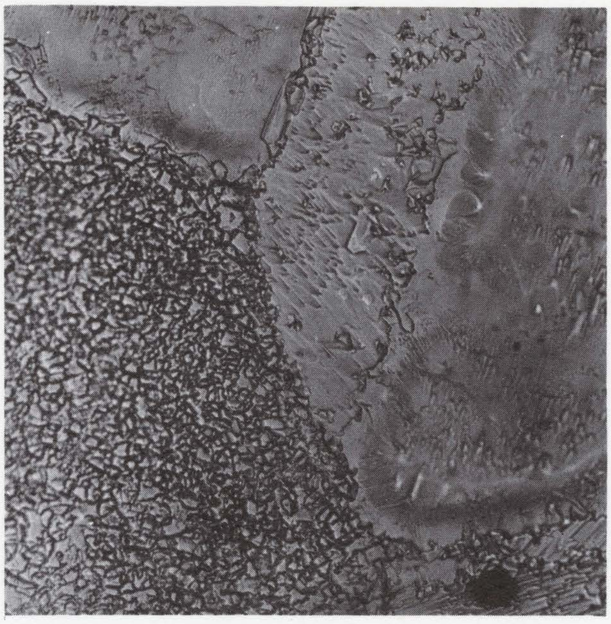

Fig. 8-36: Oxide surface topography: Formation of large grains and terraced structure. Ni-5% Fe alloy oxidized for 60 minutes. 400×.

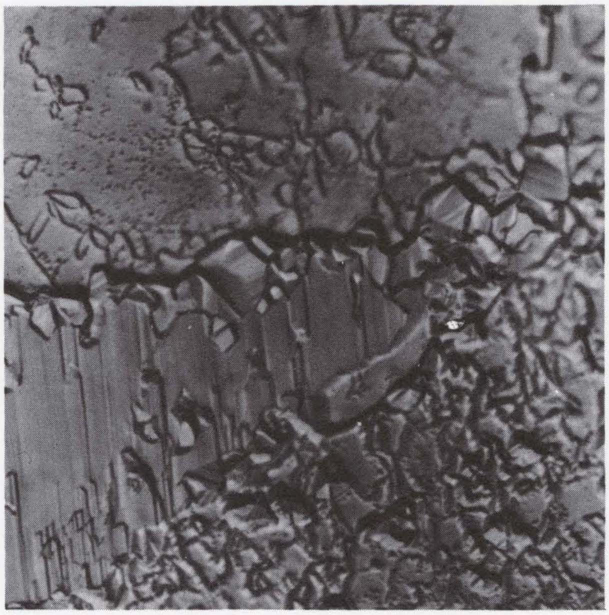

Fig.8-37: Oxide surface topography: Surface diffusion. Ni-5% Fe alloy oxidized for 60 minutes. 800×.

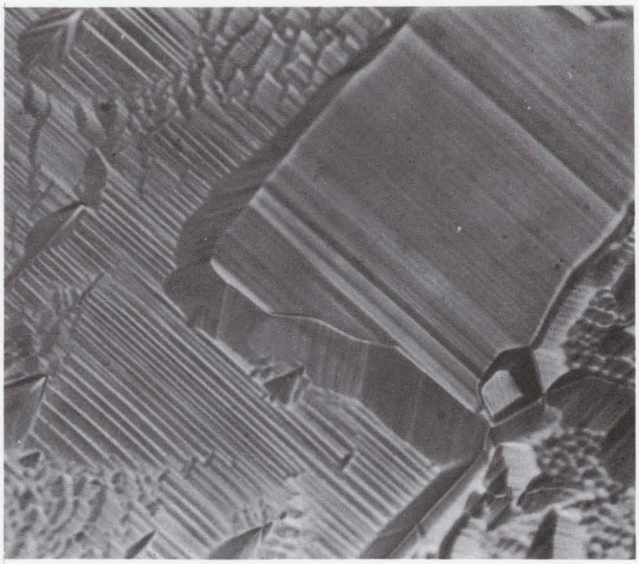

Interchange
photomicrographs
in Figs. 8-38
and 8-39

Fig. 8-38: Preferred orientation on oxide surface. Ni-10% Fe alloy oxidized for 50 hours. 400×.

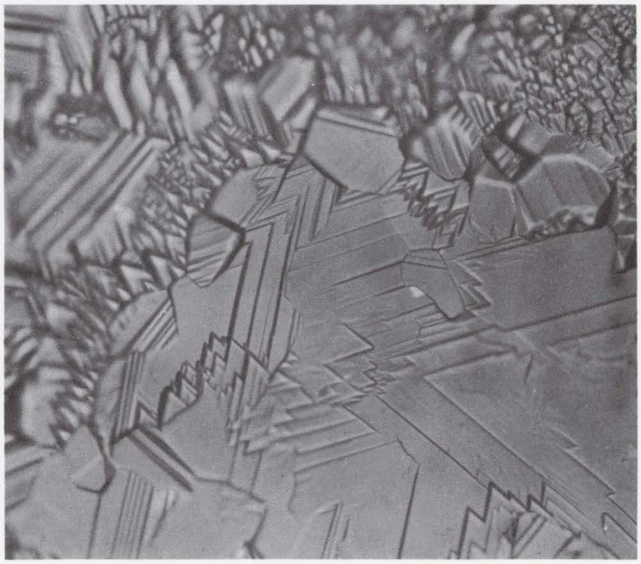

Fig. 8-39: Terraced structure of the surface oxide. Ni-5% Fe alloy oxidized for 18.5 hours. 2000×

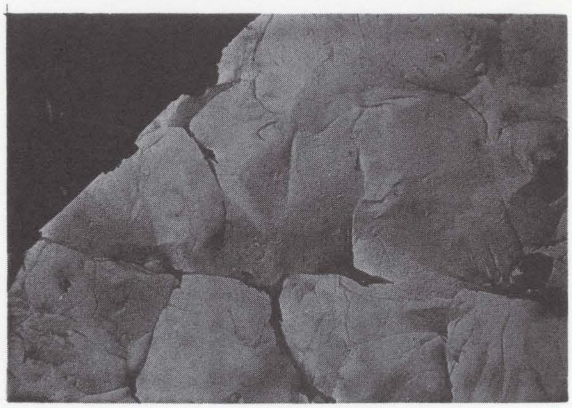

Fig. 8-40: Oxide alloy interface Ni-5% Fe alloy oxidized for 18.5 hours. Electron micrograph of replica. 10000×

Fig. 8-41: **Oxide surface** topography at low magnification. Ni-5% Fe alloy oxidized for 1 hour. 80×

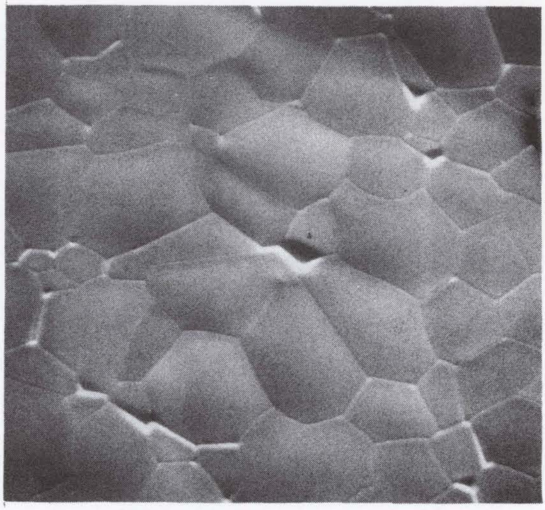

Fig. 8-42: Pure Ni oxidation for 50.5 hours. Scanning electron image of oxide surface. 840×.

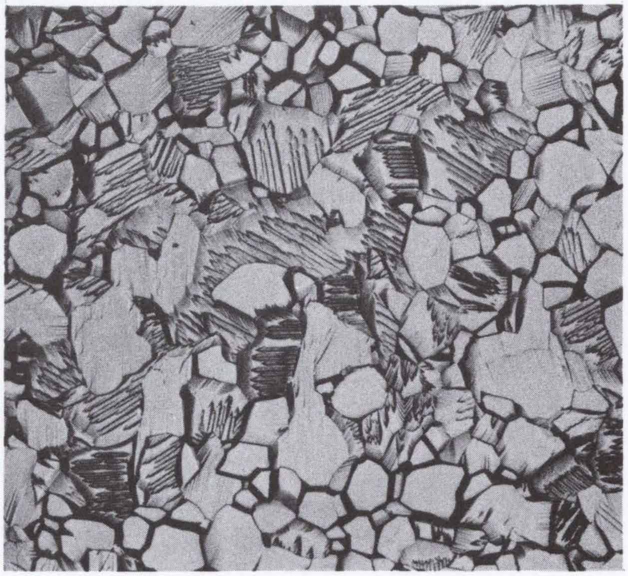

Fig. 8-43: Oxide surface topography of Ni-2% Fe alloy oxidized for 14.1 hours. 160×.

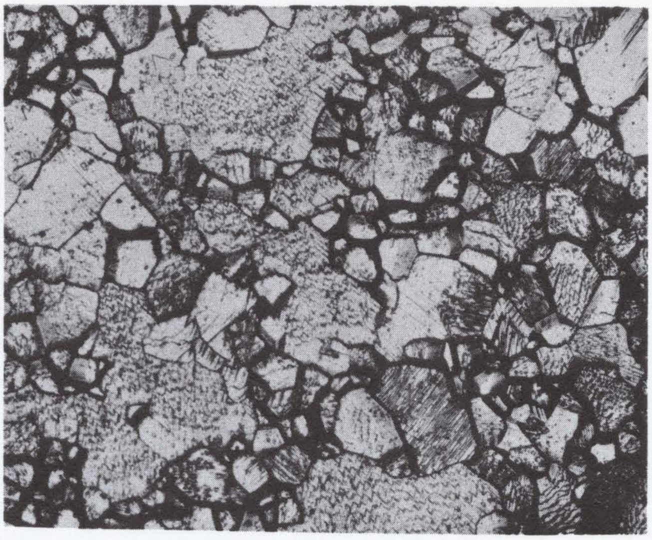

Fig. 8-44: Oxide surface topography of Ni-4% Fe alloy oxidized for 25.2 hours. 160×.

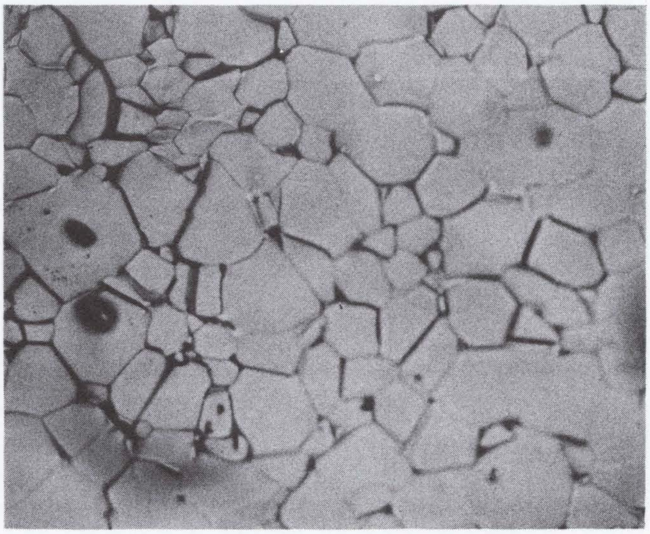

Fig.8-45: Surface topography of Ni-6% Fe alloy oxidized for 34.2 hours. 160×.

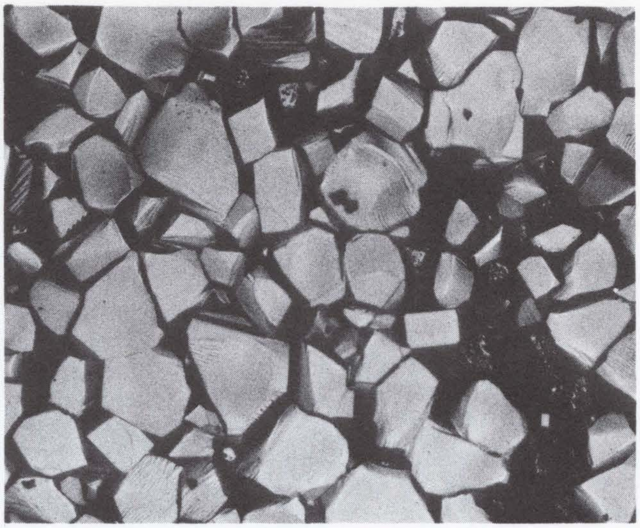

Fig. 8-46: Oxide surface topography of Ni-8%Fe alloy oxidized for 53.1 hours. 160x

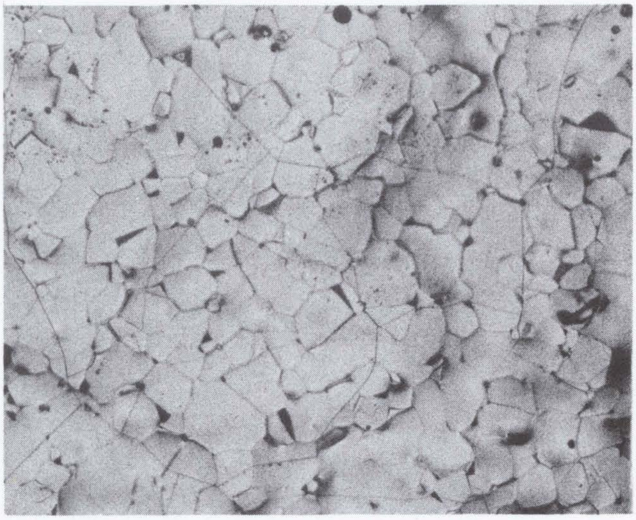

Fig. 8-47: Oxide surface topography of a Ni-10% Fe alloy oxidized for 50.0 hours. 160x.

for all these alloys is nickel oxide. The outer oxide on the Ni-25% Fe alloy is a spinel.

8.5 STRUCTURE AND COMPOSITION OF THE EXTERNAL OXIDE SCALES

Pure Ni

Figs. 8-48 and 8-49 show NiO scales formed on pure nickel at 1000°C after 51.5 hours in the polished and etched conditions. Oxide scale formed on pure nickel was uniform, compact and adherent to the metal substrate. Fig. 8-49 indicates that the oxide scale is a duplex scale consisting of an inner layer of small equiaxed grains and an outer layer of large columnar grains extending through the rest of the scale. The columnar grains are essentially perpendicular to the metal-oxide interface.

Ni-2% Fe Alloy

The external scale formed on Ni-2% Fe alloy consisted essentially of single phase nickel oxide with dissolved iron. The grain structure of the oxide was columnar with small equiaxed grains at the alloy-oxide interface (Figs. 8-50 and 8-51). No spinel precipitates could be detected in the external scale formed on this alloy.

Ni-4% Alloy and Ni-6% Fe Alloy

The external scale on Ni-4% Fe alloy showed the beginning of spinel precipitation in the nickel oxide matrix. (Fig. 8-52).

The spatial density of spinel precipitates increased with increasing iron content of the bulk alloy. Thus comparison of Figs. 8-52 and 8-54 shows a pronounced increase in the spinel precipitation in the external scale. The composition of spinel in the external scale corresponded to that of nickel ferrite, $NiFe_2O_4$. Details of the spinel precipitates in the external scale formed on a Ni-6% Fe alloy oxidized for 12.5 hrs.are shown in Fig. 8-56. Figs. 8-53 and 8-55 show the external scale on Ni-4% Fe and Ni-6% Fe alloys in the etched condition. In both of these scale structures a zone containing small equiaxed grains exists at the alloy-oxide interface. This zone has a strikingly sharp outer boundary. Beyond this zone, a zone of medium sized elongated grains exists upto the spinel precipitates in the external scale. Beyond the spinel precipitates a zone of large columnar grains exist which extends up to the oxide-gas interface. The density of spinel precipitates in the external scale formed on the Ni-4% Fe alloy is small and the distinction between medium-sized grains and columnar grains in this scale is not always sharp. However in the external scale formed on Ni-6% Fe alloy a sharp boundary between these two zones is delineated by the high density spinel precipitate. The external scale on the Ni-6% Fe alloy thus consists of three sharply divided zones with the spinel precipitates mainly occurring at the boundary between the outer zone of columnar grains and the middle zone of medium sized grains.

Ni-8% Fe Alloy

The volume density of spinel precipitates in the external scale formed on this alloy is high. It is interesting to note that the relative position of the spinel precipitation zone shifts inwards with increasing iron content of the bulk alloy. A new feature that appears in the structure of the external scale formed on Ni-8% Fe alloy is the large amount of porosity at the alloy-oxide interface (Fig. 8-57).

Ni-10% Fe, Ni-15% Fe and Ni-20% Fe Alloys

External scales formed on these alloys were fragile after quenching and hence good quality micrographs could not be obtained. However, it was noted that the extent of void formation at the alloy-oxide interface increased with increasing iron content of the bulk alloy. Also, grains of spinel started forming in the outer zone of the external scales on these alloys.

Ni-25% Fe Alloy

Oxide scale formed on this alloy did not break away from the alloy substrate and hence proper metallographic examination was possible. Again, large voids existed in the external scale at the alloy-oxide interface. The external scale consisted of an inner nickel oxide layer which gradually shaded into a predominantly spinel layer. However, no continuous spinel layer was present. Nickel oxide formed channels around the boundaries of the spinel grains.

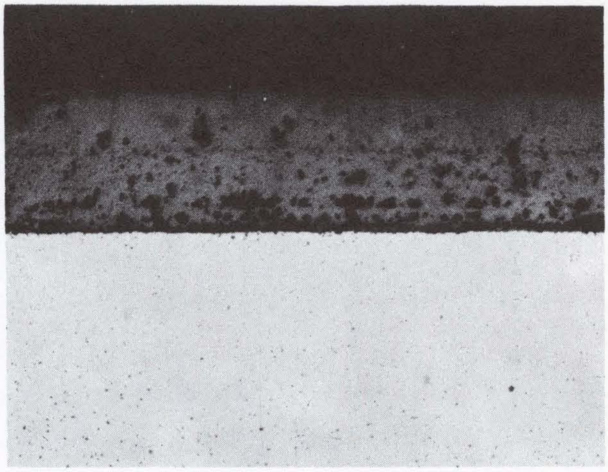

Fig. 8-48: Oxide scale on pure nickel oxidized for 51.5 hours-unetched cross section. 200x

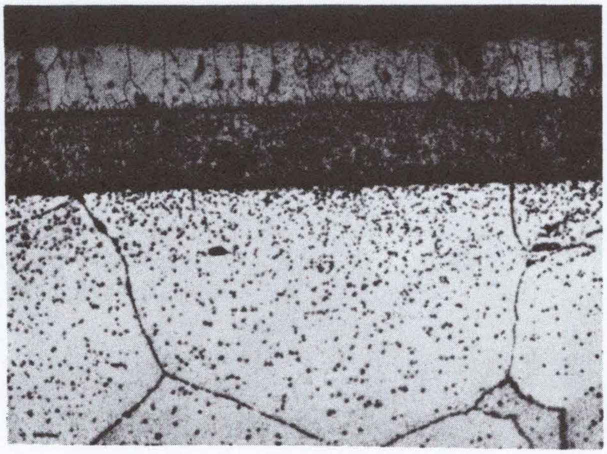

Fig. 8-49: Oxide scale on pure nickel oxidized for 51.5 hours - etched cross section, 200×

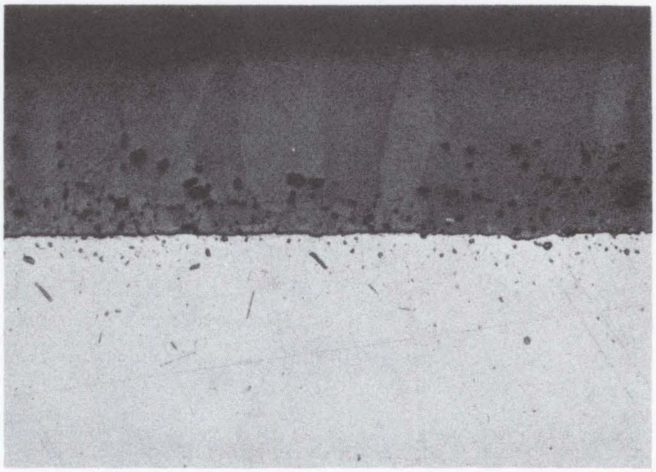

Fig. 8-50: Ni-2%Fe alloy oxidized for 50 hours-unetched cross section. 200x.

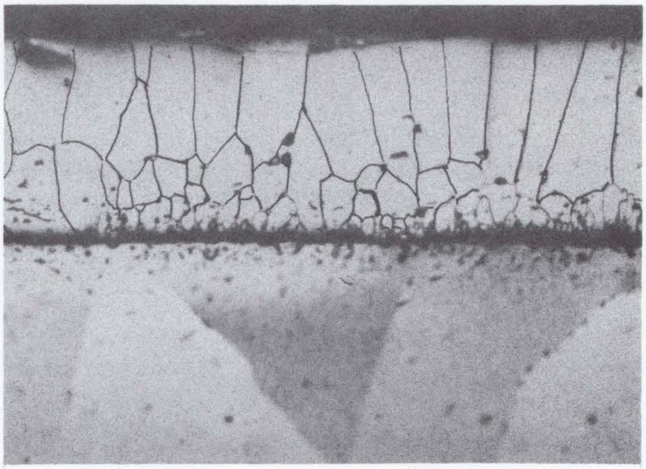

Fig. 8-51:Ni-2% Fe alloy oxidized for 50 hours - etched cross section 200×.

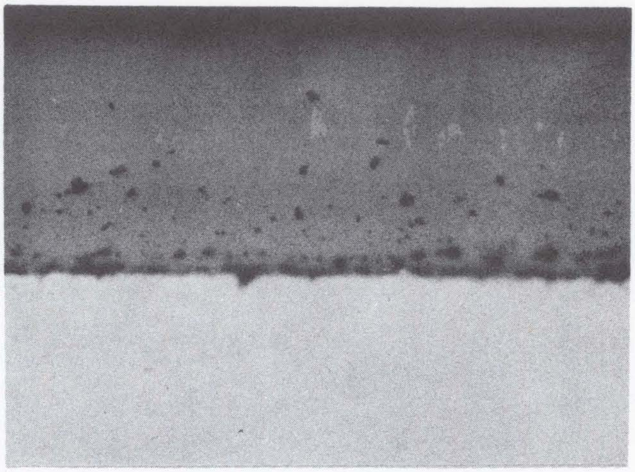

Fig. 8-52: Ni-4%Fe alloy oxidized for 13.5 hours - unetched. 400x.

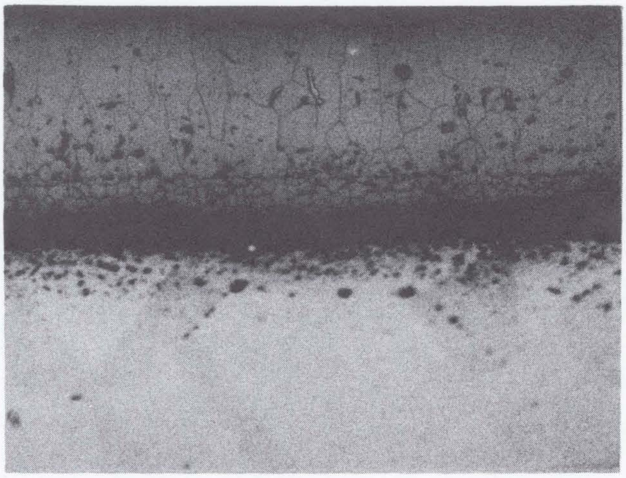

Fig. 8-53: Ni-4% Fe alloy oxidized for 25.2 hours - etched electrolytically. 250×.

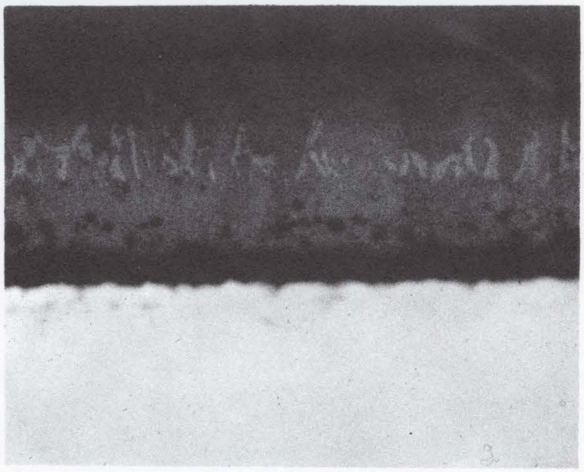

Fig. 8-54: Ni-6%Fe alloy oxidized for 12.5 hours - unetched. 400x.

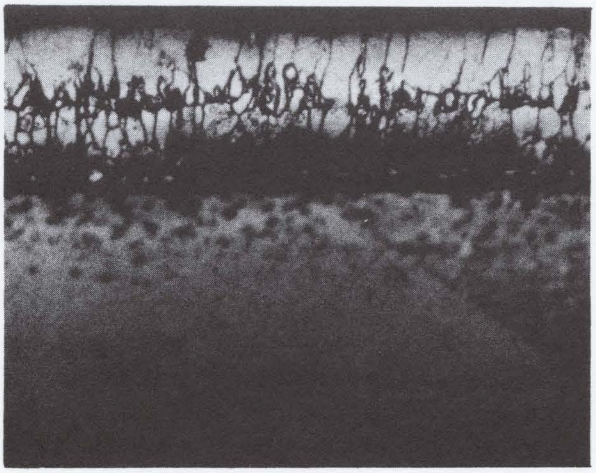

Fig. 8-55: Ni-6% Fe alloy oxidized for 12.5 hours - etched 320×.

Fig. 8-56: Ni-6%Fe alloy oxidized for 47.5 hours - unetched 800x. Spinel precipitates in the external scale.

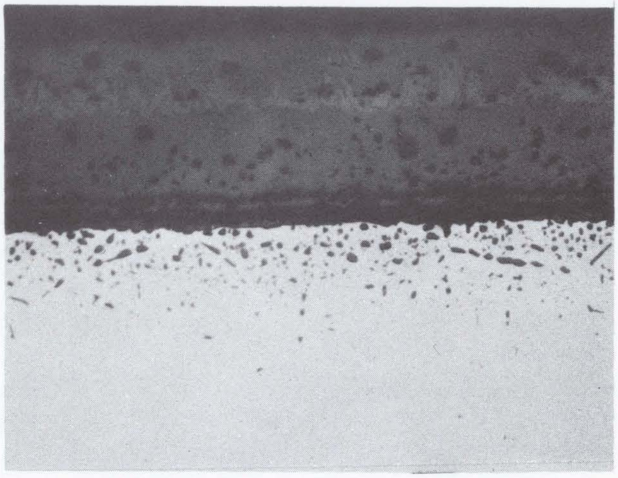

Fig. 8-57: Ni-8% Fe alloy oxidized for 48.5 hours. 200×

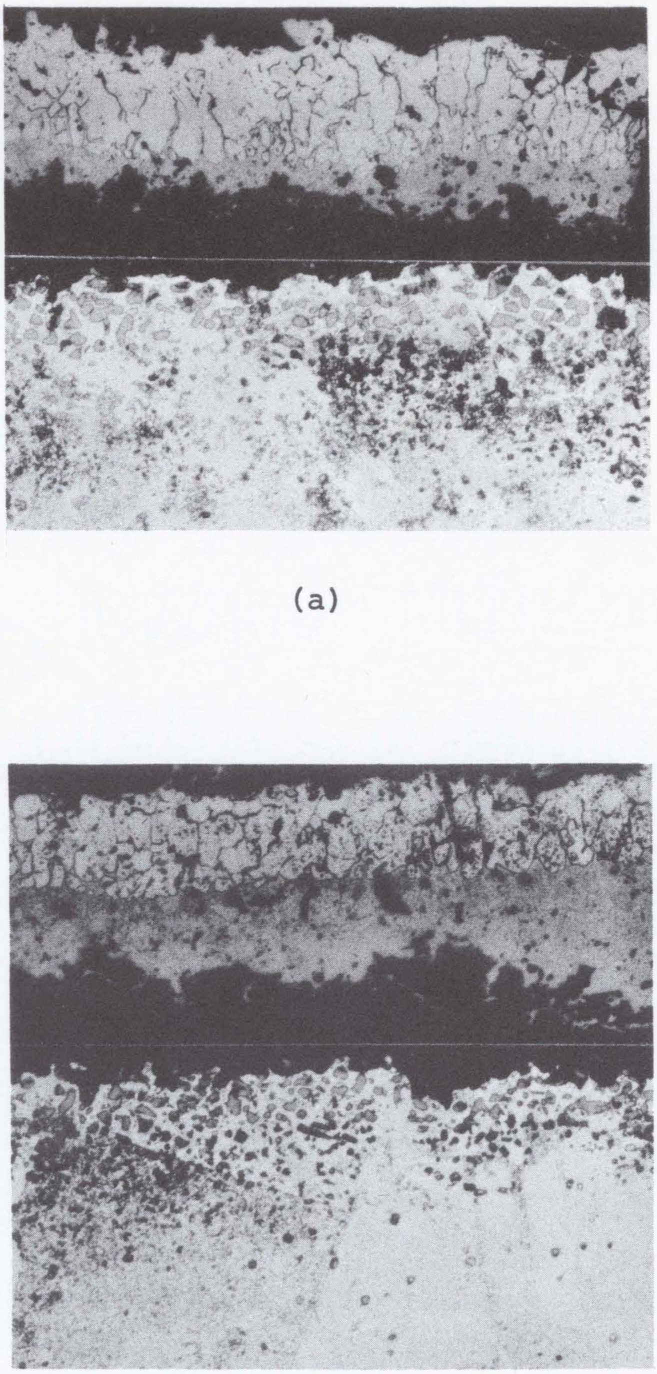

(a)

(b)

Fig. 8-58: Ni-25% Fe alloy oxidized for 61 hours - etched 272×.

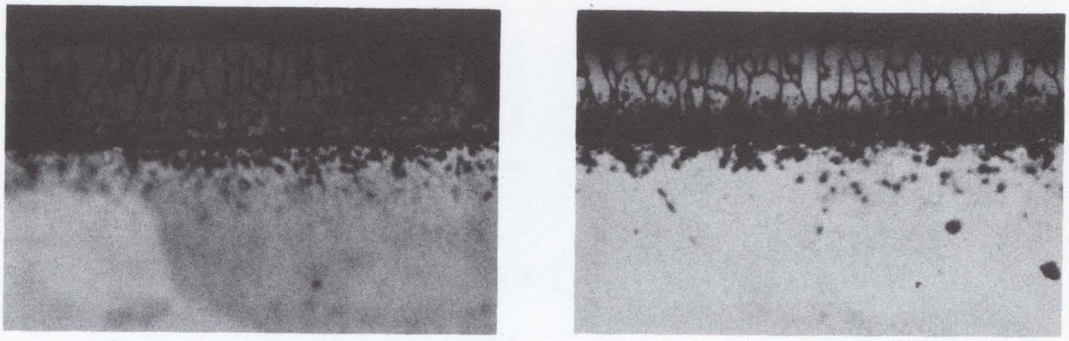

(a) (b)

Fig. 8-59: Grain structure of nickel oxide formed on Ni-4% Fe alloy oxidized for 5 hours. 400×.

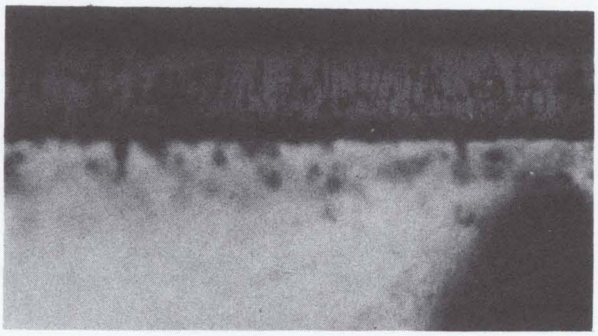

Fig. 8-60: Grain structure of external scale formed on Ni-6% Fe alloy oxidized for 2 hours. 400×.

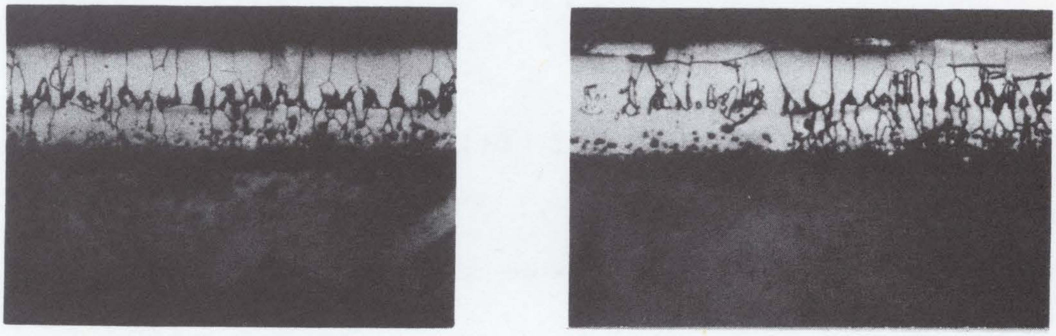

(a) (b)

Fig. 8-61: Grain structure of the exgernal scale formed on Ni-6% Fe alloy oxidized for 12.5 hours. 240×. Note the spinel precipitates at the boundary between the outer and middle zones in the picture on the right.

It was necessary to etch the oxide layer electrolytically to bring out the structure illustrated in Fig. 8-59.

Changes in the oxide grain structure during oxidation

The oxide scale formed on alloys containing 2-6% Fe consisted of single layer of small elongated grains as illustrated in Figs. 8-59 to 8-61. However on prolonged oxidation a sharply defined layer of small equiaxial grains developed. For alloys containing 4% and 6% Fe the original single layer structure transformed into the three layer structure mentioned earlier. This structure at an intermediate stage for a Ni-6% Fe alloy is shown in Fig. 8-61. The initial structures and their transformations are similar to those observed by Rhines and Wolf$^{(69)}$. The transformations in the oxide scale structure might have occurred due to growth stresses in the scale and restraints imposed by the precipitation of spinel particles in the nickel oxide matrix. However in view of limited data available it is fruitless to speculate further on the causes of this phenomenon.

8.6 CONCENTRATION PROFILES

Samples of an alloy of given composition were oxidized for different periods of time. These samples were then mounted in cross section. The concentration profiles were obtained from microprobe measurements by point counting at regular intervals. We recall from Chapter 7 that the solubility of oxygen in the alloy is too small for measurement by electron probe microanalysis. Also, since the nickel content of the samples is high the error involved in the measurement of its concentration is high. It is easier to determine the iron concentration profile accurately. Since the nickel and iron concentration profiles in the alloy and oxide phases are complementary, the nickel concentration profile can be easily calculated from the iron concentration profile. The quantitative concentration profiles were determined for alloys containing 2%, 4%, 6% and 8% Fe. The nickel concentration profile was actually measured for Ni-6% Fe alloys to illustrate the complementarity.

The line scan for the distribution of iron and nickel in a Ni-8% Fe alloy oxidized for 51 hours is shown in Fig. 8-62. This illustrates the qualitative concentration profile across the sample for each of the elements scanned. The profiles for Fe and Ni shown in Fig. 8-62 are typical of most of the samples analysed, except that Ni-2% Fe alloys do not show spinel precipitates in the external scale.

The concentrations in the external oxide scale for a given alloy composition were plotted as a function of a dimensionless parameter y defined by the following equation

$$y = x/x_s \qquad (8-1)$$

where x is the distance from the alloy/oxide interface and x_s

is the thickness of the external scale. The concentrations in the alloy matrix were plotted as a function of λ defined as

$$\lambda = xt^{-\frac{1}{2}} \qquad (8.2)$$

where x is the distance from the alloy-oxide interface in microns and t is the oxidation time for the specimen in hours.

Tables 8-3 to 8-6 give the oxidation time and oxide scale thickness for the samples analyzed. The concentration profiles in λ-space for these samples in direction perpendicular to the alloy-oxide interface are given in Figs. 8-63 to 8-66. The errors involved in the measurements of these profiles include tilting of the samples during mounting, uncertainty in measurement of the total thickness of the oxide due to edge rounding during polishing and errors associated with electron probe microanalysis. The edge rounding effect may be significant for samples oxidized for short periods of time since the total scale thicknesses for these samples are small.

Figures 8-63 to 8-66 show firstly that the interfacial compositions are constant with time and secondly that the concentration profiles are invariant in the λ-space. This indicates diffusion-controlled mechanism for the oxidation of these alloys at 1000°C.

Within the alloy we have the unoxidized alloy and the zone of internal oxidation. The concentration gradients in the unoxidized alloy were shallow whereas the gradients of Fe and Ni in the zone of internal oxidation were steep. There was a depletion of iron in the alloy matrix and hence a sharp decrease in iron concentration in the alloy matrix towards the alloy-oxide interface occurred. The iron content at the alloy-oxide interface was lower than 1%. We recall from the iron-nickel-oxygen phase diagram given in Chapter 7 that this alloy composition lies in the two phase alloy-nickel oxide region. Thus nickel oxide is stabilized in the external scale. The external scale consisted of two zones. The inner zone consisted of single phase nickel oxide with a steep iron concentration gradient. The iron concentration in this zone <u>increased</u> towards the oxide-gas interface. The outer zone, which is a two phase zone, consisted of spinel $NiFe_2O_4$, precipitates in a nickel oxide matrix. The iron concentration of the matrix nickel oxide in this zone <u>decreased</u> slowly towards the oxide-gas interface. The magnitude of the gradients increased with increasing iron content of the bulk alloy.

From the Fe-Ni-O phase diagram we observe that the nickel content of the spinel in equilibrium with the alloy should increase with increasing nickel in the alloy. Since the nickel content of the alloy increases towards the alloy-oxide interface the nickel content of the spinel internal oxide should also increase towards this interface. This was qualitatively confirmed by the microprobe analysis. Spinel particles could be detected almost upto the alloy-oxide interface within the alloy matrix; however no spinel particles were detected at the alloy-oxide interface within the external oxide scale. Also no inhomogeneities were observed within the external scale at this interface. This indicates that spinel can dissolve rapidly in the nickel oxide at the temperature of oxidation. However, the spinel precipitates in the outer region of the external scale are remarkably stable and do not show any tendency to dissolve in the matrix indicating that they must be in local equilibrium with the nickel oxide matrix.

Line scans obtained for Fe and Ni parallel to the alloy-oxide interface in the alloy and nickel oxide phases showed no gradients along this direction within these phases. The gradients thus exist only in the direction perpendicular to the alloy-oxide interface. It is therefore possible to apply a unidirectional diffusion model for the calculation of concentration profiles in these phases.

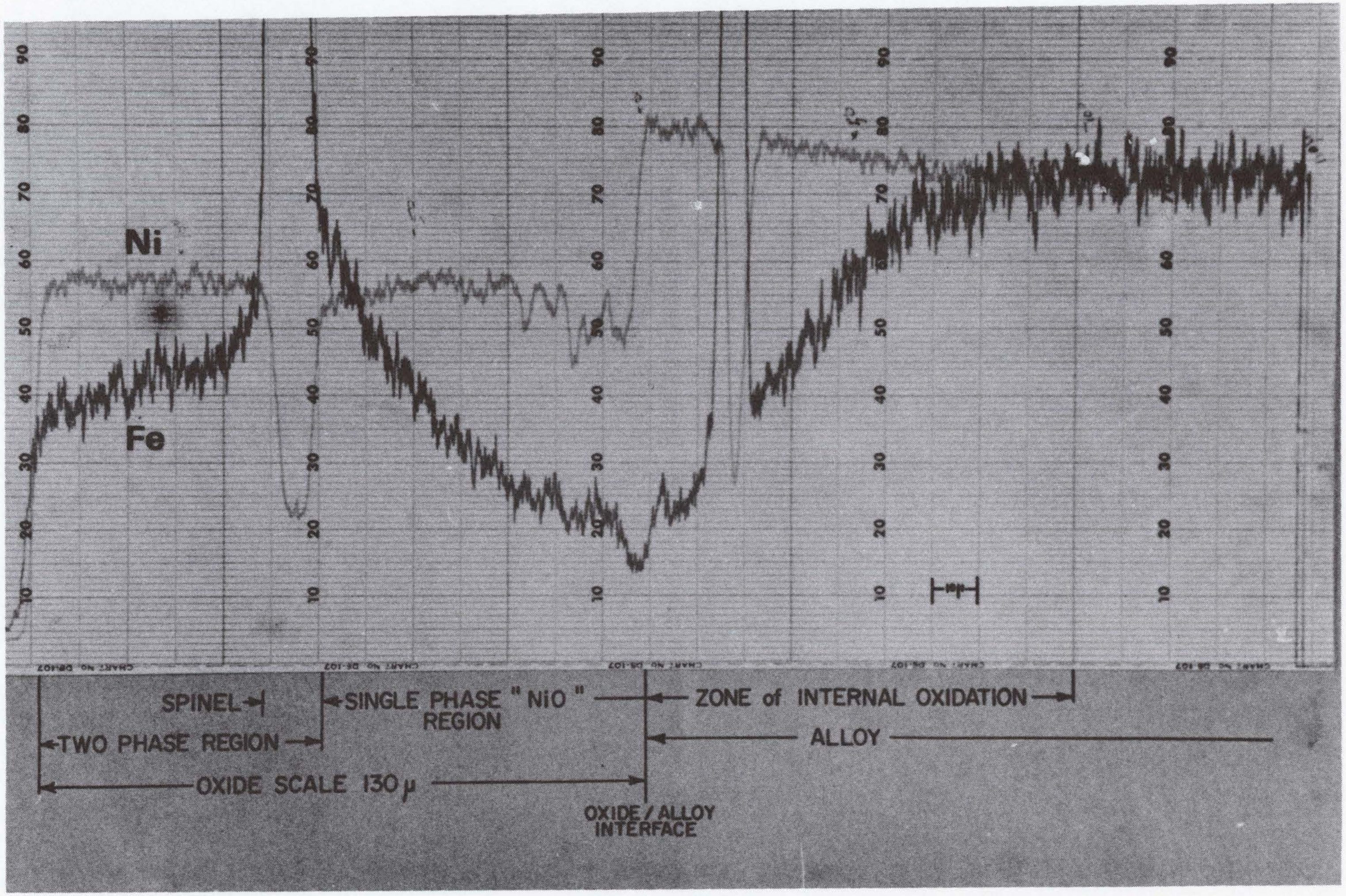

Fig. 8-62: Line scan for the distribution of iron and nickel in the alloy and oxide matrix - Ni-8% Fe alloy oxidized for 53 hours

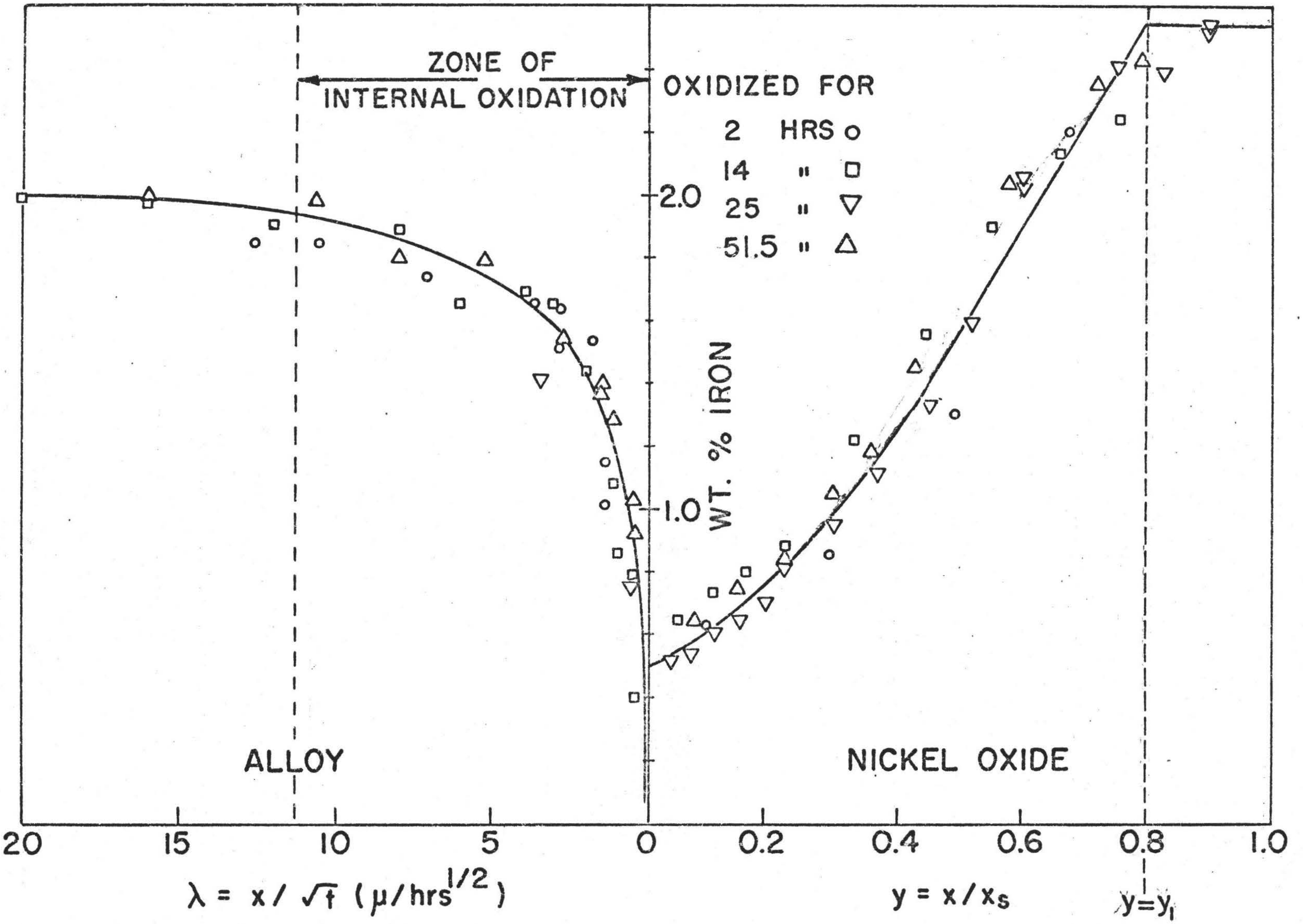

Fig. 8-63: Concentration profile for iron in alloy and oxide phases plotted in the "λ" space. Nickel - 2% Iron Alloy oxidized in pure oxygen at 1000°C.

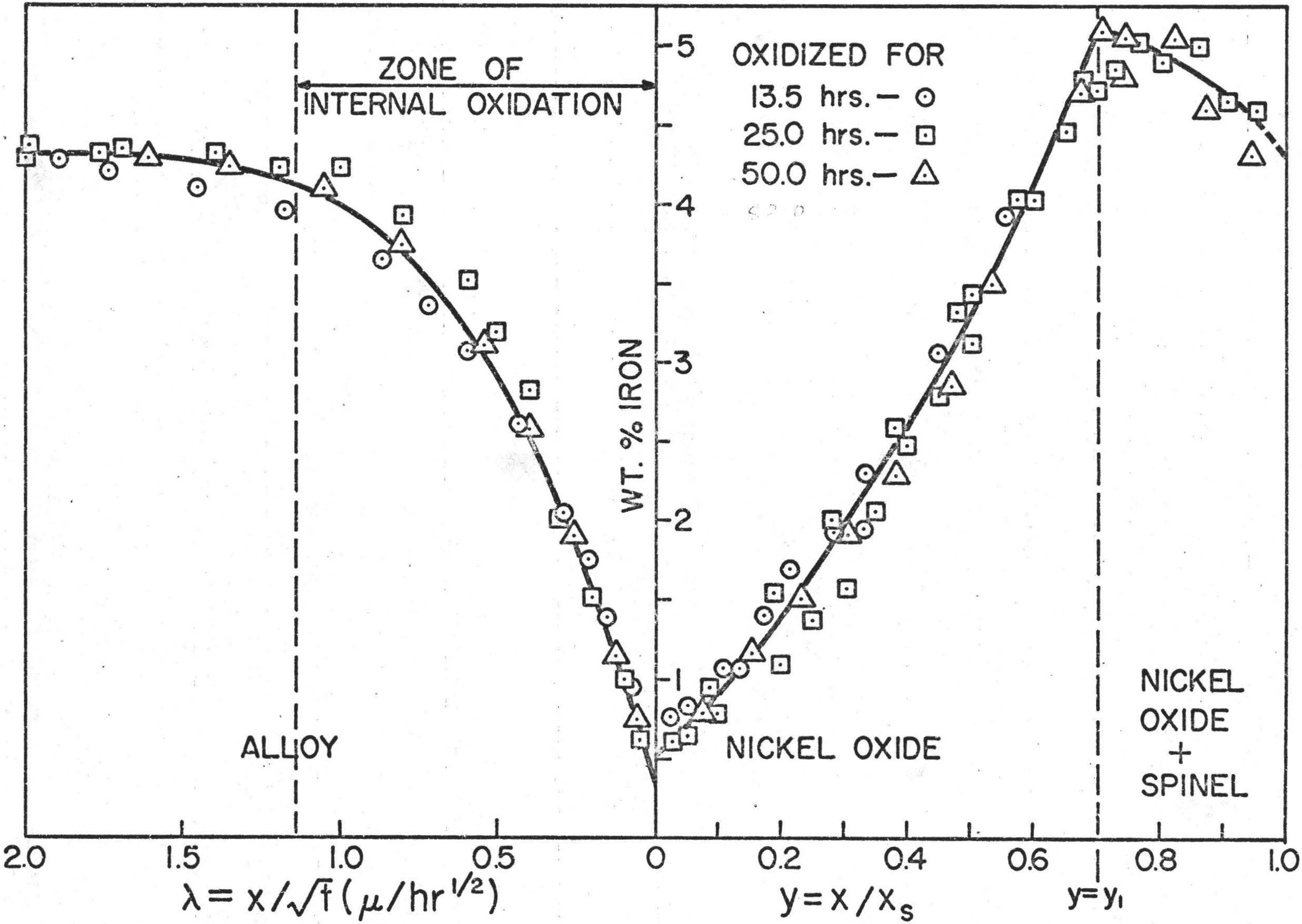

Fig. 8-64: Concentration profile for iron in alloy and oxide phases plotted in "λ" space. Nickel - 4% Iron Alloy oxidized in pure oxygen at 1000°C.

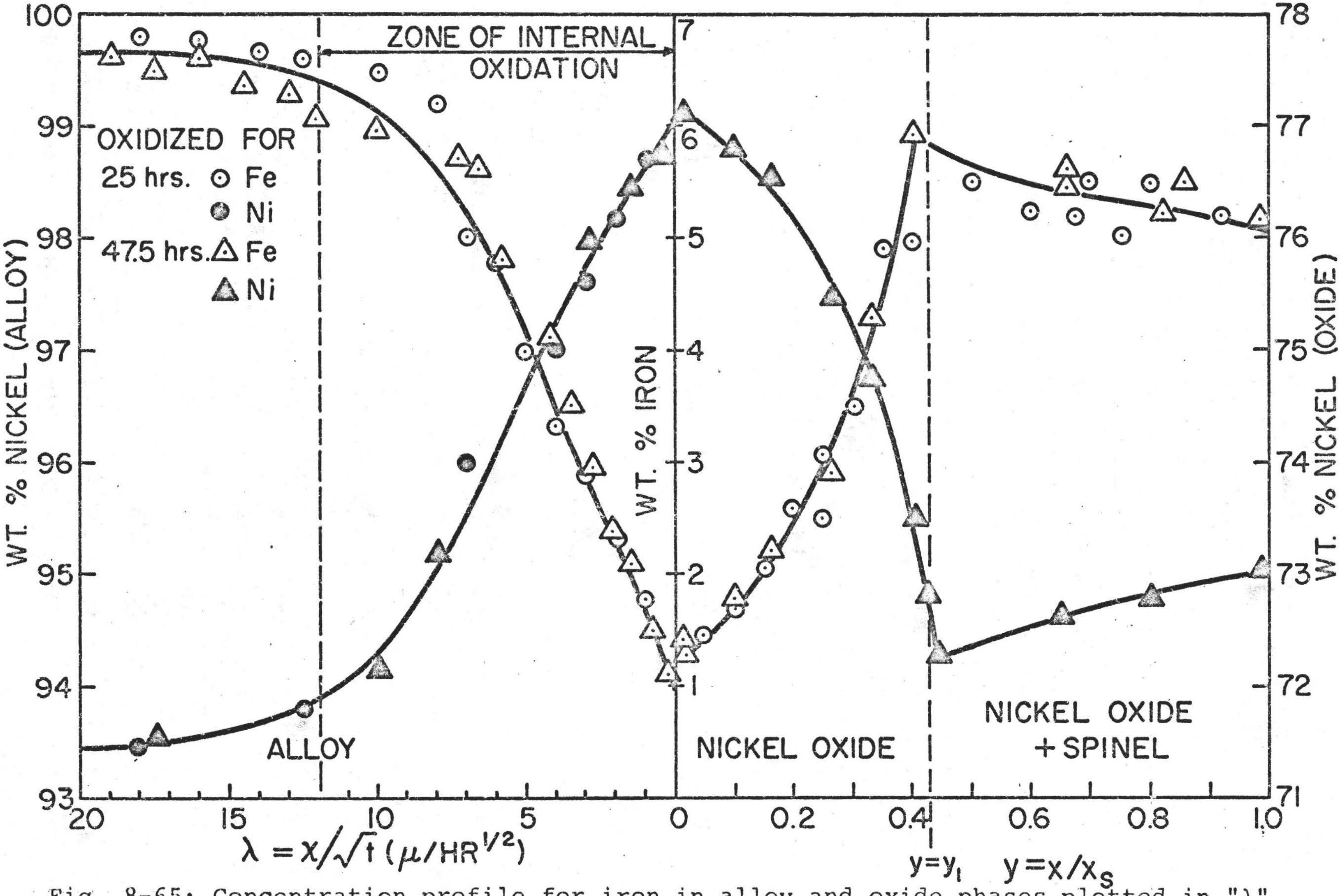

Fig. 8-65: Concentration profile for iron in alloy and oxide phases plotted in "λ" space. Nickel - 6% Iron alloy oxidized in pure oxygen at 1000°C.

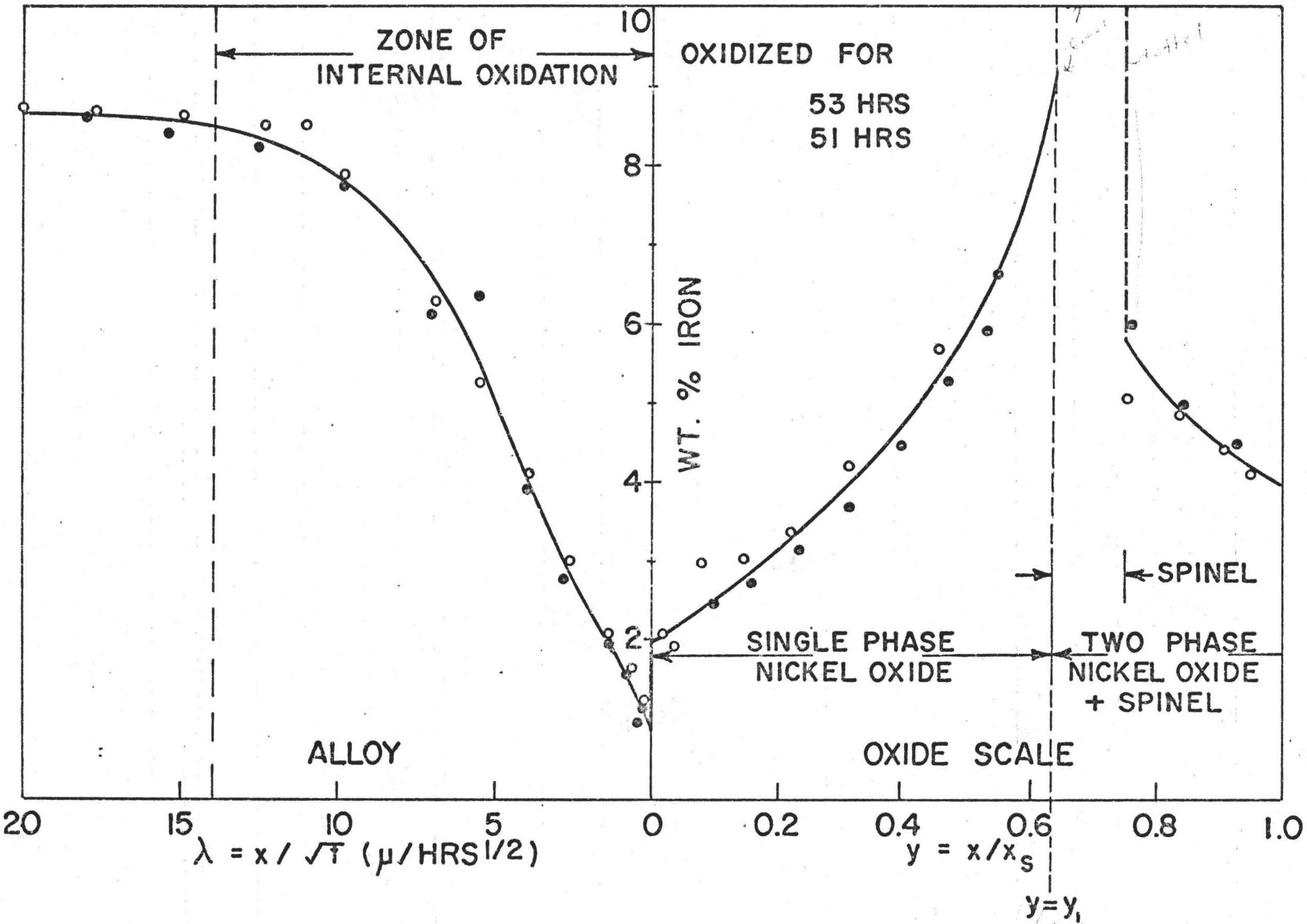

Fig. 8-66: Concentration profile for iron in alloy and oxide phases plotted in "λ" space. Nickel - 8% iron alloy oxidized in pure oxygen at 1000°C.

Table 8-1

Parabolic Rate Constants for Ni-Fe Alloys at 1000°C

Nominal Comp.	$k_p \times 10^{10}$ $g^2cm^{-4}sec^{-1}$	$\frac{k_p \text{ (Alloy)}}{k_p \text{ (Ni)}}$
Pure Ni	4.4	1.0
Ni-2%Fe	18.8	4.3
Ni-4%Fe	29.2	6.6
Ni-5%Fe	28.2	6.4
Ni-6%Fe	25.5	5.8
Ni-8%Fe	15.0	3.4
Ni-10%Fe	10.4	2.4
Ni-15%Fe	10.6	2.5
Ni-20%Fe	11.8	2.7
Ni-25%Fe	12.6	2.9

Table 8-2

Preferred Orientation of Surface Oxide on Ni-10% Fe Alloy Oxidized for 50 Hours

hkl	111	100	220
θ	18.7°	21.6°	31.4°
Relative Intensity in random orientation (pure NiO)	91	100	57
Relative Intensity for the sample	233	100	293

Table 8-3

Oxidation Time and Oxide Scale Thickness for Ni-2% Fe Alloy Samples (Fig. 8-63)

Nominal time of oxidation	Actual time of oxidation	External scale thickness (μ)
2 hours	2 hrs. 00 mts.	21
14 hours	14 hrs. 05 mts.	67
25 hours	25 hrs. 00 mts.	91
51.5 hours	51 hrs. 32 mts.	133

Table 8-4

Oxidation Time and Oxide Scale Thickness for Ni-4% Fe Alloy Samples (Fig. 8-64)

Nominal time of oxidation	Actual time of oxidation	External scale thickness (μ)
13.5 hours	13 hrs. 50 mts.	75
25.0 hours	25 hrs. 12 mts.	105
50.0 hours	50 hrs. 10 mts.	155

Table 8-5

Oxidation Time and Oxide Scale Thickness for Ni-6% Fe Alloy Samples (Fig. 8-65)

Nominal time of oxidation	Actual time of oxidation	External scale thickness (μ)
25.0 hours	25 hrs. 00 mts.	100
47.5 hours	47 hrs. 30 mts.	159

Table 8-6

Oxidation Time and Oxide Scale Thickness for Ni-8% Fe Alloy Samples (Fig. 8-66)

Nominal time of oxidation	Actual time of oxidation	External scale thickness (μ)
51.0 hours	51 hrs. 00 mts.	128
53.0 hours	53 hrs. 07 mts.	132

CHAPTER 9

KINETICS OF OXIDATION OF NICKEL-IRON ALLOYS AT 1000°C - DISCUSSION

9.1 INTRODUCTION

As noted earlier the bulk alloy compositions studied lie in three different phase regions of the ternary Fe-Ni-O phase diagram, viz., wustite-alloy, spinel-alloy and nickel oxide-alloy. However, the kinetic and thermodynamic interactions are such that only nickel oxide is stabilized in the external scale next to the alloy-oxide interface. In the following sections we will consider various factors involved in the analysis, summarize the results in an empirical model and then consider the results for dilute nickel-iron alloys containing up to 5% Fe on a more fundamental basis.

9.2 GENERAL DISCUSSION

9.2.1 Porosity in the Oxide Scale

In a p-type metal deficit oxide such as NiO the diffusion takes place via vacancies. Vacancies migrate from the oxide-gas interface to the alloy-oxide interface where they are condensed. Adhesion of oxide to the metal requires annihilation of pores by plastic flow of the oxide. Plastic flow thus plays an important part in the adhesion of oxide to metal and also in the formation of porosity in the oxide(11,12). The plasticity of an oxide increases with temperature and generally decreases with impurity addition(71). At constant temperature porosity is expected to be a minimum for pure nickel oxide. As the iron content of nickel oxide is increased the ability to flow into the pores is decreased and thus higher porosity at the metal-oxide interface is expected with increasing iron content. The iron content of nickel oxide at the alloy-oxide interface, increases from 0.5% Fe for Ni-2% Fe alloy to 1.3% Fe for Ni-6% Fe alloy. Since this variation is small the increase in porosity is not expected to be large in view of the similar ionic radii of Fe and Ni cations(7). A more important factor is expected to be precipitation and growth of spinel as a second phase in the nickel oxide matrix. The presence of a second phase will make the plastic flow of nickel oxide extremely difficult. Thus a significant increase in porosity is expected when spinel precipitates become copious and spinel grain formation occurs. This happens for alloys containing 8% Fe and more. Large amount of porosity near the alloy-oxide interface is found in the case of these alloys. Occurrence of large amounts of porosity at the alloy-oxide interface will evidently decrease the oxidation rate constant for these alloys. For alloys containing up to 6% Fe, the porosity in the oxide scale is small and hence the scale may be assumed to be compact as required for a diffusion analysis

(Section 4.5.1).

9.2.2 Grain Boundary Diffusion

Grain boundaries act as preferential paths for diffusion of migrating species at low temperatures (i.e. approximately $T < 0.6\ T_m$ where T_m is the melting point of the oxide). A grain boundary diffusion model for NiO formed on pure nickel has been proposed for low temperatures(10) where the cations are assumed to migrate preferentially along the grain boundaries and line defects. Recently, Rhines and Wolf(69) have proposed a model in which preferential migration of oxygen occurs along the grain boundaries of NiO formed at high temperatures on pure nickel. In the former case, the cation activity will be higher at the grain boundaries at constant x where x is the distance from the metal-oxide interface. In the latter case, preferential diffusion of oxygen along the grain boundaries will lead to higher oxygen activities at the grain boundaries at constant x. In the present case if significant diffusion of either species occurred along the grain boundaries it would lead to lateral concentration gradients of the metallic species. This is because in a ternary system the activities of the three components are related by the Gibbs-Duhem equation. The diffusion interactions are such that the faster moving species (in the present case iron) tend to concentrate at areas of higher oxygen activities (Section 4.5 and 4.6). Thus, higher concentrations of iron would occur at the grain boundaries at a constant value of x. However, all attempts to detect cation concentration gradients in the lateral direction have led to negative results in the case of samples oxidized for sufficiently long time, i.e. oxidized for a period of time in which a stationary state was achieved.

It is to be emphasized that the analysis attempted in this work concerns the cases where a stationary state is achieved. No quantitative or semi-quantitative analysis is attempted for processes occurring during the early transient period. A stationary state may be defined by constant interfacial concentrations and a well defined metallographic structure. Thus, the transverse cross sectional concentration profiles in x-space are well defined and reproducible, not only for different alloy samples of the same composition oxidized for similar periods of time, but also for samples oxidized for different periods of time (Figs. 8-63 to 8-66). The various zones of oxidation are distinct and their relative widths remain constant in time. This lends a strong support for a volume diffusion model.

9.2.3 Spinel Precipitation in the External Scale

It has been proposed that the spinel precipitates in the external scale might have formed at the grain boundaries of nickel oxide with oxygen being transported along the grain boundaries(200). It may also be argued that the spinel precipitates are formed during the transient state since the bulk alloy composition lies in the stability range of spinel and later remain in the external scale.

The former of these propositions is unlikely on the basis of the same arguments as in the previous section. The latter possibility may be discounted on the following basis. Spinel is likely to form during the initial stages, but is stabilized at a later stage when stationary state is obtained. This is indicated by three observations. Firstly, the concentration profiles in the two phase spinel-nickel oxide region are distinct and reproducible, and the relative widths of the inner single phase zone and the outer two phase zones remain constant with time. Secondly, unlike the case for the inner region, the iron concentration in the two-phase spinel-nickel oxide region decreases towards the oxide-gas interface, a fact which can be explained from thermodynamic considerations (see Section 9.5). Thirdly, it can be seen from Figs. 8-60 and 8-61 that the amount of spinel in the external scale increases with time, indicating that the spinel in the external scale has not merely formed during the early stages and been retained.

The discussion in this section is intended to show that the local equilibrium model may indeed be applied to the oxidation of the alloys considered and the conditions needed to apply volume diffusion model are nearly fulfilled for alloys containing up to 6% Fe.

9.3 EMPIRICAL MODEL FOR THE OXIDATION

Fig. 9-1 illustrates the schematic model for the oxidation of the alloys investigated. This may be summarized as follows:

1. Iron tends to preferentially concentrate in the oxide phases resulting in a depletion of the alloy matrix in iron. In all the alloys containing 0-25% Fe the shift in the alloy composition at the alloy-oxide interface is beyond point A_2 towards the Ni corner of the Fe-Ni-O phase diagram (Fig. 7-6) resulting in stabilization of nickel-oxide next to the alloy-oxide interface.
2. For low iron alloys (e.g. Ni-2% Fe), external scale is virtually single phase nickel oxide. Spinel in the external scale is nondetectable.
3. Spinel occurs as precipitates in the outer zone of the external scale for alloys with higher iron contents.
4. The relative thickness of the two-phase outer zone increases with increasing iron content of the bulk alloy.
5. The oxidation rates increase with increasing iron content of the bulk alloy until spinel begins to precipitate in the external scale.

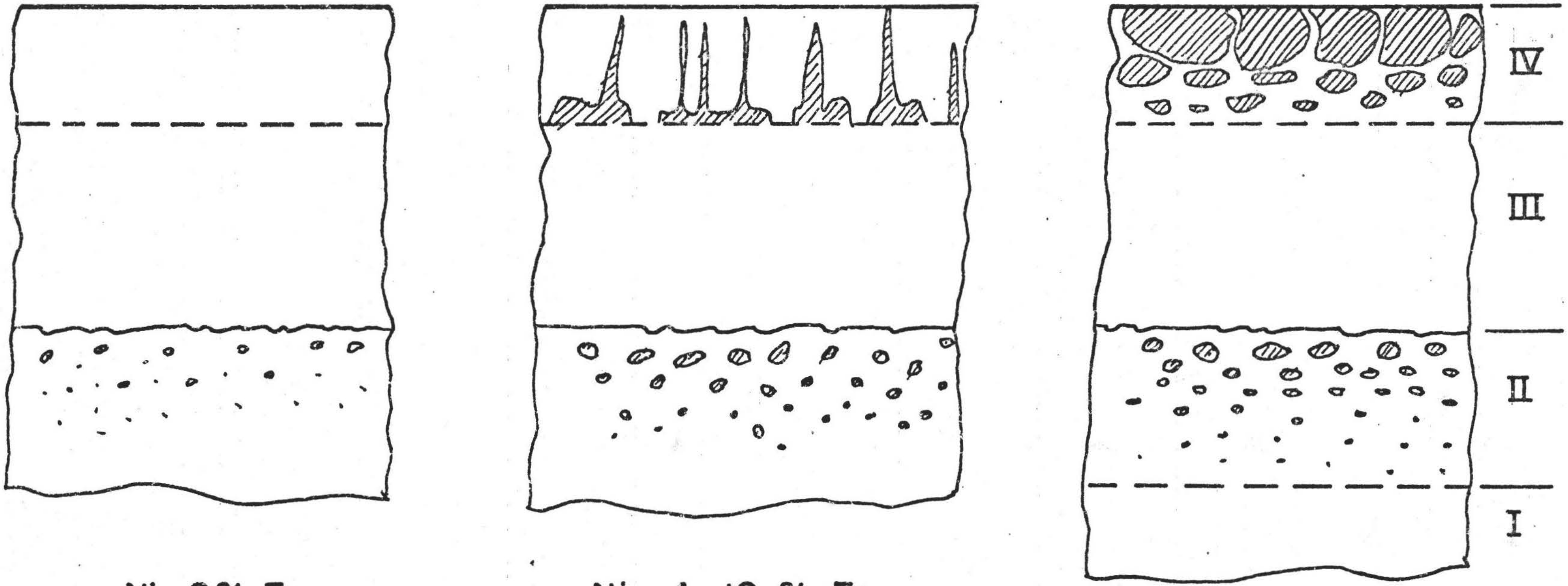

Ni-2% Fe　　Ni-4-10 % Fe　　Ni-15-25 % Fe

I - Unoxidized alloy　　II - Zone of internal oxidation
III - Single phase nickel oxide　　IV - Two phase nickel oxide + spinel
Internal Oxide-Spinel

Fig. 9-1: Schematic representation of the scale and subscale structure in nickel-iron alloys. Oxidized in pure oxygen at 1000°C.

6. Spinel forms a high resistance diffusion path. This is because the diffusion rates of cations in the spinel are much slower than in iron-doped nickel oxide (Appendix B - Table B-2).
7. Spinel in the external scale becomes more copious as the iron content of the bulk alloy is increased. This results in blocking the diffusion of cation and hence effective reduction in the cross section for diffusion.
8. The amount of internal oxide increases with increasing iron content of the bulk alloy. The spinel precipitates in the zone of internal oxidation block the diffusion in the alloy matrix.
9. The double blocking effect of spinel in the external scale and the zone of internal oxidation effectively reduces the oxidation rates for these alloys. The diffusion fluxes in the external scale and the alloy matrix are coupled at the alloy-oxide interface and a resistance to diffusion in any one phase reduces the overall flux and hence results in reduction of the oxidation rate.
10. The blocking does not change significantly upon further addition of iron to the bulk alloy. Therefore k_p remains nearly constant.

The particular shape of the k_p vs. bulk alloy composition curve illustrated in Fig. 8-21 is therefore due to the combined effect of increasing diffusivities of cations in nickel oxide with increasing iron concentration and the increasing blocking effect of spinel precipitates in the external scale and internal oxidation zone with increasing iron content of the bulk alloy.

9.4 DEFECT STRUCTURE MODEL FOR MIXED OXIDES

Before considering the diffusion model it is necessary to consider the effect of solute cations on the defect structure and consequently on the diffusivities of cations in mixed oxides, when the solute cation is that of a transition metal with variable valence. The Wagner-Hauffe valence model therefore can not be applied.

Zintl(138) has considered the general case of oxide solid solutions of two transition metals. If association of electrical charges and vacancies is neglected then the following defect equation for a pure oxide AO may be written

$$\frac{1}{2}\,O_2(\text{gas}) + 2A^{2+}(\text{cation-sublattice}) \rightarrow O^{2-}(\text{anion-sublattice}) + \square + 2A^{3+}\ (\text{cation-sublattice}) \qquad (9\text{-}1)$$

Substitution of a divalent cation B^{2+}, for a divalent cation A^{2+} sustains the electrical neutrality of the oxide. However, if the amount of energy required for the formation of a trivalent cation B^{3+} from a divalent cation B^{2+} is much less compared to the corresponding energy for A ions, then reaction (9-1) will shift to the R.H.S. This will result in formation of extra vacancies. The corresponding reaction for B ions is

$$\frac{1}{2}\,O_2(\text{gas}) + 2B^{2+}(\text{cation-sublattice}) \rightarrow O^{2-}(\text{anion-sublattice})$$
$$+ \square + 2B^{3+}(\text{cation-sublattice}) \qquad (9\text{-}2)$$

If ideal solid solution behaviour is assumed, then the equilibrium constants K_1 and K_2 for reactions (9-1) and (9-2). respectively, are,

$$K_1 = \frac{(x_{A^{3+}})^2\, x_{\square}}{(x_{A^{2+}})^2 P_{O_2}^{1/2}} \qquad (9\text{-}3)$$

and

$$K_2 = \frac{(x_{B^{3+}})^2\, x_{\square}}{(x_{B^{2+}})^2\, P_{O_2}^{1/2}} \qquad (9\text{-}4)$$

where x are the mole fractions of the respective species. The total concentration of holes in the mixed oxide AO-BO is given by

$$x_{\oplus} = x_{A^{3+}} + x_{B^{3+}}\,. \qquad (9\text{-}5)$$

Substitution of the values of $x_{A^{3+}}$ and $x_{B^{3+}}$ from Eqs. (9-3) and (9-4) yields

$$x_{\oplus} = \frac{x_{A^{2+}}\cdot K_1^{1/2}\cdot P_{O_2}^{1/4}}{x_{\square}^{1/2}} + \frac{x_{B^{2+}}\cdot K_2^{1/2}\cdot P_{O_2}^{1/4}}{x_{\square}^{1/2}} \qquad (9\text{-}6)$$

If the concentration of defects is small then

$$x_{A^{2+}} = x_{AO} - x_{A^{3+}} \simeq x_{AO} \qquad (9\text{-}7)$$

$$x_{B^{2+}} = x_{BO} - x_{B^{3+}} \simeq x_{BO} \qquad (9\text{-}8)$$

$$x_{A^{2+}} + x_{B^{2+}} \simeq x_{AO} + x_{BO} \simeq 1 \qquad (9\text{-}9)$$

For electrical neutrality we have

$$x_{\Box} = \frac{1}{2} x_{\oplus} \qquad (9\text{-}10)$$

Substitution of Eqs. (9-7) and (9-8) into Eq. (9-6) yields

$$x_{\Box} = \frac{1}{2^{2/3}} P_{O_2}^{1/6} [x_{AO} K_1^{1/2} + x_{BO} K_2^{1/2})^{2/3} \qquad (9\text{-}11)$$

If the tendency of the solute cation A^{2+} to go into trivalent state is much smaller than the corresponding tendency for cation B^{2+}, then

$$K_2 >> K_1 \qquad (9\text{-}12)$$

and Eq. (9-11) reduces to

$$x_{\Box} = (K_2/4)^{1/3} P_{O_2}^{1/6} \xi^{2/3} \qquad (9\text{-}13)$$

where $\xi \equiv x_{BO}$ is the mole fraction of the solute oxide BO in the mixed oxide AO-BO.

It should be remembered that in the above analysis formation of the associated vacancies and correlation effects are neglected. Formation of associated vacancies will tend to increase the value of the exponent of P_{O_2} in Eq. (9-13). If the cations of solute B exist only in the trivalent state, then Wagner-Hauffe rules apply and we have

$$x_{\Box} \propto \xi \qquad (9\text{-}14)$$

The vacancy concentration in this case will be independent of oxygen partial pressure.

In the case of NiO-FeO mixed oxide the solute, Fe, exists in both the divalent and trivalent states and hence Eq. (9-13) applies. The cation diffusion coefficient $D_{Me^{z+}}$ is given by

$$D_{Me^{z+}} = D_{\square}(Me^{z+}) \cdot x_{\square} \tag{9-15}$$

where $D_{\square}(Me^{z+})$ is the mobility of vacancies in the sublattice of Me^{z+} ions, which is proportional to the rate of exchange of vacancy with a Me^{z+} ion. From Eqs. (9-13) and (9-15) we obtain expressions for self-diffusion coefficients for A and B in the mixed oxide AO-BO.

$$D_A = D_A^o\, P_{O_2}^{1/6}\, \xi^{2/3} \tag{9-16}$$

$$D_B = D_B^o\, P_{O_2}^{1/6}\, \xi^{2/3} \tag{9-17}$$

where

$$D_A^o = D_{\square}(A^{z+})(K_2/4)^{1/3} \tag{9-18}$$

and

$$D_B^o = D_{\square}(B^{z+})(K_2/4)^{1/3} \tag{9-19}$$

The proportionality constants D_A^o and D_B^o thus contain the mobility terms for the respective cations. Equations (9-16) and (9-17) will be used for the self diffusion of Fe and Ni in NiO-FeO mixed oxide in the next section. In this case ξ will be the mole fraction of FeO.

9.5 DIFFUSION MODEL

We may give a theoretical basis to our experimental observations utilizing the diffusion theory and the thermodynamics of the ternary Fe-Ni-O system. Although the qualitative aspects of the diffusion model are valid for all the alloys, quantitative analysis has been attempted only for the dilute alloys. The diffusion model has already been discussed in Chapter 4. Here we will apply it to the particular system of interest.

It has been noted in the last chapter that the external scale consists of two zones. The outer zone is a two phase region consisting of spinel precipitates in a nickel oxide matrix and the inner zone is a single phase nickel oxide zone. For the purpose of simplifying the mass balance and consequently the entire mathematics, we assume that the amount of spinel precipitate in the outer zone is negligible. We also assume that the matrix composition of the outer zone is nearly constant. These assumptions are justified for dilute nickel-iron alloys (i.e. containing upto 5% Fe) from the experimental observations. All assumptions made in Chapter 4 concerning the diffusion model hold. The diffusion model as proposed above is illustrated in Fig. 9-2 for Ni-2% Fe alloy, which shows concentration distributions in weight percent of arbitrarily chosen independent components Fe and Ni schematically for time t.

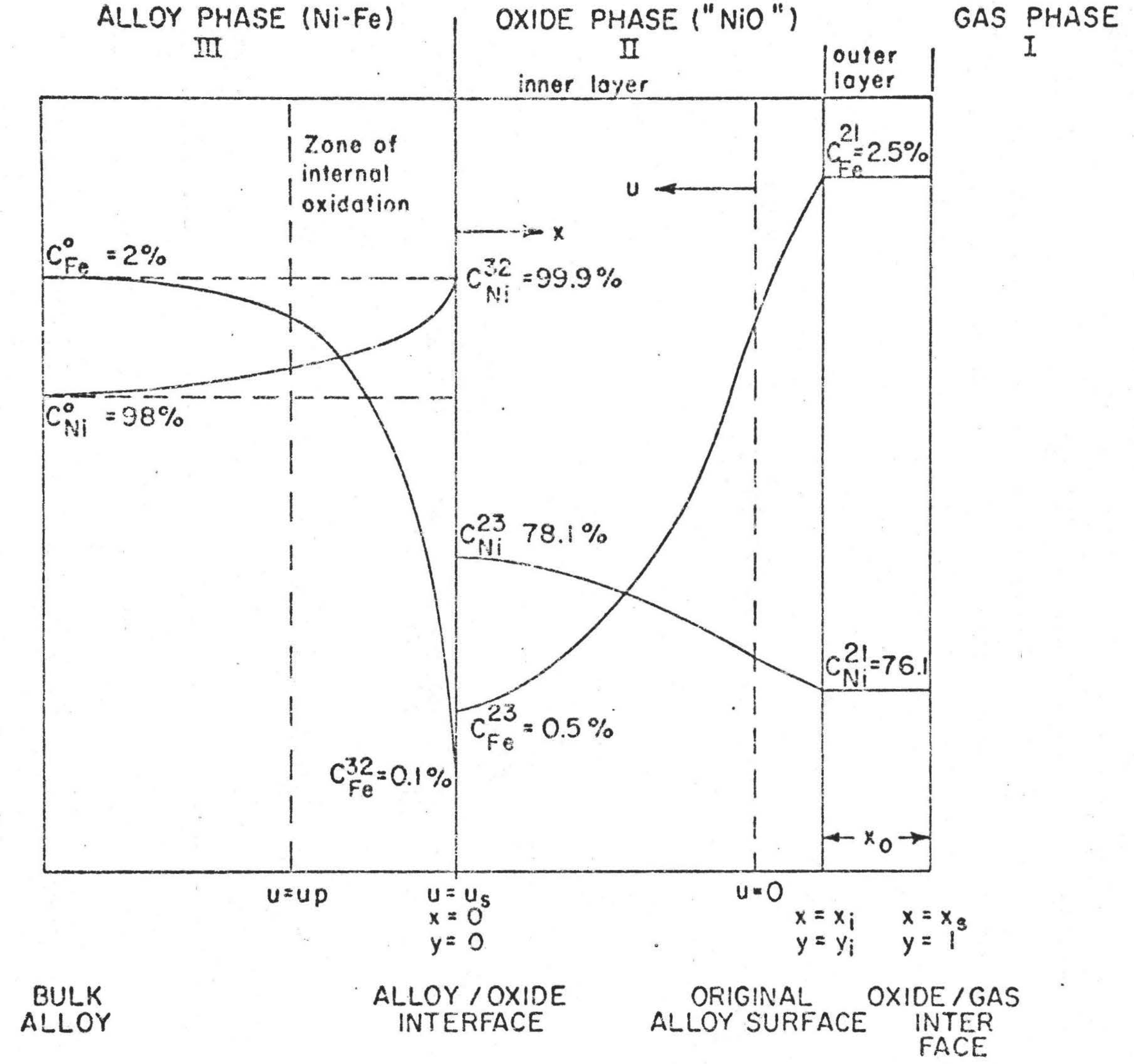

Fig. 9-2: Diffusion model for the oxidation of Ni-2% Fe alloy at 1000°C.

Although the concentrations of Fe and Ni in the outer zone are assumed to be constant for the solution of diffusion equations in the inner zone, they can be qualitatively predicted from thermodynamic considerations. Under the isothermal and isobaric conditions that are assumed, there is only one degree of freedom in the outer two phase zone from the Gibbs'phase rule. Hence specification of the variation of oxygen activity automatically specifies the variation in the cation concentration from the equations for the dissociations reaction of the oxides (i.e. Eqs. (7-13), (7-14) and (7-15)) we obtain the relation,

$$a_O \cdot a_{FeO}^2 \cdot a_{NiO} = 8.22 \times 10^{-7} \tag{9-20}$$

Since the concentration of FeO in the NiO-FeO solid solution is small, we may assume that $a_{NiO} \simeq N_{NiO} = 1-N_{FeO}$ and $a_{FeO} \simeq \gamma_{FeO}^o N_{FeO}$ where γ_{FeO}^o is the Henry law constant for solution of FeO in NiO. Thus Eq. (9-20) becomes.

$$a_O = \frac{8.22\times10^{-7}}{\gamma_{FeO}^{o2} N_{FeO}^2 (1-N_{FeO})} \tag{9-21}$$

For small values of N_{FeO} as obtained in the present case, Eq. (9-21) yields

$$a_O \propto \frac{1}{N_{FeO}^2} \tag{9-22}$$

Since the oxygen activity <u>decreases</u> inwards towards the alloy-oxide interface, Eq. (9-22) predicts that the concentration of iron in the two phase zone should increase in the same direction. This is in accord with the observations (Figs. 8-63 to 8-66). Also, knowing the iron concentration at the boundary of the inner and outer zones, the oxygen activity there can be calculated from Eq. (9-21). This will be utilized as a boundary condition for the solution of the diffusion equation in the inner region.

Using the functional values of D_{Ni} and D_{Fe} as given in Eqs. (9-16) and (9-17), where Ni≡A and Fe≡B, and carrying out an analysis similar to that in Section 4.6 one obtains the following differential equations to describe the variations of the equivalent fraction of FeO, ξ, and oxygen activity a_O in the scale

$$\frac{d\ell n a_O}{dy} = \left[\frac{k'}{\xi^{2/3} a_O^{1/3}} + (p-1)\frac{d\xi}{dy}\right] / [1 + (p-1)\xi] \qquad (9\text{-}23)$$

and
$$[1 + (p-1)\xi]\xi \frac{d^2\xi}{dy^2} + \frac{2}{3}\left(\frac{d\xi}{dy}\right)^2$$
$$+\left(\frac{\xi''}{\xi}\right)^{-1/3}\left(\frac{a_O''}{a_O}\right)^{1/3}\left\{\frac{y(1+(p-1)\xi]^2 - \frac{2}{3}p}{(p-1)(1-\xi'')}\right\}\left(\frac{d\xi}{dy}\right)_{y=y_1}\left(\frac{d\xi}{dy}\right) = 0 \qquad (9\text{-}24)$$

where y_1 is the value of y, a dimensionless parameter defined in Eq. (4-37), at the boundary between the inner and outer zones, $\xi'' = \xi(y=y_1)$ and $a_O'' = a_O(y=y_1)$. p is the ratio of jump frequencies of iron and nickel cations, respectively in an adjacent vacancy. p is assumed to be constant at all concentrations $k' = k/D^o_{Ni}$, where k is the scaling constant for the external scale, defined in Eq. (4-35). D^o_{Fe} is a proportionality constant defined in Eqs. (9-17) and (9-19). A detailed derivation of Eqs. (9-23) and (9-24) is given in Appendix A.

Equations (9-23) and (9-24) which are simultaneous non-linear differential equations in the dependent variables ξ and a_O can be solved in the same manner as for the solution of concentration profiles in NiO-CoO mixed oxide (Section 4.6).

The values of the concentrations obtained as a function of x by electron-probe microanalysis can be converted to mole fractions of FeO and NiO. This yields the boundary values $\xi(y=0)$ and $\xi(y=y_1)$. The oxygen activity $a''_O = a_O(y=y_1)$ can be obtained from equation (9-21). The value of k defined in equation (4-35) is obtained from the experimental results given in Fig. 8-22. Thus for Ni-2% Fe alloy $k = 4.7\times10^{-10}$ cm^2/sec. As discussed in Section 4.6 equations (9-23) and (9-24) need only three boundary conditions, viz., the values of ξ', ξ'' and a''_O. However, if an additional boundary condition $a'_O = a_O(y=0)$ is utilized, then these equations yield the value of k' and consequently D^o_{Ni} from Equation (A-10). The value of a'_O may be estimated from the oxidation reaction for pure Ni [Eq. (4-75)] and from the displacement reaction given by Eq. (7-8) and the corresponding expression for K (Eq. 7-9). The values of the relevant activity coefficients are calculated in Chapter 7. This procedure yields the following expression for the a_O' as a function of ξ'.

$$a_O' = (1 - 0.966\ \xi') \times 6.7 \times 10^{-6} \qquad (9\text{-}25)$$

Eq. (9-25) yields $a_O' = 6.656 \times 10^{-7}$ corresponding to $\xi' = 0.067$.

One of the parameters needed for solution is the ratio , p, of the mobilities of iron and nickel in the nickel oxide scale. We estimate the value of p as follows(138). The cation self diffusion coefficient $D_{Me^{z+}}$ is related to the mobilities of vacancies $D_\square$, and the vacancy concentrations $x_\square$, as follows:

$$D_{M^{z+}} = D_\square\, x_\square \qquad (9\text{-}26)$$

For Ni the value of $D_{Ni^{2+}}$ at 1000°C and $p_{O_2} = 1$ atm. is approximately 10^{-11} cm^2/sec.(60,63,64,75,145,148) (see Appendix B-2). The corresponding value of $x_\square$ at 1 atm. pressure is $\sim 10^{-4}$(75,76). Thus from equation (9-26)

$$D_\square\ (\text{NiO}) \simeq \frac{10^{-11}}{10^{-4}} = 10^{-7}\ \text{cm}^2/\text{sec}. \qquad (9\text{-}27)$$

The value of D_{Fe} in FeO in equilibrium with Fe corresponding to $P_{O_2} = 1.32 \times 10^{-14}$ atm. at 1000°C is approximately 3.5×10^{-8} cm^2/sec. from the data of Himmel et.al.(50) and Carter and Richardson(144). The corresponding value of $x_\square$

is 0.05(145). Thus from Eq. (9-26)

$$D_{\square}\ (\text{FeO}) \simeq \frac{3.5\times10^{-8}}{0.05} = 7.0 \times 10^{-7}\ \text{cm}^2/\text{sec}. \tag{9-28}$$

The values of $D_{\square}$ (NiO) and $D_{\square}$ (FeO) in Eqs. (9-27) and (9-28) involve uncertainties of the order of 100%. From Eqs. (9-27) and (9-28) we obtain,

$$p = \frac{D_{\square}(\text{FeO})}{D_{\square}(\text{NiO})} \simeq \frac{7.0\times10^{-7}}{10^{-7}} = 7 \tag{9-29}$$

This value of p involves a large uncertainty due to uncertainties in the values of the parameters used in the calculations. From the data of Crow(201) we have $p \sim 1$. For iron to accumulate at the external interface, it is necessary that the ratio $p = D^{o}_{Fe}/D^{o}_{Ni}$ be greater than unity(22). It can be inferred from the literature data that its value is not very much greater than unity. In solving the differential equations (9-23) and (9-24) the value which resulted in the best fit to the data was chosen. This yielded p = 3.0.

The calculated and observed values of ξ as a function of the normalized parameter y are given in Fig. 9-3 . The corresponding values of the oxygen activity a_O in the scale are given in Fig. 9-4. The results yield $(d\xi = dy)_{y=y_1} = 0.035$ and $(d\xi/dy)_{y=0} = 0.013$.

By comparing the value of a_O' obtained from the solution of the differential Eqs. (9-23) and (9-24) to the value obtained from Eq. (9-25) the value of k' can be obtained by an iterative process. For Ni-2% Fe alloy the value of k' was 0.0070. Since k is known D_{Ni}^{O} can be calculated. This yields $D_{Ni}^{O} = 7.1 \times 10^{-8}$ cm^2/sec.

The above analysis lacks a true experimental closure. This is because two unknown parameters, p and D_{Ni}^{O} were obtained from the analysis, using experimental data as boundary conditions. Eqs. (9-23) and (9-24), however, can be solved for the oxide scale on Ni-4% Fe alloy with similar assumptions and the same value of parameters p and D_{Ni}^{O} . The solution obtained should show a close agreement with the experimental data since the form of Eqs. (9-16) and (9-17) should remain the same for the NiO-FeO mixed oxide formed on Ni-4% Fe alloy and the ratio of jump frequencies of Fe and Ni should remain constant if strong correlations do not prevail.
The various boundary values for Ni-4% Fe alloy may be obtained in a manner similar to that for Ni-2% Fe alloy as discussed above. The boundary values, the values of required parameters and solutions to differential equations for Ni-2% Fe and Ni-4% Fe alloys are summarized in Tables 9-1 and 9-2 respectively. The calculated and observed values of ξ as a function of the normalized distance parameter y for Ni-4% Fe alloy are given in Fig. 9-5. An excellent agreement is obtained between the calculated and the observed values.
The corresponding values of oxygen activity a_O are given in Fig. 9-6.

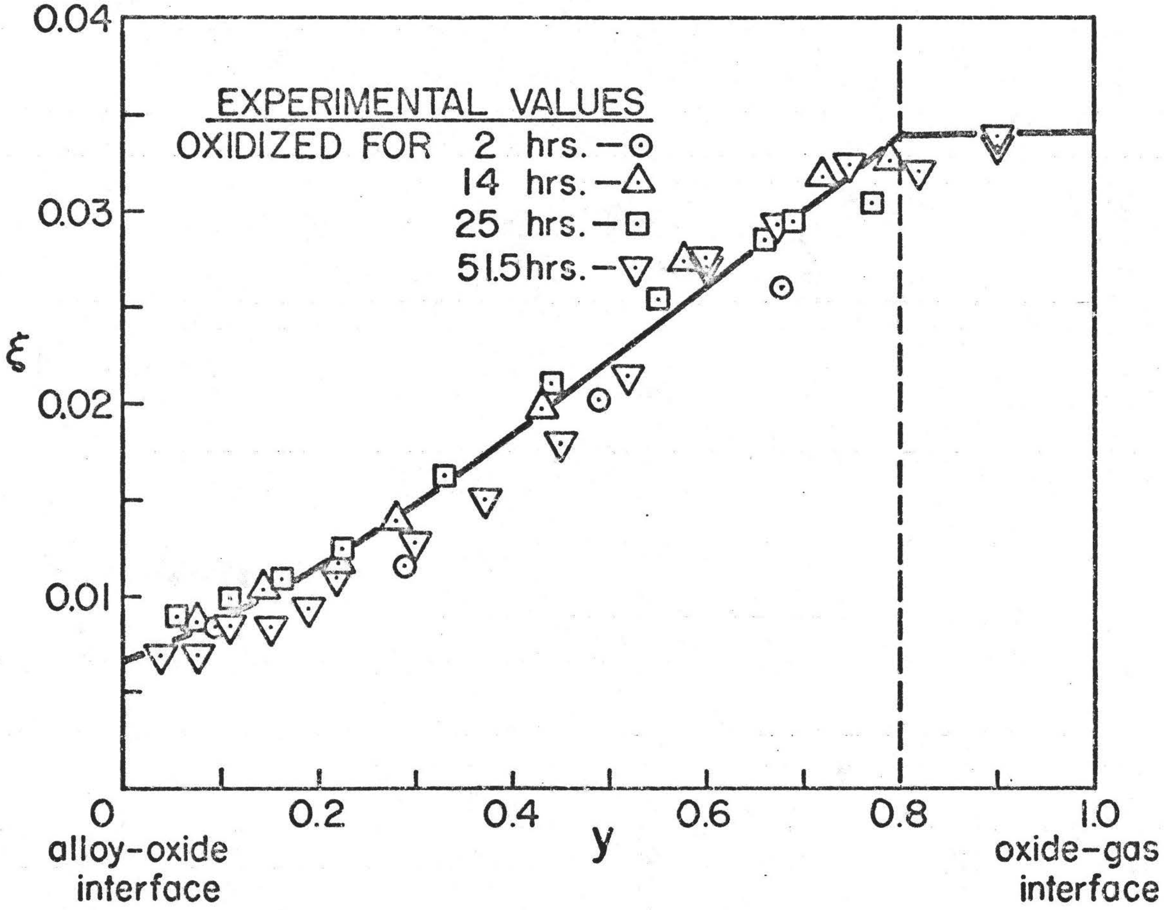

Fig. 9-3: Mole fraction of FeO, ξ, as a function of normalized distance coordinate y in the NiO-Fe oxide scale formed on Ni-2% Fe alloy oxidized at 1000°C in pure oxygen. Solid line represents calculated values from Eqs. (9-23) and (9-24). Experimental points are from Fig. 8-63

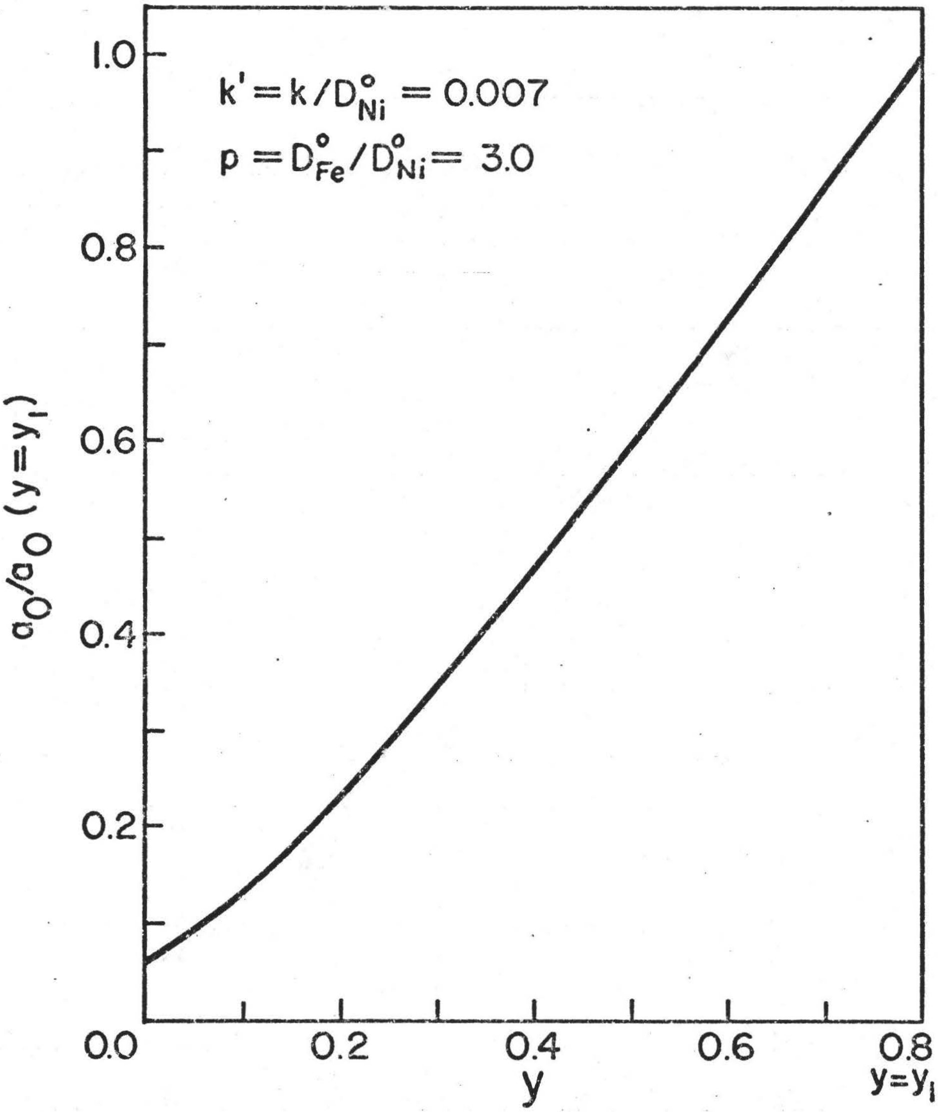

Fig. 9-4: Oxygen activity versus normalized distance in the NiO-FeO oxide scale from Eqs. (9-23) and (9-24) - Ni-2% Fe alloy.

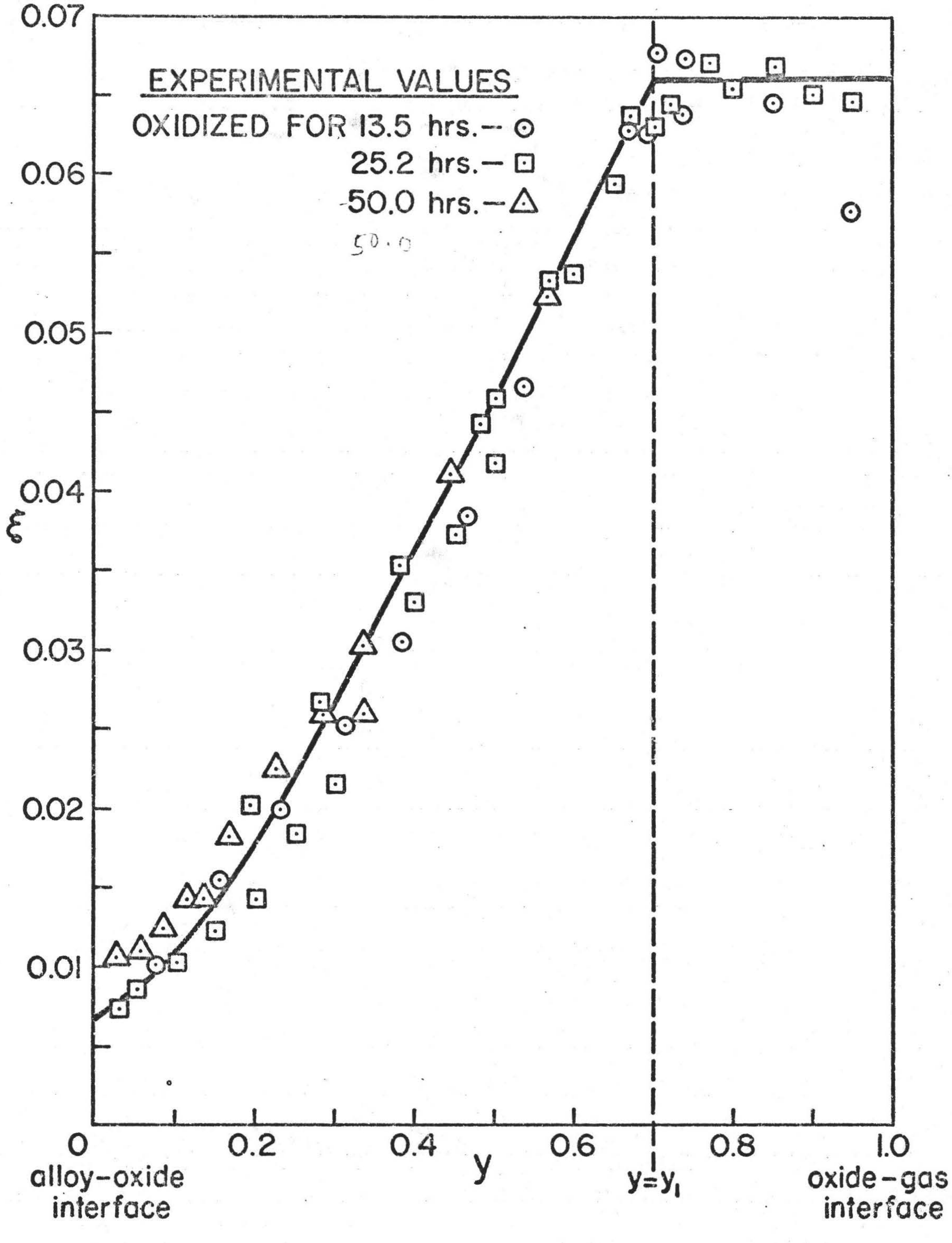

Fig. 9-5: Mole fraction of FeO, ξ, as a function of normalized distance coordinate y in the NiO-FeO oxide scale formed on Ni-4% Fe alloy oxidized at 1000°C in pure oxygen. Solid line represents calculated values from Eqs. (9-23) and (9-24). Experimental points are from Fig. 8-64.

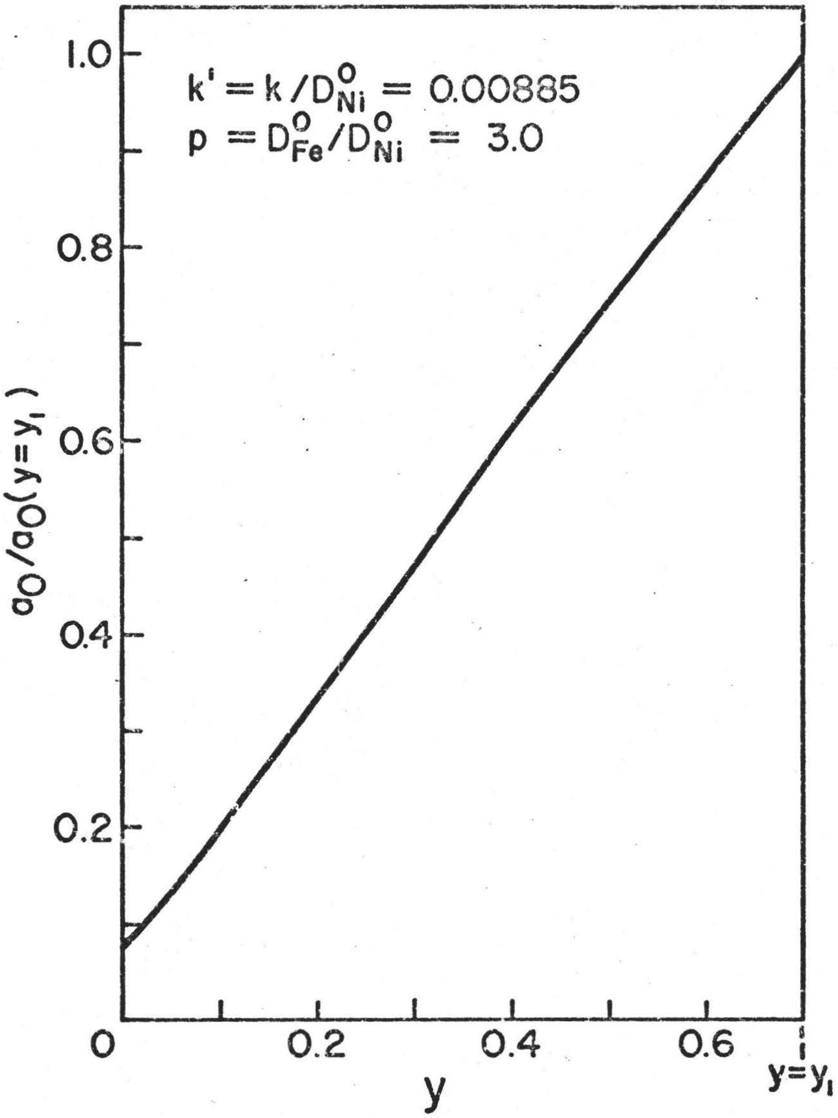

Fig. 9-6: Oxygen activity versus normalized distance in the NiO-FeO oxide scale from Eqs. (9-23) and (9-24) - Ni-4% Fe alloy.

Equation (A-17) of Appendix A can be applied to the Ni-2% Fe alloy and Ni-4% Fe alloy to obtain corresponding expressions for k/D_{Ni}^{o} for these alloys. Division of the respective expressions gives the ratio of scaling constants for these alloys.

$$\frac{k_1}{k_2} = \left(\frac{\xi_1''}{\xi_2''}\right)^{m-1} \left(\frac{a_o''(1)}{a_o''(2)}\right)^{n} \left(\frac{1-\xi_2''}{1-\xi_1''}\right) \frac{(d\xi/dy)_{y=y_1}^{(1)}}{(d\xi/dy)_{y=y_1}^{(2)}} \qquad (9\text{-}30)$$

where m = 2/3 and n = 1/3 and indices 1 and 2 correspond to Ni-2% alloy and Ni-4% Fe alloy, respectively. Since the values of a_o'' are obtained from Eq. (20) it can be seen that

$$\frac{a_o''(1)}{a_o''(2)} = \frac{\xi_2''^{\,2}(1-\xi_2'')}{\xi_1''^{\,2}(1-\xi_1'')} \qquad (9\text{-}31)$$

From Eqs. (9-30) and (9-31) we obtain after substituting the values of m and n

$$\frac{k_1}{k_2} = \left(\frac{\xi_2''}{\xi_1''}\right) \left(\frac{1-\xi_2''}{1-\xi_1''}\right)^{4/3} \frac{(d\xi/dy)_{y=y_1}^{(1)}}{(d\xi/dy)_{y=y_1}^{(2)}} \qquad (9\text{-}32)$$

Substituting the values of various parameters from Tables 9-1 and 9-2 we obtain

$$\frac{k_1}{k_2} = 0.78 \qquad (9\text{-}33)$$

The value of the above ratio as obtained from the experimental results illustrated in Figs. 8-22 and 8-23 is 0.75. The agreement between the calculated and experimental values is excellent. Two inferences can be drawn from this. As discussed in Section 4.6.3 the value of scaling constant, k, can be calculated from the diffusion merely from the concentration profiles in the oxide if the cation diffusion coefficients and the boundary values are known. This shows the predictive power of the diffusion model. In the present case since the parameter D^{o}_{Ni} is not independently known we eliminate it by taking the ratios of scaling constants for two different alloys. Nevertheless, Eq.(9-32) yields a kinetic parameter from a knowledge of concentration profiles in the oxide. The agreement between the calculated and the experimental values also indicates internal consistency of the diffusion analysis and the validity of the defect model used for the mixed oxide.

9.6 DIFFUSION IN ALLOY

Calculation of the concentration profiles in the alloy when an internal oxidation zone is present is a difficult task. However Kirkaldy(24) has shown that if the variation of oxygen solubility in the alloy with respect to the concentration of an alloying element B is negligible, i.e. $\frac{dC_O}{dC_B} << 1$, then the effective diffusion coefficient in the alloy is the interdiffusion coefficient of the metallic constituents of the alloy. An approximate estimate of the interdiffusion coefficient D_{alloy}, in the alloy can be made from the solution of the diffusion equation for the alloying element (iron in the present case) in the alloy phase. It is necessary in this analysis to neglect the blocking effect of the internal precipitate particles.

Let a parameter α be defined by the equation

$$u_s = \alpha\sqrt{t} \qquad (9\text{-}34)$$

where u_s is the coordinate of the alloy-oxide interface with respect to the original alloy surface. α therefore defines the rate of recession of the alloy-oxide interface with respect to the original alloy surface. The solution of the diffusion equation (4-40) in the alloy for a moving boundary problem, assuming D_{alloy} to be constant is,

$$C_{Fe} = C'_{Fe} + (C^{o}_{Fe} - C'_{Fe}) \frac{\mathrm{erfc}(x'/2\sqrt{D_{alloy}t})}{\mathrm{erfc}(\alpha/2\sqrt{D_{alloy}})} \qquad (9\text{-}35)$$

where x' is the distance from the alloy-oxide interface, C'_{Fe} is the concentration of Fe at the alloy-oxide interface and C^{o}_{Fe} is the concentration of iron in the bulk-alloy. α in Eq. (9-35) is defined by Eq. (9-34) and D_{alloy} is the interdiffusion coefficient in the alloy.erfc denotes complimentary error function. From Eq. (9-35) we obtain

$$\frac{dC_{Fe}}{d\lambda} = \frac{(C^{o}_{Fe} - C'_{Fe})}{\mathrm{erfc}(\alpha/2\sqrt{D_{alloy}})} \frac{1}{2\sqrt{D_{alloy}}} \exp\left(-\frac{\lambda^2}{4D_{alloy}}\right) \qquad (9\text{-}36)$$

where $\lambda = \frac{x'}{\sqrt{t}}$.

At the alloy-oxide interface $\lambda = 0$ and hence

$$\left(\frac{dC_{Fe}}{d\lambda}\right)_{\lambda=0} = \frac{(C^{o}_{Fe}-C'_{Fe})}{\mathrm{erfc}(\alpha/2\sqrt{D_{alloy}})} \quad \frac{1}{2\sqrt{D_{alloy}}} \qquad (9\text{-}37)$$

If the values of C^{o}_{Fe}, C'_{Fe}, $\left(\frac{dC_{Fe}}{d\lambda}\right)_{\lambda=0}$ and α are known then Eq. (9-37) can be solved for D_{alloy}. An estimate of the value of D_{alloy} is made from the available values for Ni-2% Fe and Ni-8% Fe alloys. The values of α for these alloys are approximately 2.4×10^{-5} cm/sec$^{1/2}$ and 1.8×10^{-5} cm/sec$^{1/2}$, respectively. From the values of C^{o}_{Fe} and C'_{Fe} from Table 9-3 and the values of $\left(\frac{dC_{Fe}}{d\lambda}\right)_{\lambda=0}$ from Figs. 8-63 and 8-66 D_{alloy} is estimated to be $\sim 10^{-10}$ cm^2/sec. a value which is about one order of magnitude higher (see Table B-1). Considering the error involved in estimating the value of error functions for large arguments and the approximations made, large errors in the calculations are expected.

9.7 OXYGEN SOLUBILITY CURVE FOR Fe-Ni ALLOYS AND INTERNAL OXIDATION

No experimental results are available on maximum oxygen solubility in solid iron-nickel alloys as a function of the alloy composition. However Swisher and Turkdogan(195) have determined the maximum oxygen solubility for pure iron at 1000°C as 3 ppm. The maximum oxygen solubility of pure Ni at 1000°C is known to be 150 ppm(180). From these terminal values, the oxygen solubility curve for Fe-Ni alloys can be qualitatively estimated from the solubility theory treated by Smith(202). Using the Gibbs-Duhem equations for the oxide and alloy phases in equilibrium and the Wagner formalism(135) for the activity coefficients, Smith determined the variation of oxygen solubility with alloy composition in terms of the composition of the alloy and oxide phases and the interaction parameters ε_{ij} in the alloy where ε_{ij} are defined by

$$\varepsilon_{ij} = \frac{\partial \ell n \gamma_i}{\partial x_j} \qquad (9\text{-}38)$$

where γ_i is activity coefficient of species i and x_j is the mole fraction of species j. In the limiting case where the maximum solubility of oxygen in the alloy is very small, i.e. $x_O^A \ll 1$, the slope of the solubility curve is given by,

$$\left.\frac{dX_O}{dX_2}\right|_{x_2 \to 0} = [1-(1+\varepsilon_{21})x_O^{ox}]\ \frac{X_O^o}{X_O} \qquad (9\text{-}39)$$

where X_O^o is the oxygen solubility in the pure metal 1, and 2 is the solute metal. $X_O^{ox} = 0.5$ for an MO compound and $X_O^{ox} = 4/7$ for an M_3O_4 compound. This equation may be applied in the two phase nickel oxide-alloy region since the maximum iron content of the alloy is less than 1% in this region. Since $X_O^o \ll 1$, $\frac{dX_O}{dX_{Fe}} \sim 0$, i.e., the solubility of oxygen in the alloy remains nearly constant and the oxygen solubility line in this region may be drawn as a straight line parallel to the Fe-Ni binary axis. Since the Fe-Ni binary system is nearly ideal(100,101) the interaction parameters ε_{ij} are expected to be small. Grundmann(203) has found the interaction parameter $\varepsilon_{O}^{(Ni)} = 1.64$ for $N_{Ni} < 0.5$ and $\varepsilon_{O}^{(Ni)} = 3.34$ for $N_{Ni} > 0.5$, in liquid nickel-iron alloys at 1600°C. This value is expected to rise with decrease in temperature. However since it is not much greater than unity, the oxygen solubility of the alloys is not expected to vary much in the two phase wustite-alloy region. The major variation in oxygen solubilities is thus expected in the two phase spinel-alloy region. This may also be inferred from the corresponding equilibrium oxygen potentials. We have

$$\left.\begin{aligned} p_{O_2}\ (\text{Fe/FeO}) &= 1.32 \times 10^{-15}\ \text{atm.} \\ p_{O_2}\ (A_1/W_1/S_1) &= 3.26 \times 10^{-14}\ \text{atm.} \\ p_{O_2}\ (A_2/N_1/F) &= 4.03 \times 10^{-11}\ \text{atm.} \\ p_{O_2}\ (\text{Ni/NiO}) &= 4.48 \times 10^{-11}\ \text{atm.} \end{aligned}\right\} \qquad (9\text{-}40)$$

where the symbols A_1, A_2, W_1, S_1, F and N_1 correspond to Fig. 7-6. The variation in the oxygen potential in the two-phase nickel-oxide alloy region is thus very small. The variation in the oxygen potential in the two phase wustite-alloy region is about one order of magnitude, whereas the variation in the two phase spinel-alloy region is about three orders of magnitude. Based on these considerations the oxygen solubility curve for Fe-Ni alloys may be plotted qualitatively, as illustrated in Fig. 9-7. This qualitative feature agrees well with the experimental results of Grundmann at 1600°C.

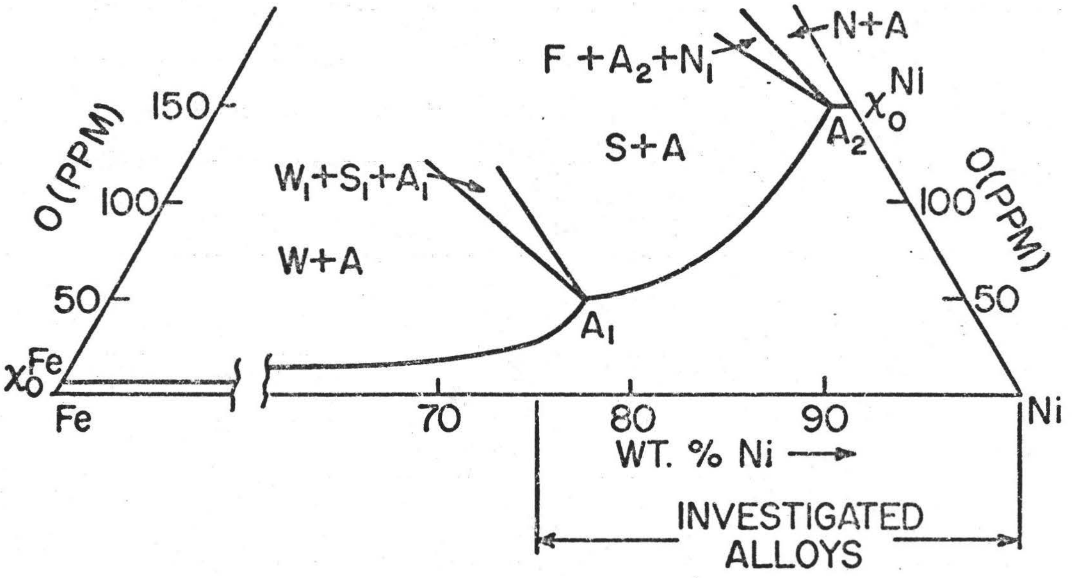

Fig. 9-7: Oxygen solubility curve for Fe-Ni alloys at 1000°C (schematic).

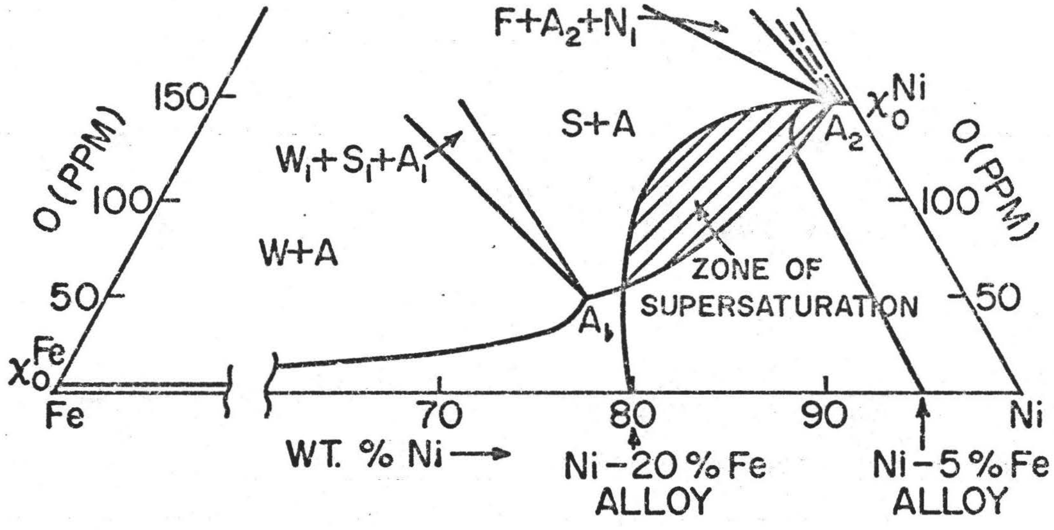

Fig. 9-8: "Virtual" diffusion paths in the alloy phase for Ni-5% Fe and Ni-20% Fe alloys showing zones of oxygen supersaturation (schematic).

The diffusion coefficients of Fe, Ni and O in the various phases are given in Appendix B (Table B-2). It can be seen from the table that the diffusion coefficient of oxygen in the alloy is more than four orders of magnitude higher than that of Fe and Ni. This will result in a steep concentration gradient for the alloying elements and a shallow gradient for oxygen. For the shape of the solubility curve illustrated in Fig. 9-5, this will easily result in constitutional supersaturation and hence internal oxidation. Fig. 9-6 shows schematic virtual diffusion paths for Ni-5% Fe and Ni-20% Fe alloys , consistent with the above considerations. It can be seen from Fig. 9-8 that for the shape of the oxygen solubility curve in the spinel-alloy region it is extremely easy to produce constitutional supersaturation even for steeper oxygen concentration gradients. Especially in the case of high iron alloys, large amounts of supersaturation can be produced. The alloys investigated (0-25% Fe) are therefore highly susceptible to internal oxidation with the extent of internal oxide increasing with increasing iron content of the bulk alloy.

9.7 COMPOSITION PATH

The results (Figs. 8-63 to 8-66) indicate that the concentration profiles for the oxidized samples in the oxide and alloy phases are invariant in λ-space. The solution

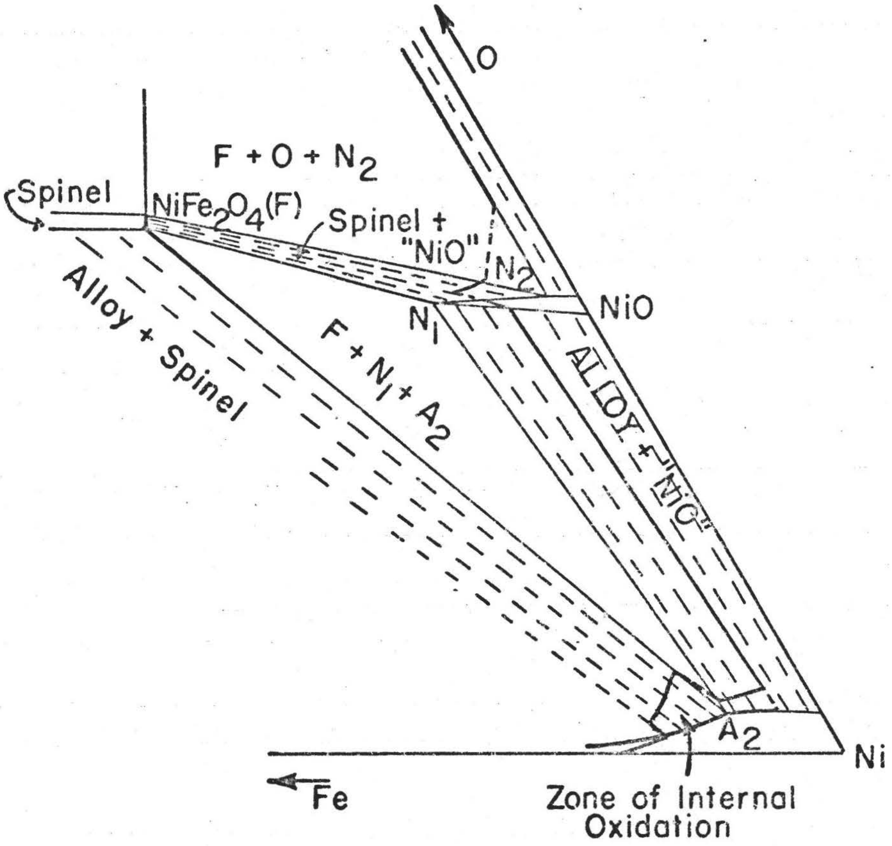

N_1 - $Fe_{0.13}Ni_{0.87}O$ N_2 - $Fe_{0.01}Ni_{0.99}O$

Fig. 9-9: Composition path for the investigated alloys (distorted scale).

of the diffusion equation are therefore parametric in λ. The concentration profiles in the λ-space can be transposed on to the phase diagram by eliminating λ. This transposition reflects the condition of mass conservation and monotonic activity gradients for the diffusing species.

The composition path for the investigated alloys in stationary state oxidation is shown in Fig. 9-9. This path is consistent with metallographic and electron-probe observations and is also consistent with the thermodynamic and kinetic considerations. The oxide-gas interface corresponds approximately to the three phase spinel ($NiFe_2O_4$)-nickel oxide-oxygen equilibrium. The zone adjacent to this interface is a two-phase spinel-nickel oxide zone, since single phase nickel-oxide can not be sustained at high oxygen potentials in this system. Below the two phase spinel-nickel oxide zone is the single phase nickel oxide zone in which the iron is enriched towards the outer interface due to higher mobility of Fe (corresponding to $p = 3$). The alloy oxide interface corresponds to the two-phase nickel oxide-alloy equilibrium. The composition path then crosses over to the two-phase spinel-alloy region via the three phase spinel-nickel oxide-alloy region. This corresponds to the zone of internal oxidation where the alloy and spinel compositions are given by the corresponding ends of the tie-lines which are cut. It can be seen from the ternary phase diagram that the iron content of spinel increases with increasing iron content of the bulk alloy. It is therefore expected that the spinel particles in the internal oxidation zone will be enriched in iron as we go towards the bulk alloy. The final segment of the composition path is traversed in the single phase alloy region corresponding to the unoxidized alloy.

The composition path shown in Fig. 9-9 shows monotonically decreasing values of oxygen activity from the outer surface of the oxide to the bulk alloy, as required from thermodynamic considerations. It has already been shown in the preceding sections that the cations show monotonically decreasing activities in the oxide scale towards the oxide-gas interface. Recall that the flux equations for the cations in the scale were written in terms of decreasing activities towards the oxide-gas interfacd, and that the profiles in the two-phase nickel-oxide-spinel zone satisfy thermodynamic relation (9-21) consistent with decreasing oxygen activity inwards.

Fig. 9-9 schematically illustrates composition path typical of all the alloys investigated. Interfacial compositions corresponding to this path for alloys containing 2-8% Fe are given in Table 9-3 from which the actual paths can be estimated.

TABLE 9-1

Data for the Solution of Diffusion Equations in NiO-FeO Mixed Oxide and the Resultant Solution .

Ni-2% Fe alloy

$p = D^{o}_{Fe}/D^{o}_{Ni} = 3$; $m = 2/3$; $n = 1/3$

$y_1 = 0.8$

$\xi'' = \xi(y = y_1) = 0.034$; $a_O'' = a_O(y = y_1) = 1.1 \times 10^{-4}$

$\xi' = \xi(y=0) = 0.0068$; $a_O' = a_O(y=o) = 6.65 \times 10^{-6}$

$k = 4.7 \times 10^{-10}$ cm^2/sec.

$D^{o}_{Ni} = 6.7 \times 10^{-8}$ cm^2/sec ; $k' = k/D^{o}_{Ni} = 0.0070$

$(\frac{d\xi}{dy})_{y=y_1} = 0.0385$; $(\frac{d\xi}{dy})_{y=0} = 0.0148$

TABLE 9-2

Data for the Solution of Diffusion Equations in NiO-FeO Mixed Oxide and the Resultant Solution

Ni-4% Fe alloy

$p = D^o_{Fe}/D^o_{Ni} = 3$; $m = 2/3$ $n = 1/3$

$y_1 = 0.7$

$\xi'' = \xi(y=y_1) = 0.066$; $a_o'' = a_o(y=y_1) = 2.9 \times 10^{-4}$

$\xi' = \xi(y=0) = 0.0069$ ' $a_o' = a_o(y=o) = 6.56 \times 10^{-6}$

$k = 6.3 \times 10^{-10}$ cm^2/sec.

$D^o_{Ni} = 6.7 \times 10^{-8}$ cm^2/sec ; $k' = k/D^o_{Ni} = 0.00885$

$(\frac{d\xi}{dy})_{y=1} = 0.099$; $(\frac{d\xi}{dy})_{y=o} = 0.0069.$

TABLE 9-3

Interfacial Compositions for Ni-Fe Alloys Containing 2-8% Fe, Oxidized at 1000°C

$\lambda = \lambda_i$ - Position of the boundary between unoxidized alloy and the zone of internal oxidation

$y = 0$ - Alloy-oxide interface

$y = y_1$ - Position of the boundary between inner single phase zone and outer two phase zones

ξ - Mole fraction of FeO in FeO-NiO solid solution

Bulk Alloy Composition	Interfacial composition at			
	Alloy		Oxide Mole fraction of NiO = 1-ξ	
	$\lambda = \lambda_i$	$y = 0$	$y = 0$ ξ	$y = y_1$ ξ
Ni-2% Fe	1.9% Fe	0.2% Fe ∿150 ppm O	0.0068	0.034
Ni-4.3% Fe	4.15% Fe	0.35% Fe ∿150 ppm O	0.008	0.066
Ni-6.6% Fe	6.4% Fe	0.65% Fe ∿150 ppm O	0.017	0.075
Ni-8.5% Fe	8.4% Fe	0.9% Fe ∿150 ppm O	0.026	0.090

CHAPTER 10

CONCLUSIONS AND REMARKS

10.1 CONCLUSIONS

The diffusion-controlled oxidation of binary alloys has been discussed on the basis of the concept of local equilibrium and phenomenological theory of diffusion (Chapter 4). A theory of stationary state oxidation was developed from this analysis and linked with the concept of the diffusion path on the isotherm. An analysis based on these concepts yielded the diffusion equation in the alloy and oxide phases. It was demonstrated that these equations lead to a complete description of the diffusion-controlled oxidation of binary alloys provided the relevant data are available.

Equations giving the variation of the cation distributions and oxygen activity in the scale [Eqs. (4-69) and (4-73)] were derived from the ternary diffusion analysis. These equations were applied to the oxidation of Ni-10.9% Co alloy at 1000°C in pure oxygen. Good agreement between the calculated and observed values was obtained. The effect of ternary interactions in causing uphill diffusion of cations was demonstrated. It was also demonstrated that the rate of thickening of the external scale can be calculated from this analysis. The ternary diffusion analysis was further developed to allow for diffusion of oxygen in the alloy and subsequent internal oxidation.

Phenomena observed in binary alloy oxidation such as supersaturation, internal oxidation and morphological instability were qualitatively discussed in Chapter 5. Certain rules in drawing diffusion paths on the ternary isotherm were discussed. The concept of diffusion path on the isotherm was applied to high temperature oxidation of such important alloy systems as Fe-Ni, Fe-Cr and Ni-Cr.

The ternary diffusion analysis and the concept of diffusion path were formulated in a sufficiently general manner that the results could be applied to oxidation or sulfidation of all binary alloys.

The diffusion analysis was applied to a specific system, viz., nickel-iron alloys at 1000°C. To this end the ternary Fe-Ni-O isotherm at 1000°C has been determined.

A detailed study of the kinetics of oxidation of nickel-iron alloys containing up to 25% iron was carried out. It was found that continuous long term kinetics (upto 75 hours) can be observed for these alloys. These alloys oxidized parabolically at long times (> 15 hours) after a period of transient oxidation. The parabolic rate constant for these alloys was obtained as a function of bulk alloy composition (Fig. 8-21).

From the metallographic study of the oxidized sample it was demonstrated that spinel ($Ni_xFe_{3-x}O_4$), and nickel oxide containing iron $Fe_xNi_{1-x}O$ are the only oxides obtained during the oxidation of these alloys. Spinel occurs internally as a precipitate phase in the alloy (internal oxide) and externally as a second phase in the outer zone of the external scale. Nickel oxide is the matrix phase of the external scale.

A model for the oxidation of these alloys was developed from the metallographic study (Figure 9-1), which qualitatively explained the variation of the parabolic rate constant, k_p,with the bulk alloy composition (Fig. 8-21).

The concentration profiles in the outer zone of the external scale were predicted on the basis of thermodynamic arguments. These agree well with the observed profiles which were determined by electron-probe microanalysis. The cation distribution and oxygen activity profile in the inner single-phase nickel oxide zone were calculated utilizing the ternary diffusion analysis developed in Chapter 4. This was carried out numerically for Ni-2% Fe and Ni-4% Fe alloys for which a diffusion model (Fig. 9-2) was developed. The theoretically predicted profiles agreed well with the observed profiles (Figs. 9-3 and 9-5). The ratio of the scaling constants for Ni-2% Fe alloy and Ni-4% Fe alloy was calculated. The good agreement between the calculated and experimental values demonstrated the predictive power as well as the internal consistency of the diffusion model.

An attempt was made to explain the occurrence of internal oxidation in these alloys. From the observed concentration profiles and metallographic structures, the diffusion path on the isotherm for these alloys was constructed, which is consistent with kinetic and thermodynamic considerations (Fig. 9-9).

The totality of the experimental observations and theoretical arguments, i.e., the metallographic and electron probe studies, kinetic data, the schematic and diffusion models, the diffusion path have considerably advanced our knowledge of the oxidation mechanism of nickel-rich nickel-iron alloys.

10.2 REMARKS

In rationalizing the complex processes that occur during the oxidation of binary alloys the assumption of local equilibrium was basic to the theoretical analysis. The experiments suggest that the assumption is valid . It was also assumed in the theoretical analysis that the oxide layers are free of pores and cracks, have uniform thickness and are adherent to the alloy substrate. Although this is somewhat idealized, experimental fact was not too far from the ideal.

In the present analysis two phase regions were assumed to be due to the morphological breakdown of the planar interface between two single phase regions or alternatively due to the occurrence of supersaturated regions within a single phase field.

Although the method seems to be the most appropriate for the analysis within the alloy matrix, it may not be the only way to consider two-phase fields in the oxide scale. Wagner$^{(110,114)}$ has considered simultaneous nucleation and growth of two phases to form a two phase region. This treatment may be extended to a generalized ternary analysis.

During any attempt at a quantitative analysis of the problem of oxidation of alloys, a lack of knowledge of the thermodynamic and the transport properties of the mixed oxide systems is felt. In a mixed oxide system, there may be interactions among like and unlike defects such as the vacancies and the solute atoms. These interactions profoundly influence the thermodynamic and the transport properties of these systems. The Wagner-Hauffe rules do not provide a useful guideline in considering transport through such systems as FeO-NiO or NiO-CoO. The Wagner-Schottky model of nonstoichiometric crystals becomes inadequate for the discreption of grossly defective oxides such as FeO or CoO, or for concentrated oxide solutions$^{(7,204,205)}$. Unfortunately, no general statistical theory of mixed oxide systems is as yet available. The specific information that is needed in the analysis of the oxidation of alloys concerns the effect of the cation and the anion activities on the defect structures of a mixed oxide system, the variation of cation activities with composition and also the functional form of the concentration dependence of the diffusion coefficients of the mobile species in the oxides. Apart from this, data on the shape of the oxygen solubility curves for various alloy systems is highly desirable for an analysis of the phenomena of internal oxidation and morphological breakdown.

The theory of oxidation of binary alloys has recently shown substantial progress(22,23,24). This together with microprobe measurements provides for the future a powerful method for the investigation of oxide scale structures, the cation distributions in the oxides and the distribution of the metallic components in the alloy. Together they should help considerably in further investigation in the near future.

APPENDIX A

DERIVATION OF DIFFERENTIAL EQUATIONS GIVING SOLUTE CATION DISTRIBUTION AND OXYGEN ACTIVITY VARIATION IN NiO-FeO MIXED OXIDE FORMED DURING OXIDATION OF Ni-Fe ALLOYS AT 1000°C

In NiO-FeO solid solutions we have $z_{Ni}=z_{Fe} = z_O = 2$. In the following analysis symbols A, B and X of Chpater 4. correspond to Ni, Fe and O respectively. Thus Eqs. (4-17) and (4-18) reduce to following expressions respectively,

$$D_{Ni}(1-\xi)\left(-\frac{\partial \ell n a_{NiO}}{\partial \xi}\frac{d\xi}{dy}+\frac{d\ell n a_O}{dy}\right)$$

$$+ D_{Fe}\,\xi\left(-\frac{\partial \ell n a_{FeO}}{\partial \xi}\frac{d\xi}{dy}+\frac{d\ell n a_O}{dy}\right) = k \qquad \text{(A-1)}$$

$$yk\frac{d\xi}{dy} = -\frac{d}{dy}\left[D_{Fe}\xi\left(\frac{\partial \ell n a_{FeO}}{\partial \xi}\frac{d\xi}{dy}-\frac{d\ell n a_O}{dy}\right)\right] \qquad \text{(A-2)}$$

where ξ is the equivalent fraction (equal to mole fraction) of FeO in NiO-FeO mixed oxide and y and k are defined in Eqs. (4-14) and (4-16) respectively.

Henry-law behaviour for FeO in NiO-FeO solid solution is assumed. This can be expressed as

$$\frac{\partial \ell n a_{FeO}}{\partial \xi} = \frac{1}{\xi} \qquad \text{(A-3)}$$

The Gibbs-Duhem equation for the oxide may be written as

$$\frac{\partial \ell a_{NiO}}{\partial \xi} = -\frac{\xi}{1-\xi}\frac{\partial \ell n a_{FeO}}{\partial \xi} \qquad \text{(A-4)}$$

From Eqs. (A-3) and (A-4) we have

$$\frac{\partial \ln a_{NiO}}{\partial \xi} = - \frac{1}{1-\xi} \; . \qquad \text{(A-5)}$$

Substitution of Eqs. (A-3) and (A-5) in Eq. (A-1) yields

$$(D_{Ni}-D_{Fe}) \frac{d\xi}{dy} + \frac{d\ln a_O}{dy} [(1-\xi)D_{Ni} + \xi D_{Fe}] = k \qquad \text{(A-6)}$$

The variation of cation diffusion coefficients with ξ and a_O in the NiO-FeO mixed oxide is given by Eqs. (9-35) and (9-36) where A ≡ Ni and B ≡ Fe. This may be generally expressed as

$$D_{Ni} = D^{o}_{Ni} \; a_O^n \xi^m \qquad \text{(A-7)}$$

$$D_{Fe} = D^{o}_{Fe} \; a_O^n \xi^m \qquad \text{(A-8)}$$

In our case $n = 1/3$ and $m = 2/3$.

Let $$p = D^{o}_{Fe}/D^{o}_{Ni} \qquad \text{(A-9)}$$

and $$k' = k/D^{o}_{Ni} \qquad \text{(A-10)}$$

Substitution of Eqs. (A-7) to (A-10) into Eq. (A-6) gives the variation of oxygen activity in the scale

$$\frac{d\ln a_O}{dy} = [\frac{k'}{\xi^m a_O^n} + (p-1) \frac{d\xi}{dy}]/[1 + (p-1)\xi] \qquad \text{(A-11)}$$

Substituting the values of various parameters above, Eq. (A-2) may be rewritten as,

$$- yk' \frac{d\xi}{dy} = \frac{d}{dy} [\xi^{m+1} a_O^n (\frac{1}{\xi} \frac{d\xi}{dy} - \frac{d\ell na_O}{dy})] \qquad \text{(A-12)}$$

From Eqs. (A-11) and (A-12), we obtain, after eliminating $\frac{d\ell na_O}{dy}$

$$-yk' \frac{d\xi}{dy} = \frac{d}{dy} [\frac{\xi^m a_O^n}{1+(p-1)\xi} \frac{d\xi}{dy} - \frac{k'\xi}{1+(p-1)\xi}] \qquad \text{(A-13)}$$

After carrying out the intended differential and eliminating $\frac{d\ell na_O}{dy}$ terms using equation (A-11) leads to

$$\xi[1+(p-1)\xi] \frac{d^2\xi}{dy^2} + [m-(1-n-m)(p-1)\xi] (\frac{d\xi}{dy})^2$$

$$+ \{\frac{y[1+(p-1)\xi]^2 - (1-n)p}{p}\} \frac{k' \frac{d\xi}{dy}}{a_O^n \xi^{m-1}} = 0 \qquad \text{(A-14)}$$

For the diffusion model used in the present analysis as illustrated in Fig. 9-2 the value of ξ is assumed constant between $y=y_1$ and $y = 1$, where $y = y_1$ is the boundary between the inner single phase region and the outer two phase region. It is therefore possible to write mass balance for Fe at this boundary. The flux of Fe at $y = y_1$ is utilized for thickening of the inner region and also the outer two phase regions. Since the amount of precipitates in the outer zone is assumed to be zero the mass balance for Fe at $y=y_1$ is

$$J_{Fe(eq)}\; y=y_1) = \frac{\xi''}{V_{eq}} \frac{dx_s}{dt} \qquad \text{(A-15)}$$

where $\xi'' = \xi(y=y_1)$.

Substitution of the expression for J_{Fe} from Eq. (4-12) leads to

$$\cdot[D_{Fe}\ \xi\left(\frac{\partial \ell n a_{FeO}}{\partial \xi}\frac{d\xi}{dy} - \frac{d\ell n a_O}{dy}\right)]_{y=y_1} = -\ \xi'' k \qquad \text{(A-16)}$$

From Eqs. (A-3) , (A-11) and A(16) we have

$$k' = \frac{p\xi''^{m-1}\ a_O''^{n}(d\xi/dy)_{y=y_1}}{(p-1)(1-\xi'')} \qquad \text{(A-17)}$$

where $a_O'' = a_O(y=y_1)$.

Substitution of Eq. (A-17) into Eq. (A-14) leads to the differenential equation describing ξ as a function of y

$$\xi[1-(p-1)\xi]\ \frac{d^2\xi}{dy^2} + [m - (p-1)(1-n-m)](\frac{d\xi}{dy})^2$$

$$+ (\xi''/\xi)^{m-1}(a_O''/a_O)^n\ \{\frac{y[1+(p-1)\xi]^2-(1-n)p}{(p-1)(1-\xi'')}\}(\frac{d\xi}{dy})_{y=y_1}(\frac{d\xi}{dy})=0 \qquad \text{(A-18)}$$

For m = 2/3 and n= 1/3 Eqs. (A-11) and (A-18) become, respectively

$$\frac{d\ell n a_O}{dy} = [\frac{k'}{\xi^{2/3}a_O^{1/3}} + (p-1)\ \frac{d\xi}{dy}]/[1+(p-1)\xi] \qquad \text{(A-19)}$$

$$\xi[1+(p-1)\xi]\ \frac{d^2\xi}{dy^2}+m(\frac{d\xi}{dy})^2+(\frac{\xi''}{\xi})^{m-1}(\frac{a_O''}{a_O})^n\{\frac{y(1+(p-1)\xi]^2-(1-n)p}{(p-1)(1-\xi'')}\}$$

$$(\frac{d\xi}{dy})_{y=1}\ (\frac{d\xi}{dy}) = 0 \qquad \text{(A-20)}$$

Equations (A-19) and (A-20) should be solved simultaneously by a numerical method to calculate ξ and a_O as functions of y.

APPENDIX B

TABLE B-1

SELF DIFFUSION COEFFICIENTS OF Fe, Ni AND O IN METALLIC PHASES AT 1000°C

Diffusing Species	Diffusion Medium	Self Diffusion Coefficient cm^2/sec	Remarks	References
Fe	γ-Fe	1.0×10^{-12}	-	206
Fe	Fe-32% Ni Alloy	6.2×10^{-12}	-	207
Ni	Ni	2.5×10^{-12}	-	208
Ni	Ni-20% Fe Alloy	9.4×10^{-12}	-	209
Ni	Ni-30% Fe Alloy	1.1×10^{-11}	-	209
Ni	Fe-19.3% Ni Alloy	2.4×10^{-12}	-	210
O	γ-Fe	6.8×10^{-7}	-	195

TABLE B-2

OXIDE PHASES

Fe	Wustite $Fe_{0.95}O$	3.5×10^{-8}	$p_{O_2}=1.32\ 10^{-15}$ Fe/FeO equilibrium	50
Fe	Magnetite $Fe_{2.993}O_4$	9.2×10^{-10}	-	50
Fe	α-Hematite= Fe_2O_3	$1\ \times10^{-14}$	-	50
O	α-Hematite Fe_2O_3	8.0×10^{-14}	-	43

(continued)

TABLE B-II (continued)

Diffusing Species	Diffusion Medium	Self Diffusion Coefficient cm^2/sec	Remarks	References
Fe	Spinel $Ni_{0.8}Fe_{2.2}O_4$	1×10^{-11}	-	211
Ni	NiO	1×10^{-11}	$p_{O_2}=1$ atm. Average	60,63,64, 84,145, 148
O	NiO	5.3×10^{-15}	Extrapolated	212
Ni	(Fe,Ni)O	7×10^{-10}	$p_{O_2}=1$ atm. mole fraction of FeO $\sim$ 0.01	Present work
Fe	(Fe,Ni)O	2×10^{-9}	$p_{O_2}=1$ atm. mole fraction of FeO $\sim$0.01	Present work

REFERENCES

CH. 1

1. G. Tammann, Z. Anorg. Chem. 111, 78 (1920).
2. N. B. Pilling and R. E. Bedworth, J. Inst. Met., 29, 529 (1923).
3. C. Wagner, Z. physik.Chem. (B) 21, 25 (1933).
4. C. Wagner, Z. physik.Chem. (B) 32, 447 (1936).
5. C. Wagner and K. Gruenewald, Z. physik. Chem. (B) 40, 455 (1938).
6. C. Wagner in *Atom Movements*, ASM, Ohio, 153 (1951).
7. N. N. Greenwood, *Ionic Crystals, Lattice Defects and Nonstoichiometry*, Butterworths, London, (1968).
8. W. W.Smeltzer, R. R. Haering and J. S. Kirkaldy, Acta Met., 9, 880 (1961).
9. B. A. Irving, Corrosion Sc., 5, 471 (1965).
10. J. M. Perrow, W. W. Smeltzer and J. D. Embury, Acta. Met., 16, 1206 (1968).
11. D. L. Douglass, J. Oxidation of Metals, 1, 127 (1969).
12. J. Stringer, Corrosion Sc., 10, 513 (1970).
13. G. C. Wood, J. Oxidation of Metals, 2, 11 (1970).
14. J. Moreau and J. Bénard, J. Rev. Met., 59, 161 (1962).
15. W. Schottky and C. Wagner, Z. physik. Chem. (B) 11, 163 (1930).
16. K. Hauffe, *Reaction in und an festen Stoffen*, Springer, Berlin, 73 (1965).

17. K.Hauffe, Oxidation of Metals, Plenum Press, New York (1965).

18. P. Kofstad, High Temperature Oxidation of Metals, John Wiley, New York (1966).

19. O. Kubaschewski and B. E. Hopkins, Oxidation of Metals and Alloys, Butterworths, London (1962).

20. R. W. Ward, Prog. Inorg. Chem., 1, 465 (1959).

21. H. Schmalzried, Prog. Solid State Chem., 2, 265 (1965).

22. C. Wagner, Corrosion Sc., 9, 91 (1969).

23. D. E. Coates and A. D. Dalvi, J. Oxidation of Metals, 2, 331 (1970).

24. J. S. Kirkaldy, Can. Met. Quart., 8, 35 (1969).

25. J. B. Clark and F. N. Rhines, Trans. ASM, 51, 179 (1959).

26. J. S. Kirkaldy and D. G. Fedak, Trans. AIME, 224, 490 (1962).

27. J. S. Kirkaldy and L. C. Brown, Met. Quart., 2, 89 (1963).

CH. 2

28. L. S. Darken and R. W. Gurry, J. Am. Chem. Soc., 67, 1398 (1945).

29. L. S. Darken and R. W. Gurry, J. Am. Chem. Soc., 68, 798 (1946).

30. J. Paidassi, Trans. AIME, 197, 1570 (1953).

31. P. Vallet and P. Raccah, Mem. Sc. Rev. Met., 62, 1 (1965).

32. C. Carel, Mem. Sc. Rev. Met., 64, 821 (1967).

33. C. Carel, Mem. Sc. Rev. Met., 64, 737 (1967).

34. F. Rizzo and J. V. Smith, J. Phys. Chem., 72, 485 (1968).

35. B. E. F. Fender and F. D. Riley, J. Phys. Chem. Solids 30, 793 (1969).

36. G. H. Geiger, R. L. Levin and J. B. Wagner, J. Phys. Chem. Solids, 27, 947 (1966).

37. D. Tannhauser, J. Phys. Chem. Solids, 23, 52 (1962).

38. I. Bransky and D. Tannhauser, Trans. Met. Soc. AIME, 239, 75 (1967).

39. B. Swaroop and J. B. Wagner, Trans. Met. Soc. AIME, 239, 1215 (1967).

40. P. Kofstad and A. Z. Hed, J. Electrochem. Soc., 115, 102 (1968).

41. M.S. Seltzer and A. Z. Hed, J. Electrochem. Soc., 117, 815 (1970).

42. H. Schmalzried, Z. physik. Chem. N.F., 31, 184 (1962).

43. W. C. Hagel, Trans. Met. Soc. AIME, 236, 179 (1966).

44. O. Kubaschewski and D. M. Brasher, Trans. Faraday Soc., 55, 1200 (1959).

45. J. Moreau and M. Cagnet, Rev. Met., 55, 1091 (1958).

46. W. H. J. Vernon, E. A. Calnan, C.J. B. Clews and T. J. Nurse, Proc. Roy. Soc., (A), 216, 375 (1953).

47. M. H. Davies, M. T. Simnad and C. E. Birchenall, J. Metals, N.Y. 3, 889 (1951).

48. M. H. Davies, M.T. Simnad and C. E. Birchenall, J. Metals, N.Y. 5, 1250 (1953).

49. N. G. Schmahl, H. Baumann and H. Schenk, Arch. Eisenhuttenw. 29, 147 (1958).

50. L. Himmel, R. F. Mehl and C. E. Birchenall, J. Metals, N.Y. 5, 827 (1953).

51. H. J. Engell, K. Hauffe and B. Ilschener, Z. Elektrochem. 58, 478 (1954).

52. H. Uhlig, J. Pickett and J. MacNairn, Acta Met. 7, 111 (1959).

53. E. A. Gulbransen and K. F. Andrew, J. Electrochem. Soc., 104, 451 (1957).

54. G. E. Zima, Trans. ASM, 49, 924 (1957).

55. L. Berry and J. Paidassi, c.r. Hebd. Séanc. Acad. Sci., Paris, 258, 2810 (1964).

56. J. D. Sartell and C. H. Li, J. Inst. Metals, 90, 92 (1961).

57. P. J. Baur, R. W. Bartlett, J. N. Ong and W. M. Fassel,Jr., J. Electrochem. Soc., 110, 185 (1963).

58. D. L. Douglass, Corrosion Sc., 8, 665 (1968).

59. E. A. Gulbransen and K. F. Andrew, J. Electrochem. Soc. 101, 128 (1954).

60. M. T. Shim and W. J. Moore, J. Chem. Phys., 26, 802 (1957).

61. B. Ilschner and H. Pfeiffer, Naturw. 40, 603 (1953).

62. N. Birks and H. Rickert, J. Inst. Metals, 91, 308 (1962).

63. W. J. Moore, U.S. Atomic Energy Commission Report, ORO-78 (1951).

64. K. Fueki and J. B. Wagner, J. Electrochem. Soc., 112, 384 (1965).

65. S. Mrowec, J. Electrochem. Soc., 112, 1260 (1965).

66. S. Mrowec, Z. physik Chem. N.F. 29, 47 (1961).

67. R. Muessner and C. E. Birchenall, Corrosion 13, 677 (1951).

68. A. Dravnieks and H. McDonald, J. Electrochem. Soc., 94, 139 (1948).

69. F. N. Rhines and J. S. Wolf, Met. Trans. 1, 1701 (1970).

70. S. Mrowec, Corrosion Sc., 7, 563 (1967).

71. I. A. Menzies and K. N. Stafford, J. Mater . Sc. 2, 358 (1967).

72. B. M. Vasyutinsky and G. N. Kartmazov, F.Z. Metal i. Metalloved, 15, 132, (1963).

73. R. F. Tylecote and I. E. Mitchell, J.I. S. I. (London) 195, 445 (1960).

74. G. Bliznakov, D. Mehandjiev and F. Elazorava, Compt. rend. de l'Acad. bulgare de Sc. 19, 385 (1966).

75. S. P. Mitoff, J. Chem. Phys. 35, 882 (1961).

76. Y. D. Tretyakov and R. A. Rapp, Trans. Met. Soc. AIME, 245, 1235 (1969).

77. S. Pizzini and R. Morlotti, J. Electrochem. Soc., 114, 1179 (1967).

78. H. H.v. Baumbach and C. Wagner, Z. physik, Chem., (Leipzig) B 24, 59 (1934).

79. A. Duquesnoy and F. Marion, Compt. Rend. 256, 2862 (1963).

80. R. Uno, J. Phys. Soc. Japan, 22, 1502 (1967).

81. I. Bransky and N. M. Tallan, J. Chem. Phys. 49, 1243 (1968).

82. J. T. Cox and C. M. Quinn, J. Mater. Sc., 4, 33 (1969).

83. Z. M. Jarzebski and S. Mrowec, J. Oxidation of Metals, 1, 267 (1969).

84. M. L. Volpe and J. Reddy, J. Chem. Phys. 53, 1117 (1970).

85. G. L. Wulf, T. J. Carter and G. R. Wallwork, Corrosion Sc., 9, 689 (1969).

86. R. T. Foley, J. Electrochem. Soc., 109, 1202 (1962).

87. L. A.Menzies and W. J. Tomlinson, JISI, 204, 1239 (1966).

88. L. A. Morris and W. W. Smeltzer, Acta Met., 15, 1591 (1967).

89. R. T. Foley, J.U . Druck and R. E. Fryxell, J. Electrochem. Soc.,102, 440 (1955).

90. R. T. Foley, C.J. Guare and H. R. Schmidt, J. Electrochem. Soc., 104, 413 (1957).

91. R. T. Foley and C. J. Guare, J. Electrochem. Soc., 106, 936 (1959).

92. R. T. Foley, J. Electrochem. Soc., 108, 216 (1961).

93. R. T. Foley, J. Electrochem. Soc., 109, 278 (1962).

94. J. Bénard and J. Moreau, Rev. Met., 47, 317 (1950).

95. P.K. Koh and B. Caugharty, J. Appl. Phys., 23, 427 (1952).

96. J. W. Hickman and E. A. Gulbransen, Trans.AIME , 171 344 (1947).

97. S. W.Kennedy, L. D. Calvert and M. Cohen, Trans. AIME, 215, 64 (1959).

98. H. J. Yearian,H. E. Boren Jr., and W. E. Warr, Corrosion, 12 , 561 (1956).

99. I. A. Menzies and W.J. Tomlinson,J. Mater. Sc., 2, 529 (1967).

100. O. Kubaschewski and O. von Goldbeck, Trans. Faraday Soc., 45, 959 (1949).

101. R. A. Oriani, Acta Met.,1, 448 (1953).

102. M. J. Brabers, W. J. Heidegar and C. E. Birchenall, Chemie Physique, 53, 810 (1956).

103. M. J. Brabers and C. E. Birchenall, Corrosion,14, 179 (1958).

104. P. E. C. Bryant, M. Sc. Thesis, McMaster University (1965).

105. G. S. Viktorovich and D. I. Lisovskii, Tsvetnye Metally, (Eng. transl.), 7, (11), 49 (1966).

106. G. S. Viktorovich, V. A. Gutin and D. I. Lisovskii, Tsvetnye Metally, (Eng . Transl.) , 7, (12), 54 (1966).

107. A. E. Paladino Jr., J. Am. Ceram. Soc., 42, 168 (1959).

108. G. A. Roeder and W. W.Smeltzer, J. Electrochem. Soc., 111, 1074 (1964).

109. K. Kiukkola and C. Wagner, J. Electrochem. Soc., 104, 379 (1957).

CH. 3

110. C. Wagner, Z. Elektrochemie, 63, 772 (1969).

111. R. A. Rapp, Corrosion, 21, 382 (1965).

112. F. N. Rhines, W. A. Johnson and W. A. Anderson, Trans. AIME, 147, 205 (1942).

113. D. E. Thomas, J. Metals N.Y. 3, 926 (1951).

114. C. Wagner, J. Electrochem. Soc., 99, 369 (1952).

115. F. Maak and C. Wagner, Werkstoffe und Korrosion, 12, 273 (1961).

116. F. N. Rhines, Trans. AIME, 137, 246 (1940).

117. L. S. Darken, Trans. AIME., 150, 157 (1942).

118. J. L. Meijering and M. J. Druyvesteyn, Philips Res. Rept., 2, 81 (1947).

119. R. A. Rapp, Acta Met., 9, 730 (1961).

120. R. A. Rapp, D.F. Frank and J. V. Armitage, Acta Met. 12, 505 (1964).

121. G. Böhm and M. Kahlweit, Acta Met., 12, 641 (1964).

122. C. Wagner, J. Electrochem. Soc., 103, 571 (1956).

123. O. Kubaschewski and O. von Goldbeck, J. Inst. Metals, 76, 455 (1938).

124. F. Maak, Z. Metallkde., 52, 545 (1961).

125. C. Wagner, Corrosion Sc., 8, 889 (1968).

126. C. Wagner, J. Colloid. Sc., 5, 85 (1950).

127. M. Kahlweit, Z. physik. Chem. N.F. 32, 1 (1962).

128. P. Bolsaits and M. Kahlweit, Acta Met., 15, 765 (1967).

CH. 4

129 A. D. Dalvi and D. E. Coates,J. Oxidation of Metals, in press.

130. L. S. Darken, Trans. Met. Soc. AIME, 221, 654 (1961).

131. L. Onsager, Ann. N.Y. Acad. Sci., 46, 241 (1945).

132. L. S. Darken in Atom Movements, ASM, Cleveland, 1 (1951).

133. J. E. Lane and J. S. Kirkaldy, Can. J. Phys. 42, 1643 (1964).

134. N. F. Mott and R. W. Gurney, Electronic Processes in Ionic Crystals , Clarendon Press, Oxford (1950).

135. C. Wagner, Thermodynamics of Alloys, Addison-Wesley Press (1952).

136. A.D.Dalvi and D. E. Coates, Unpublished work.

137. G. G. Charette and S. J. Flengas, J. Electrochem. Soc., 115, 796 (1966).

138. G. Zintl, Z. physik. Chem. N.F., 48, 340 (1966).

139. G. Zintl, Z. physik Chem., N.F., 54, 110 (1967).

140. G. C. Wood and J. M. Ferguson, Nature, 208 , 369 (1965).

141. E. Aukrust and A. Muan, Trans.Met.Soc.AIME, 227, 1378 (1963).

142. W. C.Hahn and A. Muan, Chem. Solids, 19, 338 (1961).

143. B. Fisher and S. D.Tannhauser, J. Electrochem. Soc. 111, 1194 (1964).

144. R. E. Carter and F. D. Richardson, Trans. AIME, 200, 1244 (1954).

145. J. B. Price and J. B. Wagner, Z. physik. Chem. N.F. 49, 257 (1966).

146. H. G. Sockel and H. Schmalzried, Ber. Bunsenges , physik Chem. 72, 745 (1968).

147. G. N. Error and J. B. Wagner, J. Phys. Chem. Solids, 29, 1597 (1968).

148. R. L. Lindner and A. Akerstrom, Discussions Farad. Soc., 23, 133 (1957).

149. J. S. Choi and W. J. Moore, J. Phys. Chem. 66, 1308 (1962).

150. A. Werner, Z. physik.Chem. N.F., 47, 267 (1965).

151. N. Valverde, Z. physik.Chem. N.F., 61, 92 (1968).

152. N. Valverde, Z. physik. Chem. N.F., 62, 218 (1968).

153. C. Wagner, private communication.

154. Y. Adda and J. Philibert, La Diffusion dans les solides, Vol. II, Presses Universitaires de France, Paris, 1053 (1966).

155. L. S. Darken, Trans. AIME, 180, 430 (1949).

156. H. Schmalzried and J. B. Holt, Z. physik. Chem. N.F., 60, 220 (1968).

157. C. Wagner, Acta Met. 17, 99 (1969).

158. J. S. Kirkaldy, Oxidation of Metals and Alloys, ASM Symposium (1970) in press.

CH. 5.

159. F. N. Rhines and A.H. Grobe, Trans. AIME, 147, 318 (1942).

160. J. W. Rutter and B. Chalmers, Can. J. Phys., 31, 15 (1953).

161. W.A. Tiller, K. A.Jackson, J. W. Rutter and B. Chalmers, Acta. Met., 1, 428 (1953).

162. D.E. Coates and J. S. Kirkaldy, J. Crystal Growth, 3,4 , 549 (1968).

163. D. E. Coates and J. S. Kirkaldy, Trans. ASM, 62, 426 (1969).

164. W. W. Smeltzer, Trans. Can. Min. Met. Soc. 65, 367 (1962).

165. J. M. Perrow and W. W. Smeltzer, J. Electrochem. Soc. 109, 1023 (1962).

166. A. D. Dalvi and W.W. Smeltzer, J. Electrochem. Soc., 117, 1431 (1970).

167. J. Moreau, Publ. Inst. Recherches Siderurgie, (A), No. 49 (1953).

168. D. Lai, R. J. Borg, M. J. Brabers, J. D. Mackenzie and C.E. Birchenall, Corrosion 17, 357 (1961).

169. A. U. Seybolt, J. Electrochem. Soc., 107, 147 (1960).

170. C. T. Fujii and R. A. Meussener, Trans.Met.Soc. AIME, 242, 1259 (1969).

171. H. J. Yearian, E. G. Randell and T. A. Longo, Corrosion, 12, 515 (1956).

172. G. L. Wulf, M. B. McGirr and G. R. Wallwork, Corrosion Sc., 9, 739 (1969).

173. J. E. Croll and G. R. Wallwork, J. Oxidation of Metals, 1, 55 (1969).

174. J. Moreau and J. Bénard, Compt. Rend. 237, 1417 (1953).

175. C. G. Giggins and F.S. Pettit, Trans. Met. Soc. AIME, 245, 2495 (1969).

176. G. C.Wood, J.Hodgkiess and D. P. Whittle, Corrosion Sc. 6, 129 (1966).

177. Von Irmtaud Pfeiffer, Z. Metallkde., 51, 322 (1960).

178. G. C. Wood and J. Hodgkiess , J. Electrochem. Soc., 113, 319 (1966).

179. F. Maak, Z. Metallkde., 52, 538 (1961).

180. M. Hansen, *Constitution of Binary Alloys*, McGraw Hill, New York, 1024 (1958).

181. L. E. Samuels, Metallographic Polishing by Mechanical Methods, Pitman, London (1967).

182. D. G. Wickham, Laboratory for Insulation Research, Tech. Rept. No. 89, M.I.T. (1954).

183. L. S. Birks, Electron Probe Microanalysis, Interscience. New York (1963).

184. R. Castaing, Adv. Electronics and Electron Phys. 13 317 (1960).

185. T. D. McKinley, K.F.J. Heinrich and D. B.Whittry Editors, The Electron Microcrobe, John Wiley, (1966).

186. A. D. Dalvi, The Electron Probe Microanalyser, McMaster University (1969).

187. C. A.Friskney and C. W. Haworth, Brit. J. Appl. Phys. Ser. 2, 1, 873 (1968).

188. C. A. Friskney and C. W. Haworth, J. Sci. Instr.Ser. 2, 1, 753 (1968).

189. P. Duncumb and S. J. B. Reed, Nat. Bur. Std. (U.S.) Spec. Publ. No. 298 (1968).

190. J. Philbert, X-Ray Optics and X-Ray Microanalysis, Proc. Third Int. Symp., Stanford 1962, Academic Press , N. Y. (1963).

191. P. Duncumb and P. K. Shields, in The Electron Microprobe, 284, J. Wiley, N.Y. (1966).

192. M. Green and V. E. Cosslet, Proc. Phys. Soc., (London) 78, 1206 (1961).

CH. 7

193. S. J. Reed, X-Ray Optics and Microanalysis, Hermann, Paris, p. 339 (1965).

194. S. I. Youssef, M. G. Natera, R. J. Begum, B. J. Srinivasan and N. S. Murthy, J. Phys. Chem. Solids, 30, 1948 (1969).

195. J. Swisher and E. T. Turkdogan, Trans. Met. Soc. AIME 239, 626 (1967).

196. R. Hultgren, R. L. Orr, P. D. Anderson and K. K. Kelley, Selected Values of Thermodynamic Properties of Metals and Alloys , John Wiley (1963).

197. J. D. Tretjakow and H. Schmalzried, Berichte der Bunsengesellschaft, 69, 396 (1965).

198. H. Davies, Research Report, McMaster University, (1970).

CH. 8

199. K. C. Russel in Phase Transformations, ASM, Cleveland, 219 (1970).

CH. 9

200. F. S. Pettit, Trans. Met. Soc. AIME, 239, 1296 (1967).

201. W. B. Crow, Electrochem. Soc., Extended Abstract No. 149. Atlantic City Meeting (1970).

202. P. N. Smith, Ph.D. Thesis, McMaster University, 82 (1970).

203. Rolf Grundmann, Ph.D. Thesis, Technische Hochschule, Aachen, pp. 41, 42 (1967).

CH. 10

204. J. S. Anderson, Proc. Chem. Soc., p. 166 (1964).

205. R. F. Gould, Editor, Nonstoichiometric Compounds, Adv. in Chem. Series, 39, Am. Chem. Soc., Washington, D. C. (1963).

APPENDIX

206. P. L. Gruzin, J. W. Kornew and G. W. Kurdjumor, Dokl. Akad. Nauk. U.S.S.R., 80, 49 (1951).

207. M. Badia and A. Vignes, Compt. Rend. 264, 1528 (1967).

208. I. V. Ivantsov, Fiz. Metal. metalloved, 22, 725 (1966).

209. E. W. deReca and C. Pampillo, Acta Met., 15, 1263 (1967).

210. G. F. Hancock and G. M. Leak, Met. Sc. Journal, 1, 33 (1967).

211. R. H. Condit, M. J. Brabers and C. E. Birchenall, Trans. AIME, 218, 768 (1960).

212. M. O'Keeffe and W.J. Moore, J. Phys. Chem., 65, 1438 (1961).